Title	Nanoscale Film Morphologies of Topological Polymers
Author(s)	Ree, Brian Jiwon
Citation	北海道大学. 博士(工学) 甲第14025号
Issue Date	2020-03-25
DOI	10.14943/doctoral.k14025
Doc URL	http://hdl.handle.net/2115/84649
Type	theses (doctoral)
File Information	Brian_Jiwon_Ree.pdf

Nanoscale Film Morphologies of Topological Polymers

A Dissertation for the Degree of Doctor of Philosophy

Brian J. Ree

Hokkaido University

March 2020

Acknowledgements

The study presented in this dissertation has been performed under the direction of Professor Toshifumi Satoh, Division of Applied Chemistry, Faculty of Engineering, Hokkaido University. I would like to express the biggest and sincerest appreciation to Professor Toshifumi Satoh for his tremendous support as well as thorough guidance, discussions, and words of wisdom throughout this academic journey of mine. I could not have imagined having a better advisor and mentor for the studies and research works in the Ph.D program.

I am also grateful to Professor Takuya Isono, Division of Applied Chemistry, Faculty of Engineering, Hokkaido University, for all the helpful suggestions and fruitful discussions since my first day in the laboratory.

I also thank Professor Toshikazu Takata and Professor Daisuke Aoki, Department of Chemical Sciences and Engineering, Tokyo Institute of Technology for all the collaborative works and productive discussions on the very interesting, unique polymer systems.

Much appreciation is expressed to Professor Tajima, Professor Yamamoto, Professor Sada, and Professor Tokeshi for providing helpful advice as the committee members for the evaluation of my Ph.D. dissertation.

Special thanks goes to Kodai Watanabe. It was an unforgettable experience and a great honor to have him as my friend and an academic comrade throughout the past three years. Words cannot fully describe my appreciation but I am lucky to have met him. And I also thank all the members of Polymer Chemistry Laboratory. All of you are my academic family; and it was great to work alongside with everyone over the years.

The last and not the least, I extend the greatest love and thanks to my family and friends for all the love, encouragement and support. It would not have been possible without you all.

March 2020

Brian Ree

Contents

Chapter 1

General Introduction

1.1 Topological polymers

Topology of a polymer describes the shape and spatial features of the polymer's main chain. General examples of topological polymers include linear, tadpole, cyclic, cage, star, dendritic, network and graft topologies, as shown in Figure 1.1, and many different synthetic strategies have already been reported.[1-5] Examples of more complex and exotic polymer topologies have been reported and are currently being investigated by many polymer research group's innovative synthetic strategies.[6-17] In addition to the synthesis of new types of topological polymers, many efforts are being made into establishing efficient and well-controlled synthetic routes that promote high purities and high yields, especially for cyclic polymers.[18-36] For instance, the synthesis of cyclic polymers have been evolving through many generations of polymer scientists since the first report of a synthetic cyclic polymer in 1946.[37-39] Along the discoveries of naturally-occurring cyclic polymers, such as cyclic deoxyribonucleic acids (c-DNA),[40-43] cyclic proteins[44,45] and cyclic polysaccharides,[46] many studies have also observed and established the notion that the cyclic topology influences the physical properties of polymers by exhibiting a higher thermal stability, higher glass transition temperature, higher melting temperature, lower viscosity, smaller radius of gyration, and smaller hydrodynamic volume than linear polymers.[3,24,30,31,36,47] Other topologies, such as dendritic, network and graft topologies, hold unique variations of the physical properties in comparison to linear topology.[47-50] As for more exotic topologies including the topological block copolymers, however, there is no consensus on how the physical properties of polymers are affected by such unique shapes and spatial features. Hence, it could be stated that the current perception of polymer topology remains at a rather premature stage of only recognizing the resulting effects of specific polymer topology types and lacking the fundamental comprehension of how polymer topology affects different aspects and properties of polymers. Given the great variety of polymer topology types reported thus far, the challenge of understanding such correlation appears substantially demanding and exhaustive. Additionally, the majority of the research on topological polymers are heavily focused on the synthesis whereas the number of investigations on the physical and morphological properties is rather scarce. It is, therefore, essential to address the fundamental basis in which polymer topology influences the physical and morphological properties of polymers.

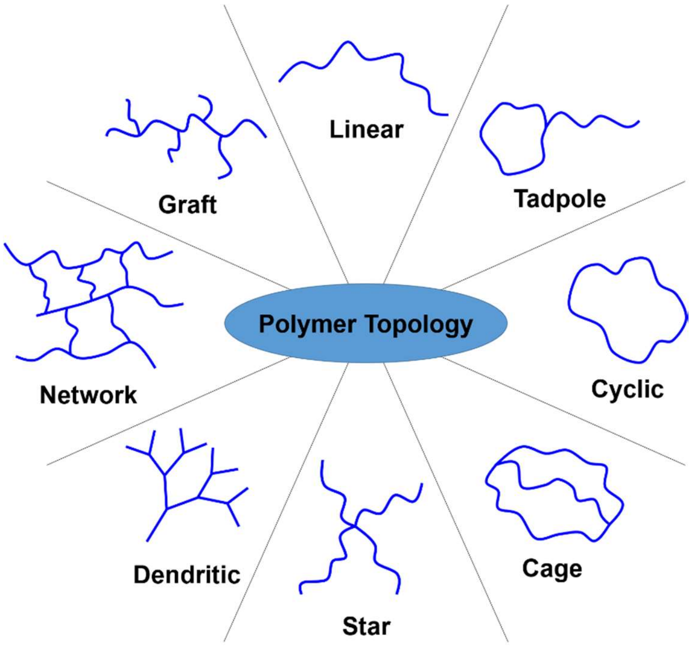

Figure 1.1. General types of polymer topologies including linear, tadpole, cyclic, cage, star, dendritic, network and graft topologies.

The first detailed discussion of the physical properties of topological polymers was pioneered by Flory in 1985,[48] which centered on the impact of the topological features of network polymers on the chain conformation and the theory of rubber elasticity. In 1989, Duplantier demonstrated the use of statistical mechanics as a tool to interpret the network topology as an assembly of star polymer constituents to predict the critical exponents of any network polymers in good and theta solvent conditions.[49] In 2001, although it does not contain discussions about the physical properties, Tezuka et al. reported the first generalized description for classifying various nonlinear topologies based on graph theory.[51] By taking the aforementioned studies into consideration, it is possible to interpret any polymer topology and discuss their impact upon the physical and morphological properties based on the following three factors: the number of chains, the number of chain ends, and the number of chain junctions. These three factors are vital aspects in comprehending the chain conformation and dynamics with respect to the molecular theories of polymer chains such as reptation theory,[52] random coil theory,[53] and entanglement theory.[54,55] Such a systematic analysis and evaluation of the spatial configuration of polymer chains in unique topologies aid in grounded discussions regarding the various properties of topological polymers such as the self-assembly characteristics and morphological properties.

1.2 Polymer Self-assembly and Thin Film Morphology

Self-assembly describes the physical rearrangement of polymeric chains from a disordered state to ordered state under the laws of thermodynamics. The concept of self-assembly could be further elaborated with the Gibb's free energy equation,

$$\Delta G = \Delta H - T\Delta S \tag{1}$$

where the enthalpic gain must outweigh the entropic loss to reach an energetically stable, ordered chain arrangement from the disordered state. A polymeric system could achieve enthalpic gain through the means of various intermolecular forces including the Coulomb force, inductive force, and dispersion force. This is an important factor that distinguishes amorphous polymers from semi-crystalline polymers, and also miscible block copolymers from immiscible block copolymers. Hence, strategic molecular designs incorporating functional monomers that exploit the balance of intermolecular forces effectively promote the self-assembly behavior. This is a powerful bottom-up approach for developing high performance polymer based nanotechnology applications in various fields, such as microelectronics, optics, sensors and microporous materials, due the following potentials: easy fabrication processes, miniaturized nanoscale dimensions, great scalability, energy efficient operation, three-dimensional stacking capability, light weight, structural flexibility, wearability, and low-cost potential.[56-65]

Miniaturization is one of the key interests in academics and industry because it serves as the foundation and driving force behind the advancements of modern information technology. Moore's law is the first empirical observation correlating the miniaturization of transistors to the increased transistor number density in integrated circuits, which resulted in an increased computing performance of microprocessors.[66] Polymer self-assembly is a promising alternative to the modern printing and patterning techniques as it reduces the number of physical fabrication processes and fabrication born structural defects. This is a critical issue in microelectronics applications because the top-down approach of current fabrication processes for silicon-based microprocessors involves high levels of mechanical stress, high sensitivity to contaminants, and multiple uses of expensive and chemically harsh materials.[67-74] The fabrication born structural faults are known to range from micro- to nanometer scale,[72-76] thereby inducing a rather broad range of microprocessor performance inconsistencies and having conjured the term "silicon lottery" amongst the users of modern microprocessors.[77] By enabling polymer self-assembly to establish structures necessary for the active layer of nanodevices, the aforementioned structural defects can be completely bypassed and achieve device performance consistency.

Polymers, however, are not the absolute alternative solution to current lithographic technologies as of yet because miniaturization of polymer morphology, while maintaining long range order, is indeed difficult to achieve. Much effort is being made to optimize the types of polymers as well as fabrication conditions to achieve small domain spacing and long range order.[59-61,64,78-81] Conceptually, the less long range order character in a polymer layer would be equivalent to having more structural defects in conventional processors. In order to achieve a long range order morphology, the aforementioned thermodynamics limit conventional polymers with two options: find a highly effective annealing condition and reduce the polymer chain length. These options, however, exhibit rather serious practical disadvantages. First, the process of finding an annealing condition is not only time consuming but it does not guarantee success. In addition, the commonly observed proportional correlation between the polymer chain length and various physical properties suggest that the chain length reduction will lessen critical properties such as wettability/coatability as well as the thermal stability, which would exert serious challenges during the fabrication processes.[82,83] Furthermore, a short chain length could drive the free energy state of the entire polymer to spontaneously favor an amorphous, disordered state. It is then essential to have another variable to control the behavior of the polymer chains in addition to determining the annealing conditions and optimizing themolecular weight, such as the polymer topology. By altering the topology to control the chain conformation in such a manner to promote the nanoscale morphology with a long range order without sacrificing the key physical properties, polymers could effectively serve as practical alternatives to the fabrication of modern microelectronic applications. Achieving such a feat would require forming a systematic development cycle consisting of a well-controlled synthesis of topological polymers and precise morphological characterizations. However, there is an obstacle regarding the morphological characterization of topological polymers. As the domain spacing of the polymer morphology becomes smaller, structural characterization becomes increasingly difficult and less precise via conventional methods such as transmission electron microscopy (TEM) and atomic force microscopy (AFM). This calls for a different characterization method, namely, X-ray scattering.

1.3 Synchrotron X-ray Scattering

There are two types of morphological characterization methods developed thus far: microscopy and scattering. Microscopy is the most common and conventional morphological method which includes various types such as AFM, TEM, and scanning electron microscopy (SEM). The greatest benefits of microscopy is direct observation of the subject's surface structure in real space. However, there are numerous shortcomings specifically for polymer microscopy as follows.[84-87] First, microscopy provides localized surface images and therefore a great number of measurements are required to provide concrete evidence supporting the observed structure does indeed represent the entire sample. A statistical analysis and averaging is simplified in the case of inorganic materials, but it may be very difficult to give definite, quantitative structural parameters in the case of polymers. Secondly, the observation of artifacts and optical aberrations further increase the difficulty in accurate measurement and data analysis. Additional difficulties and biases may also arise from the two dimensional surface images providing limited information in the cases of highly complex morphologies and/or the structural subject of interest is oriented parallel to the surface. Moreover, reduction of detection limit (i.e. shorter distance) increases vulnerability to electrical noise, vibrations, air pressure, air quality (presence of unwanted particulates), temperature fluctuation, and lowered tolerance to external forces. Furthermore, the low electron density contrast of polymers requires the addition of heavy element contrast additives in the case of TEM, thereby altering and perturbing the natural state of polymers. Additives may induce changes in the polymer morphology. The extents of sample invasion reaches further with microtomy, which could induce deformation and mechanical stress to sample. Also, polymers exhibit varying degrees of sensitivity to incident radiation as potential radiation damage could occur in TEM, and charging effect from SEM incident radiation reduces image resolution. Most critically, microscopy technique is only applicable to samples fabricated in solid state thin film.

Measurements of samples in bulk state or in solution are not available. Due to the nature of synthetic polymers always having some degree of molecular weight distribution, the polymer morphologies are less likely to have idealistic levels of structural order found in inorganic crystals. Therefore, microscopy could not be used as a universal tool for morphological characterization of polymers.

Scattering, specifically synchrotron X-ray scattering, is an alternative morphological characterization method to microscopy that has been gaining great interest and thorough utilizations from polymer scientists since the construction of third generation synchrotron facilities began in the mid-1990s. Unlike the second generation synchrotrons, the addition of wiggler or insertion devices to the third generation synchrotrons achieved in providing focused, bright X-ray beams that gave high quality signals from polymers.[88] Since mid-1990s, steady improvements in synchrotron operation yielding higher flux and tunable levels of high energy X-ray beams, along with improved detectors, have initiated a new establishment for polymer morphology research.[89] The greatest benefit of X-ray scattering as a morphological characterization method is its wide flexibility and nondestructive nature regarding the measurement conditions. Measurements on both solid (thin film and bulk) and solution states are available for obtaining ensemble averaged data from macroscopic dimensions of samples in its natural state. Therefore, the measured X-ray scattering data contains full, three dimensional structural information of any morphological features within the sample. In addition, as long as the incident X-ray beam's pathway through the sample and to the detector is not disturbed, the sample stage could be designed to accommodate a variety of conditions or in-situ, dynamic experiments.[59,90-99] Moreover, modern synchrotron X-ray radiation facilities provide ångström resolution for gathering statistical and quantitative structural information of both highly ordered and disordered structures.[90,96]

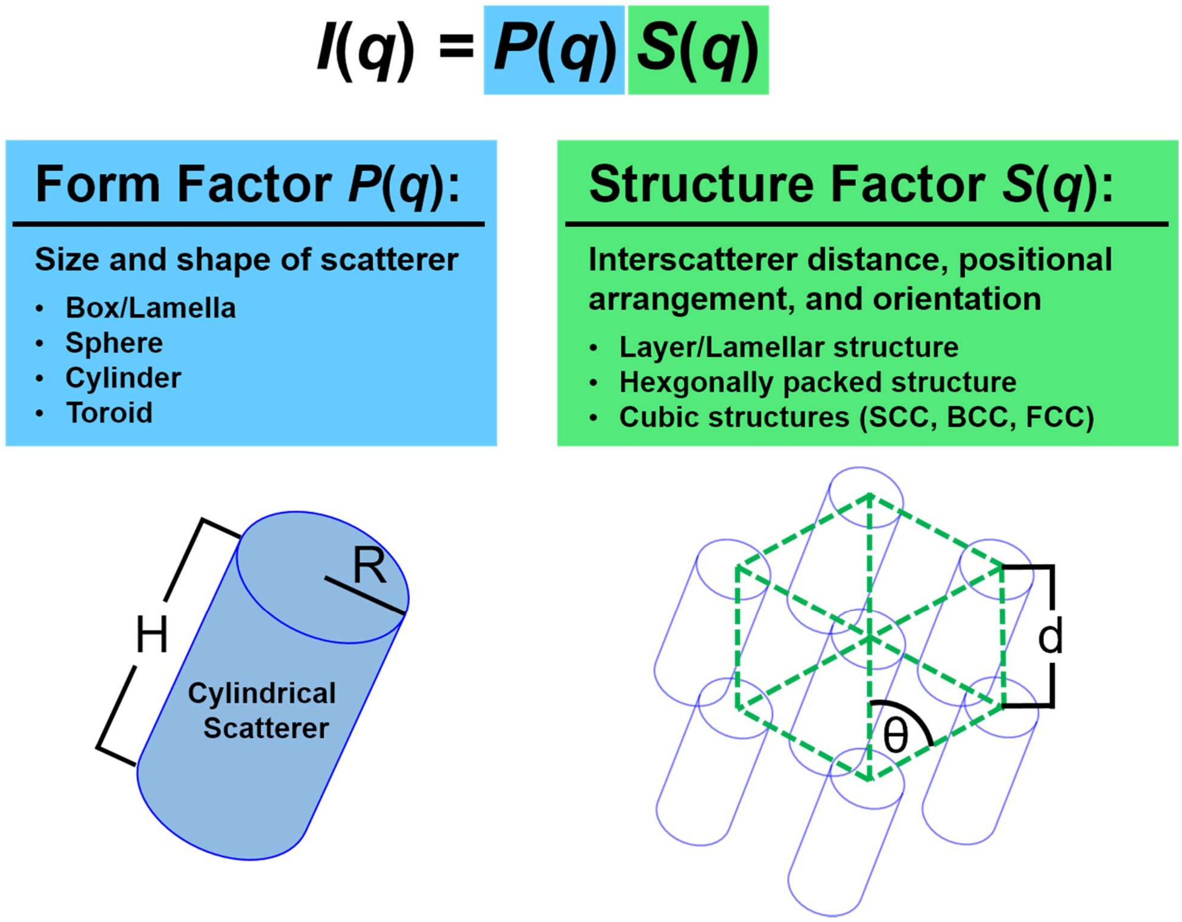

Figure 1.2. Visual overview of scattering intensity *I*(*q*), composed of the form factor *P*(*q*), and structure factor *S*(*q*).

There are, however, some challenges regarding the use of such advanced technique. Firstly, the measured scattering data is strictly based on the scattering intensity originating from electron density contrast, thereby requiring sufficient electron density contrast in the measured sample for appropriate data collection. For instance, solid state morphology of a diblock copolymer consisting of two blocks having similar chemical components may not be discernable with this technique. Secondly, X-ray scattering does not provide structural information via direct observation because the measured data resides in reciprocal space, which implies that spatial contrast of electron density at few nanometers to sub-micrometer distances occur at small angle region while distances lesser than sub-nanometers occur at wide angle region. Also, the measured scattering intensity $I(q)$ is composed of two components, the form factor $P(q)$, and the structure factor $S(q)$, as shown in Figure 1.2 and the following generalized equation of scattering intensity:[90]

$$I(q) = P(q)\, S(q) \tag{2}$$

This implies that structural information is only obtained from the data analysis of scattering data based on the principles of scattering theories. Compounded by the phase problem (shown in Figure 1.3), it is impossible to directly retrieve structural information from either the form factor or the structure factor. As a result, two data analysis approaches have been developed so far, which are the correlation function method and the modeling method. The correlation function method is considered as the classical method as many representative works[100-116] have already been established but it is often used in a complementary manner with other microscopy techniques due to the limited number of structural parameters and qualitative insights it provides. The modeling method, also referred as fine structure method, has the potential of providing a greater set of detailed structural parameters and statistical information than the correlation function method. By specifying the shape of scatterer (form factor $P(q)$) and the positional correlation of scatterers (structure factor $S(q)$) via mathematical expressions based on scattering principles, a complete set of precise structural parameters could be obtained.

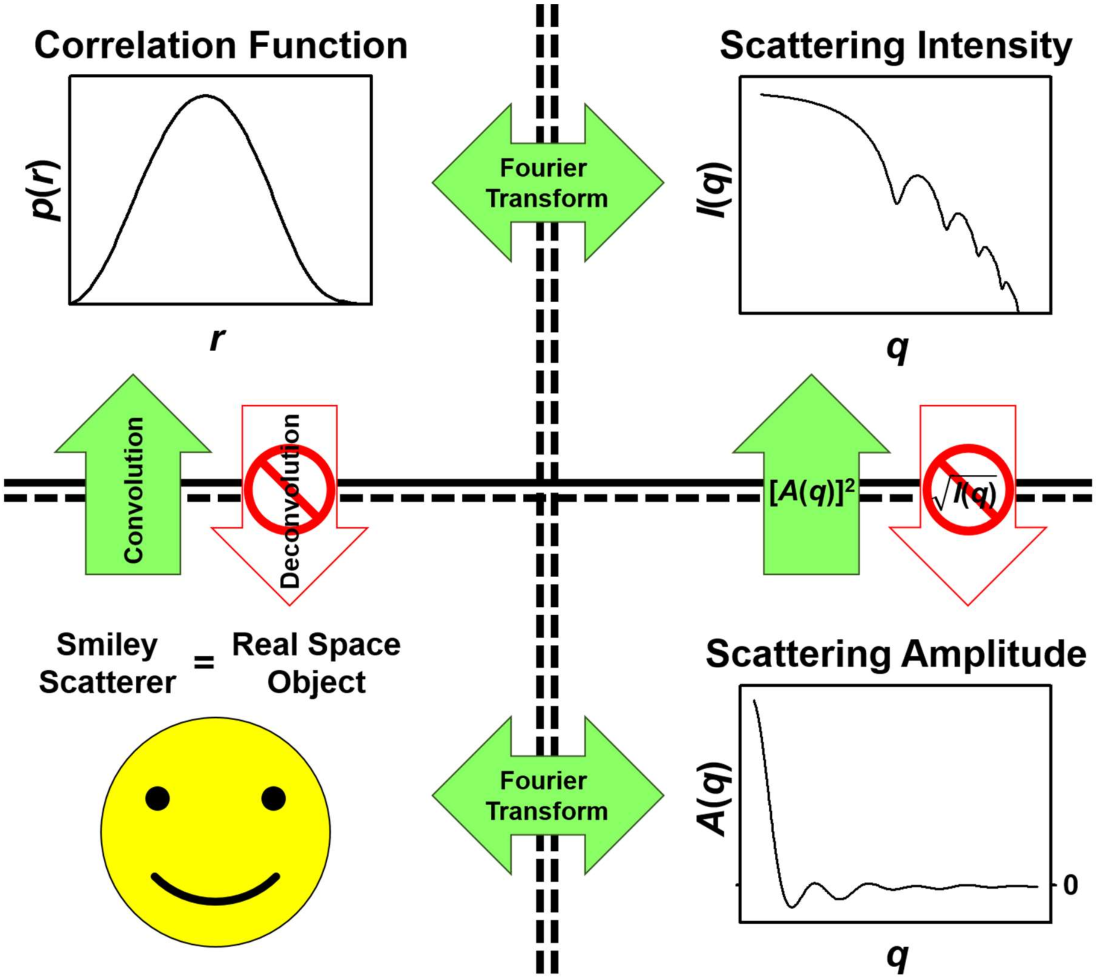

Figure 1.3. Conceptual representation of the phase problem present in X-ray scattering.

Thus far in solid state morphological investigations, the modeling method have been effectively utilized in characterizing polymer thin film morphology than polymer bulk morphology.[58-61,64,71,90-92] This is because the macroscopic dimensions of bulk state allows not only primary morphological features of polymers to occur (i.e. polymer crystals, phase-separated microstructures) but also more complex structures such as spherulites and so on. This implies the measured scattering intensity contains structural information of more than a single structure, thereby raising the complexity of the theoretical model required for data analysis. In nanoscale thin films, however, the film thickness functions as a source of dimensional restriction to impose confinement effect on polymers' chain conformation. Under such circumstance, the resulting polymer morphology is defined only by the primary morphological features, allowing theoretical models to be more precise and statistically descriptive. In addition to simplifying the polymer morphology, the unique dimensions of nanoscale thin films have also affected the data collection to take the form of grazing incidence X-ray scattering (GIXS) as shown in Figure 1.4. GIXS is a unique form of X-ray scattering which takes the reflection geometry rather than the transmission geometry present in bulk or solution X-ray scattering. The term grazing and reflection geometry implies that the incident X-ray beam makes contact with the thin film at a low angle to increase the volume and length of X-ray's path through the film.[117] It effectively increases the scattering intensity by three orders of magnitude in comparison to the intensity measured with the thin film positioned normal to the X-ray beam.[88] Also, the increased X-ray path indicates the measured scattering intensity is statistically more representative of the thin film. However, the application of such unique measurement geometry led to the development of new scattering theories on the basis of distorted-wave Born approximation (DWBA) (depicted in Figure 1.5) to accommodate the complex interference behavior of the incident and reflected X-ray beam.[88,117-120] The new GIXS theory serving as the basis for the modeling method have successfully characterized polymer thin film morphologies. In the case of polymer thin film morphology, lamellar and hexagonal packed cylinder structures are the most commonly observed morphological features. The following section contains mathematical descriptions of the theoretically constructed models for the two aforementioned structures utilized throughout this dissertation: the three layer model and the two phase elliptical hexagonal cylinder model.

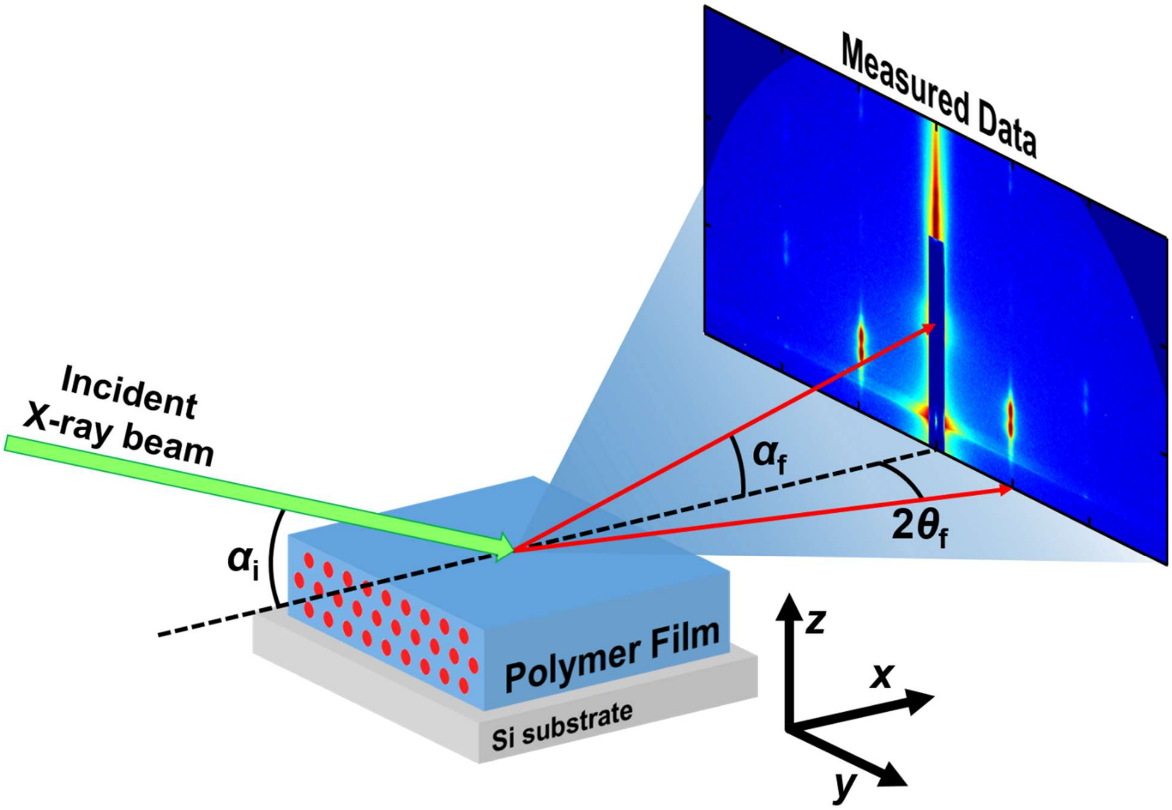

Figure 1.4. Reflection geometry of GIXS: an incident X-ray beam approaches the surface of polymer thin film at an angle α_i (incidence angle) and the scattered intensity is measured by two-dimensional charge-coupled detector (2D CCD). α_f is the exit angle of scattered X-ray with respect to the *z*-axis, and $2\theta_f$ is the exit angle of scattered X-ray with respect to the *y*-axis.

1.4 Grazing Incidence X-ray Scattering Theory

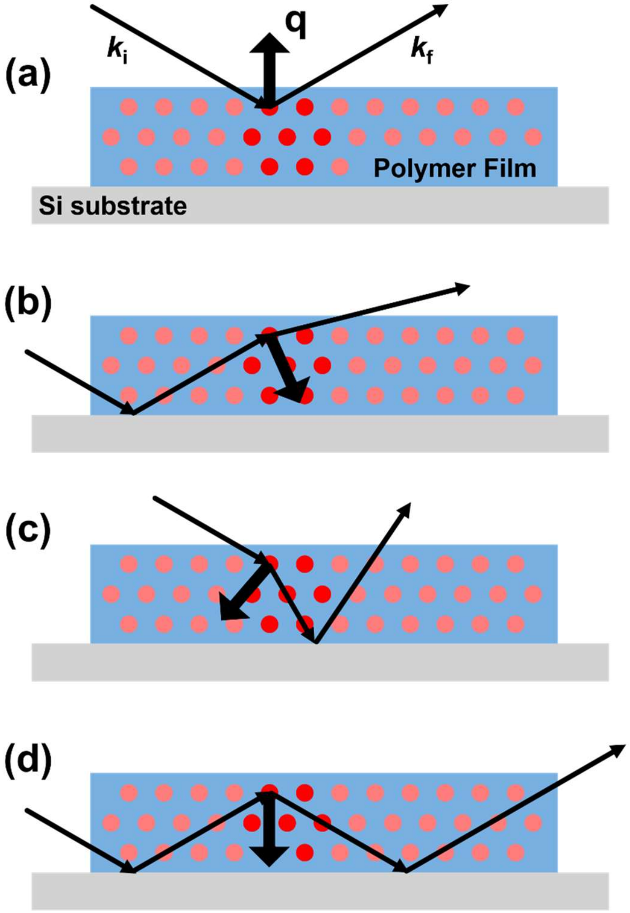

Figure 1.5. Side view depicting the four major contributions of distorted-wave Born approximation (DWBA) in reflection geometry where k_i is the wave vector of incident beam, k_f is the wave vector of scattered beam, and **q** is the scattering vector: (a) the X-ray beam is scattered by the scatterer; (b) the X-ray beam is initially reflected at the film-substrate interface and then scattered by the scatterer; (c) the X-ray beam is initially scattered by the scatterer and then reflected at the film-substrate interface; (d) the X-ray beam is initially reflected at the film-substrate interface, scattered by the scatterer, and then reflected at the film-substrate interface. The correlation of the four contributions to the measured scattering intensity is expressed in equation 3.

In GIXS, the scattering intensity from the structures residing inside a thin film can be expressed by the following scattering formula from recent reports:[117-131]

$$I_{\mathrm{GIXS}}(\alpha_{\mathrm{f}},2\theta_{\mathrm{f}}) \cong \frac{1}{16\pi^2}\cdot\frac{1-e^{-2\,\mathrm{Im}(q_z)t}}{2\,\mathrm{Im}(q_z)}\cdot\begin{bmatrix} |T_{\mathrm{i}}T_{\mathrm{f}}|^2 I_1(q_{\|},\mathrm{Re}(q_{1,z})) \; + \\ |T_{\mathrm{i}}R_{\mathrm{f}}|^2 I_1(q_{\|},\mathrm{Re}(q_{2,z})) \; + \\ |T_{\mathrm{f}}R_{\mathrm{i}}|^2 I_1(q_{\|},\mathrm{Re}(q_{3,z})) \; + \\ |R_{\mathrm{i}}R_{\mathrm{f}}|^2 I_1(q_{\|},\mathrm{Re}(q_{4,z})) \end{bmatrix} \qquad (3)$$

where α_{f} and $2\theta_{\mathrm{f}}$ are the out-of-plane and in-plane exit angle of the X-ray beam from the thin film respectively, $\mathrm{Im}(q_z) = |\mathrm{Im}(\mathrm{k}_{z,\mathrm{f}})| + |\mathrm{Im}(\mathrm{k}_{z,\mathrm{i}})|$, $\mathrm{Re}(x)$ is the real part of x, t is the film thickness, R_{i} and T_{i} are the reflected and transmitted amplitudes of the incident X-ray beam respectively, and R_{f} and T_{f} are the reflected and transmitted amplitudes of the exiting X-ray beam respectively. In addition, $q_{\|} = \sqrt{q_x^2 + q_y^2}$, $q_{1,z} = \mathrm{k}_{z,\mathrm{f}} - \mathrm{k}_{z,\mathrm{i}}$, $q_{2,z} = -\mathrm{k}_{z,\mathrm{f}} - \mathrm{k}_{z,\mathrm{i}}$, $q_{3,z} = \mathrm{k}_{z,\mathrm{f}} + \mathrm{k}_{z,\mathrm{i}}$, and $q_{4,z} = -\mathrm{k}_{z,\mathrm{f}} + \mathrm{k}_{z,\mathrm{i}}$; here, $\mathrm{k}_{z,\mathrm{i}}$ is the z-component of the wave vector of the incident X-ray beam, which is given by $\mathrm{k}_{z,\mathrm{i}} = \mathrm{k}_{\mathrm{o}}\sqrt{n_{\mathrm{R}}^2 - \cos^2\alpha_{\mathrm{i}}}$, and $\mathrm{k}_{z,\mathrm{f}}$ is the z-component of the wave vector of the exiting X-ray beam, which is given by $\mathrm{k}_{z,\mathrm{f}} = \mathrm{k}_{\mathrm{o}}\sqrt{n_{\mathrm{R}}^2 - \cos^2\alpha_{\mathrm{f}}}$, where $\mathrm{k}_{\mathrm{o}} = 2\pi/\lambda$, λ is the wavelength of the X-ray beam, n_{R} is the refractive index of the film given by $n_{\mathrm{R}} = 1 - \delta + i\zeta$ with dispersion δ and absorption ζ, and α_{i} is the out-of-plane grazing incident angle of the incident X-ray beam. q_{x}, q_{y}, and q_{z} are the components of the scattering vector $\mathbf{q}$. I_1 is the scattering intensity of the structure in the film, which can be calculated kinematically.

In equation 3, I_1 is the scattered intensity from morphological structures in a film and, thus, can be expressed similarly to equation 2:[117-136]

$$I_1(\mathbf{q}) = P(\mathbf{q})\, S(\mathbf{q}) \tag{4}$$

where $P(\mathbf{q})$ is the form factor describing the shape, size, and orientation of scatterers in the thin film, and $S(\mathbf{q})$ is the structure factor describing the interscatterer correlation including the crystal lattice parameters, orientation, dimension, and symmetry in an ordered structure and the interdistance of domains.

In the case of two phase elliptical hexagonal cylinder structure (shown in Figure 1.7), the form factor $P(\mathbf{q})$ of a cylindrical scatterer with a length L_c and cross-section semi axes r_{cz} and r_{cy} can be expressed as the following equation:[135-139]

$$P(\mathbf{q}) = \left\{ 2\pi r_{cz} r_{cy} L_c \cdot \frac{J_1\left[(q_z^2 r_{cz}^2 + q_y^2 r_{cy}^2)^{1/2} \right]}{(q_z^2 r_{cz}^2 + q_y^2 r_{cy}^2)^{1/2}} \cdot \frac{\sin(q_x L_c/2)}{q_x L_c/2} \right\}^2 \tag{5}$$

Finally, the expression for the two phase (core−shell) cylinder can be summarized as the following:

$$P(\boldsymbol{q}) = P_{core}(\boldsymbol{q})(\rho_{core} - \rho_{shell}) + P_{shell}(\boldsymbol{q})(\rho_{shell} - \rho_{matrix}) \tag{6}$$

For the lamellar structure consisted of three layers (shown in Figure 1.6), the form factor $P(\mathbf{q})$ can be expressed by the following equation:

$$P(\mathbf{q}) = \begin{bmatrix} 4L_x L_y H_{inner}(\rho_{inner} - \rho_{outer}) \cdot \dfrac{\sin(q_x L_x)}{q_x L_x} \cdot \dfrac{\sin(q_y L_y)}{q_y L_y} \cdot \dfrac{\sin(q_z H_{inner})}{q_z H_{inner}} + \\ 4L_x L_y H_{outer}(\rho_{outer} - \rho_{matrix}) \cdot \dfrac{\sin(q_x L_x)}{q_x L_x} \cdot \dfrac{\sin(q_y L_y)}{q_y L_y} \cdot \dfrac{\sin(q_z H_{outer})}{q_z H_{outer}} \end{bmatrix}^2 \tag{7}$$

where L_x and L_y are the length and width of lamellar structure respectively, H_{inner} and H_{outer} are the inner and outer layer heights respectively, and ρ_{inner} and ρ_{outer} are the relative electron densities of the inner and outer layers respectively. ρ_{matrix} is the relative electron density of the matrix layer. For the lamellar structure, H_{inner} can be assigned to the layer thickness l_1 of the first phase defined by relative electron density ρ_{inner}. The layer thickness l_2 of the second phase (namely, interfacial layer thickness l_i) defined by relative electron density ρ_{outer} (= ρ_i) can be estimated from H_{inner} and H_{outer}: $l_2 = l_i = (H_{outer} - H_{inner})/2$. The third layer thickness l_3 having the relative electron density of ρ_{matrix} can be obtained from the long period D_L of lamellar structure that is extracted from the structure factor $S(\mathbf{q})$: $l_3 = (D_L - l_1 - 2l_2)$.

For the form factors, all structural parameters can be further assumed to follow a Gaussian distribution *G(A)*:

$$G(A) = \frac{1}{\sqrt{2\pi}\sigma_A} \exp\left[-\frac{(A-\overline{A})^2}{2\sigma_A{}^2}\right] \tag{8}$$

where A can be one of the parameters, $\overline{A}$ is the mean value, and σ_A is the standard deviation of A from $\overline{A}$.

For a paracrystalline lattice consisting of the three layers described above, the structure factor $S(\mathbf{q})$ (the so-called interference function or lattice factor) can be determined from the Fourier transform of a complete set of lattice points.[117-131,139-145] In a paracrystal with distortion of the second kind, the positions of the lattice points can only be described with a positional distribution function (i.e., *g*-factor). In the simple case where the autocorrelation function of the crystal lattice is given by the convolution product of the distributions of the lattice points along three axes, and a normal distribution function, $S(\mathbf{q})$ can be expressed by the following equation:[139,140]

$$S(\mathbf{q}) = \prod_{k=1}^{3} Z_k(\mathbf{q}) \tag{9}$$

$$Z_k(\mathbf{q}) = 1 + \frac{F_k(\mathbf{q})}{1 - F_k(\mathbf{q})} + \frac{F_k^*(\mathbf{q})}{1 - F_k^*(\mathbf{q})} \tag{10}$$

$$F_k(\mathbf{q}) = |F_k(\mathbf{q})| e^{-i\mathbf{q}\cdot\mathbf{a}_k} \tag{11}$$

$$|F_k(\mathbf{q})| = \exp\left[-\frac{1}{2}(q_1^2 g_1^2 + q_2^2 g_2^2 + q_3^2 g_3^2)\right] \tag{12}$$

Here g_1, g_2, and g_3 (= g) are the components of the g-factor defined as

$$g_1 = \Delta\, \mathbf{a_1}/\mathbf{a_1} \tag{13}$$

$$g_2 = \Delta\, \mathbf{a_2}/\mathbf{a_2} \tag{14}$$

$$g_3 = \Delta\, \mathbf{a_3}/\mathbf{a_3} \tag{15}$$

where $\mathbf{a_k}$ is the component of the fundamental vector $\mathbf{a}$ of the domain structure and $\Delta\mathbf{a_k}$ is the displacement of the vector $\mathbf{a_k}$. And q_1, q_2, and q_3 are the components of the scattering vector $\mathbf{q}$.

For two phase elliptical hexagonal cylinder structure, the components of $\mathbf{q}$ in equation 12 are defined by

$$q_1 = \mathbf{a_1}\cdot q_\mathrm{y} + \mathbf{a_1}\cdot q_\mathrm{z} = \left|L_\mathrm{y} \times q_\mathrm{y} + 0 \times q_\mathrm{z}\right| \tag{16a}$$

$$q_2 = \mathbf{a_2}\cdot q_\mathrm{y} + \mathbf{a_2}\cdot q_\mathrm{z} = \left|\left(-\frac{1}{2}\cdot L_\mathrm{y}\right) \times q_\mathrm{y} + L_\mathrm{z} \times q_\mathrm{z}\right| \tag{16b}$$

$$q_3 = \mathbf{a_3} \cdot q_y + \mathbf{a_3} \cdot q_z = \left| \left(-\frac{1}{2} \cdot L_y \right) \times q_y + \left(-1 \cdot L_z \right) \times q_z \right| \tag{16c}$$

where L_y and L_z are the lattice dimension parameters (i.e., *d*-spacing values) along the q_y- and q_z-direction respectively.

For the lamellar structure composed of three layers, the components of **q** in equation 12 are defined by

$$q_1 = \mathbf{a_1} \cdot q_x = \left| d_x \times q_x \right| \tag{17a}$$

$$q_2 = \mathbf{a_2} \cdot q_y = \left| d_y \times q_y \right| \tag{17a}$$

$$q_3 = \mathbf{a_3} \cdot q_z = \left| D_L \times q_z \right| \tag{17a}$$

where d_x and d_y are the lattice dimension parameters (i.e., *d*-spacing values) along the q_x- and q_y-direction respectively, and D_L is the long period along the q_z-direction.

Moreover, for a structure with a given orientation in a film, its fundamental vectors can be rotated and transformed by a rotation matrix. When the structure of the film is randomly oriented in the plane of the film but uniaxially oriented out of plane, the peak position vector $\mathbf{q_c}$ of a certain reciprocal lattice point $\mathbf{c}^*$ in the sample reciprocal lattice is given by

$$\begin{gathered} \mathbf{q_c} = \mathbf{R} \cdot \mathbf{c}^* \\ \mathrm{q_c} \equiv \left(q_{c,x}, q_{c,y}, q_{c,z} \right) \end{gathered} \tag{18}$$

where **R** is a 3 × 3 matrix to decide the preferred orientation of the structure in the film, and $q_{c,x}$, $q_{c,y}$, and $q_{c,z}$ are the *x*, *y*, *z* components of the peak position vector $\mathbf{q_c}$, respectively. Using equation 18, every peak position can be obtained. Because of cylindrical symmetry, the Debye-Scherrer ring composed of the in-plane randomly oriented **c*** cuts an Ewald sphere at two positions in its top hemisphere: $q_{\parallel} = q_{c,\parallel} \equiv \pm\sqrt{q_{c,x}^2 + q_{c,y}^2}$ with $q_z = q_{c,z}$. Thus diffraction patterns with cylindrical symmetry are easily calculated in the **q**-space. It is then convenient to determine the preferred orientation of known structures and further to analyze anisotropic X-ray scattering patterns. However, since **q**-space is distorted in GIXS by refraction and reflection effects, the relation between the detector plane expressed as the Cartesian coordinate defined by two perpendicular axes (i.e., by $2\theta_f$ and α_f) and the reciprocal lattice points is needed. The two wave vectors $k_{z,i}$ and $k_{z,f}$ are corrected for refraction as $k_{z,i} = k_o\sqrt{n_R^2 - \cos^2\alpha_i}$ and $k_{z,f} = k_o\sqrt{n_R^2 - \cos^2\alpha_f}$ respectively. Therefore, the two sets of diffractions that result from the incoming and outgoing X-ray beams, and denoted by q_1 and q_3 respectively, are given at the exit angles by the following expression:

$$\alpha_f = \arccos\left(\sqrt{n_R^2 - \left(\frac{q_{c,z}}{k_o} \pm \sqrt{n_R^2 - \cos^2\alpha_i}\right)^2}\right) \tag{19}$$

where $q_{c,z} / k_o > \sqrt{n_R^2 - \cos^2\alpha_i}$. In eq 17, the positive sign denotes diffractions produced by the outgoing X-ray beam, and the negative sign denotes diffractions produced by the incoming X-ray beam. The in-plane incidence angle $2\theta_i$ is usually zero, so the in-plane exit angle $2\theta_f$ can be expressed as follow:

$$2\theta_{\mathrm{f}} = \arccos\left[\frac{\cos^2\alpha_{\mathrm{i}} + \cos^2\alpha_{\mathrm{f}} - \left(\dfrac{q_{\mathrm{c},||}}{\mathrm{k_o}}\right)^2}{2\cos\alpha_{\mathrm{i}}\cos\alpha_{\mathrm{f}}}\right] \tag{20}$$

Therefore, diffraction spots detected on the detector plane in GIXS measurements can be directly compared to those derived using equations 18-20 from an appropriate model and thus analyzed in terms of the model.

To obtain information on the orientation of the paracrystal lattice of the phase separated micro domain structures from GIXS data, the distribution of the orientation vector ***n*** is given by a function $D(\varphi)$, where φ is the polar angle between the ***n*** vector and the out-of-plane of the film; for example, φ is zero when the ***n*** vector in the film is oriented normal to the film plane. To calculate the 2D GIXS patterns, $D(\varphi)$ should be represented by a numerical function. In relation to the distribution of the lattice orientation, $D(\varphi)$ can generally be considered as a Gaussian distribution:

$$D(\varphi) = \frac{1}{\sqrt{2\pi}\sigma_\varphi}\exp\left[-\frac{(\varphi-\overline{\varphi})^2}{2\sigma_\varphi^2}\right] \tag{21}$$

where $\overline{\varphi}$ and σ_φ are the mean angle and standard deviation of φ from $\overline{\varphi}$, respectively. The observed scattering intensity $I_{\mathrm{GIXS},\varphi}(\mathbf{q})$ is obtained by integrating $I_{\mathrm{GIXS}}(\mathbf{q})$ over possible orientations of the lattice:

$$I_{\mathrm{GIXS},\varphi}(\mathbf{q}) = \int_{-\pi}^{\pi} I_{\mathrm{GIXS}}(\mathbf{q})D(\varphi)\mathrm{d}\varphi \tag{22}$$

The second order orientation factor O_{s} can be defined as the following equation:[142-149]

$$O_s = \int D(\varphi)\frac{(3\cos^2\varphi - 1)}{2}\,\mathrm{d}\varphi \tag{22}$$

When $D(\varphi)$ is strongly peaked around $\varphi = 0°$ (i.e. vertical alignment), $\cos\varphi = 1$ and $O_s = 1$. On the other hand, when $\varphi = 90°$, $\cos\varphi = 0$ and $O_s = -0.5$. If the orientation is entirely random, $\langle\cos^2\varphi\rangle = 1/3$ and $O_s = 0$. Thus, O_s is a measure of the orientation of nanostructures.

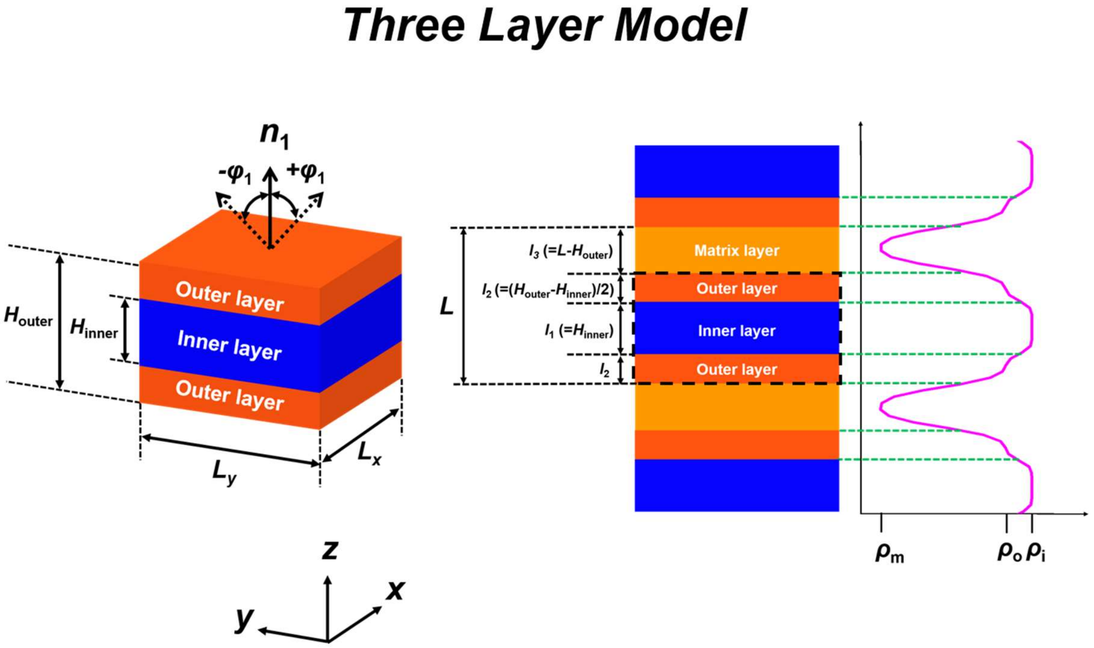
Three Layer Model

Figure 1.6. Schematic representation of the three layer model mathematically constructed based on the scattering equations described above.

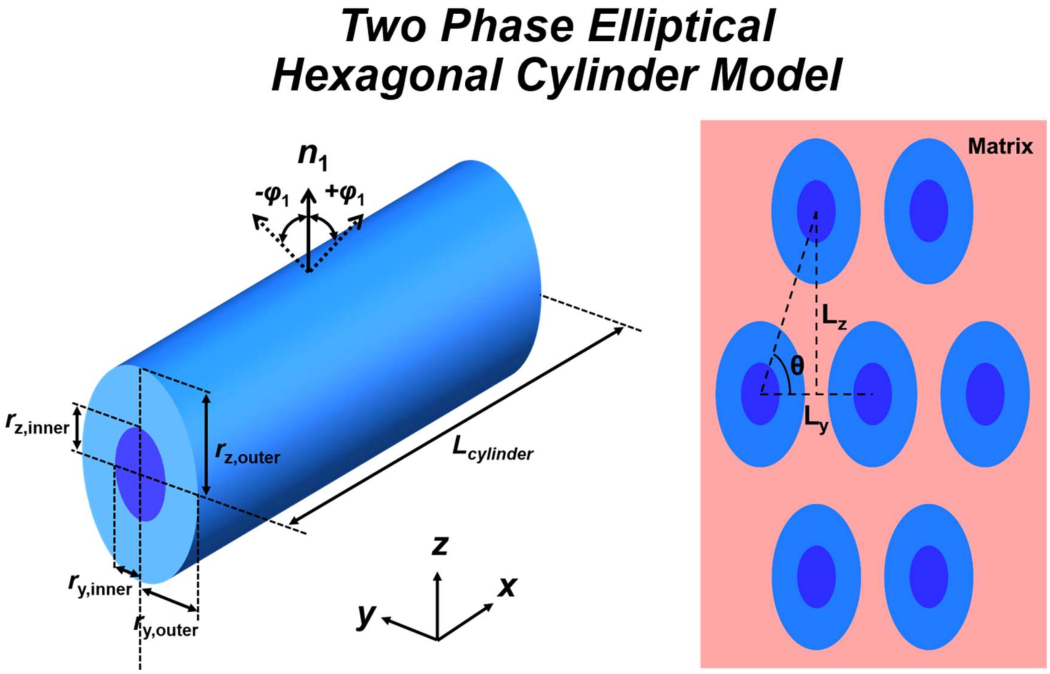

Figure 1.7. Schematic representations of the two phase elliptical hexagonal cylinder model mathematically constructed based on the scattering equations described above.

Based on the equations and formulas mentioned in this section, the three layer model and two phase elliptical hexagonal cylinder model were realized into functional GIXS data analysis programs using MATLAB software as the computation environment. The methodology of the modeling analysis is shown in Figure 1.8. Based on the measured 2D GIXS data (step 1), the appropriate choice of either the three layer or two phase elliptical hexagonal model is selected (step 2). By entering appropriate numerical values to the key variables specified in this section, the scattering intensity of the mathematical models is calculated and compared against the measured scattering intensity of one dimensional X-ray scattering profile extracted from raw 2D GIXS data (step 3). The adjustment of the values of structural parameters are iterated until the calculated scattering intensity matches the measured scattering intensity. To fully confirm the accuracy and the reliability of the structural parameter values, a 2D scattering pattern is simulated based on the structural parameters (step 4). When the overall simulated 2D scattering intensity is fully generated, it is compared against the measured 2D

GIXS data. The adjustment of the values of structural parameters are further iterated until the simulated 2D scattering pattern reaches a good agreement with the measured 2D GIXS data.

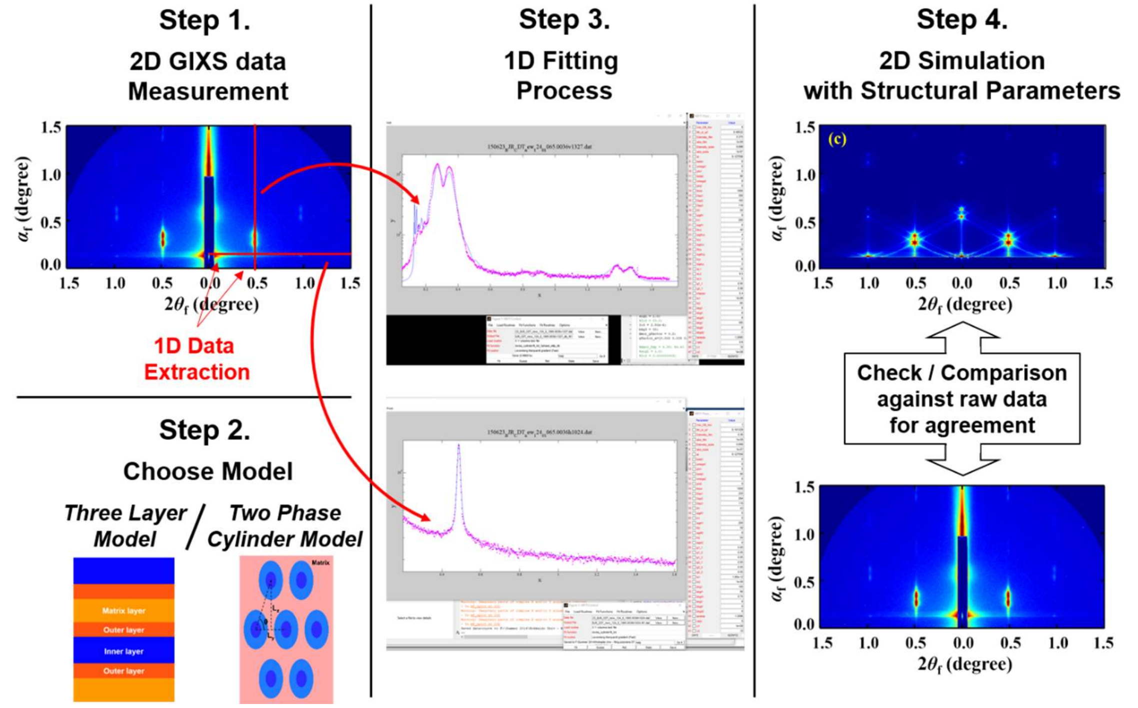

Figure 1.8. Visual overview of the methodology behind the quantitative modeling analysis via three layer and two phase elliptical hexagonal cylinder models (two phase elliptical hexagonal cylinder model shown as example).

1.5 Objective and Outline of the Dissertation

Topology of a polymer describes the shape and spatial features of the polymer's main chain. Ranging from linear, tadpole, cyclic, cage, star, dendritic, network, graft and beyond, the types and the synthesis of unique topological polymers are actively being expanded and refined by many research groups, as mentioned in Section 1.1. Particularly, all nonlinear topological polymers are defined by their vastly different physical properties such as self-assembly behavior from conventional linear polymers. This phenomenon is a result of the unique spatial features impacting the chain conformation, which directly influences the physical properties. A systematic interpretation based on the number of chains, the number of chain ends, and the number of chain junctions for all types of topologies could be effective for understanding the polymer topology influences upon self-assembly characteristics and morphological properties.

Polymer self-assembly is the physical rearrangement of polymeric chains from disordered state to ordered state driven by various intermolecular forces. Strategic molecular designs exploiting the balance of intermolecular forces to effectively promote self-assembly behavior are under the investigation from both the academia and the industry as it is a powerful bottom-up approach for developing various high performance polymer based nanotechnology applications. As discussed in Section 1.2, polymers offer various advantages such as easy fabrication processes, miniaturized nanoscale dimensions, great scalability, energy efficient operation, three-dimensional stacking capability, light weight, structural flexibility, wearability, and low-cost potential. The implementation of self-assembled polymer into nanotechnology applications haven't been realized yet because miniaturization of polymer morphology, while maintaining long range order, is indeed difficult to achieve. In addition to the optimization of polymer chain length and annealing conditions, polymer topology should be utilized as the third variable for controlling the polymer chain behavior for the purpose of achieving short domain spacing and long range order. For accurate and precise morphological characterization of topological polymers with quantitative structural parameters and statistical evaluation, synchrotron X-ray scattering technique present advantages over microscopy.

For polymer microscopy, there are many practical challenges and limitations that hinder consist and precise morphological characterization as summarized in Section 1.3. The biggest limitation of polymer microscopy is, however, the mandatory thin film fabrication specific to microscopic techniques, as well as occasional addition of image enhancing agents, that may disrupt the natural or intended state of polymers. Synchrotron X-ray scattering, in contrast, has a wide flexibility of measurement conditions allowing morphological characterization under a variety of conditions including bulk, thin film, and solution state of polymers, and also accommodate many types of external factors such as temperature, atmospheric pressure, and mechanical stress, to perform in-situ experiments. Moreover, modern synchrotron facilities provide data with ångström resolution for gathering statistical and quantitative structural information of ordered and disordered structures.

Despite the numerous advantages, the nature of X-ray scattering requires rather challenging data analysis to obtain structural parameters and statistics. Known as the phase problem, the principles of scattering does not allow direct transformation of the measured data into structural information. This have led to the development of the correlation function method and the modeling method, with the latter method having been utilized in many successful solid state thin film morphological studies. To better optimize the scattering intensity from polymer thin films, GIXS measurement and new scattering theories based on DWBA were developed. Thus far, majority of the reported polymer thin film morphology are either lamellar or hexagonal packed cylinder structures. The mathematical descriptions of the theoretically constructed models for the two aforementioned structures utilized throughout this dissertation, the three layer model and the two phase elliptical hexagonal cylinder model, are summarized in Section 1.4. The mathematical descriptions of the two models were fully realized into functional modeling analysis programs using MATLAB as the computational environment.

To achieve a fundamental comprehension of how polymer topology impacts the chain conformation and self-assembly behavior in thin film via synchrotron GIXS technique, the dissertation dives into detailed investigations on specific case studies in a systematic order as the following: a set of topologically complex poly(ε-caprolactone) homopolymers, a set of rotaxane containing poly(δ-valerolactone) homopolymers, a set of pseudo miktoarm block copolymers based on poly(δ-valerolactone)s macromolecular rotaxane linked to polystyrene, a set of cyclic and tadpole block copolyethers, a set of multicyclic and caged block copolyethers. The first two cases are intended as simplest examples for evaluating the impact of polymer topology in semi-crystalline homopolymers. The following cases are intended as more complex examples for addressing the impact of specific types or groups of similar topologies in various block copolymers. Given the specific examples of topological polymers, the novel three layer model and two phase elliptical hexagonal cylinder model developed in this dissertation will function to quantitatively analyze the nanoscale film morphologies of the polymers. Through the novel modeling analysis method, the effect and extent of polymer topology's influence upon polymer self-assembly and morphological characteristics in thin film will be thoroughly evaluated.

The outline of this dissertation is as follows:

Chapter 2 describes the nanoscale film morphologies of various poly(ε-caprolactone)s in cage shape (*cg*-PCL$_{9k}$), star shape (*st*-PCL$_{9k}$), cyclic shape (*cy*-PCL$_{6k}$), and two types of linear shape (*l*-PCL$_{3k}$-A and *l*-PCL$_{3k}$ -B) through quantitative analysis of synchrotron grazing incidence X-ray scattering. Also, their thermal properties have been examined by thermogravimetry and differential scanning calorimetry. The thermal stability, the nonisothermal crystallization and subsequent crystal melting transitions, are found to depend on the polymer topologies as well as the bulkiness of joints and chain end moieties. All PCL polymers always form lamellar structures based on orthorhombic crystal lattice in nanoscale films. However, the cage-shaped and cyclic polymers form a mixture of horizontal and vertical lamellar structures, whereas all other counterparts form only horizontal lamellar structures. The structural parameters, including overall crystallinity and orientational orthorhombic crystal domains, are further varied by the molecular topologies as well as the bulkinesses of joints and end groups. This is the first quantitative investigation of thin film morphologies of topological PCLs via modeling analysis of GIXS.

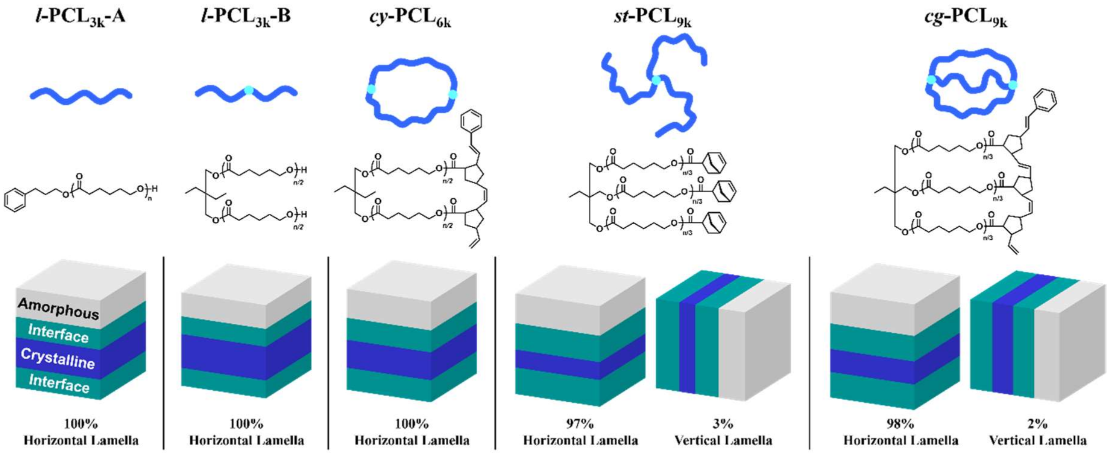

Figure 1.9. Schematic representations of the lamellar structures observed in the thin films of *l*-PCL$_{3k}$-A, *l*-PCL$_{3k}$ –B, *cy*-PCL$_{6k}$, *st*-PCL$_{9k}$, and *cg*-PCL$_{9k}$.

Chapter 3 discusses the phase transitions and nanoscale film morphologies of poly(δ-valerolactone) (PVL) axles bearing movable and fixed dibenzo-24-crown-8-ether wheels (*rot*-M and *rot*-F): PVL-*rot*-M and PVL-*rot*-F. The PVL axles exhibit a strong tendency to form horizontal lamellar structure accompanied with three different rotational crystal lattice domains residing in the nanoscale films. Overall, the thin film structural parameters show the differences as well as the influences of the movable and fixed rotaxane wheels. Particularly, the *rot*-M wheel tended to be populated in both the interfacial and amorphous layers. The *rot*-M wheel was found to significantly influence the phase transition characteristics of PVL axle because of its movability along the polymer backbone chain. In contrast, the *rot*-F wheel tended to be more localized in the interfacial layer rather than in the amorphous layer because of its immovability constrained at the polymer chain end. The *rot*-F wheel caused severe instability in the PVL axle, which could be attributed mainly to the presence of its counter anion. This is the first detailed investigation of thin film morphologies of PVL polyrotaxane system as well as the characterization of PVL crystal lattice structure in thin film through the utilization of quantitative modeling analysis.

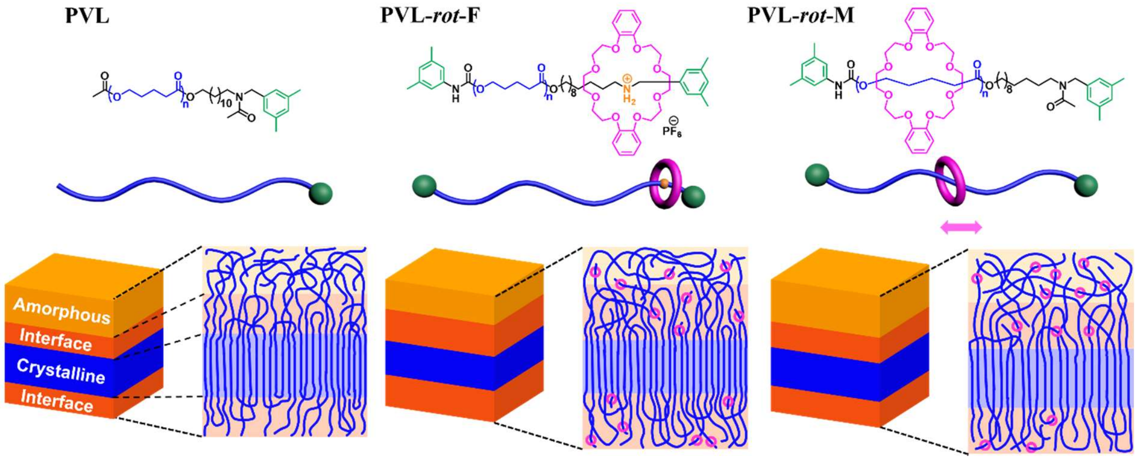

Figure 1.10. Chemical structures, differential scanning calorimetry thermograms, and schematic representations of the phase-separated lamellar structures of PVL-*b*-PS, PVL-*rot*-M and PVL-*rot*-F.

Chapter 4 describes the nanoscale film morphologies of poly(δ-valerolactone) (PVL) axles bearing movable and ionically-fixed rotaxane wheels linked with polystyrene (*rot*-PS-M and *rot*-PS-F) by synchrotron grazing incidence X-ray scattering: PVL-*rot*-PS-M and PVL-*rot*-PS-F. In addition, their thermal stabilities and phase-transition behaviors have been examined. PVL-*rot*-PS-M reveals higher thermal stability than that of PVL-*rot*-PS-F having ionic character and counter anion. The quantitative analyses of this study found that the movable rotaxane wheel could significantly enhance the mobilities of PVL axle and PS block, which are essential for their phase-separation and the PVL axle′s crystallization. With higher chain mobilities due to the movable rotaxane wheel, PVL-*rot*-PS-M always reveals much better performance in the formation of phase-separated PVL/PS lamellar structure as well as in the crystallization of PVL axle chain, compared to PVL-*rot*-PS-F and counter diblock copolymer. All morphology details, as well as thermal stability and phase transition details are discussed with considering the natures of movable, ionically-fixed and covalent-bonded linkers between PVL and PS blocks. This is the first detailed investigation of phase-separated microstructures of PVL-PS polyrotaxane system in nanoscale films via quantitative modeling analysis of GIXS.

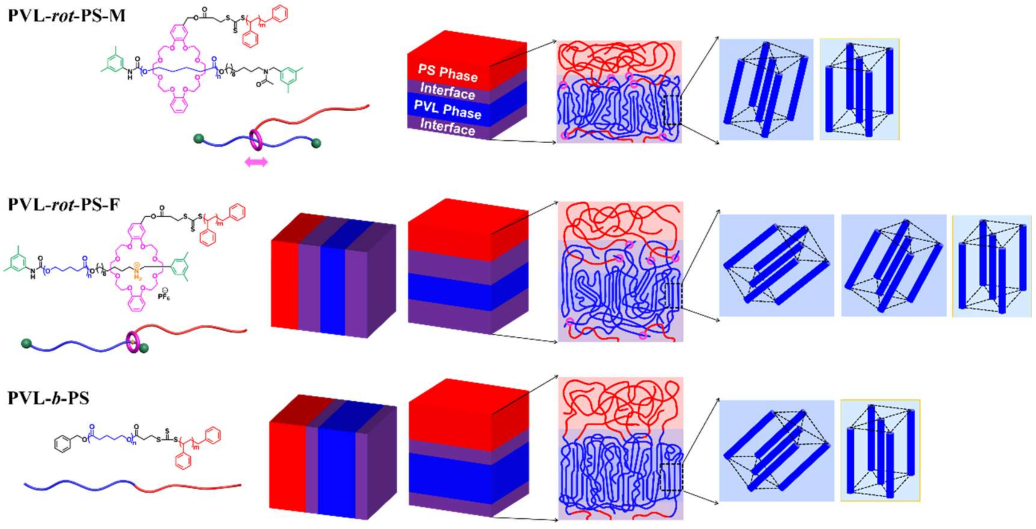

Figure 1.11. Schematic representations of the lamellar structures and orientational domains of PVL crystals observed in the thin films of PVL-*rot*-M, PVL-*rot*-F, and PVL-*b*-PS.

Chapter 5 examine the nanoscale film morphologies of a series of cyclic and tadpole-shaped poly(*n*-decyl glycidyl ether-*block*-2-(2-(2-methoxyethoxy)ethoxy)ethyl glycidyl ether)s in equivalent volume fractions, including their linear counterpart: *c*-PDGE-*b*-PTEGGE, *tp-A*-PDGE-b-PTEGGE, *tp-B*-PDGE-b-PTEGGE, and *l*-PDGE-*b*-PTEGGE. Due to their immiscibility between PDGE and PTEGGE, all polymers form nanostructures based on the micro-phase separations. However, the nanostructure type is highly dependent upon the molecular topologies. For the cyclic block copolymer film, the domain spacing reduction is nearly double in comparison to the linear counterpart than those predicted theoretically and previously reported. Even for the tadpole-shaped copolymer films, the domain spacing reductions are comparable to those predicted theoretically and previously reported. Furthermore, the cyclic and tadpole-shaped block copolymers form well-defined and oriented domain structures, unlike the linear counterpart. Overall, this study demonstrate that the cyclic and the tadpole-shaped block copolymers are highly suitable polymers for nanolithographic material development for producing advanced semiconductor chips with sub 10 nm half-pitch. This is the first detailed quantitative structural characterization of block copolymers with cyclic and tadpole topologies in nanoscale films via modeling analysis of GIXS.

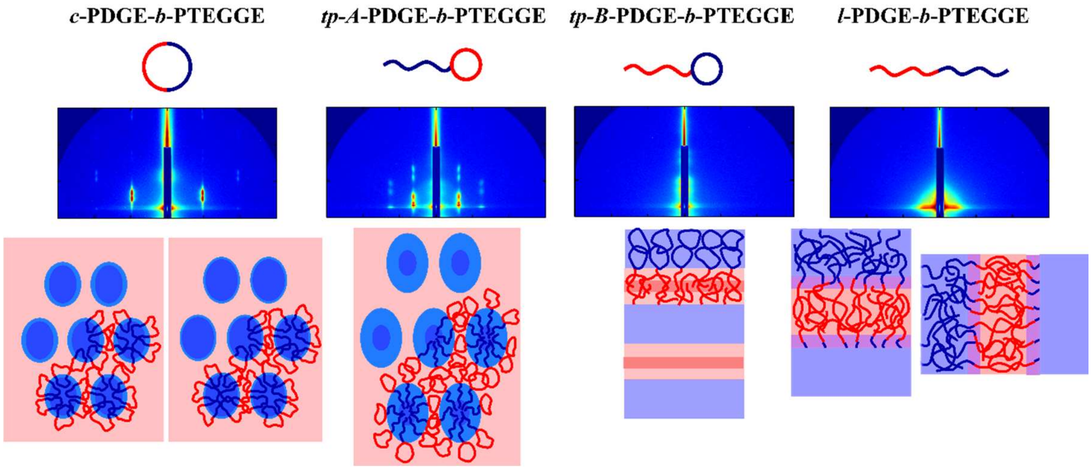

Figure 1.12. GISAXS raw scattering data and schematic representations of the hexagonal cylinder and lamellar structures of cyclic, tadpole, and linear block copolymers in the thin films.

Chapter 6 describes the nanoscale film morphologies of a series of four different bicyclic block copolymers based on poly(*n*-decyl glycidyl ether) and poly(2-(2-(2-methoxyethoxy)ethoxy)ethyl glycidyl ether) blocks in equivalent volume fractions with respect to their bicyclic topologies: *Bicycle-A*, *B*, *C*, and *D*. The quantitative synchrotron grazing incidence X-ray scattering characterization has found that all topological bicyclic copolymers generate phase-separated nanostructures. The morphological types and structural parameters of the nanostructures are highly dependent on the molecular topologies. *Bicycle-A*, which consist of two different homoblock-based rings, favorably forms hexagonal cylindrical nanostructure while *Bicycle-B*, *C*, and *D*, which contain diblock-based rings, form lamellar nanostructures. Interestingly, all bicyclic copolymers demonstrate nanostructures with significantly reduced domain spacings compared to the linear counterpart. The results collectively suggest that the bicyclic block copolymer approach is highly suitable to develop high performance nanolithographic materials which are highly demanded for the production of future advanced semiconductor chips with smaller pitches. This is the first quantitative morphological investigation of bicyclic block copolymers in nanoscale films through the utilization of modeling analysis.

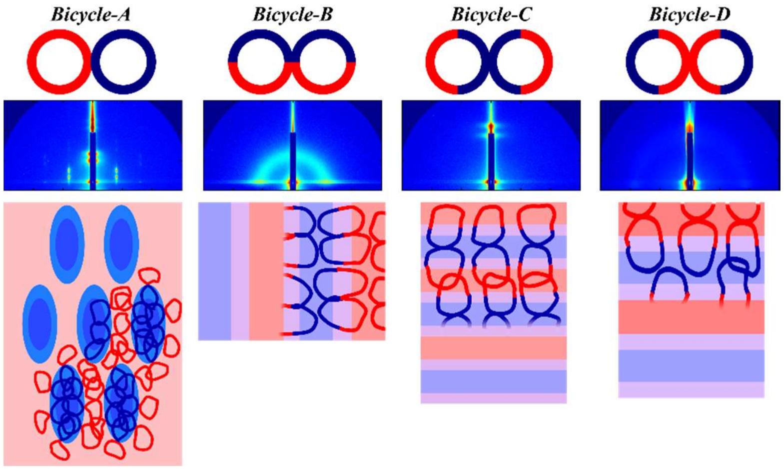

Figure 1.13. GISAXS raw scattering data and schematic representations of the hexagonal cylinder and lamellar structures of the four types of bicyclic block copolymers in the thin films.

Chapter 7 discusses the nanoscale film morphologies of a series of tricyclic heteroblock copolymers based on poly(*n*-decyl glycidyl ether) and poly(2-(2-(2-methoxyethoxy)ethoxy)ethyl glycidyl ether) blocks in equivalent volume fractions: *Tricycle-A*, *B*, and *C*. The morphological features have been identified and parameterized via synchrotron grazing incidence X-ray scattering analysis. All tricyclic copolymer films are amorphous but reveal phase-separated lamellar nanostructures. The nanostructure reveals variations in the dimensional parameters, orientation, and positional stability depending upon the molecular topologies. In particular, all nanostructures exhibit sub 10 nm domain spacings, which are remarkably smaller than that of the linear counterpart. These exceptionally smaller domain spacings are evident that the tricyclic heteroblock copolymer approach is a most efficient way to develop high performance nanolithographic materials being demanded seriously for the production of future advanced semiconductor chips with pitches of 10 nm or less. This is the first quantitative morphological characterization of tricyclic block copolymers in nanoscale films via modeling analysis of GIXS.

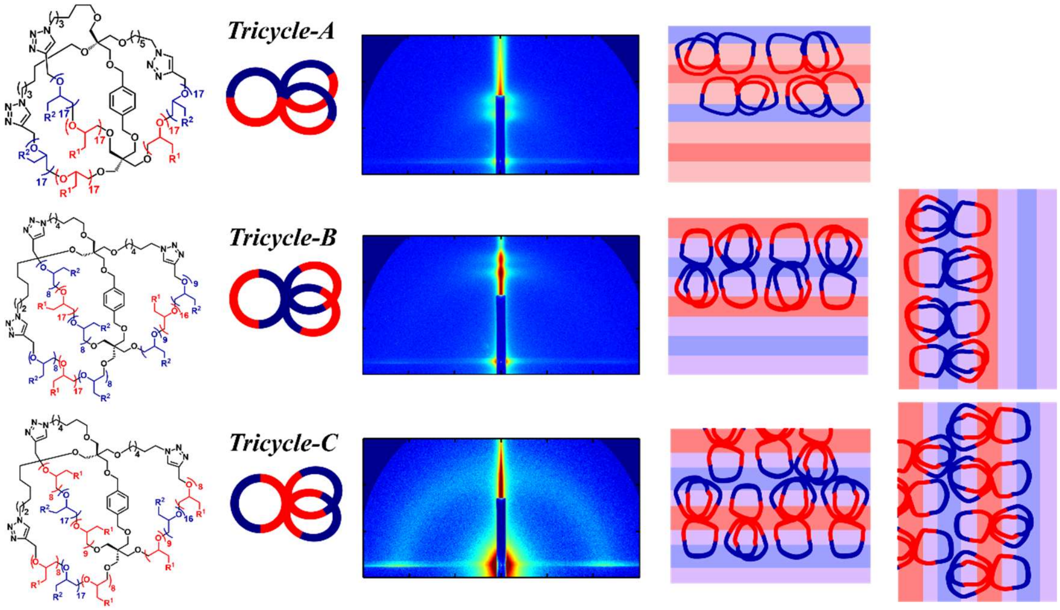

Figure 1.14. Chemical structures, GISAXS raw scattering data and schematic representations of the lamellar structures of the three types of tricyclic block copolymers in the thin films.

Chapter 8 describes the nanoscale film morphology details of cage-shaped heteroblock copolymers in three different topologies (*Cage-A*, *B*, and *C*) have been investigated for the first time by using synchrotron grazing incidence X-ray scattering. For all cage copolymers, the individual block components could not assemble at room temperature as crystallites, revealing amorphous natures. Nevertheless, they all exhibit phase-separated nanostructures. Their types and structural parameters are varied depending on the cage topologies. Very interestingly, all nanostructures show domain spacings ranged in 6.50–10.85 nm. These domain spacings are only 25.5–45.2 % of that of the linear block copolymer counterpart. Overall, this study has demonstrated that the cage-shaped heteroblock copolymer approach is a very efficient route to produce nanostructure with significantly reduced domain spacing. This is the first detailed investigation of phase-separated nanostructures formed by cage block copolymers in nanoscale films through quantitative modeling analysis.

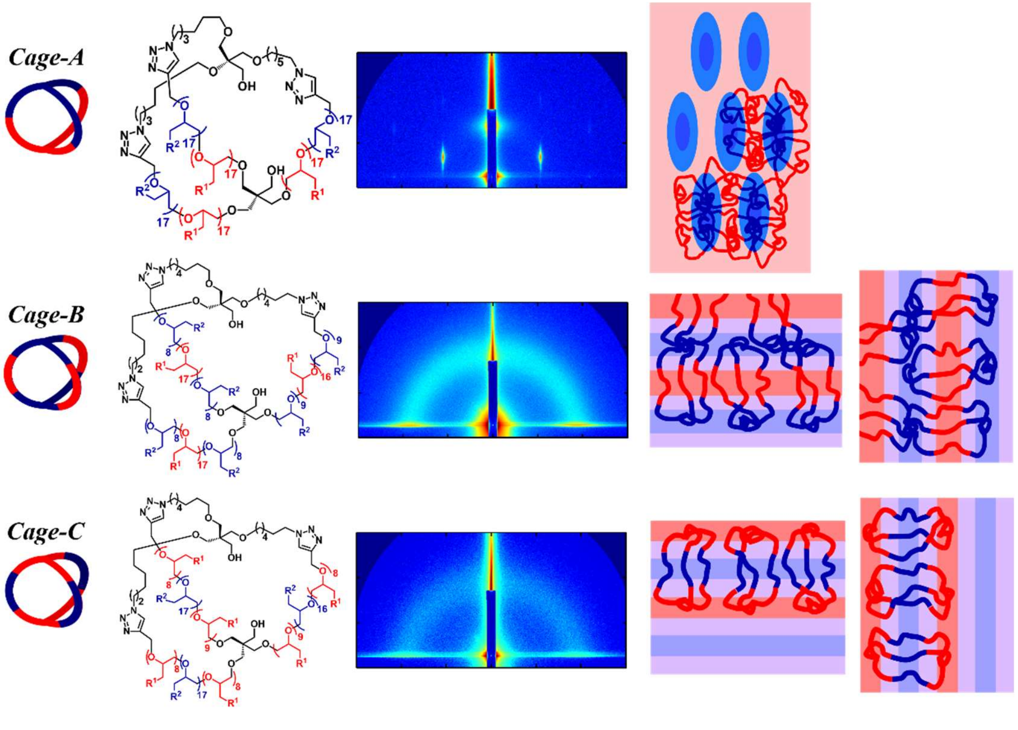

Figure 1.15. Chemical structures, GISAXS raw scattering data and schematic representations of the hexagonal cylinder and lamellar structures of the three types of cage shape block copolymers in the thin films.

Chapter 9 summarizes the effect and extent of polymer topology's impact on self-assembly behavior and thin film morphology of homopolymers and block copolymers.

1.6 References

1. Hadjichristidis, N.; Pitsikalis, M.; Pispas, S.; Iatrou, H. Polymers with Complex Architecture by Living Anionic Polymerization. *Chem. Rev.* **2001,** *101,* 3747−3792.
2. Tezuka, Y.; Oike, H. Topological polymer chemistry. *Prog. Polym. Sci.*, **2002**, *27*, 1069−1122.
3. Laurent, B. A.; Grayson, S. M. Synthetic approaches for the preparation of cyclic polymers. *Chem. Soc. Rev.*, **2009**, *38*, 2202–2213.
4. Yamamoto, T.; Tezuka, Y. Topological polymer chemistry: a cyclic approach toward novel polymer properties and functions. *Polym. Chem.*, **2011**, *2*, 1930–1941.
5. Chang, Y. A.; Waymouth, R. M. Recent Progress on the Synthesis of Cyclic Polymers via Ring-Expansion Strategies. *J. Polym. Sci, Part A: Polym Chem.*, **2017**, *55*, 2892–2902.
6. Abouelmagd, A.; Sugiyama, K.; Hirao, A. Synthesis of Well-Defined Miktoarm Star-Branched Polymers Consisting of Perfluorinated Segments by a Novel Methodology Using Soluble In-Chain-Benzyl Bromide-Functionalized AB Diblock Copolymers as Key Building Blocks. *Macromolecules*, **2011**, *44*, 826–834.
7. Junnila, S.; Houbenov, N.; Karatzas, A.; Hadjichristidis, N.; Hirao, A.; Iatrou, H.; Ikkala, O. Side-Chain-Controlled Self-Assembly of Polystyrene−Polypeptide Miktoarm Star Copolymers. *Macromolecules*, **2012**, *45*, 2850−2856.
8. Ito, S.; Goseki, R.; Senda, S.; Hirao, A. Precise Synthesis of Miktoarm Star Polymers by Using a New Dual-Functionalized 1,1-Diphenylethylene Derivative in Conjunction with Living Anionic Polymerization System. *Macromolecules*, **2012**, *45*, 4997−5011.
9. Rho, Y.; Kim, C.; Higashihara, T.; Jin, S.; Jung, J.; Shin, T. J.; Hirao, A.; Ree, M. Complex Self-Assembled Morphologies of Thin Films of an Asymmetric A3B3C3 Star Polymer. *ACS Macro Lett.*, 2013, *2*, 849−855.
10. Isono, T., Kondo, Y., Otsuka, I., Nishiyama, Y., Borsali, R., Kakuchi, T., Satoh, T., Synthesis and Stereocomplex Formation of Star-Shaped Stereoblock Polylactides Consisting of Poly(L-lactide) and Poly(D-lactide) Arms**.** *Macromolecules*, **2013**, *46*, 21, 8509−8518.
11. Isono, T., Kamoshida, K., Satoh, Y., Takaoka, T., Sato, S.-i., Satoh, T., Kakuchi, T., Synthesis of Star- and Figure-Eight-Shaped Polyethers by t-Bu-P4-Catalyzed Ring-Opening Polymerization of Butylene Oxide**.** *Macromolecules*, **2013**, *46*, 10, 3841−3849.
12. Isono, T.; Satoh, Y.; Miyachi, K.; Chen, Y.; Sato, S.-i.; Tajima, K.; Satoh, T.; Kakuchi, T. Synthesis of Linear, Cyclic, Figure-Eight-Shaped, and Tadpole-Shaped Amphiphilic Block Copolyethers via t-Bu-P4-Catalyzed Ring-Opening Polymerization of Hydrophilic and Hydrophobic Glycidyl Ethers**.** *Macromolecules*, **2014**, *47*, 2853−2863.
13. Isono, T.; Miyachi, K.; Satoh, Y.; Nakamura, R.; Zhang, Y.; Otsuka, I.; Tajima, K.; Kakuchi, T.; Borsali, R.; Satoh, T. Self-Assembly of Maltoheptaose-block-Polycaprolactone Copolymers: Carbohydrate-Decorated Nanoparticles with Tunable Morphology and Size in Aqueous Media**.** *Macromolecules*, **2016**, *49*, 4178−4194.
14. Satoh, Y.; Matsuno, H.; Yamamoto, T.; Tajima, K.; Isono, T.; Satoh, T**.** Synthesis of Well-Defined Three- and Four-Armed Cage-Shaped Polymers via “Topological Conversion” from Trefoil- and Quatrefoil- Shaped Polymers. *Macromolecules*, **2017**, *50*, 97−106.
15. Isono, T.; Sasamori, T.; Honda, K.; Mato, Y.; Yamamoto, T.; Tajima, K.; Satoh, T. Multicyclic Polymer Synthesis through Controlled/Living Cyclopolymerization of α,ω-Dinorbornenyl-Functionalized Macromonomers**.** *Macromolecules*, **2018**, *51*, 3855−3864.
16. Shingu, T.; Yamamoto, T.; Tajima, K.; Isono, T.; Satoh, T. Synthesis of μ-ABC Tricyclic Miktoarm Star Polymer via Intramolecular Click Cyclization. *Polymers*, **2018**, *10*, 877

17. Mato, Y.; Honda, K.; Tajima, K.; Yamamoto, T.; Isono, T.; Satoh, T. A versatile synthetic strategy for macromolecular cages: intramolecular consecutive cyclization of star-shaped polymers**.** *Chem. Sci.*, **2019**, *10*, 440−446.
18. Dodgson, K.; Semlyen, J. A. Studies of Cyclic and Linear Poly(dimethylsiloxanes): 1. Limiting Viscosity Number-Molecular Weight Relationships. *Polymer*, **1977**, *18*, 1265−1268.
19. Hild, G.; Kohler, A.; Rempp, P. Synthesis of Ring-Shaped Macromolecules. *Eur. Polym. J.*, **1980**, *16*, 525−527.
20. Roovers, J.; Toporowski, P. M. Synthesis of High Molecular Weight Ring Polystyrenes. *Macromolecules,* **1983**, *16*, 843−849.
21. Kricheldorf, H. R.; Lee, S.-R.; Schittenhelm, N. Macrocycles, 1. Macrocyclic Polymerizations of (Thio)lactones–Stepwise Ring Expansion and Ring Contraction. *Macromol. Chem. Phys*., **1998**, *199*, 273–282.
22. Kricheldorf, H. R.; Eggerstedt, S. Macrocycles, 2. Living Macrocyclic Polymerization of *ε*-Caprolactone with 2,2-Dibutyl-2-stanna-1,3-dioxepane as Initiator. *Macromol. Chem. Phys*., **1998**, *199*, 283−290.
23. Hadjichristidis, N.; Pitsikalis, M.; Pispas, S.; Iatrou, H. Polymers with Complex Architecture by Living Anionic Polymerization. *Chem. Rev.*, **2001**, *101*, 3747−3792.
24. Semlyen, J. A. Cyclic Polymers, 2nd ed., Kluwer Academic Publishers: Dordrecht, Netherlands, 2002.
25. Tezuka, Y.; Komiya, R. Metathesis Polymer Cyclization with Telechelic Poly(THF) Having Allyl Groups. *Macromolecules*, **2002**, *35*, 8667–8669.
26. Laurent, B. A.; Grayson, S. M. An Efficient Route to Well-Defined Macrocyclic Polymers via "Click" Cyclization. *J. Am. Chem. Soc.*, **2006**, *128*, 4238–4239.
27. Hayashi, S.; Adachi, K.; Tezuka, Y. ATRP-RCM Synthesis of 8-Shaped Poly(methyl acrylate) Using a 4-Armed Star Telechelics. *Polymer Journal*, **2008**, *40*, 572–576.
28. Durmaz, H.; Dag, A.; Hizal, G.; Tunca, U. Cyclic Homo and Block Copolymers Through Sequential Double Click Reactions. *J. Polym. Sci., Part A: Polym. Chem.*, **2010**, *48*, 5083-5091.
29. Voter, A. F.; Tillman, E. S. An Easy and Efficient Route to Macrocyclic Polymers Via Intramolecular Radical-Radical Coupling of Chain Ends. *Macromolecules*, **2010**, *43*, 10304-10310.
30. Kricheldorf, H. R. Cyclic Polymers: Synthetic Strategies and Physical Properties. *J. Polym. Sci. Part A: Polym. Chem.*, **2010**, *48*, 251− 284.
31. Jia, Z.; Monteiro, M.J. Cyclic Polymers: Methods and Strategies. *J. Polym. Sci. Part A: Polym. Chem*., **2012**, *50*, 2085−2097.
32. Liu, B.; Wang, H.; Zhang, L.; Yang, G.; Liu, X.; Kim, I. A Facile Approach for the Synthesis of Cyclic Poly(*N*-isopropylacrylamide) Based on An Anthracene–Thiol Click Reaction. *Polym. Chem.*, **2013**, *4*, 2428–2431.
33. Lu, D.; Jia, Z.; Monteiro, M. J. Synthesis of alkyne functional cyclic polymers by one-pot thiol–ene cyclization. *Polym. Chem.*, **2013**, *4*, 2080-2089.
34. Long, S.; Tang, Q.; Wua, Y.; Wang, L.; Zhang, K.; Chen, Y. A method for preparing water soluble cyclic polymers. *React. Funct. Polym.*, **2014**, *80*, 15-20.
35. Ogawa, T.; Nakazono K.; Aoki D.; Uchida S.; Takata T. Effective Approaches to Cyclic Polymer from Linear Polymer: Synthesis and Transformation of Macromolecular [1]Rotaxane. *ACS Macro Lett*. **2015**, *4*, 343−347.
36. Xiang, L.; Ryu, W.; Kim, H.; Ree, M. Precise Synthesis, Properties, and Structures of Cyclic Poly(*ε*-caprolactone)s. *Polymers*, **2018**, *10*, 577.
37. Patnode, W.; Wilcock, D. F. Methylpolysiloxanes. *J. Am. Chem. Soc.***1946**, *68*, 358−363.

38. Hunter, M. J.; Hyde, J. F.; Warrick, E. L.; Fletcher, H. J. Organo-Silicon Polymers. The Cyclic Dimethyl Siloxanes. *J. Am. Chem. Soc.***1946**, *68*, 667−672.
39. Scott, D. W. Equilibria between Linear and Cyclic Polymers in Methylpolysiloxanes. *J. Am. Chem. Soc.* **1946**, *68*, 2294−2298.
40. Fiers, W.; Sinsheimer, R. L. The structure of the DNA of bacteriophage φX174: I. The action of exopolynucleotidases. *J. Mol. Biol.* **1962**, *5*, 408−419.
41. Fiers, W.; Sinsheimer, R. L. The Structure of the DNA of Bacteriophage φX174: II. Thermal Inactivation. *J. Mol. Biol.* **1962**, *5*, 420−423.
42. Dulbecco, R.; Vogt, M. Evidence for A Ring Structure of Polyoma Virus DNA. *Proc. Natl. Acad. Sci. USA* **1963**, *50*, 236−243.
43. Weil, R.; Vinograd, J. The Cyclic Helix and Cyclic Coil Forms of Polyoma Viral DNA. *Proc. Natl. Acad. Sci. USA* **1963**, *50*, 730−738.
44. Witherup, K.M.; Bogusky, M.J.; Anderson, P.S.; Ramjit, H.; Ransom, R.W.; Wood, T.; Sardana, M. Cyclopsychotride A, A Biologically Active, 31-Residue Cyclic Peptide Isolated from Psychotria Longipes. *J. Nat. Prod.* **1994**, *57*, 1619–1625.
45. Cascales, L.; Craik, D. J. Naturally Occurring Circular Proteins: Distribution, Biosynthesis and Evolution. *Org. Biomol. Chem.* **2010**, *8*, 5035–5047.
46. Dell, A.; Oates, J.; Lugowski, C.; Romanowska, E.; Kenne, L.; Lindberg, B. The Enterobacterial Common-Antigen, A Cyclic Polysaccharide. *Carbohydr. Res.* **1984**, *133*, 95–104.
47. Zimm, B. H; Stockmayer, W. H. The Dimensions of Chain Molecules Containing Branches and Rings. *J. Chem. Phys*. **1949**, *17*, 1301−1314.
48. Flory, P. J. Network Topology and the Theory of Rubber Elasticity. *British Polymer Journal* **1985**, *17*, 96-102.
49. Duplantier, B. Statistical Mechanics of Polymer Networks of Any Topology. *Journal of Statistical Physics*, **1989**, *54*, 581-680.
50. Rubinstein, M.; Colby, R. H. Polymer Physics, Oxford University Press, Oxford, United Kingdom, 2003.
51. Tezuka, Y.; Oike, H. Topological Polymer Chemistry: Systematic Classification of Nonlinear Polymer Topologies, *J. Am. Chem. Soc.* **2001**, 123, 11570-11576.
52. de Gennes, P.G. Reptation of a Polymer Chain in the Presence of Fixed Obstacles. *J. Chem. Phys.*, **1971**, *55*, 572-579
53. Flory, P. J. The Configuration of Real Polymer Chains. *J. Chem. Phys.*, **1949**, *17*, 303-310.
54. W. W. Graessley, The entanglement concept in polymer rheology. *Adv. Polym. Sci.*, **1974**, *16*, 1.
55. Chikahisa, Y.; Morooka, T. A Theory of Entangled Polymers. *Polymer Journal*, **1979**, *11*, 145-151.
56. Hahm, S. G.; Ko, Y.-G.; Kwon, W.; Ree, M. Liquid crystal alignment in advanced flat-panel liquid crystal displays. *Curr. Opin. Chem. Eng.* **2013**, *2*, 79-87.
57. Kurosawa, T.; Higashihara, T.; Ueda, M. Polyimide memory: a pithy guideline for future applications. *Polym. Chem.*, **2013**, *4*, 16.
58. Ko, Y.-G.; Kim, D. M.; Kim, K.; Jung, S.; Wi, D.; Michinobu, T.; Ree, M. Digital Memory Versatility of Fully π-Conjugated Donor−Acceptor Hybrid Polymers *ACS Appl. Mater. Interf.*, **2014**, *6*, 8415.
59. Kim, Y. Y.; Ree, B. J.; Kido, M.; Ko, Y.-G.; Ishige, R.; Hirai, T.; Wi, D.; Kim, J.; Kim, W. J.; Takahara, A.; Ree, M. High-Performance n-Type Electrical Memory and Morphology-Induced Memory-Mode Tuning of a Well-Defined Brush Polymer Bearing Perylene Diimide Moieties. *Adv. Electron. Mater.*, **2015**, 1500197.

60. Jung, S.; Kwon, W.; Wi, D.; Kim, J.; Ree, B. J.; Kim, Y. Y.; Kim, W. J.; Ree, M. Hierarchical Self-Assembly and Digital Memory Characteristics of Crystalline–Amorphous Brush Diblock Copolymers Bearing Electroactive Moieties. *Macromolecules*, **2016**, *49*, 1369-1382.
61. Wi, D.; Ree, B. J.; Ahn, B.; Hsu, J.-C.; Kim, J.; Chen, W.-C.; Ree, M. Structural details and digital memory performances of difluorene-containing diblock copolymers in nanoscale thin films. *European Polymer Journal*, **2016**, *81*, 582–597.
62. Chen, W.-C. ed., Electrical Memory Materials and Devices, RSC Polymer Series No. 18, 2016.
63. Wang, J.-T.; Takshima, S.; Wu, H.-C.; Shih, C.-C.; Isono, T.; Kakuchi, T.; Satoh, T.; Chen, W.-C. Stretchable Conjugated Rod-Coil Poly(3-hexylthiophene)-block-poly(butyl acrylate) Thin Films for Field Effect Transistor Applications. *Macromolecules*, **2017**, *50*, 1442-1452.
64. Lee, H.; Kim, Y.; Fukuta, S.; Kim, H.; Kim, Y.; Higashihara, T.; Ree, M. Nanoscale Film Morphology and n-Type Digital Memory Characteristics of π-Conjugated Donor–Acceptor Alternating Copolymer Based on Thiophene and Thiadiazole Units. *Macromol. Rapid Commun.* **2019**, *40,* 1900005.
65. Chiang, Y.-C.; Kobayashi, S.; Isono, T.; Shih, C.-C.; Shingu, T.; Hung, C.-C.; Hsieh, H.-C.; Tung, S.-H.; Satoh, T.; Chen, W.-C**.** Effect of a conjugated/elastic block sequence on the morphology and electronic properties of polythiophene based stretchable block copolymers. *Polym. Chem.*, **2019**, *10*, 5452-5464.
66. Moore, G. E. Cramming more components onto integrated circuits. *Electronics*, **1965**, *38*, 8.
67. Roy, S. R.; Ali, I.; Shinn, G.; Furusawa, N.; Shah, R.; Peterman, S.; Witt, K.; Eastman, S.; Kumar, P. Postchemical-Mechanical Planarization Cleanup Process for Interlayer Dielectric Films. *J. Electrochem. Soc.*, **1995**, *142*, 216–226.
68. Zhang, L.; Raghavan, S.; Weling, M. Minimization of chemical-mechanical planarization (CMP) defects and post-CMP Cleaning. *J. Vac. Sci. Technol., B: Microelectron. Nanometer Struct.–Process., Meas., Phenom.*, **1999**, *17*, 2248–2255.
69. Mosig, K.; Jacobs, T.; Brennan, K.; Rasco, M.; Wolf, J.; Augur, R. Integration challenges of porous ultra low-*k* spin-on dielectrics. *Microelectron. Eng.*, **2002**, *64*, 11–24.
70. L´epinay, M.; Djourelov, N.; Marinov, H.; Broussous, L.; Courouble, K.; Licitra, C.; Bertin, F.; Rouessac, V.; Ayral, A. Depth-resolved impact of integration process on porosity and solvent diffusion in a SiOCH low-*k* material. *J. Porous Mater.*, **2014**, *21*, 475–484.
71. Heo, K.; Ree, B. J.; Choi, K.-K.; Ree, M. Structural reliability evaluation of low-k nanoporous dielectric interlayers integrated into microelectronic devices. *RSC Adv.*, **2015**, *5*, 87084.
72. Lionti, K. K.; Volksen, W.; Magbitang, T.; Darnon, M.; Dubois, G. Toward Successful Integration of Porous Low-k Materials: Strategies Addressing Plasma Damage. *ECS J. Solid State Sci. Technol.*, **2015**, *4*, N3071–N3083.
73. Hatano, M.; Kobayashi, K.; Kashiwagi, H.; Tokue, H.; Kono, T.; Tetsuro, N.; Choi, E. H.; Jung, W. "NIL defect performance toward high volume mass production", Proc. SPIE 9777, Alternative Lithographic Technologies VIII, **2016**, 97770B.
74. Nakayama, T.; Yonekawa, M.; Matsuoka, Y.; Azuma, H.; Takabayashi, Y.; Aghili, A.; Mizuno, M.; Choi, J.; Jones, C. E. "Improved defectivity and particle control for nanoimprint lithography high-volume semiconductor manufacturing", Proc. SPIE 10144, Emerging Patterning Technologies, **2017**, 1014407.
75. EUV's Stochastic Valley of Death. https://www.linkedin.com/pulse/euvs-stochastic-valley-death-frederick-chen/ (accessed Nov 25 2019)

76. De Bisschop, P.; Hendrickx, E. Stochastic printing failures in EUV lithography. *Proc. SPIE*, **2019**, *10957*, Extreme Ultraviolet (EUV) Lithography X, 109570E.
77. Historical Binning Statistics. https://siliconlottery.com/pages/statistics (accessed Nov 25, 2019)
78. Griffiths, R. A.; Williams, A.; Oakland, C.; Roberts, J.; Vijayaraghavan, A.; Thomson, T. Directed Self-Assembly of Block Copolymers for Use in Bit Patterned Media Fabrication. J. *Phys. D:Appl Phys.*, **2013**, *46*, 503001.
79. Cushen, J.; Wan, L.; Blachut, G.; Maher, M. J.; Albrecht, T. R.; Ellison, C. J.; Willson, C. G.; Ruiz, R. Double-Patterned Sidewall Directed Self-Assembly and Pattern Transfer of Sub-10 nm PTMSS-b-PMOST. *ACS Appl. Mater. Interfaces*, **2015**, *7*, 13476−13483.
80. Maher, M. J.; Rettner, C. T.; Bates, C. M.; Blachut, G.; Carlson, M. C.; Durand, W. J.; Ellison, C. J.; Sanders, D. P; Cheng, J. Y.; Willson, C. G. Directed Self-Assembly of Silicon-Containing Block Copolymer Thin Films. *ACS Appl. Mater. Interfaces*, **2015**, *7*, 3323−3328.
81. Yoshida, K.; Tian, L.; Miyagi, K.; Yamazaki, A.; Mamiya, H.; Yamamoto, T.; Tajima, K.; Isono, T.; Satoh, T. Facile and Efficient Modification of Polystyrene-block-poly(methyl methacrylate) for Achieving Sub-10 nm Feature Size. *Macromolecules*, **2018**, 51, 8064−8072.
82. de Gennes. P. G. Scaling Concepts in Polymer Physics. Cornell University Press, Ithaca and London, 1979.
83. van Krevelen, D. W.; te Nijenhuis, K. Properties of Polymers: Their Correlation with Chemical Structure; Their Numerical Estimation and Prediction from Additive Group Contributions. Elsevier Science, Oxford, 2009.
84. Butler, J. H.; Joy, D. C.; Bradley, G. F.; Krause, S. J. Low-voltage scanning electron microscopy of polymers. *Polymers*, **1995**, *36*, 1781−1790.
85. Smith, D. J. Ultimate resolution in the electron microscope? *Materials Today*, **2008**, *11*, 30−38.
86. Libera, M. R.; Egerton, R. F. Advances in the Transmission Electron Microscopy of Polymers. *Polymer Reviews*, **2010**, *50*, 321−339.
87. Aoki, H. Conformation and dynamics of single polymer chain studied by optical microscopy techniques beyond the diffraction limit. *Microscopy*, **2017**, *66*, 223–233.
88. Robinson, A. L. History of Synchrotron Radiation. https://xdb.lbl.gov/Section2/Sec_2-2.html (accessed Nov 26 2019)
89. Li, T.; Senesi, A. J.; Lee, B. Small Angle X-ray Scattering for Nanoparticle Research. *Chem. Rev.*, **2016**, *116*, 11128−11180.
90. Lee, B.; Yoon, J.; Oh, W.; Hwang, Y.; Heo, K.; Jin, K. S.; Kim, J.; Kim, K.-W.; Ree, M. In-Situ Grazing Incidence Small-Angle X-ray Scattering Studies on Nanopore Evolution in Low-*k* Organosilicate Dielectric Thin Films. *Macromolecules*, **2005**, *38,* 3395−3405.
91. Jin, K. S.; Heo, K.; Oh, W.; Yoon, J.; Lee, B.; Hwang, Y.; Kim, J.-S.; Park, Y.-H.; Kim, K.-W.; Kim, J.; Chang, T.; Ree, M. Grazing-incidence small-angle X-ray scattering studies on templating nanopores in networked polymer thin films with a multi-armed porogen. *J. Appl. Cryst.*, **2007**, *40*, s631–s636.
92. Yoon, J.; Jung, S. Y.; Ahn, B.; Heo, K.; Jin, S.; Iyoda, T.; Yoshida, H.; Ree, M. Order-Order and Order-Disorder Transitions in Thin Films of an Amphiphilic Liquid Crystalline Diblock Copolymer. *J. Phys. Chem. B*, **2008,** *112,* 8486–8495.
93. Kim, M.; Rho, Y.; Jin, K. S.; Ahn, B.; Jung, S.; Kim, H.; Ree, M. pH-Dependent Structures of Ferritin and Apoferritin in Solution: Disassembly and Reassembly. *Biomacromolecules*, **2011**, *12*, 1629–1640.
94. Kubo, G.; Sakamoto, S.; Fujii, S.; Sanada, Y.; Yasunaga, T.; Takahara, A.; Sakurai, K. Transformation from Multi- to Single-lamellar Vesicle by Addition of a Cationic Lipid

to 1,2-Dilauroyl-sn-glycero-3-phosphocholine Explored with SAXS and TEM. *Chem. Lett.*, **2014**, *43*, 1785–1787.

95. Weidman, M.; Smilgies, D.; Tisdale, W. Kinetics of the self-assembly of nanocrystal superlattices measured by real-time *in situ* X-ray scattering. *Nature Mater*, **2016**, *15*, 775–781.
96. Kim, K.-W.; Kim, J.; Yun, Y. D.; Ahn, H.; Min, B.; Kim, N. H.; Rah, S.; Kim, H.-Y.; Lee, C.-S.; Seo, I. D.; Lee, W.-W.; Choi, H. J.; Jin, K. S. Small-angle X-ray Scattering Beamline BL4C SAXS at Pohang Light Source II. *Biodesign*, **2017**, *5*, 24–29.
97. Trigg, E. B.; Middleton, L. R.; Yan, L.; Winey, K. I. Comparing Morphological Evolution during Tensile Deformation of Two Precise Polyethylenes via 2D Fitting of in Situ X-ray Scattering. *Macromolecules*, **2018**, *51*, 7942–7950.
98. Rahmawati, R.; Masuda, S.; Cheng, C.-H.; Nagano, C.; Nozaki, S.; Kamitani, K.; Kojio, K.; Takahara, A.; Shinohara, N.; Mita, K.; Uchida, K.; Yamasaki, S. Investigation of Deformation Behavior of Thiourethane Elastomers Using In Situ X-ray Scattering, Diffraction, and Absorption Methods. *Macromolecules*, **2019**, *52*, 6825−6833.
99. Nozaki, S.; Masuda, S.; Cheng, C.-H.; Nagano, C.; Yokomachi, K.; Kamitani, K.; Aoyama, K.; Masunaga, H.; Kojio, K.; Takahara, A. Direct Evaluation of Local Dynamic Viscoelastic Properties of Isotactic Polypropylene Films Based on a Dynamic μ-Beam X-ray Diffraction Method. *ACS Macro Lett.*, **2019**, *8*, 218−222.
100. Strobl, G. R.; Schneider, M. Direct Evaluation of the Electron Density Correlation Function of Partially Crystalline Polymers. *J. Polym. Sci.*, **1980**, *18*, 1343−1359.
101. Koberstein, J.; Stein R. Small-Angle X-Ray Scattering Measurements of Diffuse Phase-Boundary Thicknesses in Segmented Polyurethane Elastomers. *J. Polym. Sci. Phys. Ed.*, **1983**, *21*, 2181−2200.
102. Baltá Calleja, F. J.; Vonk, C. G. *X-ray Scattering of Synthetic Polymers*. Elsevier, Amsterdam, 1989.
103. Göschel, U.; Urban, G. Supermolecular structure of oriented and semicrystalline poly(ethylene terephthalate) as revealed by the electron density correlation function from small-angle X-ray scattering studies. *Polymer*, **1995**, *36*, 3633−3639.
104. Stribeck, N. *X-Ray Scattering of Soft Matter*. Springer, Berlin, 2007.
105. Glatter, O. J. A new method for the evaluation of small-angle scattering data. *Appl. Crystallogr.*, **1977**, *10*, 415−421.
106. Glatter, O. Evaluation of small-angle scattering data from lamellar and cylindrical particles by the indirect transformation method. *J. Appl. Crystallogr.*, **1980**, *13*, 577–584.
107. Moore, P. B. Small-angle scattering. Information content and error analysis *J. Appl. Cryst.* **1980**, 13, 168–175.
108. Svergun, D. I., Semenyuk, A. V. & Feigin, L. A. Small-angle-scattering-data treatment by the regularization method. *Acta Cryst. A*, **1988**, *44*, 244–250.
109. Porod, G. Die Abhangigkeitder Rontgen-Kleinwinkelstreuung von Form und Groβe der kolloiden Teilchen in verdunnten Systemen, IV. *Acta Phys. Austriaca*, **1948**, 2, 255–292.
110. Billinge, S. J. L. & Thorpe, M. F. Local Structure from Diffraction, edited by S. J. L. Billinge. New York, Plenum Press, 1998.
111. Peterson, P. F.; Gutmann, M.; Proffen, Th.; Billinge S. J. L. PDFgetN: a user-friendly program to extract the total scattering structure factor and the pair distribution function from neutron powder diffraction data. *J. Appl. Cryst.*, **2000**, *33*, 1192.
112. Jensen, K. M. Ø.; Blichfeld, A. B.; Bauers, S. R.; Wood, S. R.; Dooryhée, E.; Johnson, D. C.; Iversen B. B.; Billinge S. J. L. Demonstration of thin film pair distribution function analysis (tfPDF) for the study of local structure in amorphous and crystalline thin films. *IUCrJ*, **2015**, *2*, 5.

113. Debye, P.; Bueche, A. M. Scattering by an inhomogeneous solid. *J. Appl. Phys.*, **1949**, *20*, 518–525.
114. Hansen, S. Estimation of chord length distributions from small-angle scattering using indirect Fourier transformation *J. Appl. Cryst.*, **2003**, *36*, 1190–1196.
115. Fritz, G. Determination of pair correlation functions of dense colloidal systems by means of indirect Fourier transformation. *J. Chem. Phys.*, **2006**, *124*, 214707.
116. Fritz-Popovski, G. Interpretation of two-dimensional real-space functions obtained from small-angle scattering data of oriented microstructures. *J. Appl. Cryst.* **2015**, *48*, 44–51.
117. Lee, B.; Park, I.; Yoon, J.; Park, S.; Kim, J.; Kim, K.-W.; Chang, T.; Ree, M.Structural Analysis of Block Copolymer Thin Films with Grazing Incidence Small-Angle X-ray Scattering. *Macromolecules*, **2005**, *38*, 4311–4323.
118. Lee, B.; Park, Y.-H.; Hwang, Y.-T.; Oh, W.; Yoon, J.; Ree, M. Ultralow-*k* nanoporous organosilicate dielectric films imprinted with dendritic spheres. *Nature Materials*, **2005**, *4*, 147–150.
119. Lee, B.; Oh, W.; Hwang, Y.; Park, Y.-H.; Yoon, J.; Jin, K. S.; Heo, K.; Kim, J.; Kim, K.-W.; Ree, M. Imprinting Well-Controlled Nanopores in Organosilicate Dielectric Films: Triethoxysilyl-Modified Six-Armed Poly(ϵ-caprolactone) and Its Chemical Hybridization with an Organosilicate Precursor. *Adv. Mater.*, **2005**, *17*, 696–701.
120. Ree, M. Probing the Self-Assembled Nanostructures of Functional Polymers with Synchrotron Grazing Incidence X-ray Scattering. *Macromol. Rapid Commun.* **2014**, *35*, 930.
121. Lee, B.; Yoon, J.; Oh, W.; Hwang, Y.; Heo, K.; Jin, K. S.; Kim, J.; Kim, K.-W.; Ree, M. In-Situ Grazing Incidence Small-Angle X-ray Scattering Studies on Nanopore Evolution in Low-*k* Organosilicate Dielectric Thin Films. *Macromolecules* **2005**, *39*, 3395.
122. Lee, B.; Oh, W.; Yoon, J.; Hwang, Y.; Kim, J.; Landes, B. G.; Quintana, J. P.; Ree, M. Scattering Studies of Nanoporous Organosilicate Thin Films Imprinted with Reactive Star Porogens. *Macromolecules* **2005**, *38*, 8991.
123. Jin, S.; Yoon, J.; Heo, K.; Park, H.-W.; Shin, T. J.; Chang, T.; Ree, M. Detailed analysis of gyroid structures in diblock copolymer thin films with synchrotron grazing incidence X-ray scattering. *J. Appl. Crystalogr.* **2007**, *40*, 950.
124. Heo, K.; Yoon, J; Jin, S.; Kim, J.; Kim, K.-W.; Shin, T. J.; Chung, B.; Chang, T.; Ree, M. Polystyrene-*b*-polyisoprene thin films with hexagonally perforated layer structure: quantitative grazing incidence X-ray scattering analysis. *J. Appl. Cryst.* **2008**, *41*, 281.
125. Rho, Y.; Ahn, B.; Yoon, J.; Ree, M. Comprehensive synchrotron grazing incidence X-ray scattering analysis of nanostructures in porous polymethylsilsesquioxane dielectric thin films. *J. Appl. Crystallogr.* **2013**, *46*, 466.
126. Yoon, J.; Jin, S.; Ahn, B.; Rho, Y.; Hirai, T.; Maeda, R.; Hayakawa, T.; Kim, J.; Kim, K.-W.; Ree, M. Phase Transitions in Thin Films of a Diblock Copolymer Composed of a Linear Polymer Block and a Brush Polymer Block with Mesogenic Oligothiophenyl Bristles. *Macromolecules* **2008**, *41*, 8778.
127. Yoon, J.; Jung, S. Y.; Ahn, B.; Heo, K.; Jin, S.; Iyoda, T.; Yoshida, H.; Ree, M. Order-Order and Order-Disorder Transitions in Thin Films of an Amphiphilic Liquid Crystalline Diblock Copolymer. *J. Phys. Chem. B.* **2008**, *112*, 8486.
128. Heo, K.; Jin, K. S.; Yoon, J.; Jin, S.; Oh, W.; Ree, M. Synchrotron X-ray Scattering Study of the Mechanism of Nanopore Generation in Nanoporous Organosilicate Thin Films Imprinted with a Reactive Six-Armed Porogen. *J. Phys. Chem. B* **2006**, *110*, 15887.
129. Heo, K.; Oh, K. S.; Yoon, J.; Jin, K. S.; Jin, S.; Choi, C. K.; Ree, M. Synchrotron X-ray scattering and reflectivity studies of the structure of low dielectric constant SiOCH thin films prepared from bistri-methylsilylmethane by chemical vapor deposition. *J. Appl. Crystallogr.* **2007**, *40*, s614.

130. Jin, K. S.; Heo, K.; Oh, W.; Yoon, J.; Lee, B.; Hwang, Y.; Kim, J.-S.; Park, Y.-H.; Chang, T.; Ree, M. Grazing-incidence small-angle X-ray scattering studies on templating nanopores in networked polymer thin films with a multi-armed porogen. *J. Appl. Crystallogr*. **2007**, *40*, s631.
131. Heo, K.; Park, S. G.; Yoon, J.; Jin, K. S.; Jin, S.; Rhee, S. W.; Ree, M. Quantitative Structure and Property Analysis of Nanoporous Low Dielectric Constant SiCOH Thin Films. *J. Phys. Chem. C* **2007**, *111*, 10848.
132. Roe, Y. J. *Methods of X-ray and Neutron Scattering in Polymer Science*. New York: Oxford University Press; 2000.
133. Lazzari, R. IsGISAXS: a program for grazing-incidence small-angle X-ray scattering analysis of supported islands. *J. Appl. Crystallogr*. **2002**, *35*, 406.
134. Renaud, G.; Lazzari, R.; Leroy, F. Probing surface and interface morphology with Grazing Incidence Small Angle X-Ray Scattering. *Surf. Sci. Rep*. **2009**, *64*, 255.
135. Pedersen, J. S. Determination of size distribution from small-angle scattering data for systems with effective hard-sphere interactions. *J. Appl. Crystallogr*. **1994**, *27*, 595.
136. Hosemann, R.; Bagchi, S. N. *Direct analysis of diffraction by matter*. Amsterdam: North-Holland; 1962.
137. Yoon, J.; Yang, S. Y.; Heo, K.; Lee, B.; Joo, W.; Kim, J. K.; Ree, M. Nondestructive quantitative synchrotron grazing incidence X-ray scattering analysis of cylindrical nanostructures in supported thin films. *J. Appl. Cryst*. **2007**, *40*, 305.
138. Kim, G.; Yoon, J.; Kim, J.-S.; Kim, H.; Ree, M. Moelcular Fibers Based on the Honeycomb-Like Self-Assembly of an α-Helical Polypeptide. *J. Phys. Chem. B* **2008**, *112*, 8868.
139. Yoon, J; Jin, S. K; Kim, H. C; Kim, G; Heo, K; Jin, S; Kim, J; Kim, K.-W; Ree, M. Quantitative analysis of lamellar structures in brush polymer thin films by synchrotron grazing-incidence X-ray scattering. *J. Appl. Cryst*. **2007**, *40*, 476.
140. Rho, Y.; Min, J.; Yoon, J.; Ahn, B.; Jung, S.; Kim, K.; Shah, P.; Lee, J.-S.; Ree, M. Reversible conformation-driven order-order transition of peptide-mimic poly(*n*-alkyl isocyanate) in thin films via selective solvent-annealing. *NPG Asia Mater.* **2012**, *4*, e29.
141. Ahn, B.; Kim, D. M.; Hsu, J.-C.; Ko, Y.-G.; Shin, T. J.; Kim, J.; Chen, W.-C.; Ree, M. Tunable Film Morphologies of Brush-Linear Diblock Copolymer Bearing Difluorene Moieties Yield a Variety of Digital Memory Properties. *ACS Macro Letters* **2013**, *2*, 555−560.
142. Hahm, S. G.; Rho, Y.; Jung, J.; Kim, S. H.; Sajoto, T.; Kim, F. S.; Barlow, S.; Park, C. E.; Jenekhe, S. A.; Marder, S. R.; Ree, M. High-Performance n-Channel Thin-Film Field-Effect Transistors Based on a Nanowire-Forming Polymer. *Adv. Funct. Mater.* **2013**, *23*, 2060.
143. Kim, Y. Y.; Ahn, B.; Sa, S.; Jeon, M.; Roth, S. V.; Kim, S. Y.; Ree, M. Self-Assembly Characteristics of a Crystalline-Amorphous Diblock Copolymer in Nanoscale Thin Films. *Macromolecules* **2013**, *46*, 8235.
144. Kim, K.; Kim, Y. Y.; Park, S.; Ko, Y.-G.; Rho, Y.; Kwon, W.; Shin, T. J.; Kim, J.; Ree, M. Nanostructure- and Orientation-Controlled Digital Memory Behaviors of Linear-Brush Diblock Copolymers in Nanoscale Thin Films. *Macromolecules* **2014**, *47*, 4397.
145. Ahn, B.; Kwon, W.; Kim, H.; Ree, M. Cooperative and selective self-assembly behaviors of diblock copolypeptides in nanoscale thin films. *Polym. Chem.* **2014**, *5*, 1912.
146. Matsuo, M.; Tamada, M.; Terada, T.; Sawatari, C.; Niwa, M. Deformation mechanism of poly(ethylene terephthalate) film under uniaxial stretching. *Macromolecules* **1982**, *15*, 988.

Chapter 2

Nanoscale Film Morphologies and Chain Conformations of Topological Poly(ε-caprolactone)s

2.1 Introduction

Nanoscale cages are attractive to academia and industry because of their potential applications such as capsules, carriers, templates, reactors, and so on.[1-5] In general, they can be prepared in two different ways: (i) self-assembly of molecules[1,2,6-14] and (ii) molecular cage formation via chemical synthesis.[3-5,15-17]

The self-assembly approach has been practiced in various ways so far; as a result, a number of physically assembled cages have been reported, which behave various sizes, topologies, and functionalities.[1,2,6-14] However, physically assembled cages are known to be sensitively changed their dimension and stability depending on external environmental conditions such as pH, temperature, solvent nature, and other chemical ingredients. Much research effort has also been made on molecular cages because of great challenges in the synthesis and higher stability to external condition variations, but mainly limited to small organic molecule-based cages.[3-5,15-18] The synthetic approach has been extended to develop macromolecular cages. Even though difficulties in the synthesis and purification, several macromolecular cages have been reported, which are based on polytrahydrofuran,[19-23] polystyrene,[24-26] poly(ε-caprolactone),[27] and poly(*n*-decyl glycidyl ether-*block*-2-(2-(2-methoxyethoxy)ethoxy)ethyl glycidyl ether).[28] However, understanding of these interesting macromolecular cages in the aspects of morphology and properties is in very early stages.

In this chapter, the nanoscale film morphology details of cage-shaped crystallizable poly(ε-caprolactone) and its star-shaped, single cyclic, and linear counterparts have been investigated for the first time using synchrotron grazing incidence X-ray scattering (GIXS). In addition, their thermal properties are investigated by using thermogravimetry (TGA) and differential scanning calorimetry (DSC).

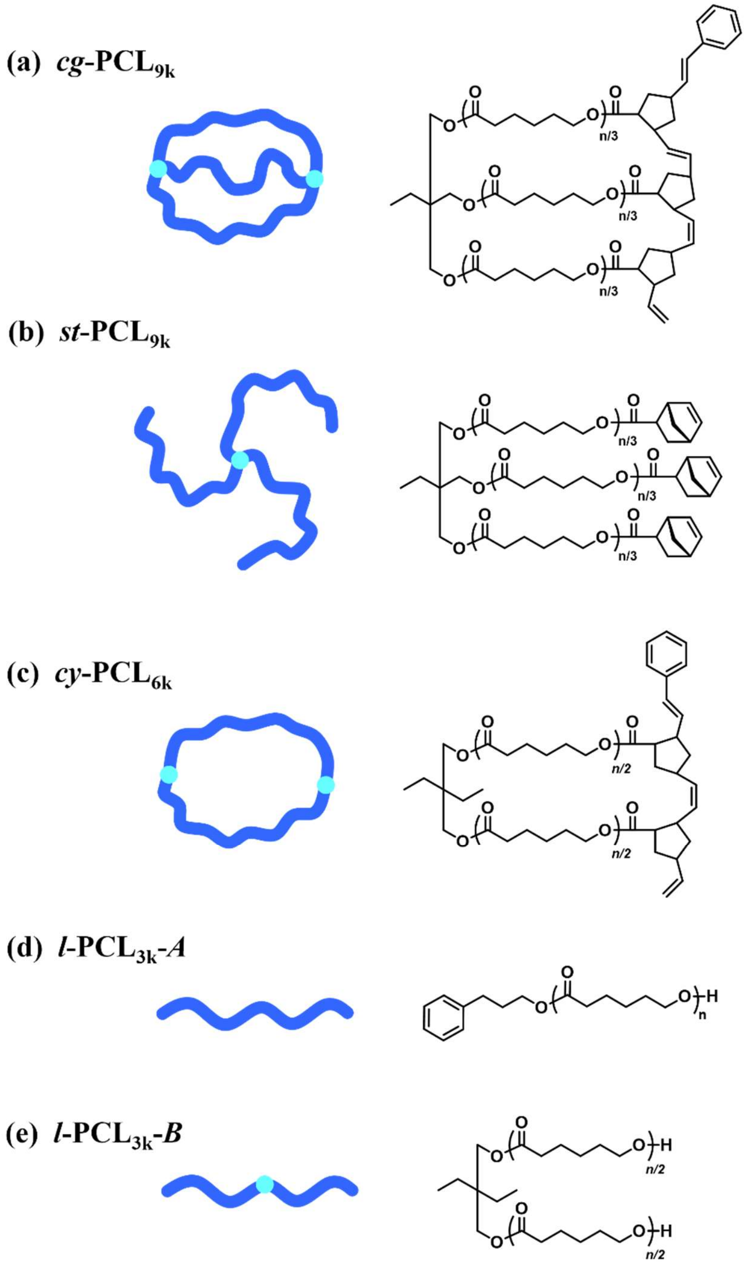

Figure 2.1. Chemical structures of cage-shaped poly(*ε*-caprolactone) and its star-shaped, single cyclic, and linear counterparts.

Table 2.1. Fundamental characteristics of cage-shaped poly(ε-caprolactone) and its star-shaped, single cyclic, and linear counterparts

Polymer	$M_{\mathrm{n,NMR}}$[a]	$M_{\mathrm{n,SEC}}$[b]	$Đ$[c]	$T_{\mathrm{d,5}}$[d] (°C)
cg-PCL$_{9k}$	10600	11900	1.08	375.0
st-PCL$_{9k}$	10600	14700	1.05	377.1
cy-PCL$_{6k}$	6500	8500	1.08	375.7
l-PCL$_{3k}$-*A*	3800	7300	1.09	370.6
l-PCL$_{3k}$-*B*	3300	5500	1.06	369.5

[a] Number-average molecular weight determined in $CDCl_3$ by ^1H NMR spectroscopy analysis. [b] Number-average molecular weight determined by size exclusion chromatography (SEC) in THF using polystyrene standards. [c] Dispersity determined by SEC in THF using polystyrene standards. [d] Temperature at which 5.0 wt % weight loss occurred under nitrogen atmosphere and temperature ramping rate of 10 °C min^{-1}.

2.2 Experimental Section

Cage-shaped poly(*ε*-caprolactone) (*cg*-PCL$_{9k}$) and its star-shaped (*st*-PCL$_{9k}$), single cyclic (*cy*-PCL$_{6k}$), and linear (*l*-PCL$_{3k}$-*A* and *l*-PCL$_{3k}$-*B*) counterparts were synthesized according to the methods reported previously in the literature;[27] Their molecular characteristics are listed in Table 2.1.

TGA and DSC analyses were carried out with a rate of 10.0 °C min^{-1} under nitrogen atmosphere using Hitachi instruments (model STA7200 and model DSC7020, Hitachi Instrument, Tokyo, Japan).

For the individual topological polymers, solutions with a concentration of 0.5 wt% were prepared in tetrahydrofuran and filtrated with polytetrafluoroethylene filter membranes (0.2 μm pore size). Each solution was spin-cast onto silicon substrates and then followed by drying in vacuum at room temperature for 24 h, giving 100−120 nm thick films. The film thicknesses were measured by using a spectroscopic ellipsometer (Model M-2000, Woollam, Lincoln, NE, USA). The films were kept at room temperature in a drying chamber before use.

All GIXS measurements were carried out with a two-dimensional (2D) charge-coupled detector (CCD) (model Rayonix 2D SX 165, Rayonix, Evanston, IL, USA) at the 3D Beamline of the PLS-II facility (3.0 GeV power, 400 mA), Pohang Accelerator Laboratory, Pohang, Korea.[29] An X-ray beam with a wavelength λ of 0.12296 nm was chosen and used; an incidence angle α_i was set in the range of 0.1240–0.1400° with respect to the film plane. Small angle grazing incidence X-ray scattering (GISAXS) measurements were conducted at a sample-to-detector distance (SDD) of 2926.0 or 2947.1 mm, whereas wide angle grazing incidence X-ray scattering (GIWAXS) measurements were performed at SDD = 209.0 or 210.9 mm. The scattering data collection time ranged in 10–30 s. All scattering measurements were conducted at room temperature. The scattering angles were corrected by using a precalibrated polystyrene-*block*-poly(ethylene-*random*-butylene)-*block*-polystyrene and silver behenate standards

(Tokyo Chemical Inc., Tokyo, Japan) were employed; the positions of the X-ray beams reflected from the silicon substrate were used additionally.

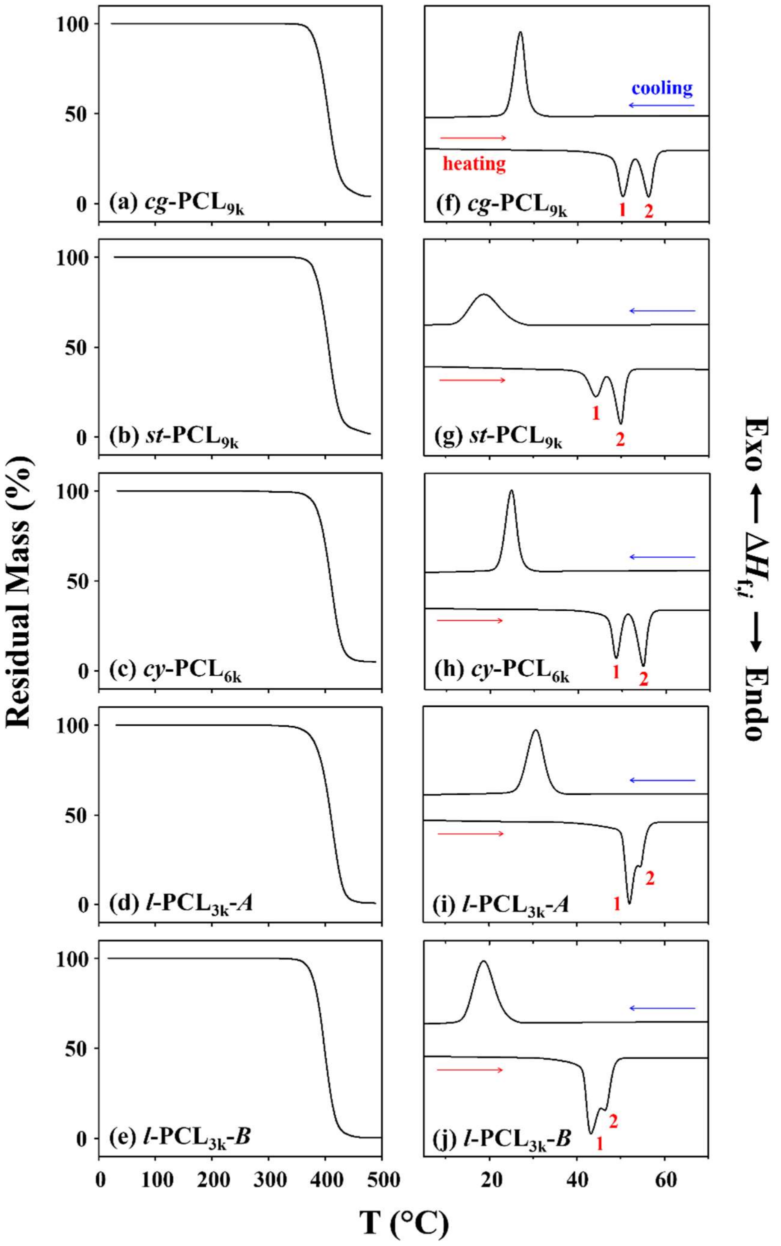

Figure 2.2. TGA and DSC thermograms of PCLs in various topologies, which were measured at a rate of 10.0 °C min^{-1} under nitrogen atmosphere: (a-e) TGA thermograms; (f-j) DSC thermograms.

Table 2.2. Thermal characteristics of cage-shaped poly(ε-caprolactone) and its star-shaped, single cyclic, and linear counterparts

Polymer	T_c^a (°C)	$-\Delta H_{f,c}^b$ ($J\ g^{-1}$)	$X_{c,c}^c$ (%)	T_{m1}^d (°C)	T_{m2}^e (°C)	$\Delta H_{f,m1}^f$ ($J\ g^{-1}$)	$\Delta H_{f,m2}^g$ ($J\ g^{-1}$)	$-\Delta H_{f,m}^h$ ($J\ g^{-1}$)	$X_{c,m1}^i$ (%)	$X_{c,m2}^j$ (%)	$X_{c,m}^k$ (%)
cg-PCL$_{9k}$	26.9	79.8^l $(75.3)^m$	57.1^n $(54.0)^o$	50.3	56.1	43.3^l $(40.9)^m$	36.7^l $(34.6)^m$	80.0^l $(75.5)^m$	31.0^n $(29.3)^o$	26.3^n $(24.8)^o$	57.3^n $(54.1)^o$
st-PCL$_{9k}$	24.8	87.5 (81.4)	62.8 (58.4)	48.7	54.9	43.7 (40.7)	46.3 (43.0)	90.0 (83.7)	31.4 (29.2)	33.1 (30.8)	64.5 (60.0)
cy-PCL$_{6k}$	18.6	64.8 (64.0)	46.5 (45.9)	44.3	49.9	24.7 (24.3)	38.3 (37.9)	63.0 (62.2)	17.7 (17.5)	27.5 (27.1)	45.2 (44.6)
l-PCL$_{3k}$-*A*	30.7	89.7 (86.5)	64.3 (62.0)	52.1	54.4	65.7 (63.4)	21.2 (20.4)	86.9 (83.8)	47.1 (45.5)	15.2 (14.6)	62.3 (60.1)
l-PCL$_{3k}$-*B*	18.7	92.7 (89.0)	65.5 (63.8)	43.2	46.4	62.3 (59.8)	34.2 (32.8)	96.5 (92.6)	44.7 (42.9)	24.5 (23.5)	69.2 (66.4)

[a] Crystallization temperature of the PCL part determined from the peak maximum of the exothermic crystallization transition measured by differential scanning calorimetry (DSC) analysis under nitrogen atmosphere and a temperature ramping rate of 10 °C min^{-1}. [b] Heat of fusion generated from the crystallization transition. [c] Crystallinity estimated from the heat of fusion of crystallization assuming $\Delta H_c^\circ = 139.5\ J\ g^{-1}$ for ideal PCL crystal. [d] Crystal melting temperature 1 of PCL determined from the maximum of the endothermic crystal melting peak 1. [e] Crystal melting temperature 2 of PCL determined from the maximum of the endothermic crystal melting peak 2. [f] Heat of fusion estimated from the crystal melting peak 1. [g] Heat of fusion estimated from the crystal melting peak 2. [h] Total heat of fusion estimated from the crystal melting peak of only PCL part. [i] Crystallinity 1 estimated from the heat of fusion of the crystal melting peak 1 under assuming $\Delta H_m^\circ = -\Delta H_c^\circ$ for ideal PCL crystal. [j] Crystallinity 2 estimated from the heat of fusion of the crystal melting peak 2 under assuming ΔH_m° for ideal PCL crystal. [k] Overall crystallinity estimated from the total heat of fusion of the crystal melting peaks under assuming ΔH_m° for ideal PCL crystal. [l] Heat of fusion of only PCL part estimated from the phase transition. [m] Heat of fusion estimated from the phase transition with respect to the total weight of polymer sample. [n] Crystallinity of only PCL part estimated from the heat of fusion of the phase transition. [o] Crystallinity estimated from the heat of fusion of the phase transition with respect to the total weight of polymer sample.

2.3 Results and Discussion

2.3.1 Thermal Stability and Phase Transitions

All PCL polymers reveal single-step degradation behaviors regardless of the topologies, as shown in Figure 2.2a-e. However, the degradation temperature is found to vary slightly with the topologies. The temperature occurring the first 5% mass loss ($T_{d,5}$) is 370.6 °C for *l*-PCL$_{3k}$-*A*, 369.5 °C for *l*-PCL$_{3k}$-*B*, 375.7 °C for *cy*-PCL$_{6k}$, 377.1 °C for *st*-PCL$_{9k}$, and 375.0 °C for *cg*-PCL$_{9k}$ (Table 2.1). The caged and cyclic polymers show ca. 5 °C higher stability, compared to the linear counterparts. These results are evident for the effects of cage and cyclic topologies, which could originate from the absence of chain ends. Surprisingly, the star-shaped polymer also reveals ca. 7 °C higher stability than do the linear counterparts although having three chain ends. In fact, such the three end groups are capped by norbornyl group, as illustrated in the chemical structure in Figure 2.1. Taking this fact into account, the higher stability of the star-shaped polymer could be attributed to the capped chain ends rather than the topology effect.

Figure 2.2f-j display representative phase-transition behaviors of the topological PCL polymers in cooling run from melt and subsequent heating run. The obtained phase-transition parameters (heat of fusion, crystallization temperature at the peak maximum, crystal melting temperature at the peak maximum, and crystallinity) are summarized in Table 2.2. In the cooling run with a rate of 10 °C min^{-1} from the melt, the individual topological polymers reveal exothermic single peaks due to favorable self-assemblies (i.e., crystallizations) of the *ε*-caprolactone (CL) repeating units. These single exotherms provide key features on the nonisothermal crystallization nature of PCL as follows.

First, the sharpness (i.e., broadness) of nonisothermal crystallization exothermic peak is in the increasing order: *st*-PCL$_{9k}$ << *l*-PCL$_{3k}$-*B* < *l*-PCL$_{3k}$-*A* << *cy*-PCL$_{6k}$ < *cg*-PCL$_{9k}$. These results inform that *cg*-PCL$_{9k}$ tends to undergo crystallization in a relatively much narrower period of temperature and time, compared to all other counterparts. *cy*-PCL$_{6k}$ tends to crystallize in a slightly wide period of temperature and time than *cg*-PCL$_{9k}$ but still in a narrower period of temperature and time in comparison to the linear and star-shaped counterparts. Even among the linear counterparts, the single-block *l*-PCL$_{3k}$-*A* behaves crystallization with a relatively narrow period of temperature and time, compared to the two-block *l*-PCL$_{3k}$-*B*. *st*-PCL$_{9k}$ undergoes crystallization over the relatively widest range of temperature and time.

Second, the peak maximum temperature (T_c) of nonisothermal crystallization exotherm is in the increasing order: *st*-PCL$_{9k}$ < *l*-PCL$_{3k}$-*B* << *cy*-PCL$_{6k}$ < *cg*-PCL$_{9k}$ << *l*-PCL$_{3k}$-*A*. Except *l*-PCL$_{3k}$-*A*, the increasing order of T_c resembles that of the crystallization peak sharpness, suggesting that narrower crystallization transition is directly related to higher crystallization temperature. These results inform again that *cg*-PCL$_{9k}$ and *cy*-PCL$_{6k}$ in the geometrical compactness and endless nature crystallize more favorably, compared to the two-block linear and star-shaped counterparts. Considering merits due to the geometrical compactness and endless nature, one may expect lower T_c for *l*-PCL$_{3k}$-*A*, compared to those of *cg*-PCL$_{9k}$ and *cy*-PCL$_{6k}$. Surprisingly, *l*-PCL$_{3k}$-*A*, however, reveals the highest T_c even though the relatively broader crystallization transition. This unexpected result might be attributed to its rather less bulky end groups. *l*-PCL$_{3k}$-*A* owns an oxypropylenylphenyl group (which originated from the used initiator in the polymerization) at one end and a hydroxyl group at the other end. In comparison, *cg*-PCL$_{9k}$ has one joint based on three *exo*-norbornenes and another joint based on trimethylolpropane, whereas *cy*-PCL$_{6k}$ owns one joint based on two *exo*-norbornenes and another joint based on 2,2-diethyl-1,3-propanediol. Such joints are bulkier than the end groups of *l*-PCL$_{3k}$-*A*. The bulky joint parts may cause somewhat retardation in the crystallization, consequently lowering T_c. In the case of *l*-PCL$_{3k}$-*B*, the 2,2-diethyl-1,3-propanediol based linker is present in addition to two hydroxyl end groups. Also, its divided blocks have a molecular weight which is a half of that of *l*-PCL$_{3k}$-*A*. These two factors may work out together, causing a certain level of reduction in T_c.

Finally, the heat of fusion of nonisothermal crystallization transition ($\Delta H_{f,c}$) as well as the resulting crystallinity ($X_{c,c}$) is in the increasing order: *st*-PCL$_{9k}$ < *cg*-PCL$_{9k}$ < *cy*-PCL$_{6k}$ < *l*-PCL$_{3k}$-*A* < *l*-PCL$_{3k}$-*B*. These are evidences that the geometrical compactness and endless nature could not be highlighted as positive merits in $\Delta H_{f,c}$ and $X_{c,c}$. These unexpected results may also be attributed to the bulkier joints in *cg*-PCL$_{9k}$ < *cy*-PCL$_{6k}$, which override the merits of such molecular compactness and endless nature. In particular, the bulky joints may cause defects on the top and bottom surfaces of growing and resultant crystals.

In the heating run with a rate of 10 °C min^{-1} just after the cooling run, all PCL polymers exhibit crystal melting endothermic thermograms. Surprisingly, *cg*-PCL_{9k} shows clearly two crystal melting peaks rather than a single melting peak; one peak appears at 50.3 °C (= T_{m1}, crystal melting temperature **1**) and another peak appears at 56.1 °C (= T_{m2}, crystal melting temperature **2**). More interestingly, similar two crystal melting behaviors are observed for all other counterparts even including *l*-PCL_{3k}-*A* and *l*-PCL_{3k}-*B*. These two crystal melting endothermic behaviors provide additional key information on the nonisothermal crystallization of PCL and the resulting crystals below.

First, T_{m1} is in the increasing order: *l*-PCL_{3k}-*B* < *st*-PCL_{9k} < *cy*-PCL_{6k} < *cg*-PCL_{9k} < *l*-PCL_{3k}-*A*. Except for *l*-PCL_{3k}-*B*, the increasing order of T_{m1} in the heating run resembles that of T_{c} in the cooling run. These results inform that the crystallization histories are directly reflected into the melting behaviors of the resulting crystals. The lower T_{m1} of *l*-PCL_{3k}-*B* may be mainly attributed to the block chain lengths that are just a half of those of the other counterparts.

Second, the heat of fusion of the crystal melting **1** ($\Delta H_{\mathrm{f,m1}}$), as well as its crystallinity ($X_{\mathrm{c,m1}}$), is in the increasing order: *st*-PCL_{9k} < *cg*-PCL_{9k} < *cy*-PCL_{6k} < *l*-PCL_{3k}-*B* < *l*-PCL_{3k}-*A*. Except for *l*-PCL_{3k}-*B*, the increasing orders of $\Delta H_{\mathrm{f,m1}}$ and $X_{\mathrm{c,m1}}$ resembles those of $\Delta H_{\mathrm{f,c}}$ and $X_{\mathrm{c,c}}$ in the cooling run. These confirm again that the crystallization histories are directly reflected into the melting behaviors of the resulting crystals. The larger $\Delta H_{\mathrm{f,m1}}$ and $X_{\mathrm{c,m1}}$ of *l*-PCL_{3k}-*B* may originate mainly from a more favorable crystallization ability of the relatively shorter block chains; such better crystallization power may stand on its proper chain mobility required in the crystallization.

Third, T_{m2} is in the increasing order: *l*-PCL$_{3k}$-*B* < *st*-PCL$_{9k}$ < *l*-PCL$_{3k}$-*A* < *cy*-PCL$_{6k}$ < *cg*-PCL$_{9k}$. This increasing order of T_{m2} is quite different from those of T_{m1} and T_c. The geometrical compactness and endless nature of *cg*-PCL$_{9k}$ as well as *cy*-PCL$_{6k}$ are clearly highlighted in the crystal melting transition peak **2**.

Fourth, the heat of fusion of the crystal melting **2** ($\Delta H_{f,m2}$) as well as its crystallinity ($X_{c,m2}$), is in the increasing order: *l*-PCL$_{3k}$-*A* < *l*-PCL$_{3k}$-*B* < *cg*-PCL$_{9k}$ < *st*-PCL$_{9k}$ < *cy*-PCL$_{6k}$. These trends are different from those of $\Delta H_{f,m1}$ and $X_{c,m1}$ as well as $\Delta H_{f,c}$ and $X_{c,c}$. These results suggest that the geometrical compactness and endless nature are beneficial, providing larger $\Delta H_{f,m2}$ and higher $X_{c,m2}$. Here it is noted that even star-shaped geometry makes great positive impact to the formation of the PCL crystal **2**, exhibiting larger $H_{f,m2}$ and higher $X_{c,m2}$ than those of *cg*-PCL$_{9k}$. It is additionally noteworthy that *cy*-PCL$_{6k}$ reveals larger $\Delta H_{f,m2}$ and higher $X_{c,m2}$ than those of *cg*-PCL$_{9k}$. The relatively lower $\Delta H_{f,m2}$ and smaller $X_{c,m2}$ of *cg*-PCL$_{9k}$ may be caused by its bulkier joints that play negative roles in the crystallization.

Fifth, the gap between T_{m1} and T_{m2}, as well as the difference between $\Delta H_{f,m1}$ and $\Delta H_{f,m2}$, is in the increasing order: *l*-PCL$_{3k}$-*A* < *l*-PCL$_{3k}$-*B* < *st*-PCL$_{9k}$ < *cg*-PCL$_{9k}$ < *cy*-PCL$_{6k}$. These results additionally highlight the impacts of molecular compactness and endless nature on the PCL crystals formed through the nonisothermal crystallization.

Sixth, the total heat of fusions of the crystal meltings ($\Delta H_{f,m}$) as well as the overall crystallinity ($X_{c,m}$) is in the increasing order: *st*-PCL$_{9k}$ < *cg*-PCL$_{9k}$ < *l*-PCL$_{3k}$-*A* < *cy*-PCL$_{6k}$ < *l*-PCL$_{3k}$-*B*. These results collectively inform that the $\Delta H_{f,m}$ and $X_{c,m}$ of PCL are influenced by at least several factors such geometrical topology, the presence and absence of end groups, the bulkiness of end groups, the bulkiness of joint linkers, and chain length.

Finally, all PCL polymers exhibit single crystallization exothermic peaks in the cooling runs but two crystal melting endothermic peaks in the subsequent heating runs, as described above. Here one question arises: Why do they all reveal two crystal melting endotherms? For *cg*-PCL$_{9k}$, slower cooling run from the melt state causes higher T_c, leading to higher T_{m1} in the subsequent heating run (Figure 2.4a). Consequently, the temperature changing rate influences significantly both T_c and T_{m1}; namely, T_c is highly correlated to T_{m1}. When the cage polymer undergoes crystallization with slower cooling rate, $\Delta H_{f,m1}$ becomes larger, whereas $\Delta H_{f,m2}$ becomes lower. Moreover, the difference between T_{m1} and T_{m2} becomes smaller with slower cooling rate. Interestingly, it is, however, found that T_{m2} is independent from the temperate changing rates in the cooling and subsequent heating runs. Similar trends are observed for all other counterparts (Figures 2.3a-e). These results collectively inform the followings. The appearance of T_{m1} (i.e., crystal melting peak **1**) is attributed to the melting phase transition of the PCL crystals formed during the cooling run from the melt. The crystal melting peak **2** (i.e., T_{m2}) is originated from the melting phase transition of the PCL crystal parts more ordered (i.e., annealed) during the subsequent heating run.

Overall, the geometrical compactness and endless nature of *cg*-PCL$_{9k}$ provides significant advantages in the crystallization of PCL chain. Such effects are also observed in the crystallization of *cy*-PCL$_{6k}$. In contrast, the star-shaped geometry of *st*-PCL$_{9k}$ causes severe demerit in the crystallization. The bulkinesses of joint and end group additionally cause a certain level of retardation in the PCL crystallization and defects in the resulting crystals.

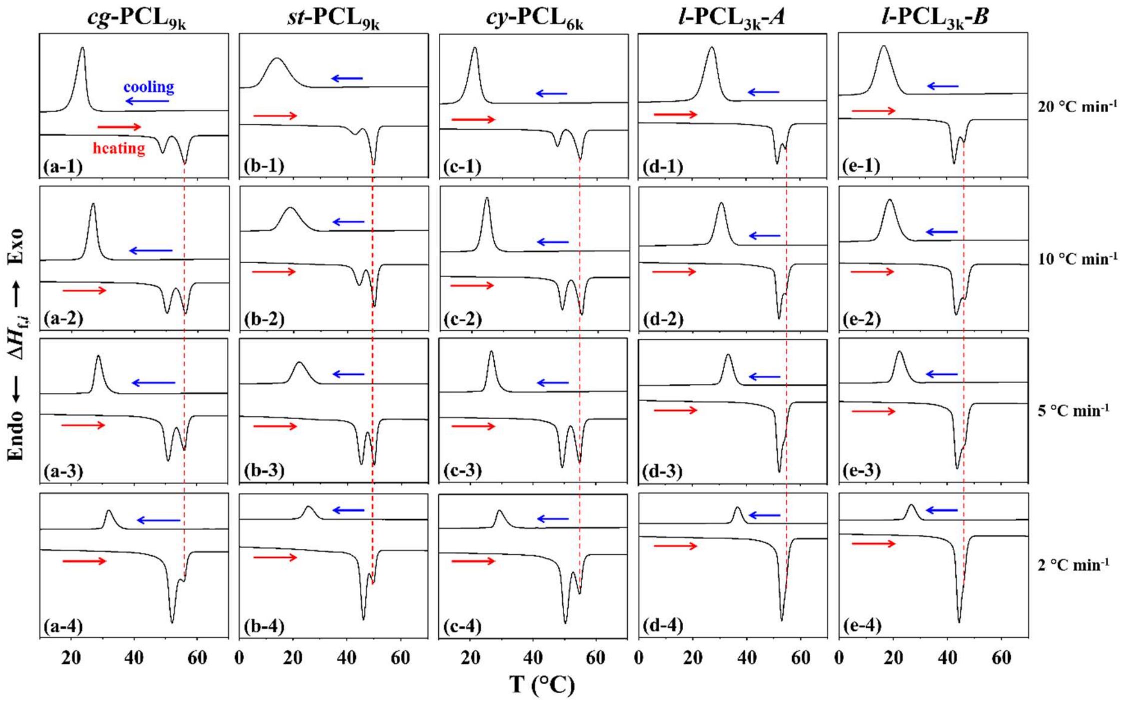

Figure 2.3. DSC thermograms of PCLs in various topologies, which were measured by cooling from the melt state and subsequent heating with various rates under nitrogen atmosphere: (a-1 to a-4) *cg*-PCL$_{9k}$; (b-1 to b-4) *st*-PCL$_{9k}$; (c-1 to c-4) *cy*-PCL$_{6k}$; (d-1 to d-4) *l*-PCL$_{3k}$-*A*; (e-1 to e-4) *l*-PCL$_{3k}$-*B*.

2.3.2. Nanoscale Film Morphologies

Figures 2.4a presents a representative of the 2D GISAXS images in scattering angle space measured from nanoscale films (100−120 nm thick) of *cg*-PCL$_{9k}$. The scattering image reveals only single broad peak along the meridian line as well as along the equatorial line; but the scattering intensity of such single peak is much stronger along the meridian line. The appearance of such single scattering peaks suggests that a mixture of horizontally- and vertically-oriented lamellae are present in the film. Thus, one-dimensional (1D) scattering profiles have been extracted along the meridian and equatorial lines and attempted to be analyzed in detail. As displayed in Figures 2.5d-e, the extracted 1D scattering profiles are satisfactorily fitted by using the GIXS formula derived with three layer model; the visual representation of the model is shown in Figure 2.4 and the formula detail is given in Section 1.4 of Chapter 1. Azimuthal scattering profile has additionally been extracted at $q = 0.509$ nm^{-}

^{1} from the scattering vector space image (i.e., q-space image) in Figure 2.5c and then analyzed well (Figure 2.5f); here, the magnitude of scattering vector q is defined by $q = (4\pi/\lambda)\sin(2\theta/2)$ where 2θ is the scattering angle. All determined structural parameters are summarized in Table 2.3.

In the film, *cg*-PCL$_{9k}$ is determined to form horizontal lamellar structure as the major structural component (98 vol%) and vertical lamellar structure as the minor component (2 vol%). The horizontal structure is characteristic of revealing a long period L of 12.4 nm (which consists of a crystalline layer l_c of 2.7 nm, an interfacial layer l_i of 3.0 nm, and an amorphous layer l_a of 3.3 nm), a positional distortion factor g of 0.23, and a second order orientation factor O_s of 0.901. Similar structural parameters are observed for the vertical lamellar structure. However, the vertical lamellar structure exhibits slightly smaller dimensional parameters and larger g factor, and $O_s = -0.474$. In comparison, the horizontal lamellar structure behaves higher dimensional stability. With the determined structural parameters, a 2D scattering image is reconstructed using the GIXS formula, as shown in Figure 2.5b. The reconstructed image is in good agreement with the measured scattering pattern, again confirming that the scattering data have been analyzed successfully.

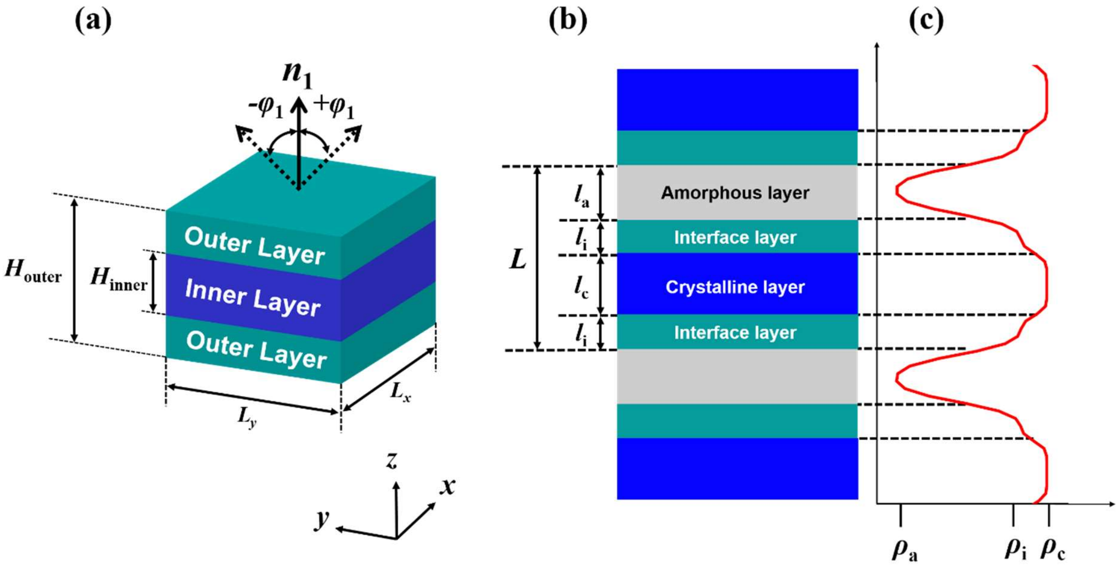

Figure 2.4. Three layer model utilized in this chapter for describing the lamellar structures formed by topological PCL homopolymers: (a) 3D representation of Inner and Outer Layers with the orientation vector $\boldsymbol{n}_1$ and polar angle φ_1 between $\boldsymbol{n}_1$ and the xy plane (parallel to the film); (b) 2D representation of three layer model where the inner layer corresponds to the crystalline layer, outer layer corresponds to the interfacial layer, and grey layer corresponds to the amorphous layer; (c) electron density profile of the three layer model indicating the highest electron density for the crystalline layer, second highest electron density for the interfacial layer, and the lowest electron density for the amorphous layer.

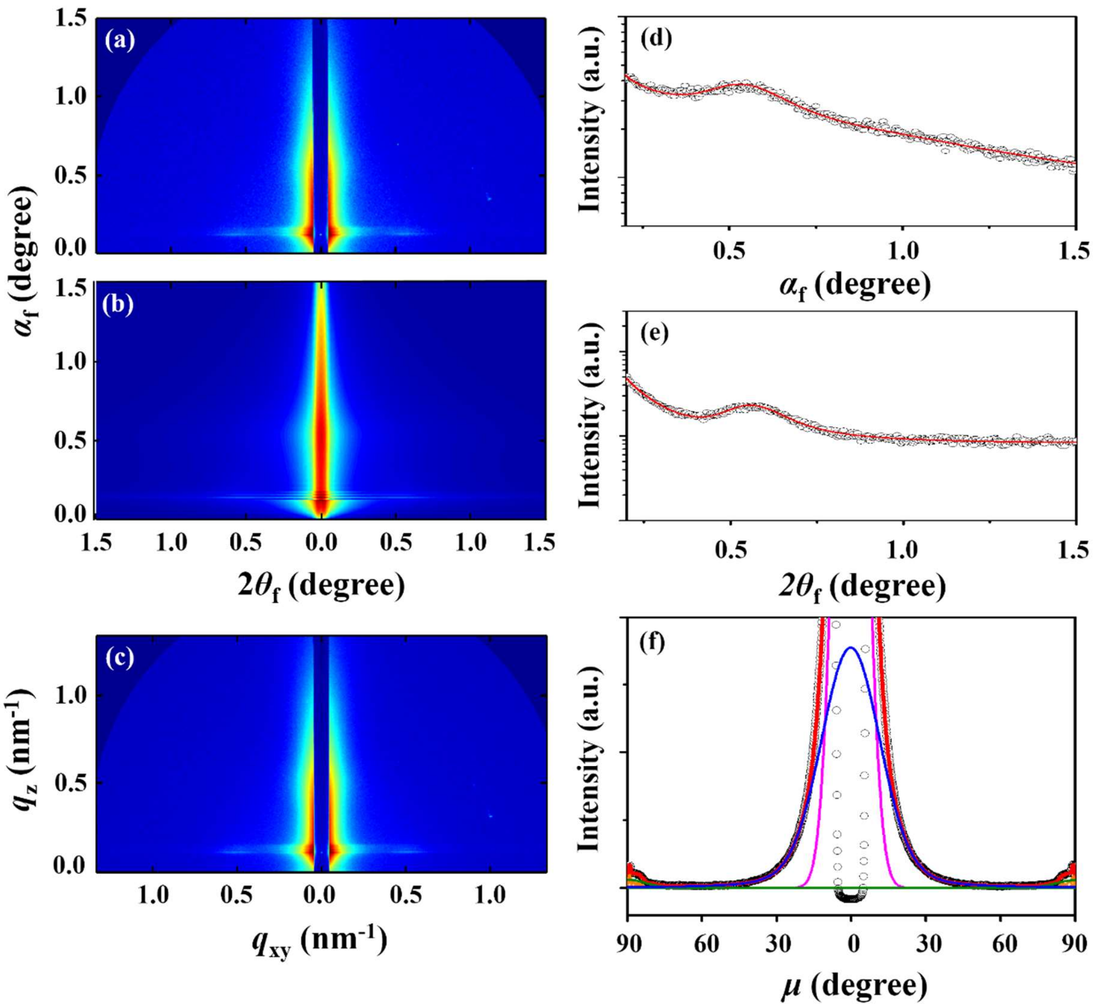

Figure 2.5. Representative scattering data of *cg*-PCL$_{9k}$ films (119.5 nm thick) measured with α_i = 0.1250° and SDD = 2926.0 mm at room temperature using a synchrotron X-ray beam (λ = 0.12296 nm): (a) 2D GISAXS image in scattering angle space; (b) 2D scattering image reconstructed with the determined structural parameters obtained from the analysis of the scattering image in (a); (c) 2D GISAXS image in scattering vector space obtained from the data in (a); (d) out-of-plane scattering profile extracted along the meridian line at $2\theta_f$ = 0.159° from the scattering images in (a); (e) in-plane scattering profile along the equatorial line at α_f = 0.155° from the data in (a); (f) azimuthal scattering profile of the annealed film extracted at q = 0.509 nm^{-1} from the data in (c). In (d) and (e), the open circles represent the measured data and the red solid lines were obtained by fitting the data using the GIXS formula driven with lamellar structure model. In (f), the open circles represent the measured data and the red solid lines represent the sum of horizontal lamella peak (blue line), vertical lamella peaks (green lines), parasitic scattering peak from reflected incident beam (pink line), and Yoneda peaks (orange lines) which were obtained by the deconvolutions of the measured data.

Table 2.3 Structural parameters of thin film morphologies of topological PCL homopolymers determined by GISAXS Analysis

Polymer	*cg*-PCL$_{9k}$		*st*-PCL$_{9k}$		*cy*-PCL$_{6k}$	*l*-PCL$_{3k}$-*A*	*l*-PCL$_{3k}$-*B*
Morphology	*horizontal lamella*	*vertical lamella*	*horizontal lamella*	*vertical lamella*	*horizontal lamella*	*horizontal lamella*	*horizontal lamella*
ϕ_L[a] (%)	98	2	97	3	100	100	100
L[b] (nm)	12.4	11.1	11.8	11.0	11.9	11.7	11.0
l_c[c] (nm)	2.7	2.6	2.1	2.0	3.3	3.5	3.2
l_i[d] (nm)	3.0	2.7	3.1	2.9	2.6	2.4	2.7
l_a[e] (nm)	3.3	3.1	3.5	3.3	3.4	3.4	2.4
σ_c[f] (nm)	1.0	1.1	1.0	0.9	0.6	0.7	0.8
σ_i[g] (nm)	1.1	1.3	1.3	1.2	0.4	0.5	0.5
g[h]	0.23	0.33	0.28	0.36	0.09	0.10	0.11
$\bar{\varphi}_1$[i] (deg.)	0	90	0	89	0	0	0
$\sigma_{\varphi 1}$[j] (deg.)	13.00	7.56	10.35	3.54	11.40	10.90	11.40
$O_{s,1}$[k]	0.901	-0.474	0.923	-0.493	0.929	0.922	0.929

[a] Volume fraction of the lamellar structure in either horizontal or vertical orientation determined from azimuthal scattering profiles. [b] Long period of lamellar structure. [c] Thickness of the crystalline layer in the phase-separated lamellar structure. [d] Thickness of interfacial layer between crystalline and amorphous layers. [e] Thickness of the amorphous layer. [f] Standard deviation for the crystalline layer. [g] Standard deviation for the interfacial layer. [h] Paracrystal distortion factor along the direction parallel to the long period of lamellar structure. [i] Mean value of the polar angle φ_1 (i.e., orientation angle) between the orientation vector $\boldsymbol{n}_1$ (which is set parallel to the axis of the long period of lamellar structure) and the out-of-plane direction of the film. [j] Standard deviation for the orientation angle φ_1 of the lamellar structure. [k] Second order orientation factor of lamellar structure.

Figures 2.6a presents a representative GISAXS image in scattering angle space of *st*-PCL$_{9k}$ films (100–120 nm thick). The 2D scattering pattern resembles that of the *cg*-PCL$_{9k}$ film. Its out-of-plane and in-plane scattering profiles are satisfactorily fitted by using the GIXS formula of lamellar structural model (Figures 2.6d-e). An azimuthal scattering profile, which has been extracted at $q = 0.511$ nm^{-1} from the q-space image, is analyzed in detail, as displayed in (Figure 2.6f; Figure 2.6c). The analysis results are compared with those of the *cg*-PCL$_{9k}$ film in Table 2.3. The 2D scattering image, which is reconstructed with the determined structural parameters, is consistent with the measured one, confirming that the scattering data analysis has been done successfully (Figure 2.6b; Figure 2.6a).

The analysis has found that *st*-PCL$_{9k}$ forms a mixture of horizontal and vertical lamellar domains in such nanoscale film as observed in the cage-shaped counterpart. The volume fractions of horizontal and vertical lamellar structures are 98 % and 2 %, respectively. The horizontal structure shows slightly larger dimensional parameters (L, l_c, l_i, and l_a) and more stable positional ordering but lower orientational order, compared to those of the vertical structure.

Similar scattering images have been measured for the nanoscale films (100−120 nm thick) of *cy*-PCL$_{6k}$, *l*-PCL$_{3k}$-*A*, and *l*-PCL$_{3k}$-*B*. They have been quantitatively analyzed in the same manner as done for those of the *cg*-PCL$_{9k}$ and *st*-PCL$_{9k}$ films (Figures 2.7, 2.8, and 2.9). The analysis results are summarized in Table 2.3.

cy-PCL$_{6k}$ reveals only horizontal lamellar structure in the nanoscale film. The lamellar structure is characteristic to exhibit much higher positional stability and better orientational order which are associated with thicker crystalline layer thickness and thinner interfacial thickness, compared to those of the cage-shaped counterpart. However, the long period is slightly smaller and the amorphous layer thickness is slightly thicker. Similar structural characteristics are observed for *l*-PCL$_{3k}$-*A* and *l*-PCL$_{3k}$-*B*.

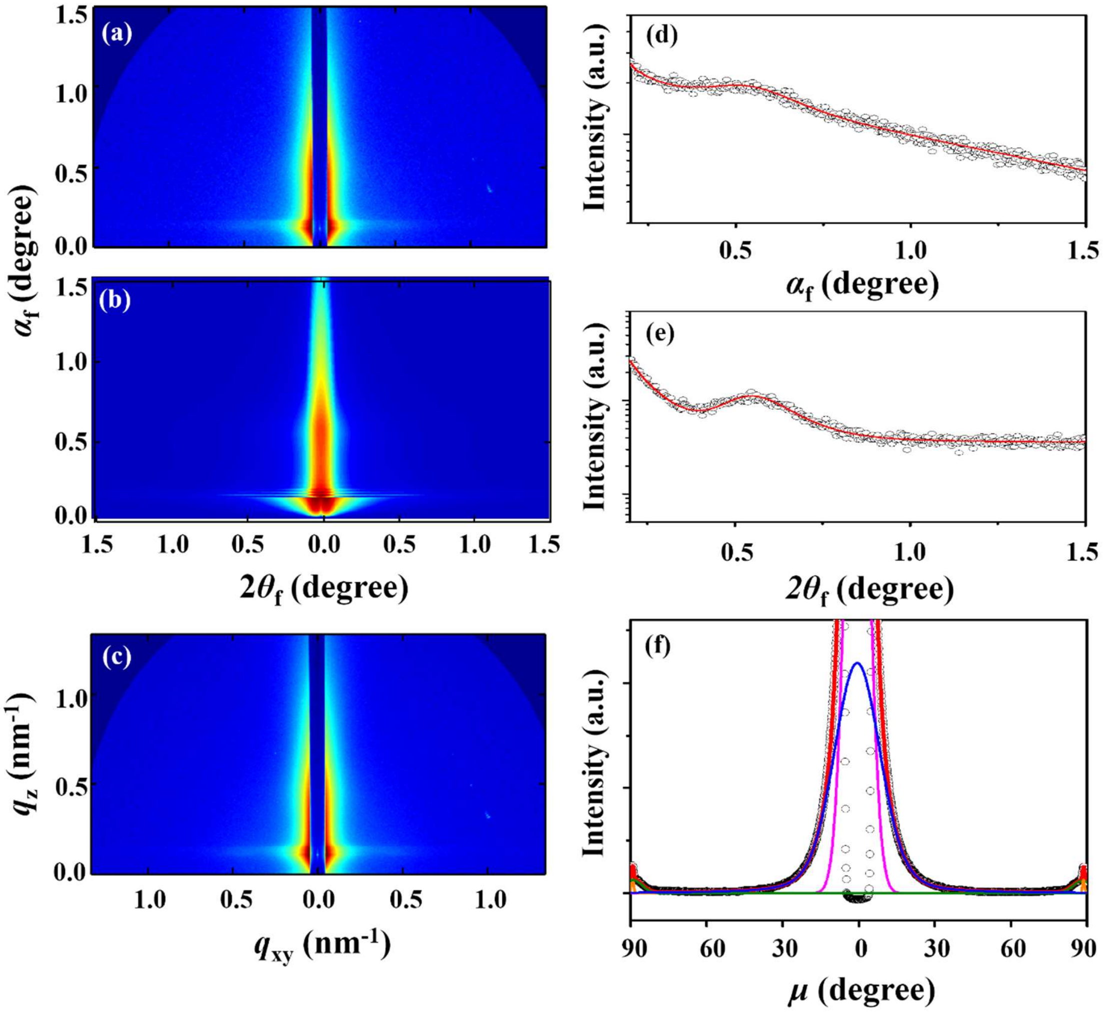

Figure 2.6. Representative scattering data of *st*-PCL$_{9k}$ films (105.3 nm thick) measured with α_i = 0.1240° and SDD = 2926.0 mm at room temperature using a synchrotron X-ray beam (λ = 0.12296 nm): (a) 2D GISAXS image in scattering angle space; (b) 2D scattering image reconstructed with the determined structural parameters obtained from the analysis of the scattering image in (a); (c) 2D GISAXS image in scattering vector space obtained from the data in (a); (d) out-of-plane scattering profile extracted along the meridian line at $2\theta_f$ = 0.159° from the data in (a); (e) in-plane scattering profile along the equatorial line at α_f = 0.135° from the data in (a); (f) azimuthal scattering profile extracted at q = 0.511 nm^{-1} from the data in (c). In (d) and (e), the open circles represent the measured data and the red solid lines were obtained by fitting the data using the GIXS formula driven with lamellar structure model. In (f), the open circles represent the measured data and the red solid lines represent the sum of horizontal lamella peak (blue line), vertical lamella peaks (green lines), parasitic scattering peak from reflected incident beam (pink line), and Yoneda peaks (orange lines) which were obtained by the deconvolutions of the measured data.

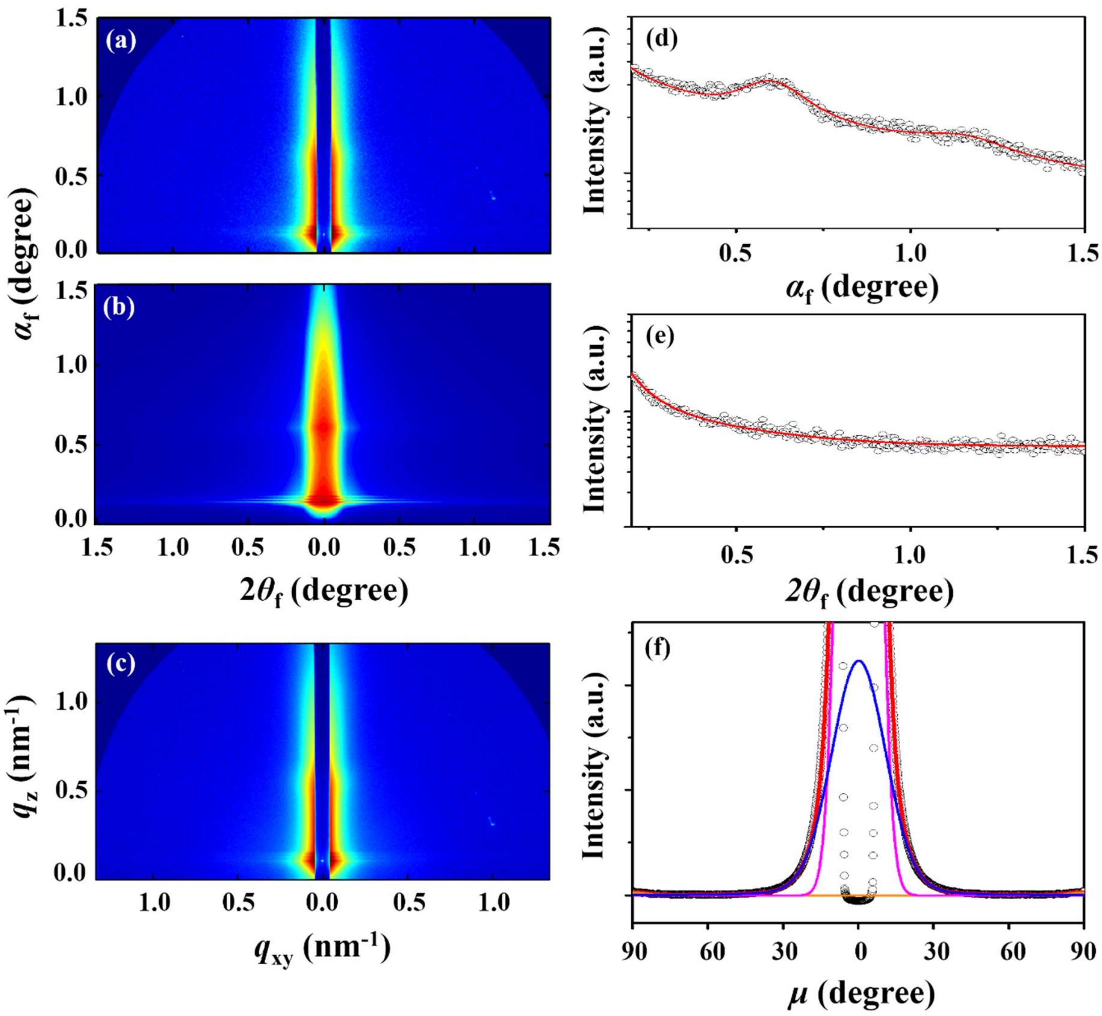

Figure 2.7. Representative scattering data of *cy*-PCL$_{6k}$ films (115.8 nm thick) measured with α_i = 0.1240° and SDD = 2926.0 mm at room temperature using a synchrotron X-ray beam (λ = 0.12296 nm): (a) 2D GISAXS image in scattering angle space; (b) 2D scattering image reconstructed with the determined structural parameters obtained from the analysis of the data in (a); (c) 2D GISAXS image in scattering vector space obtained from the data in (a); (d) out-of-plane scattering profile extracted along the meridian line at $2\theta_f$ = 0.159° from the data in (a); (e) in-plane scattering profile along the equatorial line at α_f = 0.201° from the data in (a); (f) azimuthal scattering profile extracted at q = 0.548 nm^{-1} from the data in (c). In (d) and (e), the open circles represent the measured data and the red solid lines were obtained by fitting the data using the GIXS formula driven with lamellar structure model. In (f), the open circles represent the measured data and the red solid lines represent the sum of horizontal lamella peak (blue line), vertical lamella peaks (green lines), parasitic scattering peak from reflected incident beam (pink line), and Yoneda peaks (orange lines) which were obtained by the deconvolutions of the measured data.

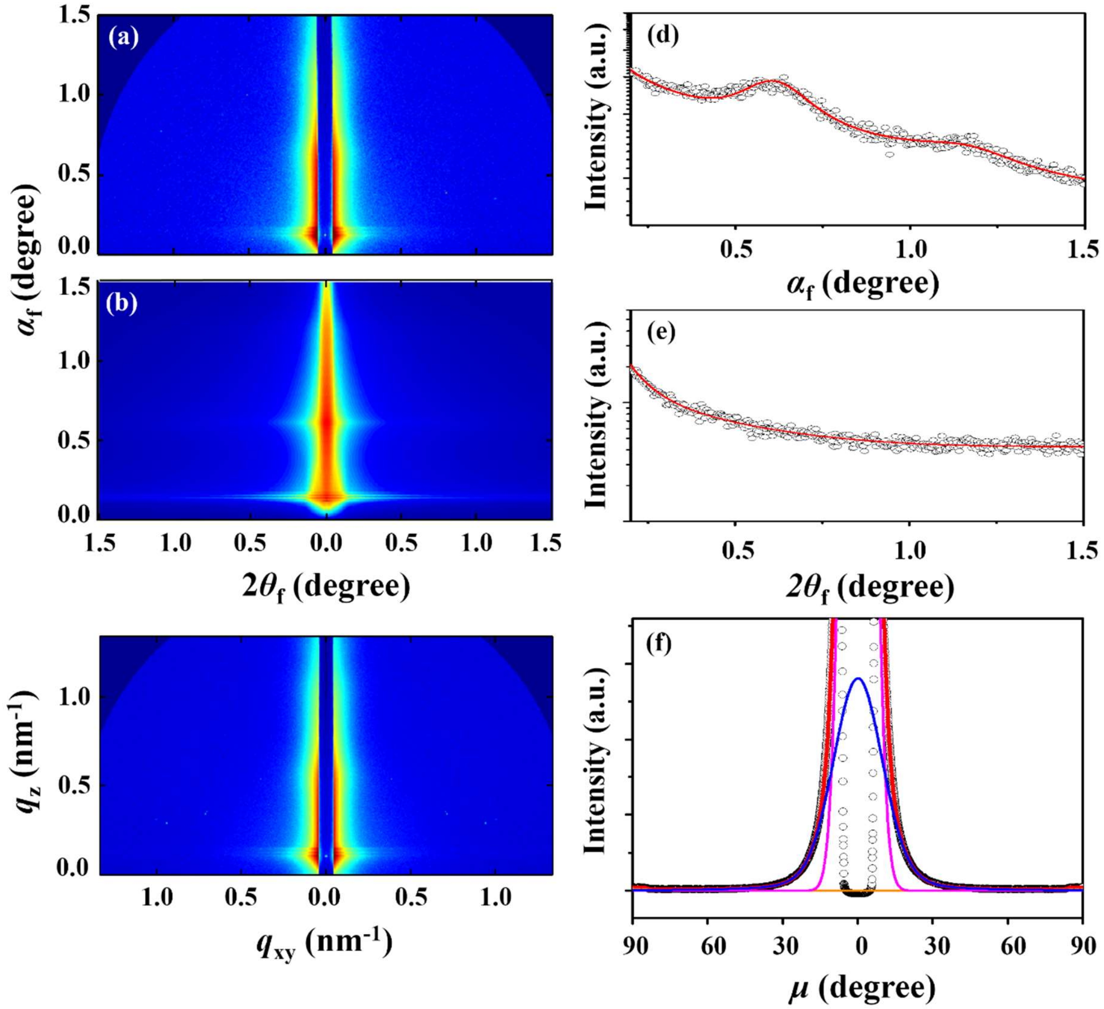

Figure 2.8. Representative scattering data of *l*-PCL$_{3k}$-*A* films (112.2 nm thick) measured with α_i = 0.1240° and SDD = 2926.0 mm at room temperature using a synchrotron X-ray beam (λ = 0.12296 nm): (a) 2D GISAXS image in scattering angle space; (b) 2D scattering image reconstructed with the determined structural parameters obtained from the analysis of the data in (a); (c) 2D GISAXS image in scattering vector space obtained from the data in (a); (d) out-of-plane scattering profile extracted along the meridian line at $2\theta_f$ = 0.159° from the data in (a); (e) in-plane scattering profile along the equatorial line at α_f = 0.201° from the data in (a); (f) azimuthal scattering profile extracted at q = 0.540 nm^{-1} from the data in (c). In (d) and (e), the open circles represent the measured data and the red solid lines were obtained by fitting the data using the GIXS formula driven with lamellar structure model. In (f), the open circles represent the measured data and the red solid lines represent the sum of horizontal lamella peak (blue line), vertical lamella peaks (green lines), parasitic scattering peak from reflected incident beam (pink line), and Yoneda peaks (orange lines) which were obtained by the deconvolutions of the measured data.

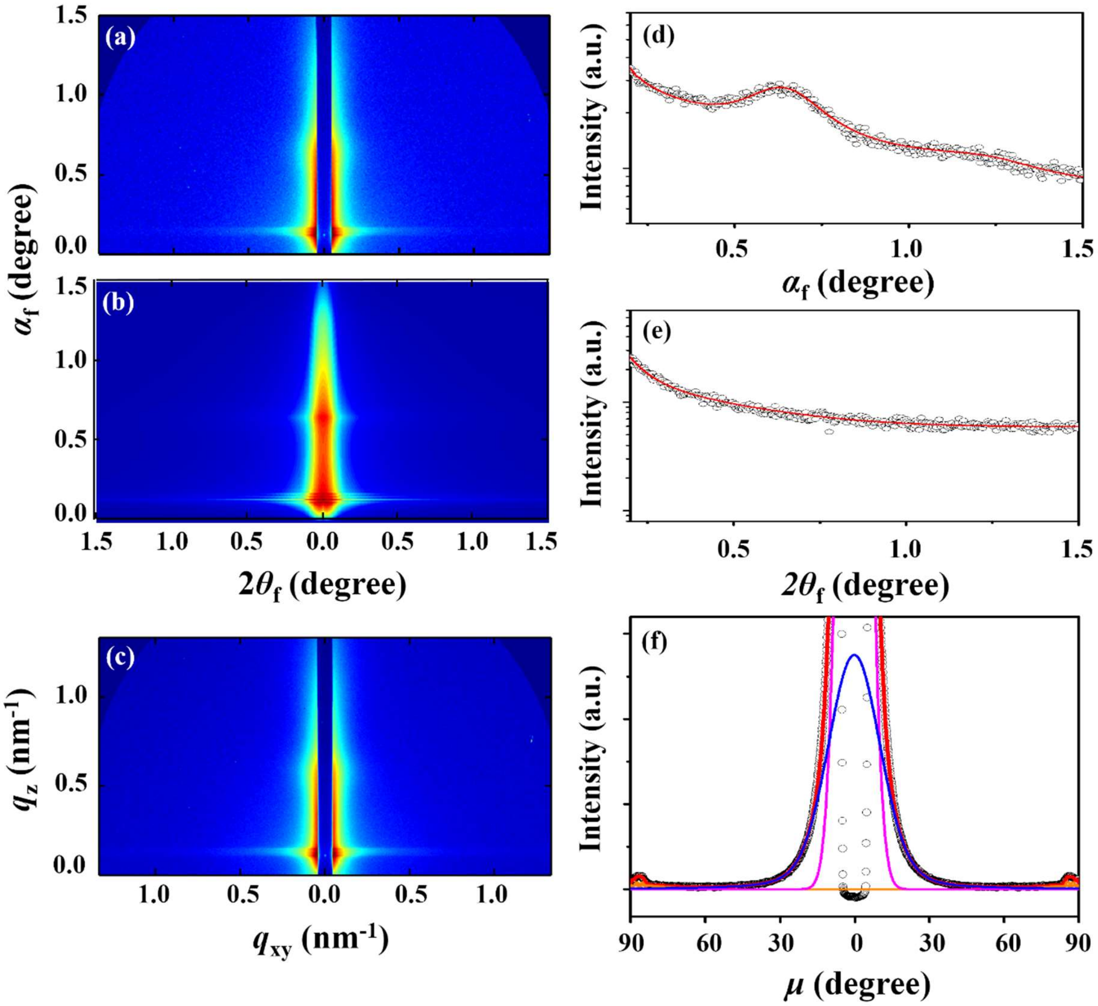

Figure 2.9. Representative scattering data of *l*-PCL$_{3k}$-*B* films (112.2 nm thick) measured with α_i = 0.1240° and SDD = 2926.0 mm at room temperature using a synchrotron X-ray beam (λ = 0.12296 nm): (a) 2D GISAXS image in scattering angle space; (b) 2D scattering image reconstructed with the determined structural parameters obtained from the analysis of the data in (a); (c) 2D GISAXS image in scattering vector space obtained from the data in (a); (d) out-of-plane scattering profile extracted along the meridian line at $2\theta_f$ = 0.160° from the data in (a); (e) in-plane scattering profile along the equatorial line at α_f = 0.182° from the data in (a); (f) azimuthal scattering profile extracted at q = 0.586 nm^{-1} from the data in (c). In (d) and (e), the open circles represent the measured data and the red solid lines were obtained by fitting the data using the GIXS formula driven with lamellar structure model. In (f), the open circles represent the measured data and the red solid lines represent the sum of horizontal lamella peak (blue line), vertical lamella peaks (green lines), parasitic scattering peak from reflected incident beam (pink line), and Yoneda peaks (orange lines) which were obtained by the deconvolutions of the measured data.

The nanoscale PCL films have been further investigated by using GIWAXS. A representative 2D GIWAXS image in scattering angle space of the *cg*-PCL$_{9k}$ film is presented in Figures 2.11a; its q-space image is shown in Figure 2.11c. The image reveals several scattering spots. PCL has been known to form laterally-packed crystals in orthorhombic lattice with a space group of $P2_12_12_1$ (3D representation shown in Figure 2.10a).[30,31] Taking this lattice into account, the individual spots are indexed: {002}, {004}, {110}, {102}, and {200}. From these reflection spots, the lattice dimension parameters are determined: a = 0.805 nm, b = 0.556 nm, and c = 1.754 nm. In particular, the {110} reflection appears around $2\theta_f = 15.8°$ ($q_{xy} = 14.2$ nm^{-1}) as the strongest peak along the equatorial line at $\alpha_f = 0°$, indicating that the majority of orthorhombic PCL crystal lattices (i.e., the c-axis of the lattices which is same with the aligned direction of the extended PCL chain units accommodated into the crystal lattice) is oriented vertically. Another {110} reflection is observed around $2\theta_f = 13.7°$ and $\alpha_f = 9.3°$ as a relatively weaker spot, suggesting a portion of orthorhombic PCL crystal lattices tilted with a certain angle. Considering the presence of vertically-oriented lamellar structure found in the GISAXS analysis above, a third {110} reflection may appear around $\alpha_f = 15.7°$ along the meridian line ($2\theta_f = 0°$). But, the population of such vertical lamellae is very small as discussed above. And the strong {004} reflection peak appears in that angle region. Collectively, a third {110} peak along the meridian line is rather unlikely. The {200} reflection clearly appears around $2\theta_f = 17.5°$ ($q_{xy} = 15.8$ nm^{-1}) along the equatorial line at $\alpha_f = 0°$, supporting that the vertically-oriented crystal lattice is present in the film which is confirmed by the appearance of the strongest {110} reflection peak along the equatorial line. Surprisingly, a strange scattering spot appears around $\alpha_f = 17.4°$ and $2\theta_f = 0°$. This peak reveals a *d*-spacing close to that of the {200} reflection and, thus, one may think that the scattering spot originates from the horizontally-oriented crystal lattice. However, its peak intensity is unrealistically strong in regard to the presence of vertically-oriented crystal lattice in the major population which is clearly confirmed by the {110} reflection. Therefore, the strong and broad scattering spot may be attributed to a different reflection source rather than the {200} reflection of horizontally-oriented crystal lattices. This kind of scattering spot could not be observed from the GIWAXS data of the cyclic and linear PCL counterpart films. Moreover, the *cg*-PCL$_{9k}$ film is found to exhibit relatively lower crystallinity compared to the cyclic and linear PCL counterpart films. Taking these facts into account, the strong spot around $\alpha_f = 17.4°$ and $2\theta_f = 0°$ could be caused by the mean interdistance of the in-plane oriented polymer chains presented in the amorphous or less ordered phase domains in the film, which have been induced by the geometrical confinement of the nanoscale film.

With these information, an azimuthal scattering profile is extracted at q = 14.2 nm^{-1} (at which the {110} reflection peak appears) from the q-space image as a function of azimuthal angle μ and then followed by the deconvolution of scattering peaks (Figure 2.11e). The {110} reflection peak is determined to appear at $\mu = 90.0°$, 57.1°, and 56.3°; the relative area fractions of the peaks are 77.6, 4.8, and 17.6 % respectively. These analysis results inform that the whole PCL crystallites in the film are composed of vertically-aligned (77.6 vol%), 57.1°-tilted (4.8 vol%) and 56.3°-tilted (17.6 vol%) orthorhombic crystals with respect to the film plane. Among these crystal lattices, the vertical crystal lattice (the major crystal lattice component) is estimated to have a second order orientation factor $O_{s,2}$ of 0.917 ($\overline{\varphi_2} = 90°$, mean value of the polar angle φ_2 between the orientation vector $\boldsymbol{n_2}$ set parallel to the c-axis of the orthorhombic PCL crystal lattice and the out-of-plane direction of the film; σ_{φ_2} = 12.48°, standard deviation of φ_2). In addition, the overall crystallinity $X_{c,\mathrm{GIWAXS}}$ is obtained to be 38.4% by analyzing the 1D scattering profile averaged quadrantly from the q-space scattering image (Figure 2.11e). The analysis results are summarized in Table 2.4.

Similar GIWAXS images are observed for the nanoscale films of all counterparts. As shown in Figures 2.11 and 2.12, the scattering data are analyzed in the same manner as for the *cg*-PCL$_{9k}$ film. All analysis results are listed in Table 2.4. All counterparts exhibit crystal lattice dimensions which are almost same with those of *cg*-PCL$_{9k}$. However, the individual counterparts reveal some differences in the orientations of PCL crystal lattices and overall crystallinities depending on the molecular topologies.

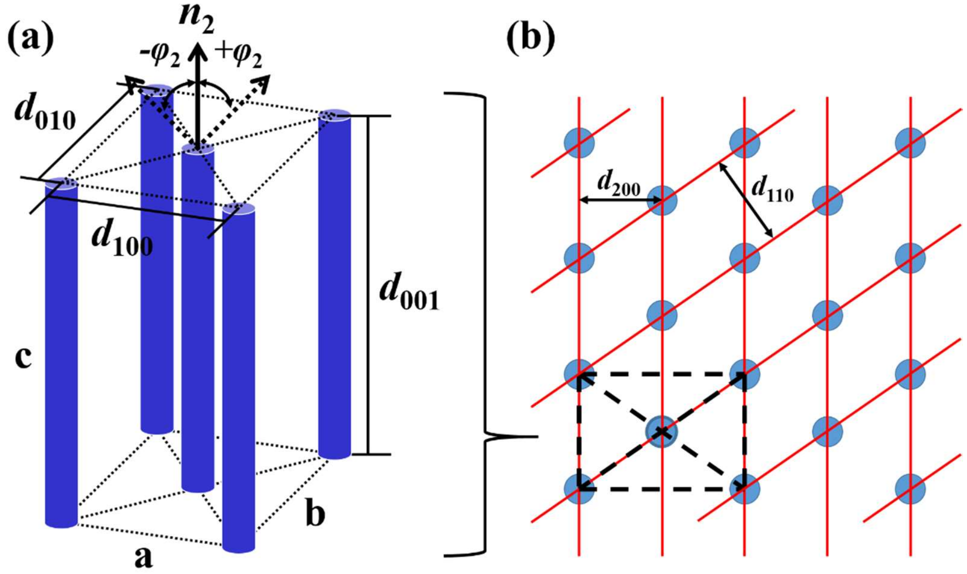

Figure 2.10. Orthorhombic unit cell of PCL crystal composed of molecular cylinders: (a) 3D schematic of orthorhombic lattice where $\boldsymbol{n}_3$ is the orientation vector and φ_2 is the polar angle between $\boldsymbol{n}_2$ and the *xy* plane (parallel to the film); (b) top view of orthorhombic lattice.

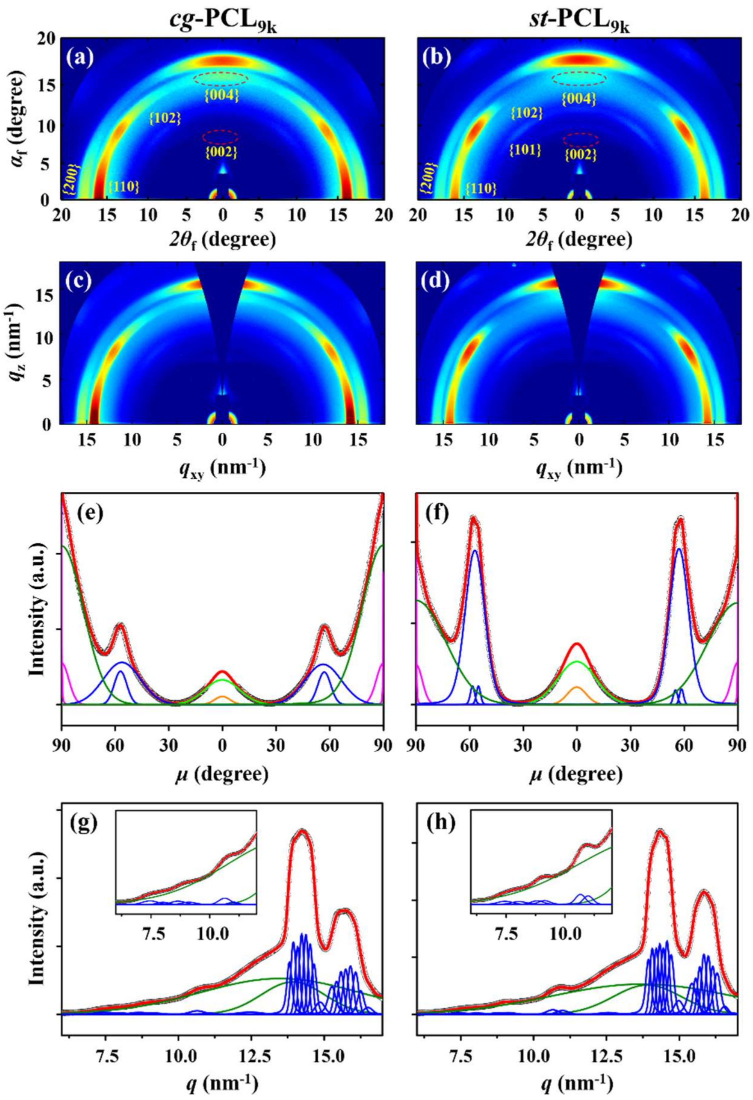

Figure 2.11. Representative GIWAXS data of *cg*-PCL$_{9k}$ and *st*-PCL$_{9k}$ films measured with SDD = 210.9 mm at room temperature using a synchrotron X-ray beam (λ = 0.12296 nm): (a) 2D image in scattering angle space of *cg*-PCL$_{9k}$ (119.5 nm thick; α_i = 0.1340°); (b) 2D image in scattering angle space of *st*-PCL$_{9k}$ (105.3 nm thick; α_i = 0.1560°); (c) 2D image in scattering vector space of *cg*-PCL$_{9k}$ obtained from the data in (a); (d) 2D image in scattering vector space of *st*-PCL$_{9k}$ obtained from the data in (b); (e) azimuthal scattering profile extracted at q = 14.2 nm^{-1} from the data in (c); (f) azimuthal scattering profile extracted at q = 14.2 nm^{-1} from the data in (d); (g) 1D scattering profile averaged quadrantly from the data in (c); (h) 1D scattering profile averaged quadrantly from the scattering image in (d). In (e) and (f), the open circles represent the measured data and the red solid lines represent the sum of the {110} peak of vertically-oriented crystals (dark green lines), the {110} peak of tilted crystals (blue lines), the {004} peak of vertically-oriented crystals (light green line), a part of the interdistance peak of horizontally-aligned polymer chains in less-ordered phases (brown line), and Yoneda peaks (pink lines) which were obtained by the deconvolutions of the measured data.

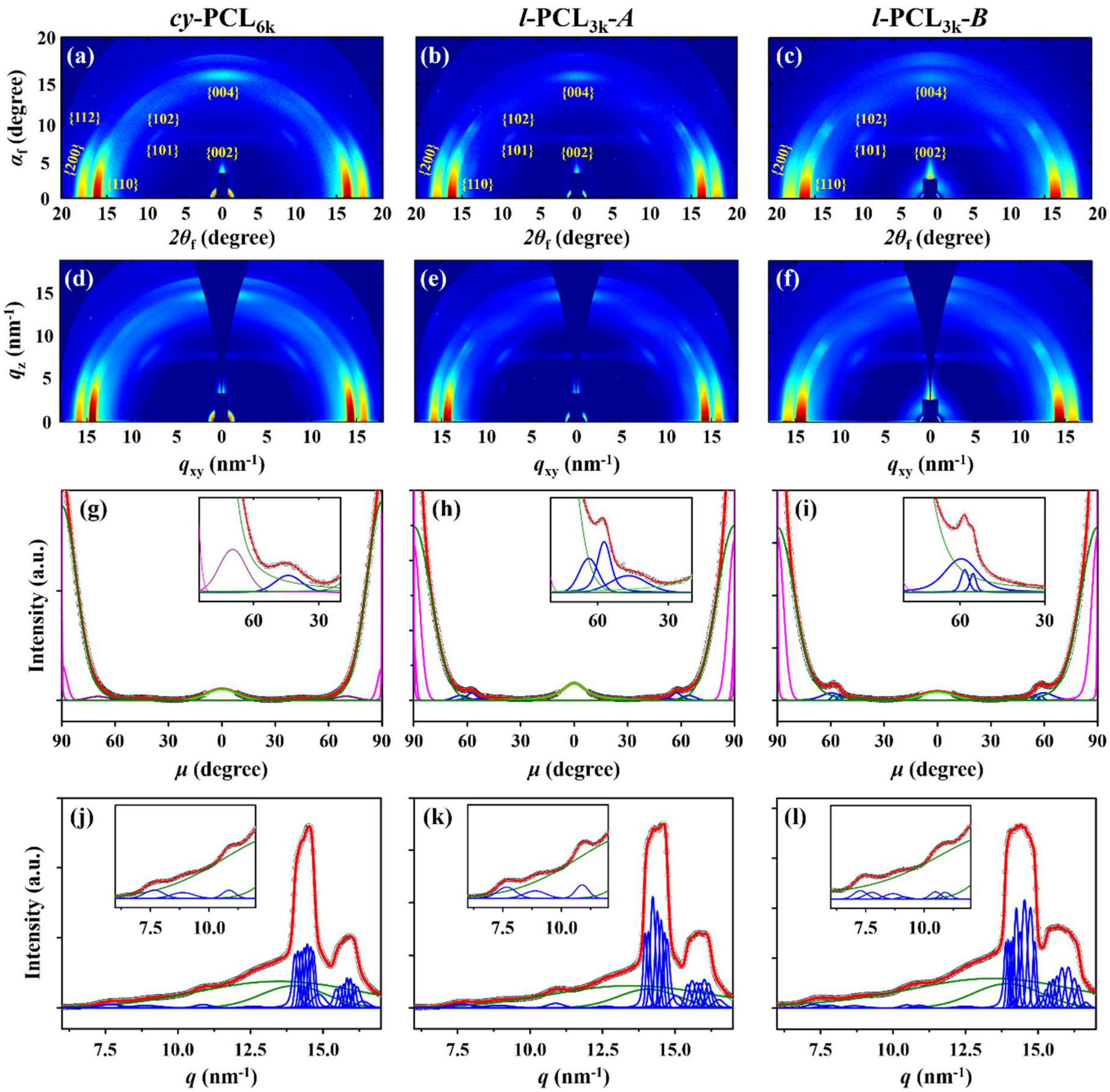

Figure 2.12. Representative GIWAXS data measured with SDD = 210.9 mm at room temperature using a synchrotron X-ray beam (λ = 0.12296 nm): (a) 2D image in scattering angle space of *cy*-PCL$_{6k}$ film (115.8 nm thick; α_i = 0.1450°); (b) 2D image in scattering angle space of *l*-PCL$_{3k}$-*A* film (112.2 nm thick; α_i = 0.1450°); (c) 2D image in scattering angle space of *l*-PCL$_{3k}$-*B* film (107.0 nm thick; α_i = 0.1340°); (d) 2D image in scattering vector space obtained from the data in (a); (e) 2D image in scattering vector space obtained from the data in (b); (f) 2D image in scattering vector space obtained from the data in (c); (g) azimuthal scattering profile extracted at q = 14.2 nm^{-1} from the data in (d); (h) azimuthal scattering profile extracted at q = 14.2 nm^{-1} from the data in (e); (i) azimuthal scattering profile extracted at q = 14.2 nm^{-1} from the data in (f); (j) 1D scattering profile averaged quadrantly from the data in (d); (k) 1D scattering profile averaged quadrantly from the data in (e); (l) 1D scattering profile averaged quadrantly from the data in (f). In (g), (h), and (i), the open circles represent the measured data and the red solid lines represent the sum of the {110} peak of vertically-oriented crystals (green lines), the {110} peaks of tilted crystals (blue lines), the {004} peak of vertically-oriented crystals (light green line), and Yoneda peaks (pink lines) which were obtained by the deconvolutions of the measured data. In (j), (k), and (l), the open circles represent the measured data and the red solid lines represent the sum of crystal peaks (blue lines), and amorphous peaks (green lines).

Table 2.4. Structural parameters of PCL crystals in thin film determined by GIWAXS Analysis

Polymer	*cg*-PCL$_{9k}$	*st*-PCL$_{9k}$	*cy*-PCL$_{6k}$	*l*-PCL$_{3k}$-*A*	*l*-PCL$_{3k}$-*B*
a^{a} (nm)	0.805	0.800	0.794	0.794	0.790
b^{b} (nm)	0.556	0.551	0.551	0.551	0.548
c^{c} (nm)	1.754	1.753	1.705	1.702	1.701
$\bar{\varphi}_2{}^{d}$ (deg.)	90	90	90	90	90
$\sigma_{\varphi_2}{}^{e}$ (deg.)	12.48	16.93	9.08	9.73	10.41
$O_{s,2}{}^{f}$	0.917	0.879	0.944	0.957	0.920
$X_{c,\mathrm{GIWAXS}}{}^{g}$ (%)	38.4	41.9	39.7	50.9	44.0

[a]Unit cell dimension along the a-axis of orthorhombic PCL crystal. [b]Unit cell dimension along the b-axis of orthorhombic PCL crystal. [c]Unit cell dimension along the c-axis of orthorhombic PCL crystal. [d]Mean value of the polar angle φ_2 (i.e., orientation angle) between the orientation vector $\boldsymbol{n}_2$ (which is set parallel to the c-axis of the orthorhombic PCL crystal lattice) and the out-of-plane direction of the film. [e]Standard deviation for the orientation angle φ_2 of the PCL crystal lattice. [f]Second-order orientation factor of PCL crystal lattice. [g]Crystallinity determined by GIWAXS analysis.

Collectively the above GISAXS and GIWAXS analyses provide key information on how the molecular topologies make impacts on the structural feature of PCL in nanoscale, as described below. In addition, these analysis results are evident of how the bulkinesses of end group and joint make influences the structural characteristics of the PCL film in the following.

First, PCL always forms lamellar crystal structure regardless of the molecular topologies. Such the strong tendency to form lamellar crystals could originate from the thermodynamically favorable self-assembling ability of PCL chains.

Second, all PCL polymers favorably form orthorhombic crystal lattices as the crystalline layer component in the lamellar structure, regardless of the topologies: a = 0.790 ~ 0.805 nm, b = 0.548 ~ 0.556 nm, c = 1.701 ~ 1.754 nm, and $\alpha = \beta = \gamma = 90°$. Here, the c value corresponds to the length of two repeat units plus one carbonyl carbon atom in a fully extended conformation.

Third, the cage- and star-shaped polymers tend to form horizontal lamellae as the major structural component (97–98 vol%) but additionally vertical lamellae as the very minor component (2–3 vol%). In comparison, the other counterparts including the cyclic counterpart favorably form only horizontal lamellae.

Fourth, the *g* value of horizontal lamellar structure is in the increasing order: *c*y-PCL$_{6k}$ < *l*-PCL$_{3k}$-*A* < *l*-PCL$_{3k}$-*B* < *cg*-PCL$_{9k}$ < *st*-PCL$_{9k}$. These results inform that the stability of horizontal lamellar structure is in the decreasing order: *c*y-PCL$_{6k}$ > *l*-PCL$_{3k}$-*A* > *l*-PCL$_{3k}$-*B* > *cg*-PCL$_{9k}$ > *st*-PCL$_{9k}$.

Fifth, the $O_{s,1}$ value (i.e., orientational order) of horizontal lamellar structure is in the increasing order: *cg*-PCL$_{9k}$ < *l*-PCL$_{3k}$-*A* < *st*-PCL$_{9k}$ < *l*-PCL$_{3k}$-*B* ~ *c*y-PCL$_{6k}$.

Sixth, the long period of lamellar structure is in the increasing order: *l*-PCL$_{3k}$-*B* < *l*-PCL$_{3k}$-*A* < *st*-PCL$_{9k}$ < *c*y-PCL$_{6k}$ < *cg*-PCL$_{9k}$.

Seventh, the crystalline layer thickness of lamellar structure is in the increasing order: *st*-PCL$_{9k}$ (l_c = 2.1 nm) < *cg*-PCL$_{9k}$ (2.7 nm) < *l*-PCL$_{3k}$-*B* (3.2 nm) < *c*y-PCL$_{6k}$ (3.3 nm) < *l*-PCL$_{3k}$-*A* (3.5 nm). It is generally known that larger l_c of a crystalline polymer exhibits higher T_m. However, the l_c and T_m values of this study are found not to follow such kind of l_c–T_m correlation. [T_{m1}]: *l*-PCL$_{3k}$-*B* < *st*-PCL$_{9k}$ < *cy*-PCL$_{6k}$ < *cg*-PCL$_{9k}$ < *l*-PCL$_{3k}$-*A*; [T_{m2}]: *l*-PCL$_{3k}$-*B* < *st*-PCL$_{9k}$ < *l*-PCL$_{3k}$-*A* < *cy*-PCL$_{6k}$ < *cg*-PCL$_{9k}$; here, it is noted that the T_m values were measured from the samples in bulk states rather than in nanoscale films. Considering the geometrical cage and cyclic shapes, *cy*-PCL$_{6k}$ and *cg*-PCL$_{9k}$ may form relatively more ordered interfacial layers in the lamellar structures, compared to those in the lamellar structures of the linear and star-shaped counterparts. Taking these into account, such more ordered interfacial layers may be included into the crystal melting process. If such interfacial layers are considered as a part of ordered crystals, the total ordered layer thickness can be in the increasing order: *st*-PCL$_{9k}$ (2.1 nm) < *l*-PCL$_{3k}$-*B* (3.2 nm) < *l*-PCL$_{3k}$-*A* (3.5 nm) < *c*y-PCL$_{6k}$ [8.5 nm = 3.3 (l_c) + 5.2 ($2l_i$)] < *cg*-PCL$_{9k}$ [8.7 nm = 2.7 (l_c) + 6.0 ($2l_i$)]. This trend is reasonably correlated to that of T_{m2} values, except for PCL$_{3k}$-*B*. The lowest T_{m2} of *l*-PCL$_{3k}$-*B* may be attributed to a cooperative effort of the low molecular weight of its PCL blocks and the presences of a joint and two end groups which can cause defects on the crystals.

Eighth, the interfacial layer thickness is in the increasing order: *l*-PCL$_{3k}$-*A* < *c*y-PCL$_{6k}$ < *l*-PCL$_{3k}$-*B* < *st*-PCL$_{9k}$ < *cg*-PCL$_{9k}$.

Ninth, the amorphous layer thickness of lamellar structure is in the increasing order: *l*-PCL$_{3k}$-*B* < *cg*-PCL$_{9k}$ < *c*y-PCL$_{6k}$ ~ *l*-PCL$_{3k}$-*A* < *st*-PCL$_{9k}$.

Tenth, the orthorhombic crystal lattice present in the lamellar structure, however, reveals one to four orientational domains depending on the topologies; the number of orientational domains is 2 for *c*y-PCL$_{6k}$, 3 for *cg*-PCL$_{9k}$, and 4 for *st*-PCL$_{9k}$, *l*-PCL$_{3k}$-*A* and *l*-PCL$_{3k}$-*B*. Among these domains, the vertically-oriented crystal lattice domain is the major component for all topological polymer films. The $O_{s,2}$ value (i.e., orientational order) of vertically-oriented orthorhombic crystal lattices in the lamellar structure is in the increasing order: *st*-PCL$_{9k}$ < *cg*-PCL$_{9k}$ < *l*-PCL$_{3k}$-*B* < *c*y-PCL$_{6k}$ < *l*-PCL$_{3k}$-*A*.

Finally, the overall crystallinity is in the increasing order: *cg*-PCL$_{9k}$ < *c*y-PCL$_{6k}$ < *st*-PCL$_{9k}$ < *l*-PCL$_{3k}$-*B* < *l*-PCL$_{3k}$-*A*.

All determined film morphologies are schematically depicted in Figure 2.13. Overall, all topological PCL polymers reveal to form lamellar structures based on orthorhombic crystal lattice. The structural parameters including overall crystallinity and orientational orthorhombic crystal domains are, however, found to vary depending on the molecular topologies. Nevertheless, the topological impacts on the structural parameters could not be rationalized easily. This situation may be caused by the bulkinesses of joints and end groups which can be either against or cooperative to the molecular topologies in functioning to the nanoscale film morphology.

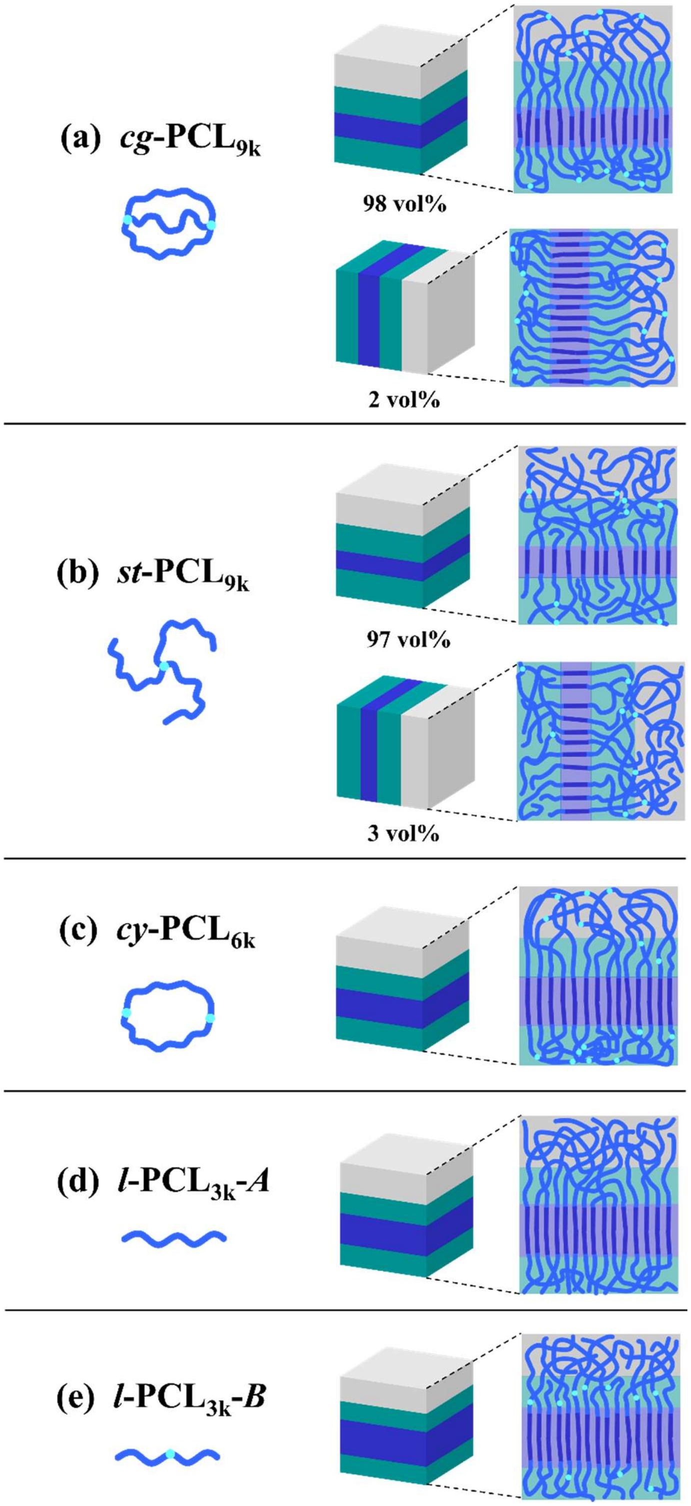

Figure 2.13. Schematic representations of molecular chain conformations and packing orders in the nanoscale films of various topological PCL polymers.

2.4 Conclusions

In this chapter, a cage-shaped PCL polymer and its various counterparts have been examined in terms of thermal stability and phase transitions by using TGA and DSC analyses. The nanoscale film morphologies of this series of topological PCL polymers have been also investigated quantitatively by using synchrotron GISAXS and GIWAXS analyses.

The PCL polymers show topology and end group dependent thermal stabilities: *l*-PCL$_{3k}$-*B* ~ *l*-PCL$_{3k}$-*A* < *cg*-PCL$_{9k}$ ~ *cy*-PCL$_{6k}$ < *st*-PCL$_{9k}$. In particular, the highest stability of *st*-PCL$_{9k}$ could be attributed to the capped chain ends rather than the topology effect.

The phase transitions (nonisothermal crystallization and subsequent crystal melting transitions: T_c, T_{m1}, T_{m2}, heat of fusion of crystallization, heat of fusion of crystal melting, and crystallinity) are also dependent upon the molecular topologies as well as the bulkinesses of joints and end groups.

All PCL homopolymers always form lamellar structures based on orthorhombic crystal lattice in nanoscale films, regardless of the molecular topologies as well as the bulkinesses of joints and end groups. Both *cg*-PCL$_{9k}$ and *st*-PCL$_{9k}$ tend to form a mixture of horizontal (major) and vertical (minor) lamellar structures, whereas all other counterparts form only horizontal lamellar structures. The structural parameters, including overall crystallinity and orientational orthorhombic crystal domains, vary with the molecular topologies, and the bulkinesses of joints and end groups. Overall, the structural parameter details could not be rationalized easily in regard to the effects of molecular topology, joint and end group because the functions of molecular topologies are either against or cooperative to those of joints and end groups. In this chapter, the novel three layer model was successful in precisely and accurately parameterizing the morphological details as well as differentiating the extent of topological impact upon the self-assembly behavior of topological PCL homopolymers in thin films, providing useful insights in the topology-morphology correlation of semi-crystalline polymers.

2.5 References

1. Juul, S.; Iacovelli, F.; Falconi, M.; Kragh, S. L.; Christensen, B.; Frøhlich, R.; Franch, O.; Kristoffersen, E. L.; Stougaard, M.; Leong, K. W.; Ho, Y. P.; Sørensen, E. S.; Birkedal, V.; Desideri, A.; Knudsen, B. R. Temperature-Controlled Encapsulation and Release of an Active Enzyme in the Cavity of a Self-Assembled DNA Nanocage. *ACS Nano* **2013**, *7*, 9724–9734.
2. Yoshizawa, M.; Klosterman, J. K.; Fujita, M. Functional Molecular Flasks: New Properties and Reactions within Discrete, Self-Assembled Hosts. *Angew. Chem. Int. Ed.* **2009**, *48*, 3418–3438.
3. McCaffrey, R.; Long, H.; Jin, Y.; Sanders, A.; Park, W.; Zhang, W. Template Synthesis of Gold Nanoparticles with an Organic Molecular Cage. *J. Am. Chem. Soc.* **2014**, *136*, 1782–1785.
4. Mastalerz, M. Shape-Persistent Organic Cage Compounds by Dynamic Covalent Bond Formation. *Angew. Chem. Int. Ed.* **2010**, *49*, 5042–5053.
5. Cook, T. R.; Zheng, Y. R.; Stang, P. J. Metal–Organic Frameworks and Self-Assembled Supramolecular Coordination Complexes: Comparing and Contrasting the Design, Synthesis, and Functionality of Metal–Organic Materials. *Chem. Rev.* **2013**, 113, 734–777.
6. Erben, C. M.; Goodman, R. P.; Turberfield, A. J. Single-Molecule Protein Encapsulation in a Rigid DNA Cage. *Angew. Chem. Int. Ed.*, 2006, **45**, 7414–7417.
7. Edwardson, T. G. W.; Carneiro, K. M. M.; McLaughlin, C. K.; Serpell, C. J.; Sleiman, H. F. Site-specific positioning of dendritic alkyl chains on DNA cages enables their geometry-dependent self-assembly. *Nat. Chem.* **2013**, *5*, 868–875.
8. Lai, Y. T.; Cascio, D.; Yeates, T. O. Structure of a 16-nm Cage Designed by Using Protein Oligomers. *Science* **2012**, *336*, 1129–1129.
9. Kim, M.; Rho, Y.; Jin, K. S.; Ahn, B.; Jung, S.; Kim, H.; Re, M. pH-Dependent Structures of Ferritin and Apoferritin in Solution: Disassembly and Reassembly. *Biomacromolecules* **2011**, *12*, 1629-1640.
10. Jutz, G.; van Rijn, P.; Miranda, B. S.; Böker, A. Ferritin: A Versatile Building Block for Bionanotechnology. *Chem. Rev.*, 2015, **115**, 1653–1701.
11. Ueda, Y.; Ito, H.; Fujita, D.; Fujita, M. Permeable Self-Assembled Molecular Containers for Catalyst Isolation Enabling Two-Step Cascade Reactions. *J. Am. Chem. Soc.* **2017**, *139*, 6090–6093.
12. Fujita, D.; Ueda, Y.; S. Sato, N. Mizuno, T. Kumasaka and M. Fujita, Self-assembly of tetravalent Goldberg polyhedra from 144 small components. *Nature* **2016**, *540*, 563–566.
13. Hubert, D. H.; Jung, M.; German, A. L. Vesicle Templating. *Adv. Mater.* **2000**, *12*, 1291-1294.
14. Yavuz, M. S.; Cheng, Y.; Chen, J.; Cobley, C. M.; Zhang, Q.; Rycenga, M.; Xie, J.; Kim, C.; Song, K. H.; Schwartz, A. G.; Wang, L. V.; Xia, Y. Gold nanocages covered by smart polymers for controlled release with near-infrared light. *Nat. Mater.* **2009**, *8*, 935–939.
15. Cook, T. R.; Stang, P. J. Recent Developments in the Preparation and Chemistry of Metallacycles and Metallacages via Coordination. *Chem. Rev.* **2015**, *115*, 7001–7045.
16. Zhang, D.; Martinez, A.; Dutasta, J. P. Emergence of Hemicryptophanes: From Synthesis to Applications for Recognition, Molecular Machines, and Supramolecular Catalysis. *Chem. Rev.* **2017**, *117*, 4900–4942.
17. Durot, S.; Taesch, J.; Heitz, V. Multiporphyrinic Cages: Architectures and Functions. *Chem. Rev.* **2014**, *114*, 8542–8578.

18. Lehn, J. M. Cryptates: Inclusion complexes of macropolycyclic receptor molecules. *Pure Appl. Chem.* **1978**, *50*, 871–892.
19. Tezuka, Y. Topological polymer chemistry for designing multicyclic macromolecular architectures. *Polymer J.* **2012**, *44*, 1159–1169.
20. Tezuka, Y.; Tsuchitani, A.; Yoshioka, Y.; Oike, H. Synthesis of θ-Shaped Poly(THF) by Electrostatic Self-Assembly and Covalent Fixation with Three-Armed Star Telechelics Having Cyclic Ammonium Salt Groups. *Macromolecules* **2003**, *36*, 65–70.
21. Igari, M.; Heguri, H.; Yamamoto, T.; Tezuka, Y. Folding Construction of Doubly *Fused* Tricyclic, β- and γ-Graph Polymer Topologies with *kyklo*-Telechelic Precursors Obtained through an Orthogonal Click/ESA-CF Protocol. *Macromolecules* **2013**, *46*, 7303−7315.
22. Tezuka Y.; Fujiyama, K. Construction of Polymeric *δ*-Graph: A Doubly Fused Tricyclic Topology. *J. Am. Chem. Soc.* **2005**, *127*, 6266–6270.
23. Kyoda, K.; Yamamoto, T.; Tezuka, Y. Programmed Polymer Folding with Periodically Positioned Tetrafunctional Telechelic Precursors by Cyclic Ammonium Salt Units as Nodal Points. *J. Am. Chem. Soc.* **2019**, *141*, 7526−7536.
24. Jeong, J.; Kim, K.; Lee, R.; Lee, S.; Kim, H.; Jung, H.; Kadir, M. A.; Jang, Y.; Jeon, H. B.; Matyjaszewski, K.; Chang, T.; Paik, H. J. Preparation and Analysis of Bicyclic Polystyrene. *Macromolecules* **2014**, *47*, 3791–3796.
25. Zhao, J.; Zhou, Y.; Li, Y.; Pan, X.; Zhang, W.; Zhou, N.; Zhang, K.; Zhang, Z.; Zhu, X. Modular construction of macrocycle-based topological polymers via high-efficient thiol chemistry. *Polym. Chem.* **2015**, *6*, 2879−2891.
26. Mohanty, A. K.; Ye, J.; Ahn, J.; Yun, T.; Lee, T.; Kim, K.-s.; Jeon, H. B.; Chang, T.; Paik, H.-j. Topologically Reversible Transformation of Tricyclic Polymer into Polyring Using Disulfide/Thiol Redox Chemistry. *Macromolecules* **2018**, *51*, 5313-5322.
27. Mato, Y.; Honda, K.; Tajima, K.; Yamamoto, T.; Isono, T.; Satoh, T. A Versatile Synthetic Strategy for Macromolecular Cages: Intramolecular Consecutive Cyclization of Star-Shaped Polymers. *Chem. Sci.* **2019**, *10*, 440–446.
28. Satoh, Y.; Matsuno, H.; Yamamoto, T.; Tajima, K.; Isono, T.; Satoh, T. Synthesis of Well-Defined Three- and Four-Armed Cage-Shaped Polymers via "Topological Conversion" from Trefoil- and Quatrefoil- Shaped Polymers. *Macromolecules* **2017**, *50*, 97−106.
29. Kim, Y. Y.; Ree, B. J.; Kido, M.; Ko, Y.-G.; Ishige, R.; Hirai, T.; Wi, D.; Kim, J.; Kim, W. J.; Takahara, A.; Ree, M. High Performance n-Type Electrical Memory and Morphology-Induced Memory-Mode Tuning of A Well-Defined Brush Polymer Bearing Perylene Diimide Moieties. *Adv. Electronic Mater.* **2015**, *1*, 1500197.
30. Brittiger, H.; Marchessault, R. H.; Niegsch, W. D. *Acta Crystallogr., Sect. B* **1970**, *26*, 1923−1927.
31. Kim, Y. Y.; Jung, S.; Kim, C.; Ree, B. J.; Kawato, D.; Nishikawa, N.; Suemasa, D.; Isono, T.; Kakuchi, T.; Satoh, T.; Ree, M. Hierarchical Structures in Thin Films of Miktoarm Star Polymers: Poly(n-hexyl isocyanate)(12K)−Poly(ε-caprolactone)$_{1-3}$(5K). *Macromolecules* **2014**, *47*, 7510−7524.

Chapter 3

Nanoscale Film Morphologies and Chain Conformations of Poly(δ-valerolactone)s Bearing Mobile and Immobile Rotaxane Wheels

3.1 Introduction

Rotaxane topology is defined by the polymer chain acting as an axle for a mobile or immobile molecular wheel positioned along the macromolecular axle. From the perspective of supramolecular polymers, the presence of rotaxane wheel has attracted great attention from both academia and industry because of their potential in self-assembling ability of desired functional chemical components via non-covalent interactions.[1-8] Thus far, many research efforts have been made to design and synthesize polyrotaxanes and a number of polyrotaxanes were introduced with advanced synthetic schemes.[2-10]

Due to the interesting molecular topologies, one expects that polyrotaxanes exhibit unique properties and morphological structures. Nevertheless, their properties have been rarely investigated so far; for example, the phase transitions of polyrotaxanes were examined in qualitative manner using mainly calorimetric technique.[7,8,11-14] Moreover, their morphological structures have been yet examined. Overall, understanding of polyrotaxanes in the aspects of morphologies and properties still remains in very early stages.

In this chapter, quantitative characterization of a series of macromolecular [2]rotaxanes based on a poly(δ-valerolactone) (PVL) axle and a fixed and mobile dibenzo-24-crown-8-ether (*rot*) wheel in the aspects of thermal stability, phase transition and nanoscale film morphology have been carried out for the first time: PVL, PVL-*rot*-F, PVL-*rot*-M (Figure 3.1). Interestingly, the thermal stability of PVL axle is found to be influenced depending on the fixed and mobile [2]rotaxane wheels. The phase transition characteristics are also affected severely by the fixed and mobile characters of [2]rotaxane wheel. The presences of such fixed and mobile wheels are found to further make impacts on the nanoscale film morphology. All results are interpreted and discussed with taking into consideration all relating factors.

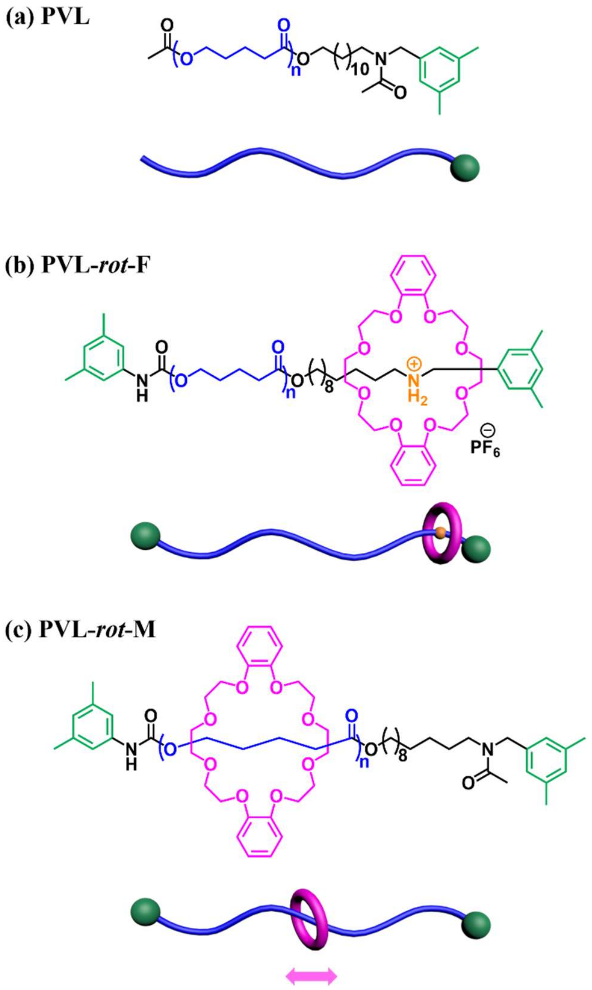

Figure 3.1. Chemical structures of PVL and its axles bearing fixed and movable [2]rotaxane wheels used in this chapter.

3.2 Experimental Section

3.2.1 Materials and Nanoscale Film Preparation

A series of macromolecular [2]rotaxanes based on a PVL axle and a rotaxane wheel, including PVL homopolymer were prepared according to the synthetic method reported previously in the literature:[15] PVL, PVL-*rot*-F, and PVL-*rot*-M (Figure 3.1). The molecular characteristics of macromolecular [2]rotaxanes are summarized in Table 3.1. The individual polymers were dissolved in chloroform ($CHCl_3$) and filtered using disposable syringes equipped with polytetrafluoroethylene filter membranes of 0.22 μm pore size, producing polymer solutions with a concentration of 0.5 wt%. Each polymer solution was deposited on silicon (Si) substrates via spin coating process and dried in vacuum at room temperature for 24 h. Some of the obtained films were further annealed under a vapor of THF at room temperature for 1 h. The obtained polymer films were determined to have thicknesses of 110−130 nm by using a spectroscopic ellipsometer (Model M-2000, Woollam, Lincoln, NE, USA).

3.2.2 Measurements

Thermal stability and phase transitions were examined with a rate of 10.0 °C/min under nitrogen atmosphere by thermogravimetry (TGA; model TG/DGA-6300, Seiko Instrument, Tokyo, Japan; model Dynamic TGA 2950, TA Instruments, New Castle, DE, USA) and differential scanning calorimetry (DSC) (model DSC-220CU, Seiko Instrument, Tokyo, Japan; model DSC TA 910, TA Instruments, New Castle, DE, USA). Synchrotron GIXS measurements were performed at the 3C beamline of the Pohang Accelerator Laboratory (PAL), Pohang, Korea.[16-18] Scattering data were normally collected for 10−30 s using X-ray radiation sources with a wavelength λ of 0.11201 and 0.12479 nm and a two-dimensional (2D) charge-coupled detector (CCD) (model Rayonix 2D MAR, Evanston, IL, USA). The sample-to-detector distance (SDD) was 225 mm for grazing incidence wide angle X-ray scattering (GIWAXS) measurements and 3949 mm for grazing incidence small angle X-ray scattering (GISAXS) measurements. The incidence angle α_i of X-ray beam with respect to the film sample surface was set in the range 0.110–0.160°, which is between the critical angle of the polymer film and the silicon substrate ($\alpha_{c,f}$ and $\alpha_{c,s}$). Scattering angles were corrected according to the positions of the X-ray beams reflected from the silicon substrate as well as by using precalibrated standards (polystyrene-*block*-poly(ethylene-*ran*-butylene)-*block*-polystyrene; sucrose and silver behenate standards (TCI, Tokyo, Japan)). Aluminum foils were used as a semi-transparent beam stop, because the intensity of the specular reflection from the substrate is much stronger than the intensity of GIXS near the critical angle.

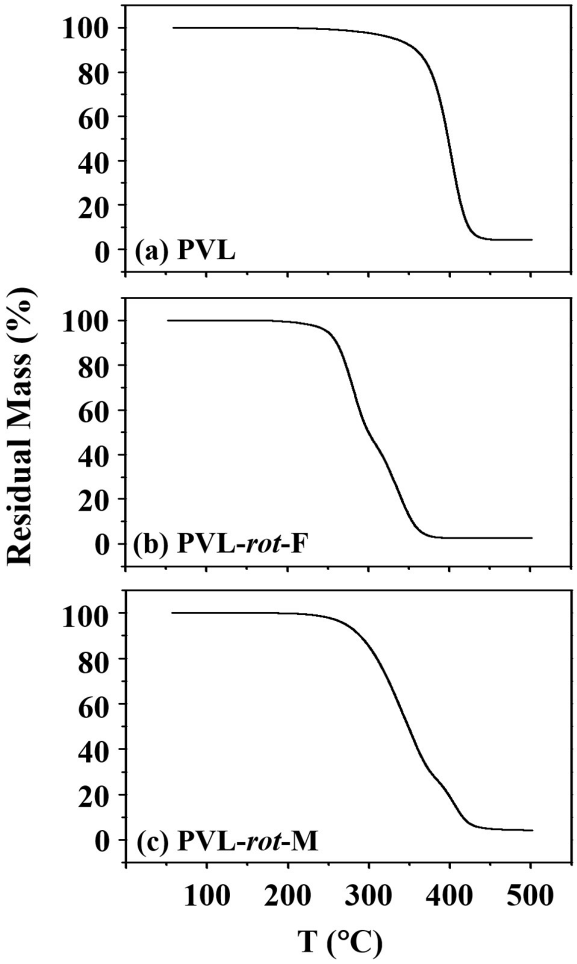

Figure 3.2. TGA thermograms of PVL and PVL-based macromolecular [2]rotaxanes, which were measured at a rate of 10.0 °C/min under nitrogen atmosphere.

Table 3.1. Characteristics of PVL and its axles bearing fixed and movable [2]rotaxane wheels

Polymer	DP_{NMR} [a]	$M_{\mathrm{n,NMR}}$ [b] (g/mol)	$M_{\mathrm{n,NMR}}$ [c] (g/mol)	$M_{\mathrm{n,SEC}}$ [d] (g/mol)	PDI [e]	f_{PVL} [f]	ϕ_{PVL} [g]	$T_{\mathrm{d,5}}$ [h] (°C)
PVL	48	4800	5190	7100	1.20	0.925	0.912	332
PVL-*rot*-F	48	4800	5810 [i]	5400	1.22	0.826 [j] (0.847) [k]	0.818 [l] (0.828) [m]	249
PVL-*rot*-M	48	4800	5700	5900	1.19	0.842	0.823	271

[a] Number-average degree of polymerization of only PVL part determined by proton nuclear magnetic resonance (^{1}H NMR) spectroscopy analysis. [b] Number-average molecular weight of only PVL part determined by ^{1}H NMR spectroscopy analysis. [c] Number-average molecular weight of the polymer, including the whole components (linkers, end group, and so on), which was determined by ^{1}H NMR spectroscopy analysis. [d] Number average molecular weight of polymer determined by size exclusion chromatography (SEC) analysis. [e] Polydispersity index of polymer determined by SEC analysis. [f] Weight fraction of only PVL part. [g] Volume fraction of only PVL part with respect to the polymer. [h] Temperature at which 5% mass loss occurred in TGA analysis. [i] Included the molar mass of the counter anion. [j] Weight fraction of only PVL part with respect to the total molecular mass included the counter anion. [k] Weight fraction of only PVL part with respect to the total molecular mass excluded the counter anion. [l] Volume fraction of only PVL part with respect to the polymer included the counter anion; here the volume fraction was estimated using a method reported in literature.[19] [m] Volume fraction of only PVL part with respect to the polymer excluded the counter anion.

3.3 Results and Discussion

3.3.1 Thermal Stabilities

In the TGA analysis with a heating rate of 10.0 °C/min, PVL undergoes a single-step degradation in nitrogen atmosphere, revealing 5% mass loss at 332 °C (= $T_{\mathrm{d,5}}$) (Figure 3.2a; Table 3.1). Different from PVL, PVL-*rot*-F reveals a two-step degradation (Figure 3.2b). Considering the TGA thermogram of PVL, the first-step degradation could be attributed to the fixed rotaxane wheel, whereas the second-step degradation could originate from the PVL axle. A mass loss of 5% occurs at 249 °C (= $T_{\mathrm{d,5}}$) in the first-step degradation region, which is 83 °C lower than that of the PVL homopolymer. Surprisingly, about 50% mass loss, however, takes place apparently through the first-step degradation regime although the rotaxane wheel has a weight faction of only 7.7% (without the anion counterpart) or 10.2% (including the anion counterpart). It is additionally noted that the degradation of the PVL axle part is ended around 400 °C, which is approximately 50 °C lower than that of the PVL homopolymer. These results suggest that in PVL-*rot*-F the ionically-fixed rotaxane wheel undergoes thermal degradation first and further stimulates the PVL axle to degrade. Perhaps, the anionic counterpart could make contribution in part to such the accelerated degradation of PVL axle.

PVL-*rot*-M also depicts a two-step degradation behavior (Figure 3.2c). The first-step degradation is apparently continued up to about 70% mass loss. These results suggest that the movable rotaxane wheel also starts thermal degradation first and further induces the PVL axle to undergo degradation in lower temperatures. However, $T_{\mathrm{d},5}$ = 271 °C, which is 22 higher than that of PVL-*rot*-F. Moreover, the degradation of the PVL axle is ended by around 450 °C, which is much higher than that of PVL-*rot*-F but almost same with that of the PVL homopolymer.

Overall, the TGA analysis results collectively provide clues as follows. The rotaxane wheel has relatively less thermal stability than that of the PVL axle, regardless of its fixation and movability. Such the less stability of the wheel may be attributed to its low molecular mass and aliphatic ether components. However, the movable rotaxane wheel could make relatively less negative impact on the overall thermal stability of PVL-based macromolecular [2]rotaxane, compared to the ionically-fixed wheel with the anionic counter ion. Such merit may be originated from a certain degree of physical independency of the wheel from the PVL axle due to the movability as well as its freedom from any associations with ionic character and counter anion.

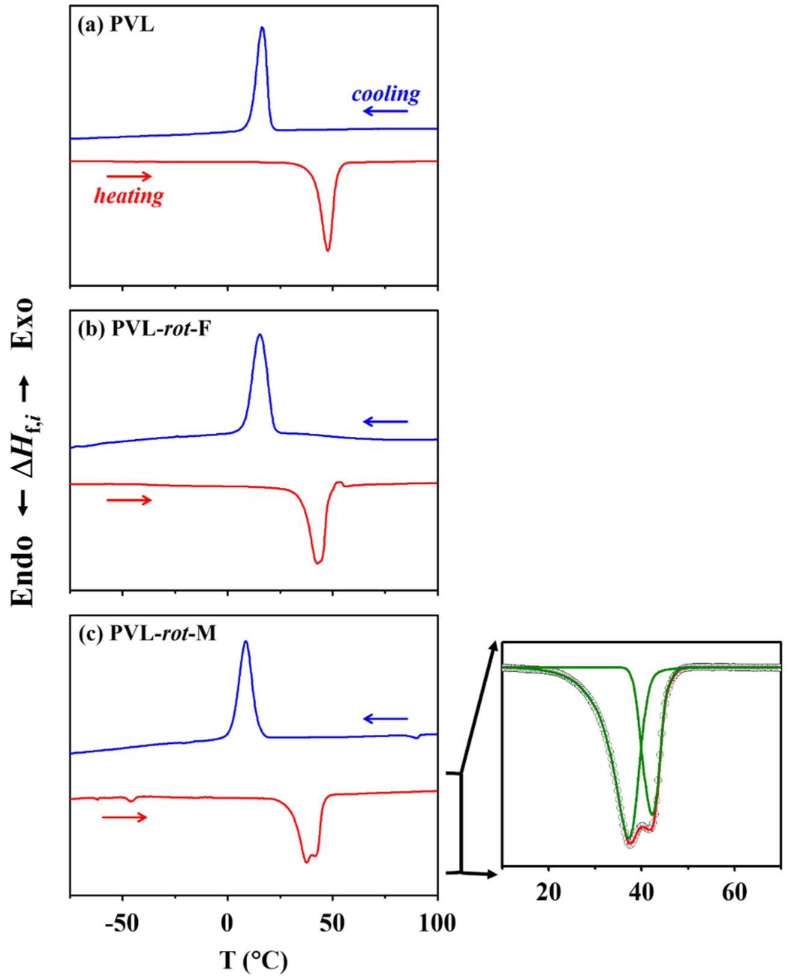

Figure 3.3. DSC thermograms of PVL and its axles bearing fixed and movable [2]rotaxane wheels, which were measured at a rate of 10.0 °C/min under nitrogen atmosphere.

3.3.2 Phase Transition Behaviors

For PVL and its [2]rotaxanes, DSC analysis has been carried out with a rate of 10.0 °C/min. PVL nicely reveals a single exothermic crystallization peak centered at 16.3 °C (= T_c) in cooling run from the melt and a single endothermic crystal melting peak centered at 47.7 °C (= T_m) in reheating run (Figure 3.3a). The heat of fusion of crystallization $\Delta H_{f,c}$ is determined to be 116.0 J/g for the whole PVL homopolymer, which corresponds to 125.3 J/g for only PVL part under an assumption that the other parts are noncrystallizable. The heat of fusion of crystal melting $\Delta H_{f,m}$ is determined to be 119.0 J/g for the whole PVL homopolymer, which corresponds to 128.5 J/g for only PVL part. The crystallinity of only PVL part is estimated to be 89.8% (= $X_{\mathrm{c,c}}$) from the nonisothermal crystallization and 92.1% (= $X_{\mathrm{c,m}}$) from the crystal melting using an equilibrium heat of fusion of crystallization or crystal melting assumed to be same with that ($\Delta H_{\mathrm{c}}^{\circ} = \Delta H_{\mathrm{m}}^{\circ} = 139.5$ J/g)[20,21] of poly(ε-caprolactone) whose chemical structure is similar to that of PVL. PVL-*rot*-F and PVL-*rot*-M reveal thermogram profiles similar to those of PVL (Figures 3.3b-c); but they show somewhat differences in phase transition details, as compared in Table 3.2.

The DSC analysis results collectively could provide important information on the effects of ionically-fixed and movable rotaxane wheels in the phase transition characteristics of PVL axle as follows.

First, PVL-*rot*-F exhibits slightly broader crystallization and crystal melting peaks, compared to those of PVL homopolymer. PVL-*rot*-F further reveals relatively lower T_{c}, $\Delta H_{\mathrm{f,c}}$, $X_{\mathrm{c,c}}$, T_{m}, $\Delta H_{\mathrm{f,m}}$, and $X_{\mathrm{c,m}}$. T_{c} = 15.1 °C and T_{m} = 43.5 °C, which are 1.2 and 4.3 °C lower than those of PVL respectively; $X_{\mathrm{c,c}}$ = 82.7% and $X_{\mathrm{c,m}}$ = 84.9%, which are 7.1 and 7.2% lower than those of PVL respectively. Such the broadenings and reductions might be caused by the presence of the ionically-fixed rotaxane wheel at a chain end, which is bulky. The presence of its counter anion may cause additional contribution on such broadenings and reductions.

Second, the crystallization peak is also broadened in PVL-*rot*-M. But the crystallization parameters are reduced more significantly: for example, T_{c} and $X_{\mathrm{c,c}}$ are lowered to 11.3 °C and 63.0% respectively. These results suggest that the crystallization of PVL axle is severely retarded by the presence of mobile [2]rotaxane wheel component. In the cooling run, the sliding motion of rotaxane wheel along the PVL axle may compete with the crystallization (i.e., self-assembling process) of PVL axle itself. The sliding motion of rotaxane seems to be more favorable around 20 °C or higher temperature, compared to the crystallization process of PVL axle. Below 20 °C, the sliding motion of rotaxane wheel may become slow down, whereas the

PVL axle may experience much higher degrees of supercooling and thus accelerate its crystallization; such crystallization with higher degrees of supercooling results in lower T_c and $X_\mathrm{c,c}$.

Table 3.2. Phase transition characteristics of PVL and its axles bearing fixed and movable [2]rotaxane wheels [a]

Polymer	Cooling run			Heating run		
	T_c [b] (°C)	$-\Delta H_\mathrm{f,c}$ [c] (J/g)	$X_\mathrm{c,c}$ [d] (%)	T_m [h] (°C)	$\Delta H_\mathrm{f,m}$ [i] (J/g)	$X_\mathrm{c,m}$ [j] (%)
PVL	16.3	125.3 [k] (116.0) [l]	89.8 [m] (83.2) [n]	47.7	128.5 [k] (119.0) [l]	92.1 [m] (85.3) [n]
PVL-*rot*-F	15.1	115.3 (95.3)	82.7 (68.3)	42.4	118.5 (97.9)	84.9 (70.2)
PVL-*rot*-M	11.3	87.9 (74.0)	63.0 (53.0)	37.2	59.6 (50.2)	42.7 (36.0)
				42.3	29.9 (25.2)	21.4 (18.1)

[a]Measured during cooling run with a rate of 10.0 °C/min from the melt state and subsequent heating run with a rate of 10.0 °C/min in DSC analysis. [b]Crystallization temperature at the maximum of exothermic heat of fusion peak occurred during cooling run. [c]Heat of fusion of crystallization occurred during cooling run. [d]Crystallinity estimated from the heat of fusion of crystallization by assuming that the equilibrium heat of fusion $\Delta H_\mathrm{c}^\circ$ of PVL is same with that (−139.5 J/g) of poly(ε-caprolactone).[20,21] [e]Cold crystallization temperature at the maximum of exothermic heat of fusion peak occurred during heating run. [f]Heat of fusion of cold crystallization occurred during heating run. [g]Crystallinity estimated from the heat of fusion of cold crystallization using $\Delta H_\mathrm{c}^\circ = -139.5$ J/g. [h]Crystal melting temperature at the maximum of endothermic heat of fusion peak occurred during heating run. [i]Heat of fusion of crystal melting occurred during heating run. [j]Crystallinity estimated from the heat of fusion of crystal melting using $\Delta H_\mathrm{m}^\circ = 139.5$ J/g. [k]Heat of fusion of only PVL component, which was estimated from that of the whole polymer sample using the weight fraction of PVL component. [l]Heat of fusion of whole polymer sample. [m]Calculated from the measured heat of fusion with respect to the weight of only PVL component in the sample. [n]Calculated from the measured heat of fusion with respect to the total weight of the polymer sample.

Finally, competitions between the sliding motion of rotaxane wheel and the crystallization of PVL axle are further evident in the crystal melting transition. Interestingly, the crystal melting transition appears as two endothermic peaks rather than a single peak, which is different from those of PVL homopolymer and PVL-*rot*-F. The first peak is centered at 37.2 °C, which is lower than that of PVL-*rot*-F; but the second one is centered at 42.3 °C, which is almost same with that of PVL-*rot*-F. The first peak is relatively stronger, revealing $\Delta H_{f,m}$ = 59.6 J/g ($X_{c,m}$ = 42.7%); the second peak shows $\Delta H_{f,m}$ = 29.9 J/g ($X_{c,m}$ = 21.4%); the overall $\Delta H_{f,m}$ and $X_{c,m}$ are 89.5 J/g and 64.2% respectively, which are smaller than those of PVL-*rot*-F and further much smaller than those of PVL. In general, larger (i.e., thicker) crystal reveals higher T_m. Taking this fact into account, the PVL axle in PVL-*rot*-M could form two different thicknesses of crystals. One sort of crystals has a thickness comparable to that formed in PVL-*rot*-F; another sort of crystals has a thickness slightly shorter than that formed in PVL-*rot*-F. The [2]rotaxane wheel is bulky and, furthermore, is dissimilar to PVL chemically and physically; thus the rotaxane wheel moiety could be excluded from the PVL crystal formation. Considering the bulkiness and movability of [2]rotaxane wheel, the thicker crystals would be made of the PVL axle chains in which the wheel is located near to or at an end of the axle chain. On the other hand, the thinner crystals could be formed by the PVL axle chains where the wheel is located somewhere between the axle chain ends. The thinner crystals are formed in relatively higher population, compared to the thicker crystals. The results collectively indicate that the bulky, movable rotaxane wheel could cause a certain level of hindrance in the crystallization of PVL axle. Such hindrance may vary with time lag between the kinetics of wheel moving and axle crystallization; the time lag is governed by the degree of supercooling. Overall, the movable wheel could cause more significant impact on the phase transitions of PVL-based [2]rotaxane, compared to the ionically-fixed wheel.

3.3.3 Nanoscale Film Morphologies

Figure 3.4a presents a representative 2D GISAXS pattern of PVL films. Two broad scattering peaks appear in the out-of-plane profile but could not be discernible in the in-plane profile (Figures 3.4g and 3.4j). Considering the grazing incidence optics in the measurement, one peak around 0.63° could be generated by the transmitted X-ray beam while another peak around 0.79° could be generated by the reflected X-ray beam. Thus, these scattering peaks could be originated from a same reflection plane in horizontally-oriented structure; they are the first-order reflection peaks respectively. These scattering characteristics suggest that PVL formed horizontal lamellar structure in the film. The out-of-plane and in-plane scattering profiles could be satisfactorily fitted using a GIXS formula of three-phase lamellar structure model;[22-24] a detail of the GIXS formula is given in Section 1.4 of Chapter 1. As an analysis result, it is found that in the film, PVL formed lamellar crystals having a long period L of 9.6 nm composed of a folded crystalline layer thickness l_c of 3.2 nm, an amorphous layer thickness l_a of 2.4 nm and an interfacial layer thickness of l_i of 2.0 nm; its orientation factor $O_{s,1}$ is further estimated to be 0.899 with respect to the out-of-plane direction of the film from the azimuthal scattering profile in Figure 3.4m (Table 3.3). Overall, the GISAXS analysis confirms that PVL formed horizontally-oriented lamellar crystals in the thin film.

The GISAXS analysis has been extended for PVL-*rot*-F and PVL-*rot*-M films and then found that they also form horizontally-oriented lamellar structures (Figures 3.4b-c, 3.4h-i, 3.4k-l and 3.4n-o). The determined structural parameters are compared in Table 3.3. From the obtained parameters, 2D scattering images have been attempted to reconstruct. The reconstructed scattering images are in good agreement with the measured ones, as shown in Figures 3.4a-f. It turns out that all GISAXS data have been successfully analyzed in detail.

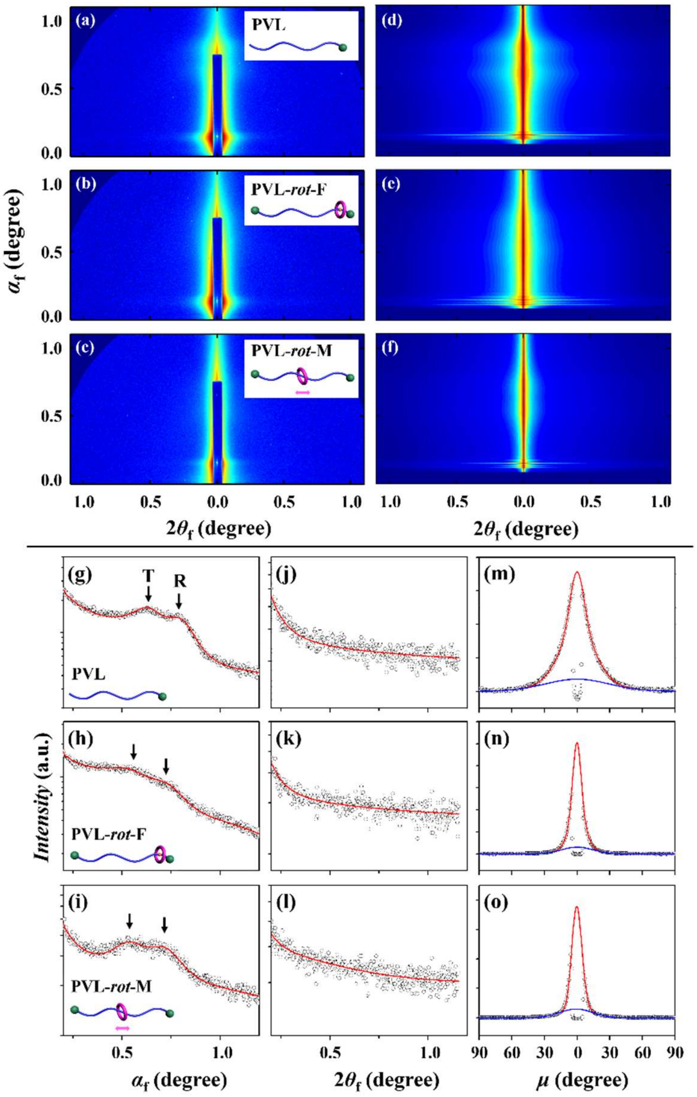

Figure 3.4. Representative GISAXS data of nanoscale films (110-130 nm thick) of PVL, PVL-*rot*-F, and PVL-*rot*-M measured at SDD = 3949 mm using a synchrotron X-ray beam (λ = 0.12479 nm). PVL: (a) 2D scattering image measured with of α_i = 0.155°; (d) 2D image reconstructed from the structural parameters in Table 3 using the GIXS formula; (g) out-of-plane scattering profile extracted along the meridian line at $2\theta_f$ = 0.095°; (j) in-plane scattering profile extracted along the equatorial line at α_f = 0.192°; (m) azimuthal scattering profile of the first-order lamellar peak at 0.715°. PVL-*rot*-F: (b) 2D scattering image measured with of α_i = 0.151°; (e) 2D image reconstructed from the structural parameters in Table 3 using the GIXS formula; (h) out-of-plane scattering profile extracted along the meridian line at $2\theta_f$ = 0.095°; (k) in-plane scattering profile extracted along the equatorial line at α_f = 0.196°; (n) azimuthal scattering profile of the first-order lamellar peak at 0.654°. PVL-*rot*-M: (c) 2D scattering image measured with of α_i = 0.151°; (f) 2D image reconstructed from the structural parameters in Table 3 using the GIXS formula; (i) out-of-plane scattering profile extracted along the meridian line at $2\theta_f$ = 0.095°; (l) in-plane scattering profile extracted along the equatorial line at α_f = 0.195°; (o) azimuthal scattering profile of the first-order lamellar peak at 0.634°. In (g–l), the symbols are the measured data and the solid lines were obtained by fitting the data using the GIXS formula of lamellar structure model. In (m–o), the symbols are the measured data and the sold lines were obtained by fitting the data using the Gaussian functions.

Table 3.3. Structural parameters of PVL, PVL-*rot*-F, and PVL-*rot*-M in thin films determined by quantitative GIXS analysis

Structure and parameters	PVL	PVL-*rot*-F	PVL-*rot*-M
Nanostructure	Horizontal lamella	Horizontal lamella	Horizontal lamella
Parameters			
L [a] (nm)	9.6	10.2	10.7
l_c [b] (nm)	3.2	2.7	3.0
l_i [c] (nm)	2.0	2.8	2.3
l_a [d] (nm)	2.4	1.9	2.7
σ_c [e] (nm)	0.7	0.9	0.8
σ_I [f] (nm)	0.9	1.1	0.7
g [g]	0.21	0.27	0.26
$\bar{\varphi}_1$ [h] (deg.)	0	0	0
σ_{φ_1} [i] (deg.)	13.0	10.9	11.0
$O_{s,1}$ [j]	0.899	0.908	0.903
Lattice structure	Orthorhombic (a = 0.77 nm, b = 0.525nm, c = 1.922 m, $\alpha = \beta = \gamma =$ 90°) [k]		
Orientational domain A			
$\bar{\varphi}_2$ [l] (deg.)	0	0	0
σ_{φ_2} [m] (deg.)	4.5	7.5	6.0
$O_{s,2}$ [n]	0.937	0.863	0.903
$\phi_{v,2}$ [o] (%)	100	94.8	98.9
Orientational domain B			
$\bar{\varphi}_3$ (deg.)		43.1	51.9
σ_{φ_3} (deg.)		3.4	3.4
$O_{s,3}$		0.315	0.091
$\phi_{tilt,3}$ (%)		5.2	1.1
Rotational domain I			
ω_I [p] (deg.)	0	0	0
ϕ_I [q] (%)	9.4	12.8	22.0
Rotational domain II			
ω_{II} (deg.)	10.29	9.52	8.71
ϕ_{II} (%)	69.1	73.8	51.9
Rotational domain III			
ω_{III} (deg.)	14.04	15.07	12.32
ϕ_{III} (%)	21.5	13.4	26.1
$X_{c,GIWAXS}$ [r] (%)	54.6 [s]	52.1	42.6
	(49.8) [t]	(42.6)	(35.1)

[a]Long period of lamellar structure. [b]Thickness of crystalline layer in the horizontal lamellar structure. [c]Thickness of interfacial layer between crystalline layer and amorphous layers. [d]Thickness of amorphous layer. [e]Standard deviation for the crystalline layer in lamellar structure. [f]Standard deviation for the interfacial layer in lamellar structure. [g]Paracrystal distortion factor along the direction parallel to the long period of lamellar structure. [h]Mean value of the polar angle φ_1 (i.e., orientation angle) between the orientation vector $\boldsymbol{n}_1$ (which is set parallel along the axis of the long period of lamellar structure) and the out-of-plane direction of the film. [i]Standard deviation for the polar angle φ_1 of lamellar structure. [j]Second order orientation factor of lamellar structure. [k]Lattice parameters determined from the measured reflection peaks. [l]Mean value of the polar angle φ_i (i.e., orientation angle) between the orientation vector $\boldsymbol{n}_i$ (which is set along a direction normal to the {110} plane stacks (namely, parallel to the *c*-axis of orthorhombic lattice unit cell)) and the out-of-plane direction of the film. [m]Standard deviation for the polar angle φ_i. [n]Second order orientation factor of orthorhombic crystal lattice. [o]Volume fraction of orthorhombic crystals with $\bar{\varphi}_i$ (i.e., a preferred direction *i*). [p]Rotational angle of orthorhombic crystals where the rotational axis is parallel to a normal direction to the film plane. [q]Relative volume fraction of orthorhombic crystals with rotational angle ω_I where the rotational axis is parallel to a normal direction to the film plane. [r]Crystallinity determined by the analysis of from

GIWAXS data. [s]Crystallinity of only PVL component determined by the analysis of GIWAXS data using the volume fraction of only PVL component. [t]Crystallinity of the whole polymer (which includes PVL and all other components) determined by the analysis of from GIWAXS data.

The PVL films have further been examined by GIWAXS analysis in order to get more information on the lattice structure of the crystalline layers in the horizontal lamellar structure. The polymer film clearly reveals three scattering peaks at ($\alpha_f = 8.66°$, $2\theta_f = 6.37°$), ($\alpha_f = 0°$, $2\theta_f = 15.04°$), and ($\alpha_f = 0°$, $2\theta_f = 16.81°$), as shown in Figure 3.5a. It is known that PVL crystallizes, forming crystals with orthorhombic lattice.[25] Taking into considering such crystal lattice, the scattering peaks could be assigned as {102}, {110} and {200} reflections respectively. The 2D GIWAXS image has been quadrantly averaged and deconvoluted, as shown in Figure 3.5d. In particular, the {110} and {200} reflections appear only along the equatorial line, indicating that the {110} planes, as well as the {200} planes are stacked only along the in-plane direction of the film. From the azimuthal scattering profile of {110} reflection, the orthorhombic crystals are determined to have an orientation factor $O_{s,2}$ of 0.937 with respect to the out-of-plane direction of the film (Figure 3.5g; Table 3.3). These results inform that the orthorhombic crystals are preferentially oriented along the out-of-plane direction of the film.

However, both the {110} and {200} reflection peaks are unusually broad rather than sharper. Each reflection could be deconvoluted into three peaks (I, II, and III), as shown in Figures 3.5d and 3.6. These results suggest that the vertically-oriented orthorhombic PVL crystals are present as three different types of rotational domains in the film: (i) type-I rotational crystal domain ($\omega_I = 0°$ (rotational angle where the rotational axis is parallel to a normal direction to the film plane); $\phi_I = 9.4\%$ (relative volume fraction)), (ii) type-II rotational crystal domain ($\omega_{II} = 10.29°$; $\phi_{II} = 69.1\%$), and (iii) type-III rotational crystal domain ($\omega_{III} = 14.04°$; $\phi_{III} = 21.5\%$) (Figure 3.6; Table 3.3).

For the orthorhombic crystals, the lattice parameters could be determined to be a = 0.778 nm, b = 0.525 nm, c = 1.922 nm, and $\alpha = \beta = \gamma = 90°$ from the {102}, {110} (peak I) and {200} (peak I) reflections. Here, it is noted that the c value is close to the length (2.204 nm) of three repeat units in a fully extended conformation. The c value is 40% shorter than the crystalline layer thickness (l_c = 3.2 nm) of the horizontal lamellar structure. In addition, the crystallinity $X_{c,\mathrm{GIWAXS}}$ is determined to be 54.6% from the quadrant-averaged scattering profile in Figure 3.5d.

In similar manner, the 2D GIWAXS images of PVL-*rot*-F and PVL-*rot*-M films have been analyzed (Figures 3.5b-c, 3.5e-f, and 3.5h-i; Figures 3.7 and 3.8). All analysis results are compared with those of PVL homopolymer film, as listed in Table 3.3.

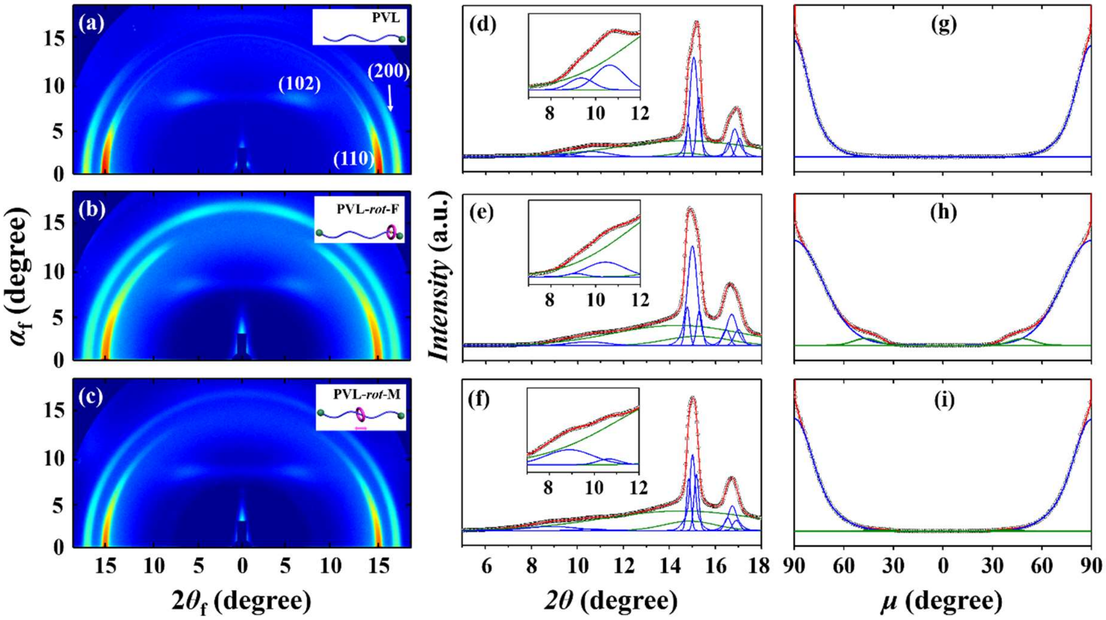

Figure 3.5. Representative GIWAXS data of nanoscale films (110-130 nm thick) of PVL, PVL-*rot*-F, and PVL-*rot*-M measured at SDD = 225 mm using a synchrotron X-ray beam (λ = 0.11201 nm). PVL: (a) 2D scattering image measured with of α_i = 0.111°; (d) 1D scattering profile averaged quadrantly from the 2D image in (a); (g) azimuthal scattering profile of the {110} peak. PVL-*rot*-F: (b) 2D scattering image measured with of α_i = 0.111°; (e) 1D scattering profile averaged quadrantly from the 2D image in (b); (h) azimuthal scattering profile of the {110} peak. PVL-*rot*-M: (c) 2D scattering image measured with of α_i = 0.111°; 1D scattering profile averaged quadrantly from the 2D image in (c); (i) azimuthal scattering profile of the {110} peak.

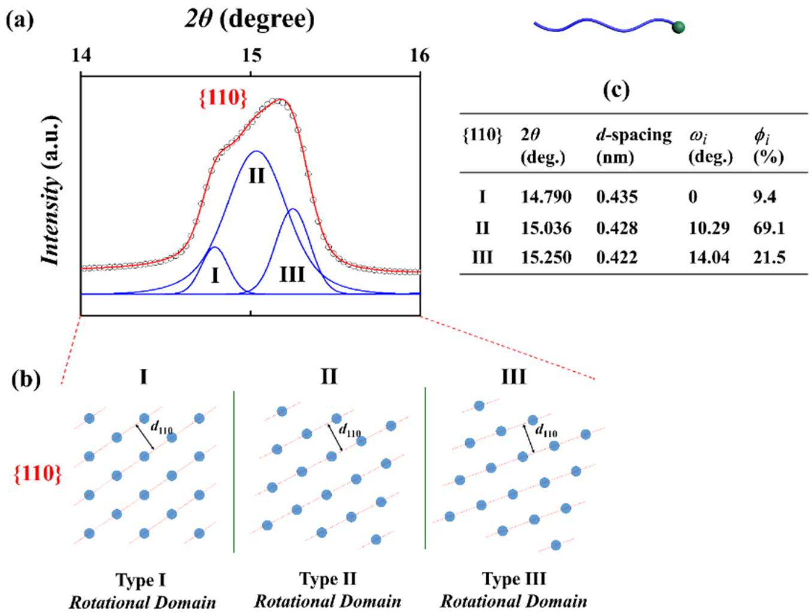

{110}	2θ (deg.)	*d*-spacing (nm)	ω_i (deg.)	ϕ_i (%)
I	14.790	0.435	0	9.4
II	15.036	0.428	10.29	69.1
III	15.250	0.422	14.04	21.5

Figure 3.6. (a) Enlarged {110} reflection profile of PVL film, which was obtained from the 1D scattering profile in Figure 3.5d. The symbols represent the measured data; the blue curves represent the scattering profiles obtained by the deconvolution of the {110} reflection profile; the red curve represents the sum of the deconvoluted scattering profiles in blue color. (b) Top views of orthorhombic lattices in three different rotational domains which were determined by the deconvolution analysis of the scattering profile in (a); d_{110} is the *d*-spacing of {110} reflection. (c) Deconvolution analysis results of the scattering profile in (a); ω_i and ϕ_i are the rotational angle and relative volume fraction of orthorhombic lattice domain *i* respectively where the rotational axis is parallel to the *c*-axis of the lattice (which is also parallel to the out-of-plane of the film).

The GISAXS and GIWAXS analysis results collectively could provide for the first time important structural features on the nanoscale film morphologies of macromolecular [2]rotaxanes as follows.

First, the $X_{\mathrm{c,GIWAXS}}$ of nanoscale film is in the decreasing order PVL > PVL-*rot*-F >> PVL-*rot*-M. This trend is coincident with that in the overall crystallinity data measured for the bulk samples using DSC. These results collectively are clear clues that the movable rotaxane wheel causes more negative impact on the overall crystallization of PVL axle, compared to the ionically-fixed wheel.

Second, PVL and its [2]rotaxanes, nevertheless, favorably form horizontally-oriented lamellar structures in nanoscale films, regardless of the incorporation of fixed and movable rotaxane wheel. The results confirm that the PVL axle owns a strong self-assembling power and can indeed crystallize against any possible obstacles due to the bulky rotaxane wheel and its movability. However, the positional distortion factor g is in the increasing order PVL < PVL-*rot*-M < PVL-*rot*-F. Namely, the level of disorder in the horizontal lamellar structure is increased by incorporating fixed and movable rotaxane wheels. Such disordering level is increased slightly more by the ionically-fixed wheel.

Third, for the horizontal lamellar crystals, the long period L, as well as the sum of interfacial and amorphous layer thicknesses ($= l_i + l_a$) is in the increasing order PVL < PVL-*rot*-F < PVL-*rot*-M. Thus, the increments in the L value are attributed mainly to the thickenings in the sum of interfacial and amorphous layer by incorporated fixed and movable wheels. The results further inform that the incorporated rotaxane wheels could be ejected from the folded PVL crystal formation because their bulkiness and structural heterogeneity and, indeed, present in the amorphous layer and interfacial layer. Overall, the movable rotaxane wheel makes more contribution to increase both long period and sum of interfacial and amorphous layers, compared to the fixed wheel.

Fourth, surprisingly the crystalline layer thickness l_c, however, is in the decreasing order PVL > PVL-*rot*-M > PVL-*rot*-F. The results are an indication that the bulky rotaxane wheel fixed to the relatively large size of end group causes more severe impact to decrease the crystalline layer thickness, compared to the movable wheel having freedom in positioning along the whole PVL axle chain.

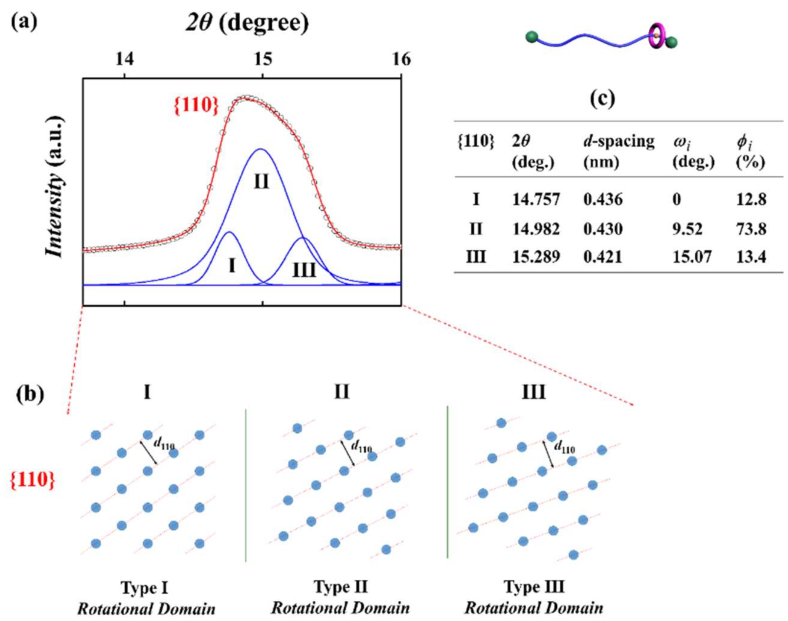

{110}	2θ (deg.)	*d*-spacing (nm)	ω_i (deg.)	ϕ_i (%)
I	14.757	0.436	0	12.8
II	14.982	0.430	9.52	73.8
III	15.289	0.421	15.07	13.4

Figure 3.7. (a) Enlarged {110} reflection profile of PVL-*rot*-F film obtained from the 1D scattering profile in Figure 3.5e. The symbols represent the measured data; the blue curves represent the scattering profiles obtained by the deconvolution of the {110} reflection profile; the red curve represents the sum of the deconvoluted scattering profiles in blue color. (b) Top views of orthorhombic lattices in three different rotational domains which were determined by the deconvolution analysis of the scattering profile in (a); d_{110} is the *d*-spacing of {110} reflection. (c) Deconvolution analysis results of the scattering profile in (a); ω_i and ϕ_i are the rotational angle and relative volume fraction of orthorhombic lattice domain *i* respectively where the rotational axis is parallel to the *c*-axis of the lattice (which is also parallel to the out-of-plane of the film).

Fifth, interestingly the amorphous layer thickness l_a is in the increasing order PVL-*rot*-F < PVL < PVL-*rot*-M. Moreover, the interfacial layer thickness l_i is in the increasing order PVL < PVL-*rot*-M < PVL-*rot*-F. These results collectively inform that the ionically-fixed rotaxane wheel is more highly populated in the interfacial layer than in the amorphous layer, whereas the movable wheel is located in the interfacial layer as well as in the amorphous layer. Furthermore, the results could be a clue for why the relatively thicker crystalline layer forms in the PVL-*rot*-M film than the PVL-*rot*-F film.

Sixth, in the lamellar structure of PVL, the crystalline layers reveal orthorhombic lattice whose *c*-axis is parallel to the direction of lamellar stacks as well as the out-of-plane of the film. Namely, the crystalline layers consist of only vertically-oriented orthorhombic crystals (i.e, type A orientational crystals). Interestingly, such the type A orientational crystals are, however, found to be composed of three different types (I, II, and III) of rotational lattice domains (Table 3.3; Figures 3.6 and 3.9a).

Seventh, in the horizontal lamellar structure of PVL-*rot*-F, the crystalline layers also reveal type A orientational lattices together with three types of rotational lattice domains as observed for the PVL homopolymer film. However, another type (type B) of orientational lattice domains are present in a minor population, only 5.2%; its tilt angle and orientation factor are 43.1° and 0.315 respectively (Table 3.3; Figures 3.9b and 3.7). Moreover, the rotational angles and populations of the individual rotational domains are changed. The formation of such type B orientational lattice domains, as well as the influences in the rotational lattice domains could be attributed to the ionically-fixed rotaxane wheel with a bulkiness even though the wheel is ejected from the crystalline layer.

Finally, the crystalline layers in the horizontal lamellar structure of PVL-*rot*-M are found to show similar morphological feature as observed for PVL-*rot*-F. However, such type B orientational lattice domain is formed in an extremely low population; its tilt angle and population are 51.9° and 1.1% respectively (Table 3.3; Figures 3.9c and 3.8). These results suggest that the movable rotaxane wheel also influences the morphological characteristics of the crystalline layer but its impact is relatively weaker than that of the fixed wheel.

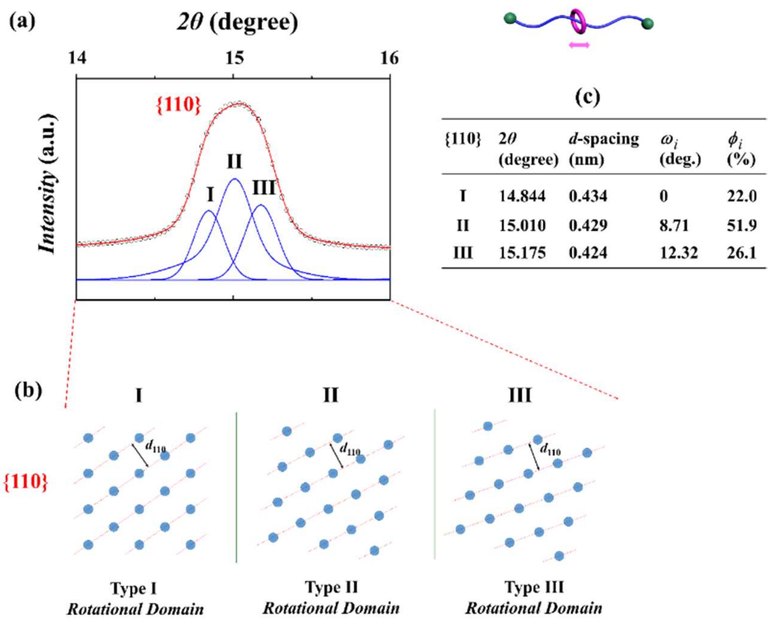

{110}	2θ (degree)	d-spacing (nm)	ω_i (deg.)	ϕ_i (%)
I	14.844	0.434	0	22.0
II	15.010	0.429	8.71	51.9
III	15.175	0.424	12.32	26.1

Figure 3.8. (a) Enlarged {110} reflection profile of PVL-*rot*-M film obtained from the 1D scattering profile in Figure 3.5f. The symbols represent the measured data; the blue curves represent the scattering profiles obtained by the deconvolution of the {110} reflection profile; the red curve represents the sum of the deconvoluted scattering profiles in blue color. (b) Top views of orthorhombic lattices in three different rotational domains which were determined by the deconvolution analysis of the scattering profile in (a); d_{110} is the *d*-spacing of {110} reflection. (c) Deconvolution analysis results of the scattering profile in (a); ω_i and ϕ_i are the rotational angle and relative volume fraction of orthorhombic lattice domain *i* respectively where the rotational axis is parallel to the *c*-axis of the lattice (which is also parallel to the out-of-plane of the film).

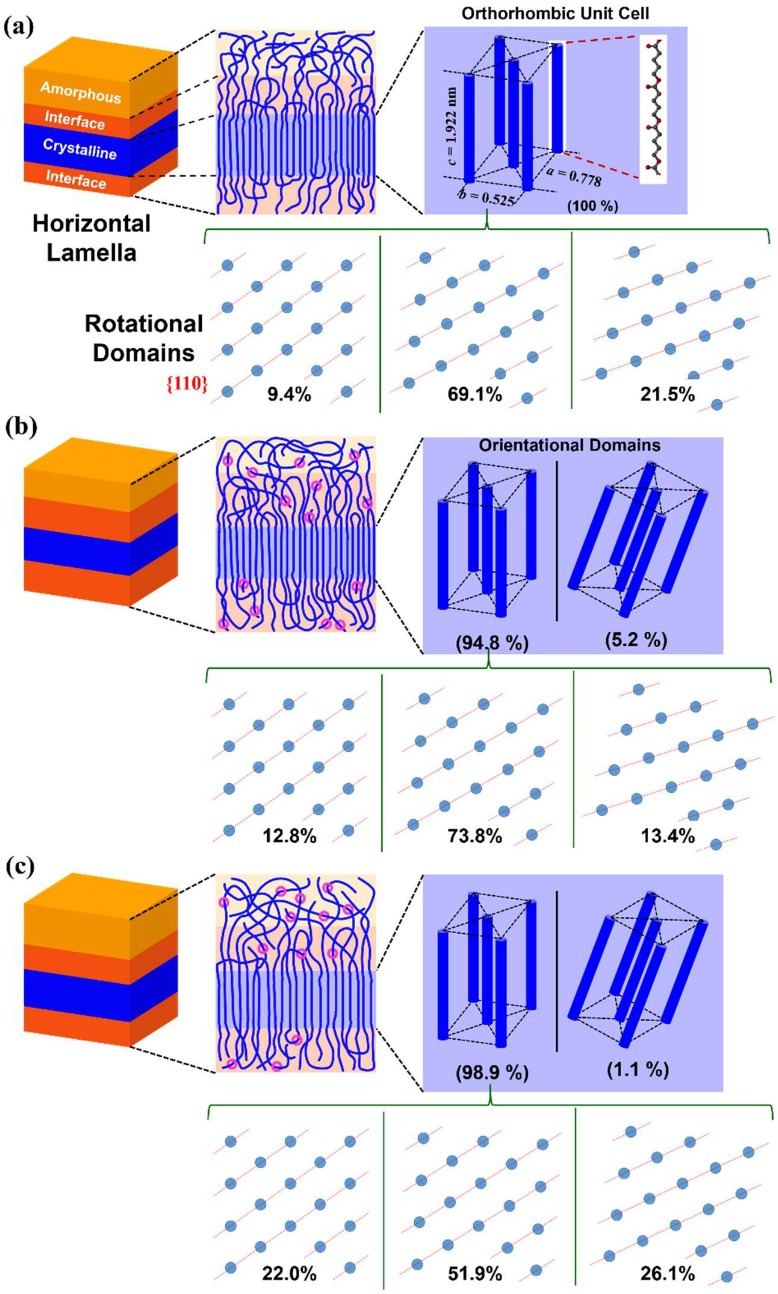

Figure 3.9. Schematic representations of molecular chain conformations and packing orders in nanoscale films. (a) PVL: Horizontal lamellar structure in which the crystalline layer consists of vertically-oriented orthorhombic lattices in three different rotational domains. (b) PVL-*rot*-F: Horizontal lamellar structure in which the crystalline layer consists of vertically-oriented orthorhombic lattices in three different rotational domains as a major structural component; orientationally-tilted orthorhombic lattice domains are additionally present as a minor component; the ionically-fixed rotaxane (purple-colored ring) is more highly populated in the interface than in the amorphous layer. (c) PVL-*rot*-M: Horizontal lamellar structure in which the crystalline layer consists of vertically-oriented orthorhombic lattice as a major component and tilt-oriented orthorhombic lattice as a minor component; the major component is present in three different rotational domains; the movable rotaxane (purple-colored ring) is populated in the interface as well as in the amorphous layer.

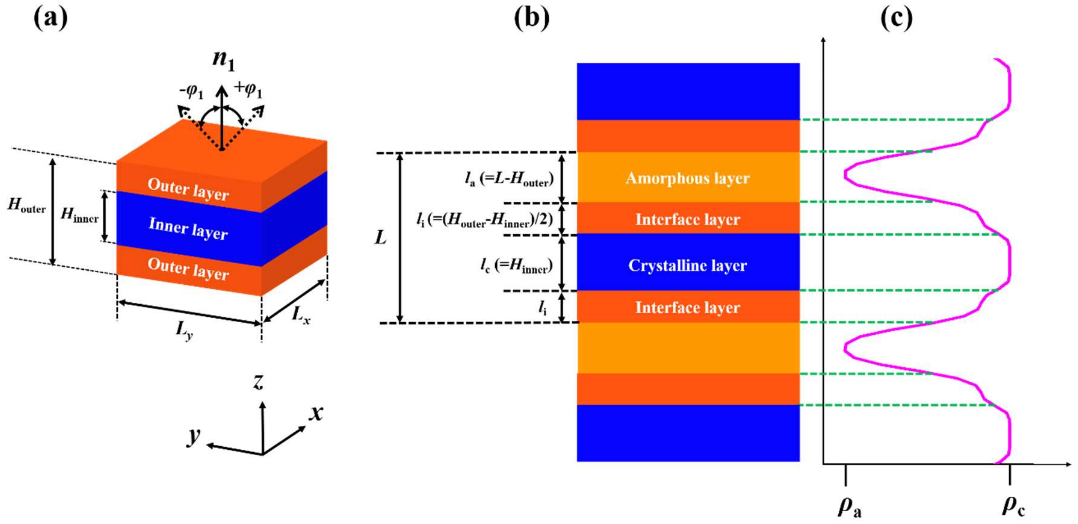

Figure 3.10. A lamellar structure model composed of three layers: (a) 3D representation of lamellar structure where $\boldsymbol{n}_1$ is the orientation vector of the structure and φ_1 is the polar angle between the $\boldsymbol{n}_1$ vector and the out-of-plane of the film; (b) 2D representation of lamellar structure. The inner and outer layers in (a) correspond to the dense and interfacial layers in (b) respectively; the blue colored layer in (b) corresponds to the less dense layer; (c) The electron density profile along the direction of layer stacks in the lamellar structure where ρ_c and ρ_a are the electron densities of crystalline (dense) and amorphous (less dense) layers respectively. The dimension of the lamellar structure is defined by L (long period), L_x, L_y, l_c (= H_{inner}), l_i (= (H_{outer} – H_{inner})/2), and l_a (= L – H_{outer}).

3.4 Conclusions

In this chapter, PVL and its [2]rotaxanes (PVL-*rot*-F and PVL-*rot*-M) have been investigated in a comparative manner from views of thermal stability, phase transitions and nanoscale film morphology using TGA, DSC, GISAXS, and GIWAXS analyses. These analyses have found the topological effects of fixed and movable rotaxane moieties on the properties and morphological structure of PVL as follows:

The thermal stability of PVL axle is severely reduced by the presence of ionically-fixed rotaxane moiety with its counter anion, but is slightly influenced by the movable rotaxane.

All crystallization and crystal melting transition parameters of PVL axle are lowered by the fixed rotaxane with the counter anion, but more significantly lowered by the movable rotaxane. Nevertheless, interestingly PVL-*rot*-M is confirmed to form a certain fraction of crystals which reveal melting temperature equivalent to that of the crystals formed in PVL-*rot*-F.

Very interestingly, all polymers favorably form horizontal lamellar structures in nanoscale thin films, regardless of the presences of fixed and movable rotaxane moieties. Moreover, the crystalline layers in the lamellar structure are composed of three different rotational lattice domains, regardless of the presences of fixed and movable rotaxane moieties. These microstructure formations are originated from an inherently excellent self-assembling ability of PVL as well as the relatively low volume fraction of roxtane moiety compared to that of the PVL axle.

However, structural details of such horizontal lamellar structure are discernibly influenced by the fixed and movable rotaxane moieties. The crystalline layer is thinned by the fixed and movable rotaxanes. The long period, as well as the sum of interfacial and amorphous layers is thickened by the fixed and movable rotaxanes. Both fixed and movable rotaxane moieties further cause to form tilted orientational crystal lattice domains as very minor portions in addition to the vertically-oriented lattice domain formation of PVL. The ionically-fixed rotaxane moiety tends to be highly populated in the interfacial layer rather than in the amorphous layer, resulting in thickening of the interfacial layer. In contrast, the movable rotaxane moiety is populated in both interfacial and amorphous layers, causing thickenings in the interfacial and amorphous layers. In this chapter, the novel three layer model was successful in parameterizing the morphological details with precision and also identifying the rotaxane wheel's influence as a topological feature on the self-assembly behavior of PVL axles in thin films, successfully establishing new insights in the topology-morphology correlation of semi-crystalline polymers.

3.5 References

1. Raymo, F. M.; Stoddart, J. F. Interlocked Macromolecules. *Chem. Rev.* **1999**, *99*, 1643–1663.
2. Yang, L.; Tan, X.; Wang, Z.; Zhang, X. Supramolecular Polymers: Historical Development, Preparation, Characterization, and Functions. *Chem. Rev.* **2015**, *115*, 7196–7239.
3. Takata, T. Polyrotaxane and Polyrotaxane Network: Supramolecular Architectures Based on the Concept of Dynamic Covalent Bond Chemistry. *Polymer J.* **2006**, *38*, 1–20.
4. Harada, A.; Hashidzume, A.; Yamaguchi, H.; Takashima, Y. Polymeric Rotaxanes. *Chem. Rev.* **2009**, *109*, 5974–6023.
5. Arunachalam, M.; Gibson, H. W. Recent Developments in Polypseudorotaxanes and Polyrotaxanes. *Prog. Polym. Sci.* **2014**, *39*, 1043–1073.
6. Takata, T.; Kihara, N.; Furusho, Y. Polyrotaxanes and Polycatenanes: Recent Advances in Syntheses and Applications of Polymers Comprising of Interlocked Structures. *Adv. Polym. Sci.* **2004**, *171*, 1–75.
7. Aoki, D.; Takata, T. Mechanically Linked Supramolecular Polymer Architectures Derived from Macromolecular [2]Rotaxanes: Synthesis and Topology Transformation. *Polymer* **2017**, *128*, 276–296.
8. Takata, T.; Aoki, D. Topology-Transformable Polymers: Linear–Branched Polymer Structural Transformation via the Mechanical Linking of Polymer Chains. *Polymer J.* **2018**, *50*, 127–147.
9. Ogi, S.; Sugiyasu, K.; Manna, S.; Samitsu, S.; Takeuchi, M. Living supramolecular polymerization realized through a biomimetic approach. *Nat. Chem.* **2014**, *6*, 188–195.
10. Kang, J.; Miyajima, D.; Mori, T.; Inoue, Y.; Itoh, Y.; Aida, T. Noncovalent assembly. A rational strategy for the realization of chain-growth supramolecular polymerization. *Science* **2015**, *347*, 646–651.
11. Chen, Z.; Aoki, D.; Uchida, S.; Marubayashi, H.; Nojima, S.; Takata, T. Effect of Component Mobility on the Properties of Macromolecular [2]Rotaxanes. *Angew. Chem. Int. Ed.* **2016**, *55*, 2778–2781.
12. Nagapudi, K.; Hunt, J.; Shepherd, C.; Baker, J.; Beckham, H. W. Synthesis, dynamic mechanical, and solid-state NMR spectroscopy of crown-ether-based linear aliphatic polyurethane rotaxanes. *Macromol. Chem. Phys.* **1999**, *200*, 2541–2550.
13. Gong, C. G.; Ji, Q.; Subramaniam, C.; Gibson, H. W. Main chain polyrotaxanes by threading crown ethers onto a preformed polyurethane: preparation and properties. *Macromolecules* **1998**, *31*, 1814–1818.
14. K. Nakazono, T. Ishino, T. Takashima, D. Saeki, D. Natsui, N. Kihara, T. Takata, Directed One-Pot Syntheses of Crown Ether Wheel-Containing Main Chain-Type Polyrotaxanes with Controlled Rotaxanation Ratios? *Chem. Commun.* **2014**, *50*, 15341–15344.
15. Aoki, D.; Uchida, S.; Nakazono, K.; Koyama, Y.; Takata, T. Macromolecular [2]Rotaxanes: Effective Synthesis and Characterization, *ACS Macro Lett.* **2013**, *2*, 461−465.
16. Lee, B.; Park, Y.-H.; Hwang, Y.-T.; Oh, W.; Yoon, J.; Ree, M. Ultralow-*k* Nanoporous Organosilicate Dielectric Films Imprinted with Dendritic Spheres. *Nat. Mater.* **2005**, *4*, 147–150.
17. Ree, M. Probing the Self-Assembled Nanostructures of Functional Polymers with Synchrotron Grazing Incidence X-Ray Scattering. *Macromol. Rapid Commun.* **2014**, *35*, 930–959.

18. Kim, Y. Y.; Ree, B. J.; Kido, M.; Ko, Y.-G.; Ishige, R.; Hirai, T.; Wi, D.; Kim, J.; Kim, W. J.; Takahara, A.; Ree, M. High Performance n-Type Electrical Memory and Morphology-Induced Memory-Mode Tuning of A Well-Defined Brush Polymer Bearing Perylene Diimide Moieties. *Adv. Electronic Mater.* **2015**, *1*, 1500197.
19. Durchschlag, H.; Zipper, P. Calculation of the Partial Volume of Organic Compounds and Polymers. *Progr. Colloid Polym. Sci.* **1994**, *94*, 20–39.
20. Xiang, L.; Ryu, W.; Kim, H.; Ree, M. Precise Synthesis, Properties, and Structures of Cyclic Poly(ε-caprolactone)s. *Polymers* **2018**, *10*, 577.
21. Pitt, C. G.; Chasalow, F. I.; Hibionada, Y. M. Aliphatic Polyesters, I. The Degradation of Poly(ε-caprolactone) in vivo. *J. Appl. Polym. Sci.* **1981**, *26*, 3779–3787.
22. Ahn, B.; Hirai, T.; Jin, S.; Rho, Y.; Kim, K.-W.; Kakimoto, M.-a.; Gopalan, P.; Hayakawa, T.; Ree, M. Hierarchical Structure in Nanoscale Thin Films of a Poly(styrene-*b*-methacrylate grafted with POSS) (PS_{214}-*b*-$PMAPOSS_{27}$). *Macromolecules* **2010**, *43*, 10568–10581.
23. Ahn, B.; Kim, D. M.; Hsu, J.-C.; Ko, Y.-G.; Shin, T. J.; Kim, J.; Chen, W.-C.; Ree, M. Tunable Film Morphologies of Brush–Linear Diblock Copolymer Bearing Difluorene Moieties Yield a Variety of Digital Memory Properties. *ACS Macro Lett.* **2013**, *2*, 555–560.
24. Kim, Y. Y.; Jung, S.; Kim, C.; Ree, B. J.; Kawato, D.; Nishikawa, N.; Suemasa, D.; Isono, T.; Kakuchi, T.; Satoh, T.; Ree, M. Hierarchical Structures in Thin Films of Miktoarm Star Polymers: Poly(n-hexyl isocyanate)(12K)−Poly(ε-caprolactone)$_{1-3}$(5K), *Macromolecules* **2014**, *47*, 7510−7524.
25. Furuhashi, Y.; Sikorski, P.; Atkins, E.; Iwata, T.; Doi, Y. Structure and Morphology of the Aliphatic Polyester Poly(δ-valerolactone) in Solution-Grown, Chain-Folded Lamellar Crystals. *J. Polym. Sci.: Part B: Polym. Phys.* **2001**, *39*, 2622–2634.

Chapter 4

Nanoscale Film Morphologies and Chain Conformations of Pseudo Miktoarm Block Copolymers based on Poly(δ-valerolactone) Macromolecular Rotaxane Linked to Polystyrene

4.1 Introduction

Polyrotaxanes have attracted great interests as one of supramolecular polymer families because of unique topological features.[1-4] As a result of many research effort, several polyrotaxane systems and their derivatives were reported along with corresponding advanced synthetic schemes.[5-17]

In particular, rotaxane-linked linear block, star, and crosslinked polymers were introduced.[12-29] These polymer systems were extensively studied in the aspect of synthetic methods with improving product yield and purity. Among the developed polymers, crosslinking systems were intensively investigated to understand crosslinking or gelation behaviors and find potential applications.[21-29] Crosslinked polyrotaxane systems demonstrated excellent mechanical properties, such as high toughness and stretchability, as well as good gel formations and high efficiency in releasing drug molecules that were loaded within. However, other properties such as morphology and structural characteristics were rarely investigated. Furthermore, the other polymer systems were yet studied although expecting to exhibit unusual properties and morphological structures. Overall, rotaxane-linked linear block, star, and crosslinked polymers have their property and morphology details under veils and are need of thorough studies to fully realize their potential applications.

In this chapter, a set of pseudo-miktoarm polyrotaxane system based on semi-crystalline poly(δ-valerolactone) (PVL) axles bearing fixed and movable dibenzo-24-crown-8-ether (rotaxane: *rot*) wheels linked with amorphous polystyrene (PS) were investigated for the first time regarding their morphology details, and thermal and phase transition characteristics: PVL-*rot*-PS-M and PVL-*rot*-PS-F (Figure 4.1). The quantitative synchrotron grazing incidence X-ray scattering (GIXS) analysis found that they all form phase-separated lamellar structures in nanoscale films as observed in films of their counterpart, diblock copolymer (PVL-*b*-PS). Interestingly, all PVL layers form fringed-micelle like crystals rather than folded crystals; such crystals are present as three different rotational lattice domains. However, PVL-*rot*-PS-M forms only horizontal lamellar structure, whereas PVL-*rot*-PS-F, as well as PVL-*b*-PS makes horizontal lamellar structure domains as a major component and vertical lamellar structure domains as a minor component. In the PVL layers, PVL-*rot*-PS-M, as well as PVL-*b*-PS, forms two different orientational crystal domains, whereas PVL-*rot*-PS-F forms three different orientational crystal domains. Moreover, the structural parameters further vary depending upon the movable and fixed PS-linked rotaxane wheels. The movable PS-linked rotaxane wheel remarkably stimulates the PVL axle to crystallize. In contrast, the crystallization of PVL axle is significantly retarded or discouraged by the ionically-fixed rotaxane wheel. The PVL axle maintains its own thermal stability, regardless of the fixed and movable PS-linked rotaxane wheels. Instead, the ionically-fixed PS-linked wheel reveals relatively lower stability than the movable wheel.

(a) PVL-*rot*-PS-M

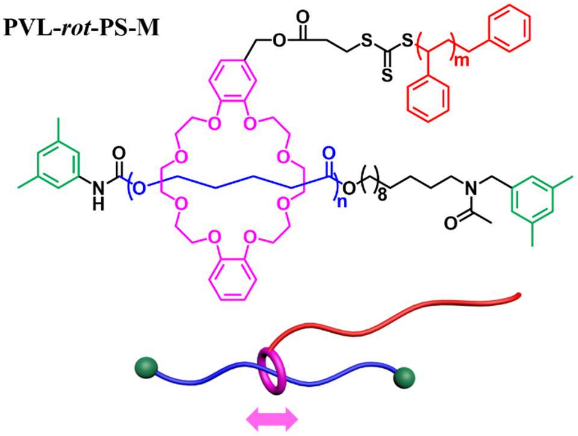

(b) PVL-*rot*-PS-F

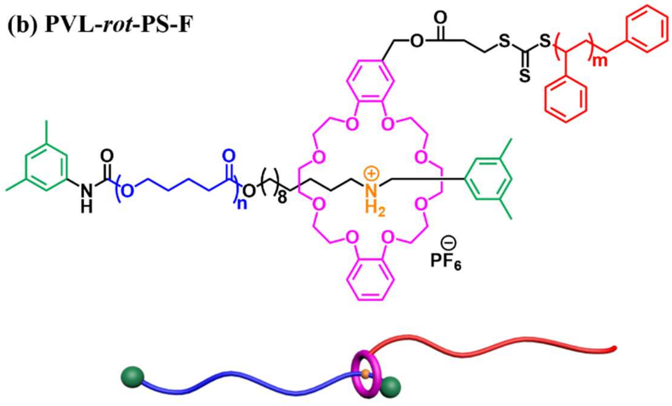

(c) PVL-*b*-PS

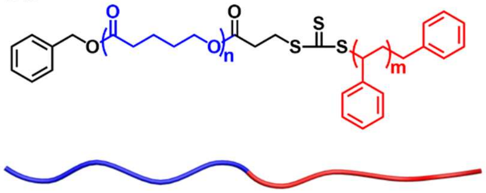

Figure 4.1. Chemical structures of the macromolecular [2]rotaxanes linked with a polystyrene: (a) PVL-*rot*-PS-M, (b) PVL-*rot*-PS-F and PVL-*b*-PS.

4.2 Experimental Section

A series of macromolecular [2]rotaxanes based on a PVL axle and a rotaxane wheel-linked PS, including a diblock copolymer of PVL and PS were prepared according to the synthetic methods in the literature:[18] PVL-*rot*-PS-M, PVL-*rot*-PS-F and PVL-*b*-PS (Figure 4.1). The molecular characteristics of the prepared polymers are summarized in Table 4.1.

Each polymer sample was dissolved in chloroform ($CHCl_3$) and filtered using disposable syringes equipped with polytetrafluoroethylene filter membranes of 0.2 μm pore size, producing polymer solutions with a concentration of 0.5 wt%. Each polymer solution was deposited on silicon (Si) substrates via spin coating process and dried in vacuum at room temperature for 24 h. Some of the obtained films were further annealed under a vapor of tetrahydrofuran (THF) at room temperature for 1 h. The obtained polymer films were determined to have a thickness of 110−130 nm by using a spectroscopic ellipsometer (Model M-2000, Woollam, Lincoln, NE, USA).

Thermogravimetry (TGA) and differential scanning calorimetry (DSC) analyses were conducted with a rate of 10.0 °C/min under nitrogen atmosphere using Seiko and TA instruments (model TG/DGA-6300 and model DSC-220CU, Seiko Instrument, Tokyo, Japan; model Dynamic TGA 2950, TA Instruments, New Castle, DE, USA). Synchrotron X-ray scattering analysis was carried out at the 3C beamline[30-32] of the Pohang Accelerator Laboratory (PAL), Pohang, Korea. Scattering data were normally collected for 10–30 s using X-ray radiation sources with a wavelength λ of 0.12096 nm and a two-dimensional (2D) charge-coupled detector (CCD) (model Rayonix 2D MAR, Evanston, IL, USA). The sample-to-detector distance (SDD) was 209 mm for grazing incidence wide angle X-ray scattering (GIWAXS) measurements and 2824 and 29100 mm for grazing incidence small angle X-ray scattering (GISAXS) measurements. The incidence angle α_i of X-ray beam with respect to the film sample surface was set in the range 0.130–0.180°, which is between the critical angle of the polymer film and the silicon substrate ($\alpha_{c,f}$ and $\alpha_{c,s}$). Aluminum foils were used as a semi-transparent beam stop. Scattering angles were corrected according to the positions of the X-ray beams reflected from the silicon substrate as well as by using precalibrated standards (polystyrene-*block*-poly(ethylene-*ran*-butylene)-*block*-polystyrene; sucrose and silver behenate standards (Tokyo Chemical Inc., Tokyo, Japan)).

4.3 Results and Discussion

4.3.1 Thermal Stabilities

PVL-*b*-PS exhibits a single-step degradation behavior even though it is a copolymer of immiscible blocks, as shown in Figure 4.2a. The first 5% mass loss takes place at 345 °C (= $T_{\mathrm{d},5}$); the degradation is completed at 461 °C (= $T_{\mathrm{d,f}}$) (Table 4.1). The $T_{\mathrm{d},5}$ and $T_{\mathrm{d,f}}$ values are higher than those (332 and 450 °C) of PVL homopolymer (Figure 4.2a), respectively. This enhanced stability could be attributed to the increased molar mass due to the incorporated PS block as well as the high stability of PS.

Table 4.1. Characteristics of poly(δ-valerolactone)s (PVL) bearing fixed and movable rotaxane wheels (rot) linked with polystyrene (PS)

Polymer	$M_{\mathrm{n,NMR}}$[a]	*PDI*[b]	PVL				PS				$T_{\mathrm{d},5}$[g] (°C)	$T_{\mathrm{d,f}}$[h] (°C)
			DP_{NMR}[c]	$M_{\mathrm{n,NMR}}$[d]	f_{PVL}[e]	ϕ_{PVL}[f]	DP_{NMR}[c]	$M_{\mathrm{n,NMR}}$[d]	f_{PS}[e]	ϕ_{PS}[f]		
PVL-*b*-PS [i]	8910	1.15	47	4700	0.527	0.491	37	3850	0.432	0.484	345	461
PVL-*rot*-PS-F	10020 [j]	1.18	48	4800	0.479	0.441	39	4060	0.405	0.448	263	461
PVL-*rot*-PS-M	9900	1.33	48	4800	0.485	0.443	39	4060	0.410	0.450	318	461

[a] Number-average molecular weight of the polymer, including the whole components (linkers, end group, and so on), which was determined by proton nuclear magnetic resonance (^{1}H NMR) spectroscopy analysis. [b] Polydispersity index of polymer determined by gel permeation chromatography (GPC) analysis. [c] Number-average degree of polymerization of only PVL or PS part determined by ^{1}H NMR) spectroscopy analysis. [d] Number-average molecular weight of only PVL or PS part determined by ^{1}H NMR spectroscopy analysis. [e] Weight fraction of only PVL or PS part with respect to the molar mass of the whole polymer. [f] Volume fraction of only PVL or PS part with respect to the total volume of the whole polymer; here, the volume fraction was estimated using a method reported in literature.[33] [g] Temperature at which 5% mass loss occurred in TGA analysis. [h] Temperature at which the degradation is completed in TGA analysis. [i] Diblock copolymer of PVL and PS prepared as a reference polymer for PVL-*rot*-PS-F and PVL-*rot*-PS-M. [j] Included the molar mass of the counter anion.

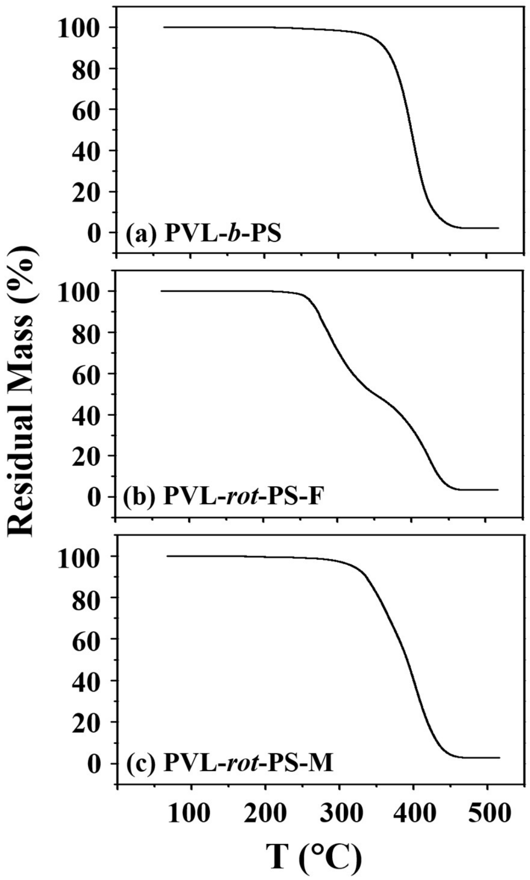

Figure 4.2. TGA thermograms of macromolecular [2]rotaxanes linked with a polystyrene, which were measured at a rate of 10.0 °C/min under nitrogen atmosphere.

Different from the diblock copolymer above, PVL-*rot*-PS-F depicts clearly a two-step degradation behavior; here, it is measured that $T_{d,5}$ = 263 °C and $T_{d,f}$ = 461 °C (Figure 4.2b; Table 4.1). In particular, the $T_{d,5}$ value is much lower than those (332 and 345 °C) of PVL and PVL-*b*-PS. The $T_{d,f}$ value is higher than that (450 °C) of PVL homopolymer and same with that of PVL-*b*-PS. Furthermore, the degradation in the second-step begins around 330 °C, which is close to $T_{d,5}$ of PVL homopolymer. Taking into account the degradation characteristics of PVL and PVL-*b*-PS, the thermal degradation in the first-step could originate from the ionically-fixed rotaxane wheel linked PS, where that of the second-step could be attributed to the PVL axle. It is apparently sound that the PS-linked wheel and PVL axle parts behave independent thermal degradation behaviors respectively even though they are ionically linked together as one macromolecular [2]rotaxane system. However, the results further inform that the thermal stability of the PS part is severely affected by the rotaxane wheel together with its counter anion. Considering a relatively high thermal stability of PVL-*rot*-PS-M, such large decrease in the stability of the ionically-fixed wheel linked with PS might be caused by the counter anion species.

PVL-*rot*-PS-M also shows a two-step degradation behavior (Figure 4.2c). However, the first-step degradation is significantly shifted to the higher temperature region and its temperature window becomes narrower; the later part of the first-step is further overlapped heavily with the second-step degradation. $T_{d,5}$ = 318 °C, which is higher than that of PVL-*rot*-PS-F but lower than those of PVL and PVL-*b*-PS; $T_{d,f}$ = 461 °C, which is same with that of PVL-*b*-PS (Table 4.1). The results collectively indicate that in the PVL-*rot*-PS-M, the PVL axle and the movable wheel linked with PS behave independent thermal degradation behaviors respectively. The slight decrease in the stability of the PS part is due to the chemically-bonded rotaxane wheel.

Overall, the thermal stability is in the increasing order PVL-*rot*-PS-F << PVL-*rot*-PS-M < PVL-*b*-PS.

Table 4.2. Phase transition characteristics of poly(δ-valerolactone)s (PVL) axle bearing fixed and movable rotaxane wheel (rot) and its polystyrene (PS) [a]

Polymer	Cooling run			Cold crystallization in heating run			Heating run		
	T_c [b] (°C)	$-\Delta H_{f,c}$ [c] (J/g)	$X_{c,c}$ [d] (%)	$T_{c,cold}$ [e] (°C)	$-\Delta H_{f,cold}$ [f] (J/g)	$X_{c,cold}$ [g] (°C)	T_m [h] (°C)	$\Delta H_{f,m}$ [i] (J/g)	$X_{c,m}$ [j] (%)
PVL-*b*-PS	9.1	24.5[k] (12.9)[l]	17.5[m] (9.3)[n]	-4.8	54.2 (28.6)	38.9 (20.5)	46.1	81.7 (43.1)	58.6 (30.9)
PVL-*rot*-PS-F	11.8	26.1 (12.5)	18.7 (9.0)	2.8	56.6 (27.1)	40.6 (19.4)	47.5	85.4 (40.9)	61.2 (29.3)
PVL-*rot*-PS-M	-2.3	80.6 (39.1)	57.8 (28.0)	-10.0	3.8 (1.8)	2.7 (1.3)	43.8	92.0 (44.6)	65.9 (42.0)

[a] Measured during cooling run with a rate of 10.0 °C/min from the melt state and subsequent heating run with a rate of 10.0 °C/min in DSC analysis. [b] Crystallization temperature at the maximum of exothermic heat of fusion peak occurred during cooling run. [c] Heat of fusion of crystallization occurred during cooling run. [d] Crystallinity estimated from the heat of fusion of crystallization by assuming that the ΔH_c° of PVL is same with that (–139.5 J/g) of poly(*ε*-caprolactone) (PCL).[34,35] [e] Cold crystallization temperature at the maximum of exothermic heat of fusion peak occurred during heating run. [f] Heat of fusion of cold crystallization occurred during heating run. [g] Crystallinity estimated from the heat of fusion of cold crystallization using $\Delta H_c^\circ = -139.5$ J/g. [h] Crystal melting temperature at the maximum of endothermic heat of fusion peak occurred during heating run. [i] Heat of fusion of crystal melting occurred during heating run. [j] Crystallinity estimated from the heat of fusion of crystal melting using $\Delta H_m^\circ = 139.5$ J/g. [k] Heat of fusion of only PVL component, which was estimated from that of the whole polymer sample using the weight fraction of PVL component. [l] Heat of fusion of whole polymer sample. [m] Calculated from the measured heat of fusion with respect to the weight of only PVL component in the sample. [n] Calculated from the measured heat of fusion with respect to the total weight of the polymer sample.

4.3.2 Phase Transition Behaviors

A PVL homopolymer (5190 $M_{\mathrm{n,NMR}}$; 3850 $M_{\mathrm{n,NMR}}$ for only PVL part excluded end groups) was found to exhibit a distinct, strong crystallization exothermic at 16.3 °C (= T_{c}, crystallization temperature) in a cooling run with 10.0 °C/min from melt (Figure 4.4b). PS (3850 $M_{\mathrm{n,NMR}}$) is estimated to have a glass transition temperature T_{g} of 77 °C from the data reported in the literature.[36] Considering these, one can expect that PVL-*b*-PS reveals distinct exothermic signals for the crystallization of PVL block and the glass transition of PS block when phase-separation occurs. However, such signals could not easily be discernible in a cooling run with 10.0 °C/min from the melt (140 °C) (Figure 4.3a). Instead, a very weak exothermic peak starts to show up at 58 °C (which is marked with the arrow "**1**") and then increases slightly with decreasing temperature until 23 °C (**2**). Thereafter, a discernible, but still weak exothermic peak appears in the range of 23 to –25 °C (**2→3**). An additional broad transition is observed over the range of –52 to –72 °C (**4→5**). These results collectively could provide important information as follows. Firstly, glass transition of the PS block could not be detected until cooled down to 58 °C, which is much lower than its T_{g}. This is an indication that the PS block is fully or substantially miscible with the PVL block in melt at >58 °C. Thus, the PS block could already lose opportunity to reveal a glass transition even when below 58 °C it is phase-separated and builds up of its own domains. Secondly, the weak, broad exothermic signals observed in the **1→2** period (i.e., 58→23 °C) would be a clue that phase-separation is initiated at 58 °C (= $T_{\mathrm{ps,onset}}$, the onset temperature of phase-separation) and then continued with further decreasing temperature in the cooling run. As a result, the individual blocks have chances to develop their own domains in a certain size as well as a certain level of population. Thirdly, the PVL block domains, which are being developed below $T_{\mathrm{ps,onset}}$, could experience degrees of supercooling enough to crystallize under continued cooling process. Therefore, the slightly enhanced exothermic signals in the **2→3** period (i.e., the range 23 to −25 °C) could be attributed to crystallization occurring in the PVL block domains; here, the crystallization temperature T_c is estimated to be 9.1 °C (which corresponds to the peak maximum) (Table 4.2). In this temperature region, the phase-separation would be also continued. However, such phase-separation could take place in kinetically slow manner, consequently allowed very limited crystallization in the resulting PVL block domains. Finally, considering the T_g of PVL homopolymer, the phase transition at the **4→5** period (i.e., the region −52 to −72 °C) could be assigned to the glass transition of PVL block. This transition is discernible, indicating that the phase-separation has taken place in a substantial quantity until getting into freezing, leading to that the resultant PVL block domains mainly remain amorphous.

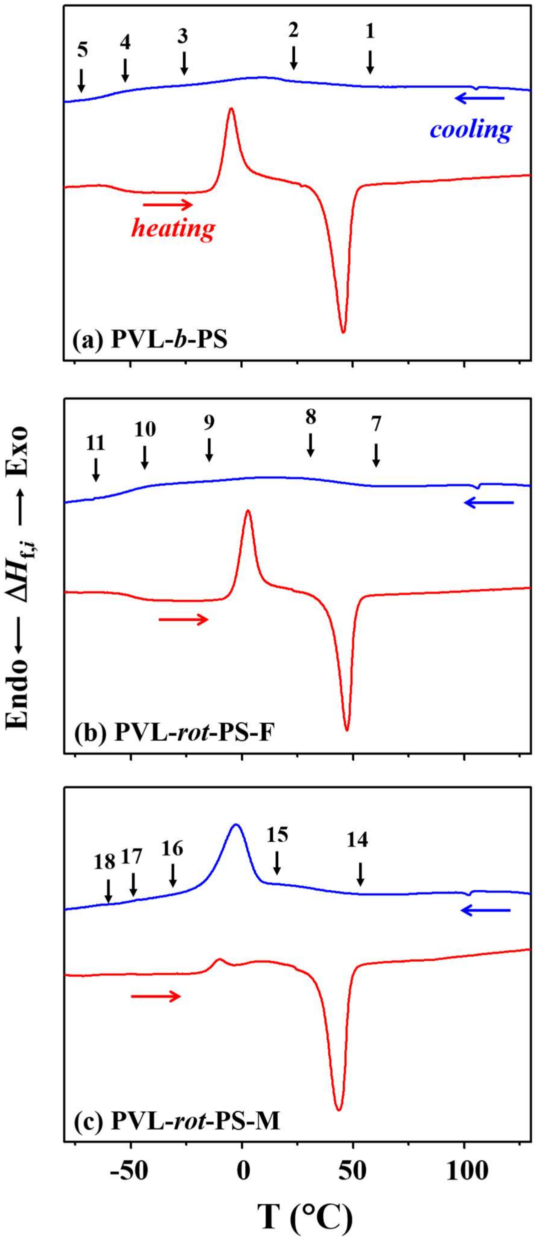

Figure 4.3. DSC thermograms of macromolecular [2]rotaxanes linked with a polystyrene, which were measured at a rate of 10.0 °C/min under nitrogen atmosphere. In the thermogram of each cooling run, the black colored arrows with numbers are the indications for the starting and ending points of phase transitions.

The crystallization exothermic peak of PVL block chains is found to be enhanced discernibly in the cooling run with a rate of 5.0 °C/min and more significantly with a cooling rate of 2.0 °C/min; T_c is determined to be 4.7 °C in the cooling run with 5.0 °C/min and 13.7 °C in the cooling run with 2.0 °C/min (Figure 4.5). All determined T_c values are much lower than that of PVL homopolymer in the cooling run with 10.0 °C/min. These low T_c values are clues for the presence of a time lag between the kinetics of phase-separation and PVL block chain crystallization. In fact, the crystallization of PVL block can be feasible only when its own domains are formed. Considering this point, PVL-*b*-PS should first undergo phase-separation kinetically in advance and then in resulting phase domains the PVL block chains could commence crystallization. Overall, the DSC results inform that in the cooling runs of PVL-*b*-PS, phase-separation tends to occur in advance and then followed by crystallization in the resulting PVL block domains. The results further confirm that slower cooling process could induce more significant level of phase-separation in PVL-*b*-PS in relatively higher temperature region, consequently leading to larger size of phase domains in which the PVL block chains commence crystallization more favorably.

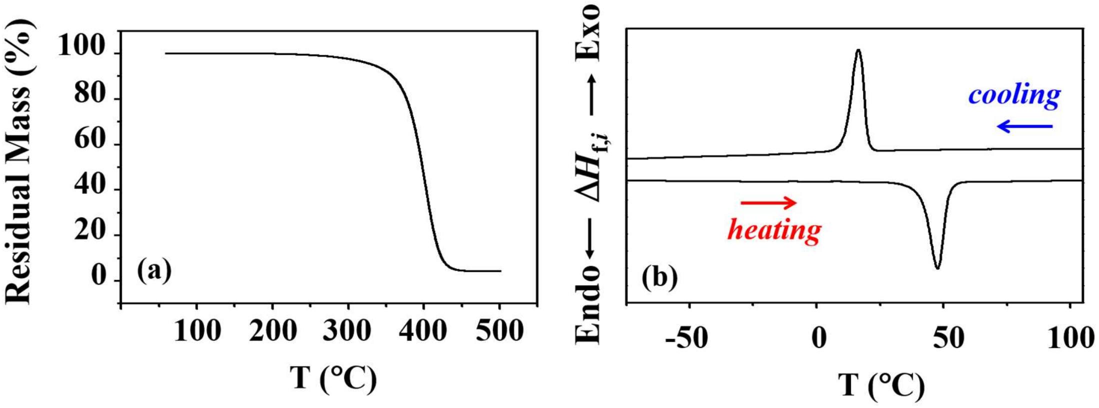

Figure 4.4. Thermograms of PVL homopolymer (5190 $M_{n,NMR}$; 3850 $M_{n,NMR}$ for only PVL part excluded end groups): (a) TGA thermogram; (b) DSC thermograms. All thermograms were measured at a rate of 10.0 °C/min under nitrogen atmosphere.

In the subsequent heating run after cooled with 10.0 °C/min (Figure 4.3a), PVL-*b*-PS clearly exhibits glass transition endothermic peak over the range of −60 to −46 °C. Furthermore, the block copolymer surprisingly shows a strong peak in the region of −14 to 13 °C, which is exothermic rather than endothermic although in heating run. These results indicate that the PVL block domains, which were formed in the cooling run from the melt, are mainly amorphous and thus could reveal glass transition distinctly over the region of −60 to −46 °C and further favorably undergo cold crystallization far above the T_g; the cold crystallization temperature $T_{c,cold}$ is measured to be −4.8 °C (Table 4.2). The appearances of such distinct glass transition and intensive cold crystallization confirm again that in the cooling run, PVL-*b*-PS underwent phase-separation substantially and, however, crystallization of the PVL block chains was highly suppressed.

Such cold crystallization is drastically reduced in the subsequent heating run after cooled with 5.0 °C/min; here $T_{c,cold} = -5.9$ °C. Furthermore, the cold crystallization is no longer observed in the heating run after cooled with 2.0 °C/min (Figure 4.5). In addition, it is very hard to observe signals for the glass transition of PVL block chains in such cooling runs and subsequent heating runs. These results collectively inform again that slower cooling process could cause phase-separation more substantially prior to the commencement of crystallization, producing larger sizes of domains which are necessary to enhance crystallization of the PVL block chains.

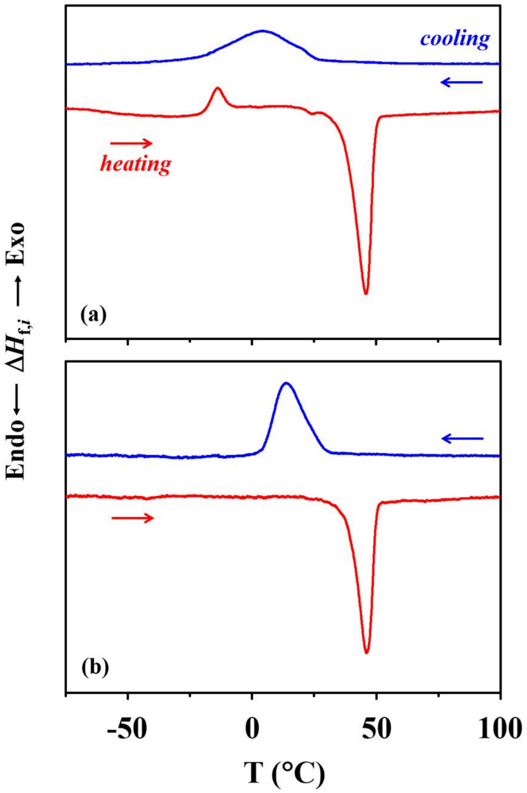

Figure 4.5. DSC thermograms of PVL-*b*-PS measured at two different rates: (a) 5.0 °C/min; (b) 2.0 °C/min. All measurements were conducted under nitrogen atmosphere.

The crystals in the PVL block domains, which were formed through cooling process as well as by cold crystallization in the subsequent heating run, are found to melt over the range of 25 to 60 °C; the melting temperature T_{m} is measured to be 46.1 °C for the 10.0 and 5.0 °C/min cooled samples and 46.0 °C for the 2.0 °C/min cooled sample.

Very similar thermograms are observed for PVL-*rot*-PS-F, as shown in Figures 4.3b and 4.6. The analysis results are compared with those of PVL-*b*-PS in Table 4.2. The results inform that the ionically-fixed PVL-*rot*-PS-F exhibit phase-separation and phase transition behaviors similar to the covalently-bonded PVL-*b*-PS; namely, the ionically-fixed rotaxane wheel linked with PS successfully mimics roles of the covalently-bonded PS in the block copolymer. However, some differences are still distinguished in the phase transition behaviors. PVL-*rot*-PS-F exhibits relatively higher cold crystallization temperature $T_{\mathrm{c,cold}}$, enthalpy

$\Delta H_{\mathrm{f,cold}}$ and crystallinity $X_{\mathrm{c,cold}}$ than those of PVL-*b*-PS. As a result, PVL-*rot*-PS-F shows higher crystal melting temperature T_{m}, enthalpy $\Delta H_{\mathrm{f,m}}$ and crystallinity $X_{\mathrm{c,m}}$, compared to those of PVL-*b*-PS. These results collectively suggest that PVL-*rot*-PS-F requires higher thermal energy to undergo phase-separation, which is necessary before crystallization of the PVL axle, compared to that needed for PVL-*b*-PS. Such higher thermal energy requirement would be attributed to the heavy rotaxane wheel. However, once phase-separation is proceeded, due to the bulkiness and flexibility the ionically-fixed wheel may additionally stimulate the PVL axle to mobilize in a certain level and thus crystallize more, consequently leading to larger enthalpy and crystallinity.

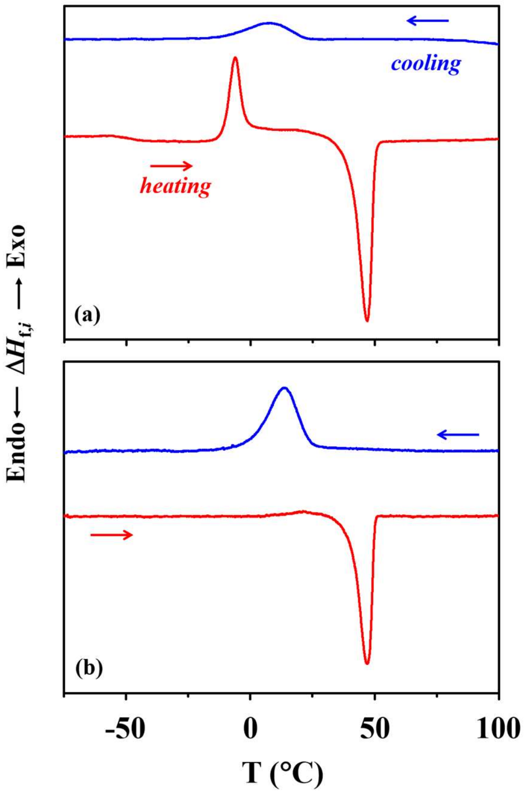

Figure 4.6. DSC thermograms of PVL-*rot*-PS-F measured at two different rates: (a) 5.0 °C/min; (b) 2.0 °C/min. All measurements were conducted under nitrogen atmosphere.

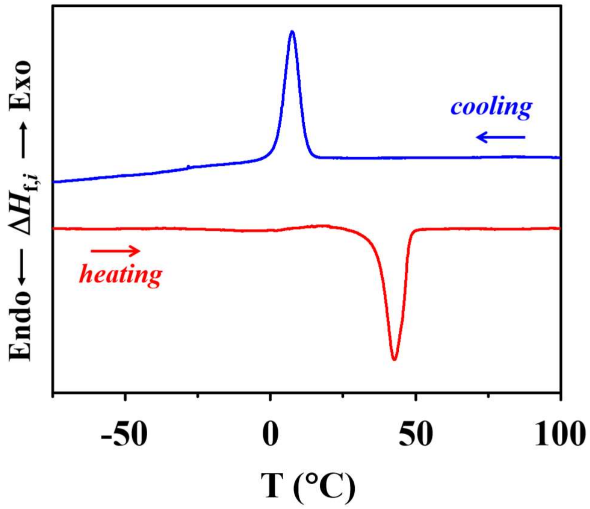

Figure 4.7. DSC thermograms of PVL-*rot*-PS-M measured at 5.0 °C/min under nitrogen atmosphere.

Interestingly, PVL-*rot*-PS-M, however, shows quite different features in DSC thermograms. The measured thermograms and analysis results are given in Figures 4.3c and 4.7, and Table 4.2. These results inform unique phase transition characteristics of PVL-*rot*-PS-M as follows. First, regarding relatively higher mobilities of the blocks due to their physical connection (i.e., mechanical connection), one can expect that PVL-*rot*-PS-M undergoes phase-separation more easily and thus reveals relatively narrower temperature window of miscibility, compared to the covalently-bonded and ionically-fixed systems. However, in the cooling run with 10.0 °C/min, phase-separation is found to begin around 53 °C (= $T_{\mathrm{ps,onset}}$, marked with the arrow "**14**"), which is 5 °C lower than those of PVL-*b*-PS and PVL-*rot*-PS-F. Namely, different from the expectation, PVL-*rot*-PS-M behaves relatively wider temperature window of miscibility, compared to PVL-*b*-PS and PVL-*rot*-PS-F. This interesting phase behavior would be attributed to the movable rotaxane wheel linked with PS that can translate along the PVL axle. In PVL-*rot*-PS-M, phase-separation process could be more feasible and pronounced when the PS-linked wheel translates to the ends of PVL axle. Such translational motion requires a certain amount of time, consequently causing a time lag in the phase-separation process; as a result, phase-separation process is retarded kinetically in cooling run, revealing low $T_{ps,onset}$. Second, a crystallization exothermic peak of the PVL axle appears strongly over the range of 15 to −31 °C (**15→16** period) even in a cooling run with 10.0 °C/min and further becomes much stronger in slower cooling run (5.0 °C/min). T_c is determined to be −2.3 °C in the cooling run with 10.0 °C/min and 7.5 °C in the cooling run with 5.0 °C/min. These T_c values are much lower than the $T_{ps,onset}$. Moreover, the T_c values are lower than those of PVL-*b*-PS and PVL-*rot*-PS-F. These results inform that the phase-separation process below $T_{ps,onset}$ still need a time to build up of PVL axle phase domains larger than a certain size which can induce crystallization of the axle chains, because of accompanying the PS-linked wheels in sliding motion along the axle chains; and then followed by crystallization within the resulting PVL axle domains. On the other hand, the PVL axle inherently experiences freedom in part from the PS-linked rotaxane wheel, because of the physical or mechanical connectivity, revealing relatively high mobility. Thus, the PVL axle needs relatively higher degrees of supercooling to crystallize. This is a clue for how the PVL axle domains could demonstrate a significant quantity of crystallization even under the conditions with high degrees of supercooling caused by the slow phase-separation process in cooling run. Third, the glass transition of PVL axle appears very weakly over the region −49 to −60 °C (**17→18** period) in the cooling run with 10.0 °C/min but could not be discernible in the cooling run with 5.0 °C/min. These data support that the PVL axle domains, which are being formed in cooling run, undergo crystallization substantially; the PVL axle domains crystallize more substantially in slower cooling run. As a result, uncrystallized PVL axles remain in a low fraction and so could reveal very weak or no glass transition. Fourth, in subsequent heating runs no glass transition could be observed for the samples cooled with and 10.0 and 5.0 °C/min. In addition, a cold crystallization peak is observed weakly for the sample cooled with 10.0 °C/min but no longer discernible for the sample cooled with 5.0 °C/min. These results confirm again that a significant level of crystallization has taken place in the PVL axle domains in the cooling runs and, therefore, a small fraction of PVL axles remained amorphous. Fifth, $T_{c,cold} = -10.0$ °C, which is determined from the subsequent heating run of the sample cooled at 10.0 °C/min. This $T_{c,cold}$ is lower than those of PVL-*b*-PS and PVL-*rot*-PS-F. This low $T_{c,cold}$ again confirms that the movable wheel with PS could mobilize PVL axle chains properly and accelerate their crystallization even in low temperature condition. Finally, $T_m = 43.8$ °C, which is slightly lower than those (47.5 and 46.1 °C) of PVL-*b*-PS and PVL-*rot*-PS-F and that (47.7 °C) of PVL homopolymer. The low T_m could be correlated to the low T_c in the cooling run as well as the low $T_{c,cold}$ in the subsequent heating run. Namely, the low T_m could be originated mainly from the slightly thinner crystals formed with relatively higher degrees of supercooling via cooling run and subsequent heating run. In addition, the low T_m could be further attributed in part to the slightly thinner crystals formed with the PVL axle chains in which the movable wheel is located a little far from the axle chain ends. However, $\Delta H_{f,m} = 92.0$ J/g and $X_{c,m} = 65.9$ %, which are relatively larger than those of PVL-*b*-PS and PVL-*rot*-PS-F. These indicate that the movable wheel with linked with PS could encourage the PVL axle to crystalize more via stimulating chain mobility, but cause a little reduction in the crystal size and/or some defects on the crystal surface.

4.3.3 Thin Film Morphologies

For all polymers, nanoscale films have been prepared with a thickness of 110−130 nm and subjected to synchrotron GISAXS analysis. The as-cast film of PVL-*b*-PS reveals a broad scattering peak around 0.400° along the meridian line in the 2D GISAXS image (Figures 4.8a). Such peak broadness would be attributed to the heavy overlap between the scattering features along the meridian line which were generated by the reflected and transmitted X-ray beams. This kind of scattering peaks are one of the typical characteristics from horizontal lamellar structure. Considering this information together with almost equal volume fractions of the blocks, the scattering data was analyzed using possible structural models. As a result, a three-phase lamellar structure model is found suitable for analyzing the scattering data. The out-of-plane and in-plane scattering profiles, which are extracted from the 2D scattering image, could be satisfactorily analyzed using a GISAXS formula of three-phase lamellar structure model, as shown in Figures 4.8g and 4.8j; a detail of the GIXS formula is given in Section 1.4 of Chapter 1. In addition, an azimuthal scattering profile of the scattering peak at 0.400° is extracted and then successfully analyzed in order to get information on the structural orientation (Figures 4.8m). In similar manner, 2D GISAXS images of the as-cast films of PVL-*rot*-PS-F and PVL-*rot*-PS-M could be analyzed satisfactorily with three-phase lamellar structural models, as shown in Figure 4.8. Furthermore, these analysis schemes have been successfully extended for the scattering patterns measured for the THF-annealed polymer films (Figure 4.9). These analyses find that all polymers form lamellar structures in the nanoscale films. All obtained structural parameters are summarized in Table 4.3. From the obtained parameters, simulated 2D GISAXS scattering images were regenerated. As presented in Figures 4.8d-f and 4.9d-f, the reconstructed scattering images are in good agreement with the measured patterns, confirming that the scattering data have been analyzed successfully.

Table 4.3. Morphological structural parameters of nanoscale films of PVL-*b*-PS, PVL-*rot*-PS-F, and PVL-*rot*-PS-M determined by quantitative GISAXS analysis

Polymer system	PVL-*b*-PS		PVL-*rot*-PS-F		PVL-*rot*-PS-M	
Phase-separated nanostructure	horizontal lamella	vertical lamella	horizontal lamella	vertical lamella	horizontal lamella	vertical lamella
As-cast film						
ϕ_{L} [a] (%)	90.3	9.7	90.8	9.2	100	
Parameters						
D_{L} [b] (nm)	15.7	14.2	15.4	14.5	11.3	
d_{PVL} [c] (nm)	6.0	5.4	4.0	4.5	3.5	
d_{i} [d] (nm)	2.0	1.6	3.6	2.3	2.0	
d_{PS} [e] (nm)	5.7	5.6	4.2	5.1	3.8	
σ_{PVL} [f] (nm)	0.4	0.6	1.1	1.0	0.6	
σ_{i} [g] (nm)	0.6	0.8	0.6	0.9	0.8	
g [h]	0.27	0.45	0.39	0.48	0.45	
$\bar{\varphi}_1$ [i] (deg.)	0	85.3	0	86.4	0.2	
σ_{φ_1} [j] (deg.)	8.8	2.0	8.5	2.3	7.3	
$O_{\mathrm{s},1}$ [k]	0.838	-0.479	0.845	-0.478	0.885	
THF-annealed film						
ϕ_{L} (%)	97.8	2.2	96.4	3.6	100	
Parameters						
D_{L} (nm)	15.0	14.0	14.0	15.3	11.8	
d_{PVL} (nm)	3.9	4.6	4.8	4.3	3.5	
d_{i} (nm)	3.6	2.5	2.3	3.3	2.2	
d_{PS} (nm)	3.9	4.4	4.6	4.4	3.7	
σ_{PVL} (nm)	1.0	1.0	0.8	1.2	0.8	
σ_{i} (nm)	1.2	1.3	1.3	1.7	1.1	
g	0.37	0.48	0.43	0.51	0.39	
$\bar{\varphi}_1$ (deg.)	1.0	88.4	1.0	86.8	1.2	
σ_{φ_1} (deg.)	9.4	2.2	10.8	2.0	9.0	
$O_{\mathrm{s},1}$	0.819	-0.486	0.770	-0.430	0.826	

[a] Volume fraction of lamellar structure in either horizontal or vertical orientation determined by the analysis of azimuthal scattering profiles. [b] Long period of lamellar structure. [c] Thickness of PVL layer in the phase separated lamellar structure. [d] Thickness of interfacial layer between PVL and PS layers. [e] Thickness of PS layer. [f] Standard deviation for the PVL layer in lamellar structure. [g] Standard deviation for the interfacial layer in lamellar structure. [h] Paracrystal distortion factor along the direction parallel to the long period of lamellar structure. [i] Mean value of the polar angle φ_1 (i.e., orientation angle) between the orientation vector $\boldsymbol{n}_1$ (which is set parallel to the axis of the long period of lamellar structure) and the out-of-plane direction of the film. [j] Standard deviation for the orientation angle φ_1 of lamellar structure. [k] Second order orientation factor.

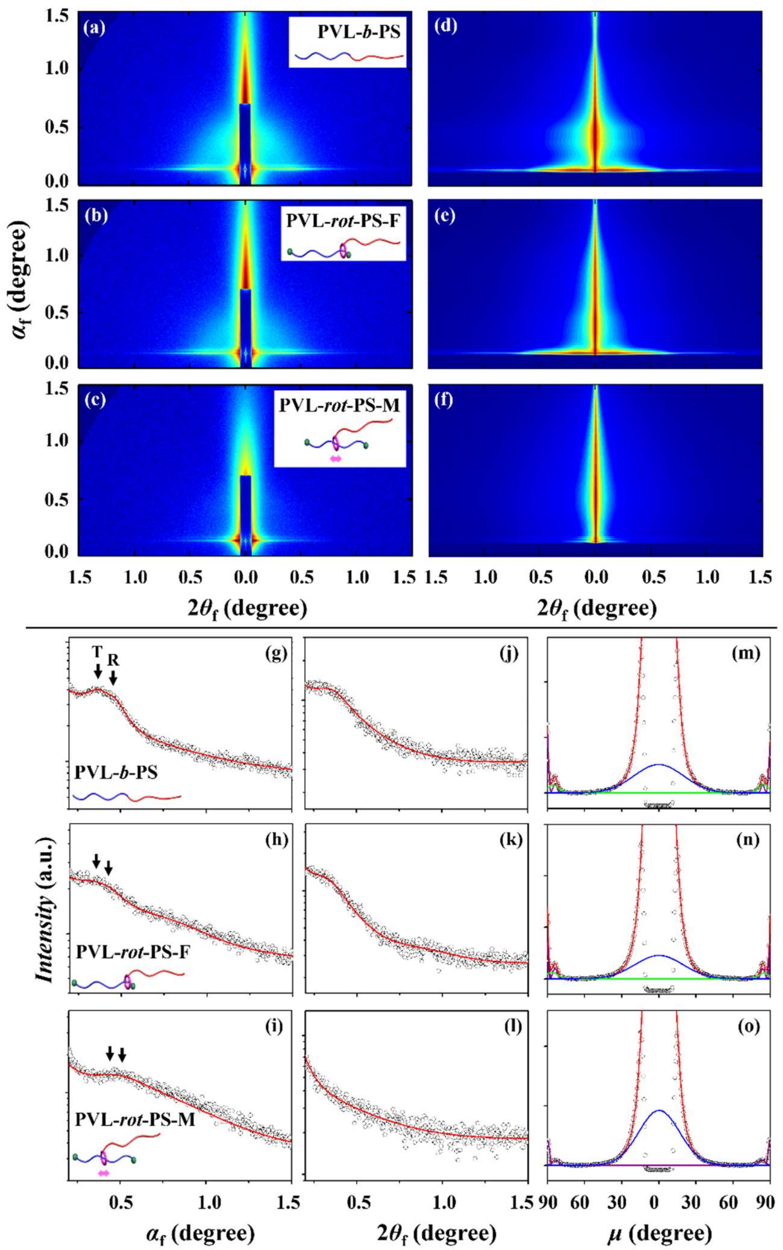

Figure 4.8. Representative GISAXS data of the as-cast films (110-130 nm thick) of PVL-*b*-PS, PVL-*rot*-PS-F, and PVL-*rot*-PS-M measured with a sample-to-detector distance (SDD) of 2824 mm using a synchrotron X-ray beam (λ = 0.12096 nm). PVL-*b*-PS: (a) 2D scattering image measured with of α_i = 0.138°; (d) 2D image reconstructed from the structural parameters in Table 4.3 using the GIXS formula; (g) out-of-plane scattering profile extracted along the meridian line at $2\theta_f$ = 0.123°; (j) in-plane scattering profile extracted along the equatorial line at α_f = 0.218°; (m) azimuthal scattering profile of the first-order lamellar peak at 0.400°. PVL-*rot*-PS-F: (b) 2D scattering image measured with of α_i = 0.137°; (e) 2D image reconstructed from the structural parameters in Table 4.3 using the GIXS formula; (h) out-of-plane scattering profile extracted along the meridian line at $2\theta_f$ = 0.139°; (k) in-plane scattering profile extracted along the equatorial line at α_f = 0.210°; (n) azimuthal scattering profile of the first-order lamellar peak at 0.373°. PVL-*rot*-PS-M: (c) 2D scattering image measured with of α_i = 0.137°; (f) 2D image reconstructed from the structural parameters in Table 3 using the GIXS formula; (i) out-of-plane scattering profile extracted along the meridian line at $2\theta_f$ = 0.058°; (l) in-plane scattering profile

extracted along the equatorial line at α_f = 0.200°; (o) azimuthal scattering profile of the first-order lamellar peak at 0.520°. In (g–l), the symbols are the measured data and the solid lines were obtained by fitting the data using the GIXS formula of lamellar structure model; the scattering peak generated by the transmitted X-ray beam, is marked with "**T**", whereas that generated by the reflected X-ray beam is marked with "**R**". In (m–o), the symbols are the measured data and the sold lines were obtained by fitting the data using the Gaussian functions.

Interestingly, the as-cast PVL-*b*-PS film is characterized by forming lamellar structure domains in two distinct orientations: horizontal and vertical structures. The horizontal lamellar structure is present as the major structural component ($\phi_{L,h}$ = 90.3%, relative volume fraction), whereas the vertical lamellar structure is found as the minor component ($\phi_{L,v}$ = 9.7%). The horizontal structure is determined to have an orientational factor $O_{s,1}$ of 0.838 ($\overline{\varphi_1}$ = 0°, mean polar (i.e., orientation) angle between the orientation vector n_1 (which is set parallel to the direction of lamellar stacks) and the out-of-plane direction of the film; σ_{φ_1} = 8.8°, standard deviation of polar angle) and a paracrystal distortion factor g (= g_{33}) of 0.27 (this factor along the direction of lamellar stacks). The vertical structure reveals $O_{s,1}$ = –0.479 ($\overline{\varphi_1}$ = 85.3° and σ_{φ_1} = 2.0°) and g = 0.45. These g values suggest that the horizontal lamellar structure is more stable than the vertical one. The lamellar structures are determined to have a long period D_L of 14.2 to 15.7 nm which is composed of a dense PVL block layer d_{PVL} (5.4–6.0 nm), a less dense PS block layer d_{PS} (5.6–5.7 nm), and an interfacial layer d_i (1.6–2.0 nm).

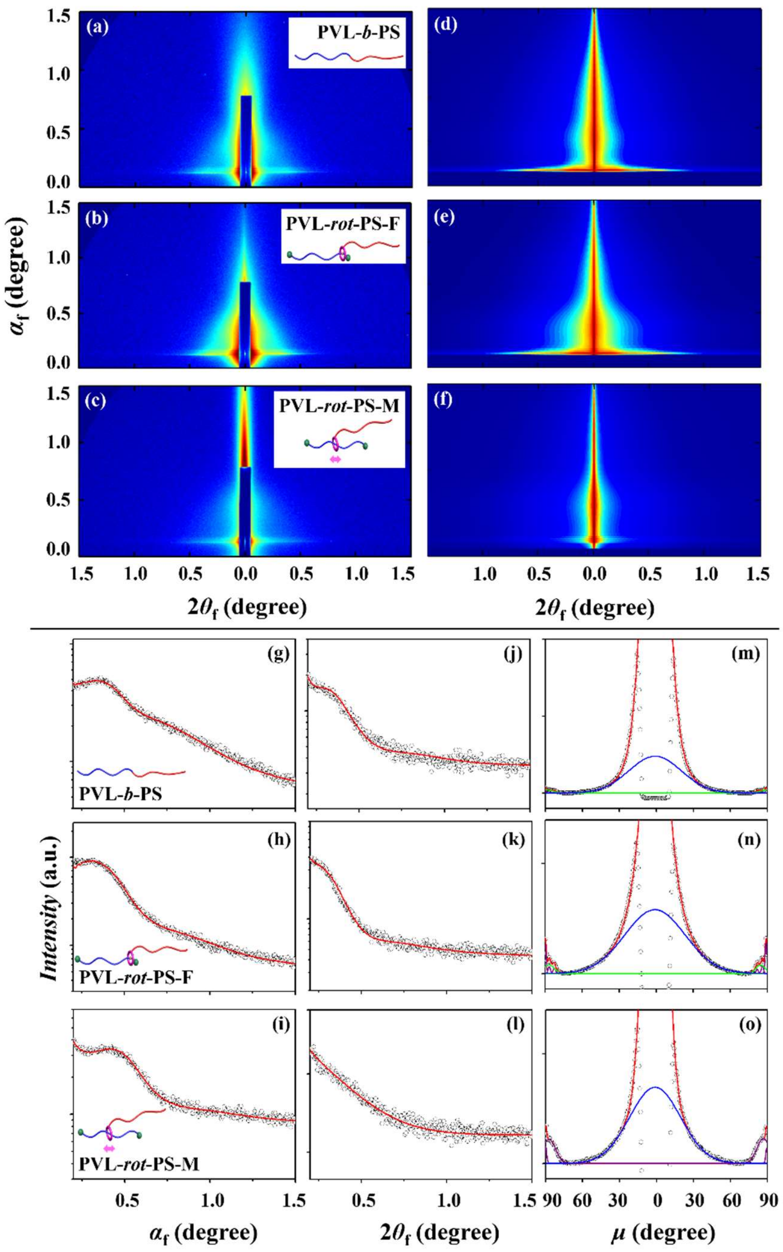

Figure 4.9. Representative GISAXS data of the THF-annealed films (110-130 nm thick) of PVL-*b*-PS, PVL-*rot*-PS-F, and PVL-*rot*-PS-M measured with a sample-to-detector distance (SDD) of 2910 mm using a synchrotron X-ray beam (λ = 0.12096 nm). PVL-*b*-PS: (a) 2D scattering image measured with of α_i = 0.133°; (d) 2D image reconstructed from the structural parameters in Table 4.3 using the GIXS formula; (g) out-of-plane scattering profile extracted along the meridian line at $2\theta_f$ = 0.123°; (j) in-plane scattering profile extracted along the equatorial line at α_f = 0.198°; (m) azimuthal scattering profile of the first-order lamellar peak at 0.371°. PVL-*rot*-PS-F: (b) 2D scattering image measured with of α_i = 0.134°; (e) 2D image reconstructed from the structural parameters in Table 4.3 using the GIXS formula; (h) out-of-plane scattering profile extracted along the meridian line at $2\theta_f$ = 0.123°; (k) in-plane scattering profile extracted along the equatorial line at α_f = 0.198°; (n) azimuthal scattering profile of the first-order lamellar peak at 0.357°. PVL-*rot*-PS-M: (c) 2D scattering image measured with of α_i = 0.131°; (f) 2D image reconstructed from the structural parameters in Table 3 using the GIXS formula; (i) out-of-plane scattering profile extracted along the meridian line at $2\theta_f$ = 0.107°; (l) in-plane scattering

profile extracted along the equatorial line at α_f = 0.238°; (o) azimuthal scattering profile of the first-order lamellar peak at 0.520°. In (g–l), the symbols are the measured data and the solid lines were obtained by fitting the data using the GIXS formula of lamellar structure model. In (m–o), the symbols are the measured data and the sold lines were obtained by fitting the data using the Gaussian functions.

The as-cast PVL-*rot*-PS-F film is also characterized by forming lamellar structures in a mixture of horizontal and vertical orientations. The most of structural parameters are close to those of the PVL-*b*-PS film. However, the d_{PVL} and d_{PS} values are smaller, whereas the d_i value is larger, compared to those of the PVL-*b*-PS film. Considering the connectivity of PVL axle and PS block, such structural parameter variations could be attributed to the ionically-fixed rotaxane wheel. These results are clues that the bulky rotaxane wheel is mainly located in the interfacial layer and further causes thinning in both the PVL axle and PS layers.

In contrast, the as-cast PVL-*rot*-PS-M film reveals quite different structural features. Surprisingly PVL-*rot*-PS-M is found to form only horizontal lamellar structure. The horizontal lamellar structure is characterized by having relatively smaller long period and, thinner PVL axle and PS layers, compared to those of the PVL-*b*-PS and PVL-*rot*-PS-F films. However, the interfacial layer thickness is comparable with that of the PVL-*b*-PS film. These results collectively inform that the movable rotaxane wheel linker plays key roles to induce the formation of only uniorientational lamellar structure through phase-separation and form narrow interface between the PVL axle and PS layer even though the bulkiness.

The nanoscale film morphologies are further influenced in some aspects by THF-annealing process. After the solvent annealing, the PVL-*b*-PS film reveals significantly enhanced population of horizontal lamellar structure accompanied with shortened long period, thinned PVL and PS block layers, and thickened interfacial layer. The solvent-annealed PVL-*rot*-PS-F film also exhibits highly enhanced population of horizontal lamellar structure with shortened long period and thinned PVL axle and PS layers. Interestingly the interfacial layer, however, becomes thinner. This is a clue that the rotaxane linker can make a certain level of positive impact for the phase-separated PVL axle and PS layers to form narrower or sharper interface via the THF-annealing process, although it owns ionic linking nature and bulkiness. This positive effect may be attributed to a certain level of flexibility of the rotaxane wheel based on crown ether ring and ionic linking character which can mobile both the PVL axle and PS chains.

Quite different from the polymers above, the PVL-*rot*-PS-M film is found to well maintain horizontal lamellar structure in 100 % population and furthermore show very little variations on the structural parameters throughout the THF-annealing process. These results collectively suggest that the movable rotaxane wheel linker could play a great role to mobilize the PVL axle and PS block chains enough which is necessary for phase-separation in kinetically-favorable manner. Due to the movable rotaxane wheel, the phase-separation has taken place fully in the film through the polymer solution cast and subsequent drying process. Thus, the obtained film morphology could not be improved discernibly by the post solvent annealing process. It is additionally noted that due to the remarkable role of movable rotaxane wheel linker, the lamellar structure in the PVL-*rot*-PS-M film could build up of sharper interface between the PVL axle and PS layers, compared to those of the PVL-*b*-PS and PVL-*rot*-PS-F films.

Overall, all polymer systems of this study tend to do phase-separation due to an inherent immiscibility of the PVL and PS components as well as a high self-assembling (i.e., crystallization) nature of the PVL component, forming lamellar structures. However, the phase-separation behaviors, as well as the structural parameters including orientation and distortion factors, are different depending upon the connection natures of PVL and PS components. In particular, the mechanically movable connection using rotaxane wheel is most powerful to enhance mobilities of the PVL and PS components significantly and further help their phase-separation more feasible kinetically, consequently leading to a very unique structure, namely only horizontally-oriented and better-defined lamellar structure in nanoscale films.

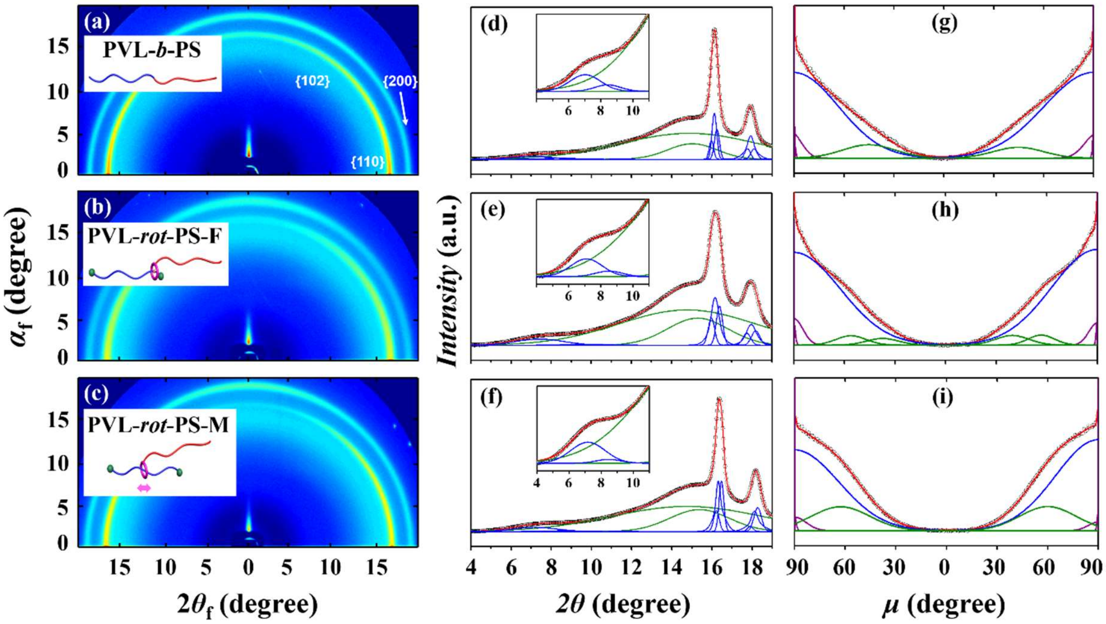

Figure 4.10. Representative GIWAXS patterns of the as-cast films (110-130 nm thick) of PVL-*b*-PS, PVL-*rot*-PS-F, and PVL-*rot*-PS-M films measured with α_i = 0.174° at SDD = 209 mm using a synchrotron X-ray beam (λ = 0.12096 nm). PVL-*b*-PS: (a) 2D scattering image; (d) 1D scattering profile averaged quadrantly from the 2D image in (a); (g) azimuthal scattering profile of the {110} peak. PVL-*rot*-PS-F: (b) 2D scattering image; (e) 1D scattering profile averaged quadrantly from the 2D image in (b); (h) azimuthal scattering profile of the {110} peak. PVL-*rot*-PS-M: (c) 2D scattering image; 1D scattering profile averaged quadrantly from the 2D image in (c); (i) azimuthal scattering profile of the {110} peak.

Table 4.4. Crystalline structural parameters of PVL layers in the lamellar structures formed in nanoscale films of PVL-*b*-PS, PVL-*rot*-PS-F, and PVL-*rot*-PS-M determined by quantitative GIWAXS analysis

Polymer	PVL-*b*-PS		PVL-*rot*-PS-F		PVL-*rot*-PS-M	
	As-cast film	THF-annealed film	As-cast film	THF-annealed film	As-cast film	THF-annealed film
Nanostructure in the PVL layer	Fringed-micelle like structure		Fringed-micelle like structure		Fringed-micelle like structure	
Crystal lattice structure in the PVL layer	Orthorhombic lattice; unit dimensions: $a = 0.787$ nm, $b = 0.525$ nm, $c = 1.876$ nm, $\alpha = \beta = \gamma = 90°$					
<u>*Orientational domain* A</u>						
$\bar{\varphi}_2$[a] (deg.)	0	0	0	0	0	0
σ_{φ_2}[b] (deg.)	11.8	10.5	12.3	9.8	11.5	7.8
$O_{s,2}$[c]	0.713	0.771	0.727	0.799	0.752	0.864
$\phi_{v,2}$[d] (%)	86.5	95.4	88.7	93.1	74.0	76.6
<u>*Orientational domain* B</u>						
$\bar{\varphi}_3$ (deg.)	45.0	37.6	34.0	31.0	27.2	29.7
σ_{φ_3} (deg.)	16.0	4.9	4.0	3.5	7.5	5.3
$O_{s,3}$	0.248	0.453	0.527	0.588	0.571	0.598
$\phi_{tilt,3}$ (%)	13.5	4.6	5.7	5.3	26.0	23.4
<u>*Orientational domain* C</u>						
$\bar{\varphi}_4$ (deg.)			52.5	43.1		
σ_{φ_4} (deg.)			4.3	3.4		
$O_{s,4}$			0.095	0.305		
$\phi_{tilt,4}$ (%)			5.6	1.6		
<u>*Rotational domain* I</u>						
ω_I[e] (deg.)	0	0	0	0	0	0
ϕ_I[f] (%)	18.2	17.1	20.2	16.0	15.8	21.4
<u>*Rotational domain* II</u>						
ω_{II} (deg.)	7.8	10.3	8.7	7.8	6.8	9.5
ϕ_{II} (%)	48.4	58.7	52.0	61.2	51.3	61.8
<u>*Rotational domain* III</u>						
ω_{III} (deg.)	10.3	14.0	12.9	11.0	10.4	12.9
ϕ_{III} (%)	33.4	24.2	27.8	22.8	32.9	16.8
$X_{c,GIWAXS}$[g] (%)	48.9 [h]	54.6	49.2	65.1	51.1	50.18
	(24.0) [i]	(26.8)	(21.7)	(28.7)	(22.6)	(22.2)

[a] Mean value of the polar angle φ_i (i.e., orientation angle) between the orientation vector $\boldsymbol{n}_i$ (which is set along a direction normal to the {110} plane stacks (namely, parallel to the *c*-axis of orthorhombic lattice unit cell)) and the out-of-plane direction of the film. [b] Standard deviation for the polar angle φ_i. [c] Second order orientation factor of orthorhombic crystal lattice. [d] Volume fraction of orthorhombic crystals with $\bar{\varphi}_i$ (i.e., a preferred direction *i*). [e] Rotational angle of orthorhombic crystals where the rotational axis is parallel to a

normal direction to the film plane. [f]Relative volume fraction of orthorhombic crystals with rotational angle ω_i where the rotational axis is parallel to a normal direction to the film plane. [g]Crystallinity determined by the analysis of from GIWAXS data. [h]Crystallinity of only PVL component determined by the analysis of GIWAXS data using the volume fraction of only PVL component. [i]Crystallinity of the whole polymer (which includes PVL and all other components) determined by the analysis of from GIWAXS data.

To get more information on the crystallizable PVL layer in the lamellar structure, synchrotron GIWAXS analysis has been carried for all polymers above. Representatives and analysis results of the measured GIWAXS images are presented in Figures 4.10 and 4.11. The as-cast PVL-*b*-PS film depicts two anisotropic scattering rings at 16.13° and 17.92° in addition to a weak, broad amorphous halo peak centered at 15.00°; another scattering peak appears very weakly at 7.65°. Similar scattering patterns are observed for the as-cast PVL-*rot*-PS-F and PVL-*rot*-PS-F films and for the THF-annealed films. Here it is additionally noted that the scattering spot at 7.65° becomes stronger in the THF-annealed films. Taking into account the crystallizability of PVL homopolymer and the amorphous characteristics of PS homopolymer, such three distinct scattering peaks could be generated by the crystals of the PVL components in the individual films. PVL is known to self-assemble in orthorhombic crystal lattice.[37] Based on the orthorhombic lattice, these scattering peaks could be assigned as {102}, {110} and {200} reflections, respectively. From these scattering peaks, the crystal lattice parameters are determined. For each film, the crystallinity $X_{\mathrm{c,GIWAXS}}$ of the PVL layer could be estimated from the integrals of the crystalline and amorphous scattering peaks deconvolued from the quadrant-averaged scattering profile which has been obtained from the 2D GIWAXS image. The orientations of orthorhombic crystals are estimated by analyzing the azimuthal scattering profile of {110} scattering peak obtained from the 2D scattering image; as a result, the crystals are found to be present as two or three different orientational domains. In addition, the PVL crystals are determined to have three different rotational domains from the deconvoluted {110} peaks and their integrals. The analysis results are summarized in Table 4.4. These GIWAXS analyses provide key structural features below.

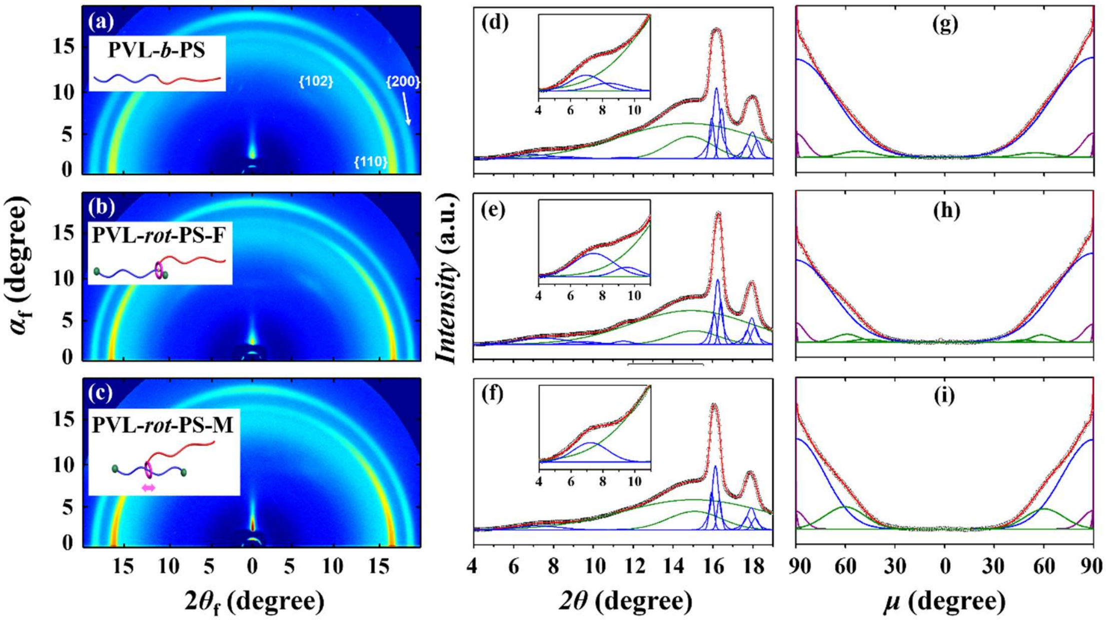

Figure 4.11. Representative GIWAXS patterns of the THF-annealed films (110-130 nm thick) of PVL-*b*-PS, PVL-*rot*-PS-F, and PVL-*rot*-PS-M films measured with α_i = 0.174° at SDD = 209 mm using a synchrotron X-ray beam (λ = 0.1209 nm). PVL-*b*-PS: (a) 2D scattering image; (d) 1D scattering profile averaged quadrantly from the 2D image in (a); (g) azimuthal scattering profile of the {110} peak. PVL-*rot*-PS-F: (b) 2D scattering image; (e) 1D scattering profile averaged quadrantly from the 2D image in (b); (h) azimuthal scattering profile of the {110} peak. PVL-*rot*-PS-M: (c) 2D scattering image; 1D scattering profile averaged quadrantly from the 2D image in (c); (i) azimuthal scattering profile of the {110} peak.

First, The PVL layers in the lamellar structures are characterized to form orthorhombic crystals which have a lattice dimension of a = 0.787 nm, b = 0.525 nm, c = 1.876 nm, and $\alpha = \beta = \gamma$ = 90°, regardless of the polymer systems and their as-cast and THF-annealed films.

Second, for the as-cast PVL-*b*-PS film, the PVL layer is determined to form two different orientational crystal domains: (i) vertically-oriented orthorhombic crystal domain (type **A**, $\phi_{v,2}$ = 86.5 %, relative volume fraction) and (ii) 45.0°-tilted orthorhombic crystal domain (type **B**, $\phi_{tilt,3}$ = 13.5 %) (Figure 4.12). Differently, the as-cast PVL-*rot*-PS-F film forms three types of orientational crystal domains in the PVL axle layers: (i) **A**-type crystal domain ($\phi_{\mathrm{v},2}$ = 788.7 %), (ii) **B**-type crystal domain (tilt angle = 34.0°; $\phi_{\mathrm{tilt},3}$ = 5.7 %), and (iii) **C**-type crystal domain (tilt angle = 52.5°; $\phi_{\mathrm{tilt},4}$ = 5.6 %). The as-cast PVL-*rot*-PS-M film forms two types of orientational crystal domains in the PVL axle layers: (i) **A**-type crystal domain ($\phi_{\mathrm{v},2}$ = 74.0 %) and (ii) **B**-type crystal domain (tilt angle = 27.2°; $\phi_{\mathrm{tilt},3}$ = 26.0 %). Overall, in each polymer film the vertically-orientated crystal domain is formed in the PVL layers as the major component. These PVL crystal domains are retained through the THF-annealing process (Figure 4.13). But, the THF-annealing process is found to improve the population of vertically-oriented crystal domain in each polymer film and, instead, suppress the population(s) of tilted crystal domain(s) and decrease or increase its or their tilt angle(s).

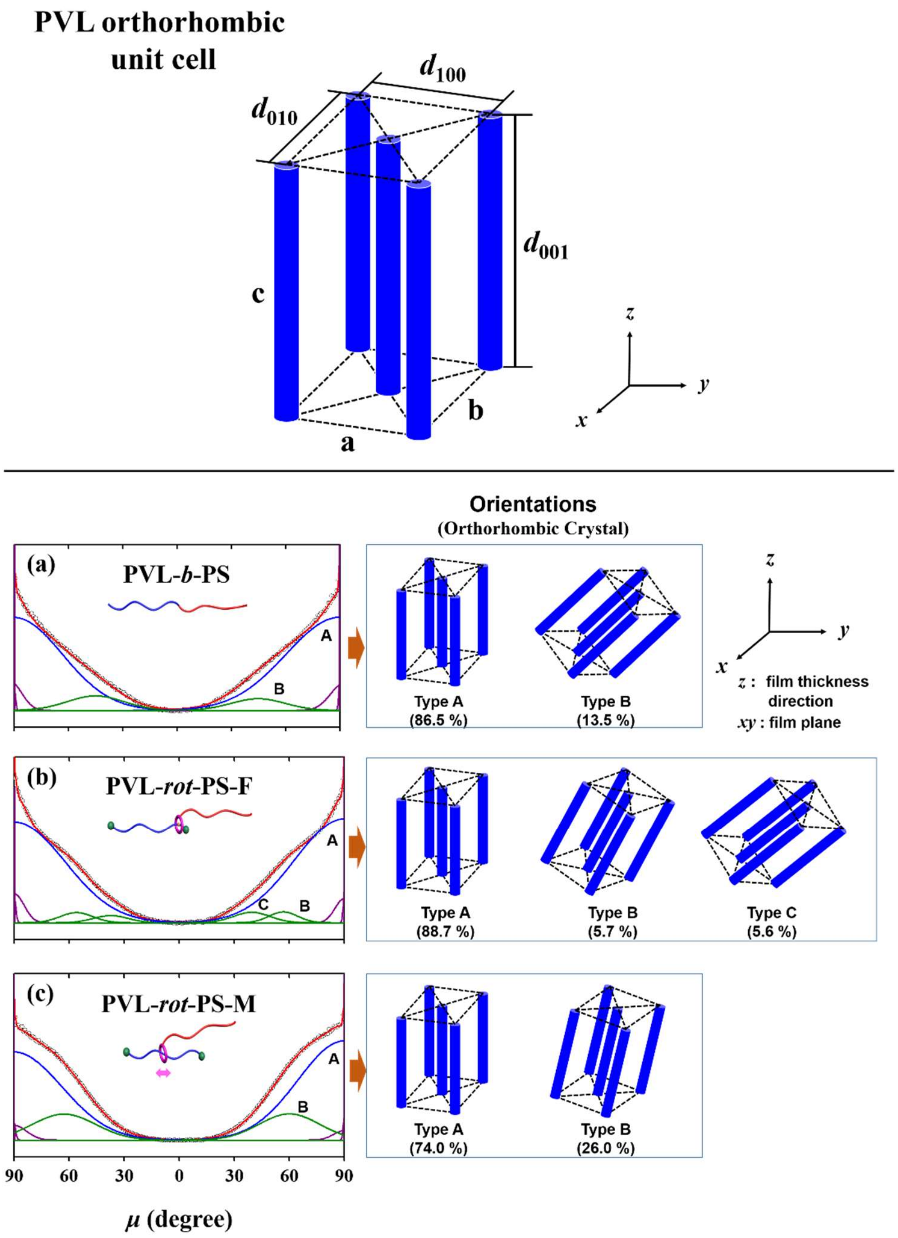

Figure 4.12. 3D schematic of orthorhombic unit cell of PVL crystal and azimuthal scattering profiles and analysis results of the {110} peaks of PVL crystals in Figure 4.10 and orientational crystal domains: (a) as-cast PVL-*b*-PS film; (b) as-cast PVL-*rot*-PS-F film; (c) as-cast PVL-*rot*-PS-M film.

Third, vertically-oriented orthorhombic crystals are mainly formed in the individual PVL layers in the horizontal lamellar structure which is predominantly formed in each polymer film, regardless of the as-cast and THF-annealing processes. Namely, the *c*-axis in the majority (90.3–100 %) of orthorhombic crystal domains is parallel to the thickness direction of the PVL layer in the horizontal PVL/PS lamellar structure. The *c* value (= 1.876 nm, one of the crystal lattice parameter) is close to the length (2.204 nm) of three repeat units in a fully extended conformation. The *c* value corresponds to about one third or a half of the PVL layer thickness (d_{PVL} = 3.5–6.0 nm). Thus, one expects that the PVL block or axle chains may form folded-crystals (i.e., lamellae) in the PVL layer phase. However, in nanoscale film of a similar thickness (110-130 nm) PVL hompolymer tends to strongly form horizontal lamellar structure with 9.6 long period (= 3.2 nm (crystalline layer) + 2.4 nm (amorphous layer) + 2 x 2.0 nm (interfacial layer)). The d_{PVL} values are only 1.1 to 1.9 times larger than the crystal layer thickness (3.2 nm) but 1.6 to 2.7 times smaller than the long period (9.6 nm) of lamellar crystals formed in PVL hompolymer film. Taking these facts into account, the PVL layer thicknesses in the lamellar structures of PVL-*b*-PS, PVL-*rot*-PS-F and PVL-*rot*-PS-M films could not provide enough spaces for folded-crystal formations. Due to such severe confined geometry, the PVL block or PVL axle chains could make only *fringed-micelle like crystals* rather than folded-crystals in the PVL layers of PVL/PS lamellar structure.

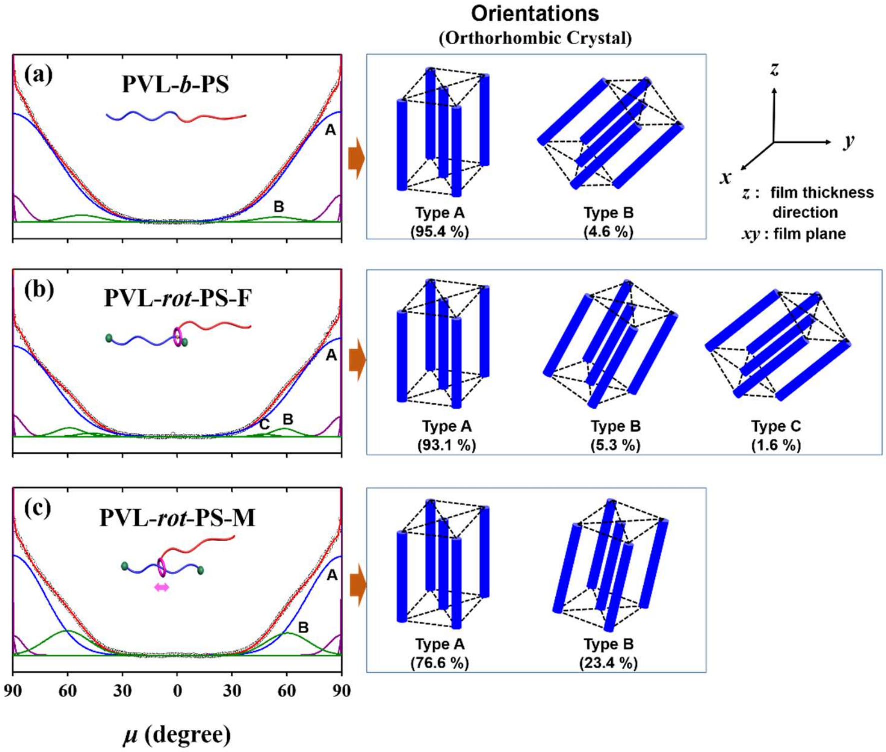

Figure 4.13. Azimuthal scattering profiles and analysis results of the {110} peaks of PVL crystals in Figure 4.11 and orientational crystal domains: (a) THF-annealed PVL-*b*-PS film; (b) THF-annealed PVL-*rot*-PS-F film; (c) THF-annealed PVL-*rot*-PS-M film.

Fourth, the vertically-oriented orthorhombic PVL crystals are further determined to consist of three different types of rotational domains, namely (i) type-**I** rotational crystal domain (ω_{I} = 0°, rotational angle where the rotational axis is parallel to a normal direction to the film plane; ϕ_{I} = 15.8~21.4 %, relative volume fraction), (ii) type-**II** rotational crystal domain (ω_{II} = 6.8~10.3°; ϕ_{II} = 48.4~61.8 %), and (iii) type-**III** rotational crystal domain (ω_{III} = 10.3~14.0°; ϕ_{III}) = 16.8~33.4 %) (Figures 4.14-4.19). The rotational angles and populations of rotational crystal domains vary depending on the polymer systems and film fabrication processes. In particular, for the individual polymer films, the population of rotational domain is in the increasing order type-**I** < type-**III** < type-**II**.

Fifth, for the as-cast films, the crystallinity $X_{\mathrm{c,GIWAXS}}$ is in the increasing order PVL-*b*-PS < PVL-*rot*-PS-F < PVL-*rot*-PS-M. These results are an obvious clue that in PVL-*rot*-PS-M the movable rotaxane linker could induce both the PVL axle and PS block to mobilze more and indeed undergo phase-separation more favorably, forming PVL axle and PS phase domains (i.e., lamellae); in the resulting PVL axle domains (i.e., PVL axle layers in the PVL/PS lamellar structure) the axle chains crystalize more favorably.

Finally, for the THF-annealed films, $X_{\mathrm{c,GIWAXS}}$ is in the increasing order PVL-*rot*-PS-M < PVL-*b*-PS < PVL-*rot*-PS-F. Here, it is noted that the $X_{\mathrm{c,GIWAXS}}$ of PVL-*rot*-PS-M film is almost same before and after the THF-annealing. Moreover, the dimension of its lamellar structure is kept almost same through the THF-annealing process. In contrast, the $X_{\mathrm{c,GIWAXS}}$ values of both PVL-*b*-PS and PVL-*rot*-PS-F films are increased by the THF-annealing process. Furthermore, the dimension parameters of their lamellar structures are discernibly changed through the THF-annealing process. These results collectively confirm again that the movable rotaxane linker could mobilize the PVL axle and PS block chains enough for phase-separation and further crystallization of the PVL axle chains in the resulting phase-domains via the film casting and subsequent drying process. Instead, the covalent linker, as well as the rotaxane-based ionic linker could not provide enough mobilities to the block chains for phase-separation and crystallization of the PVL block chains through the film casting and subsequent drying process; as a result, the phase-separation, as well as the PVL crystallization might be undergone in limited bases. Thus, such phase-separation and PVL crystallization might proceed further through the post THF-annealing process, enhancing lamellar structure and crystallinity.

As discussed above, PVL-*b*-PS, PVL-*rot*-PS-F and PVL-*rot*-PS-M have been investigated in detail in the aspect of nanoscale film morphologies by using GISAXS and GIWAXS. The nanoscale film morphologies of all polymer systems are basically composed of two structural elements: (i) lamellar structure based on the phase-separation of PVL and PS components; (ii) fringed-micelle like crystals in the PVL layers in the phase-separated lamellar structure. Overall, these structural characteristics are influenced by the natures of linkers between PVL and PS blocks. In particular, the movable rotaxane linker could make significantly positive impact on the phase-separation and the crystallization of PVL component. The structural parameter details have been determined by these GISAXS and GIWAXS analyses. With such determined structural parameters, overall morphological features of the nanoscale polymer films are presented schematically in Figure 4.20.

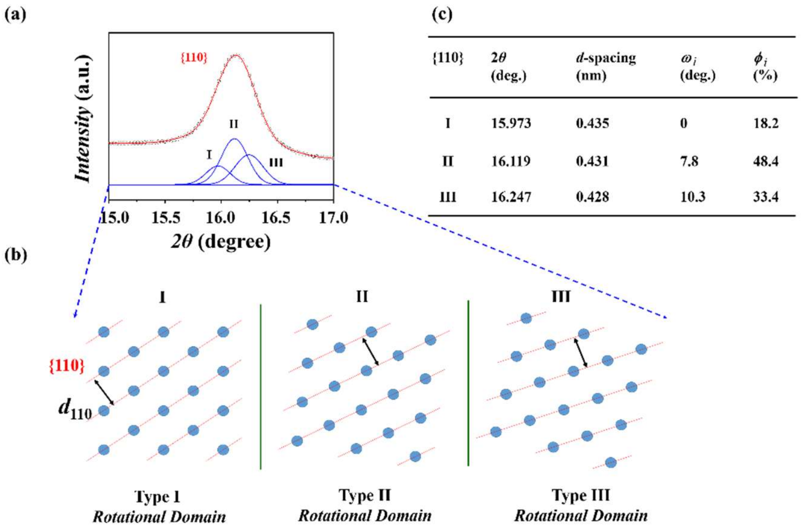

{110}	2θ (deg.)	d-spacing (nm)	ω_i (deg.)	ϕ_i (%)
I	15.973	0.435	0	18.2
II	16.119	0.431	7.8	48.4
III	16.247	0.428	10.3	33.4

Figure 4.14. (a) Enlarged {110} reflection profile of PVL-*b*-PS-F film (as-cast film) obtained from the 1D scattering profile in Figure 4.10d. The symbols represent the measured data; the blue curves represent the scattering profiles obtained by the deconvolution of the {110} reflection profile; the red curve represents the sum of the deconvoluted scattering profiles in blue color. (b) Top views of orthorhombic lattices in three different rotational domains which were determined by the deconvolution analysis of the scattering profile in (a); d_{110} is the *d*-spacing of {110} reflection. (c) Deconvolution analysis results of the scattering profile in (a); ω_i and ϕ_i are the rotational angle and relative volume fraction of orthorhombic lattice domain *i* respectively where the rotational axis is parallel to the *c*-axis of the lattice (which is also parallel to the out-of-plane of the film).

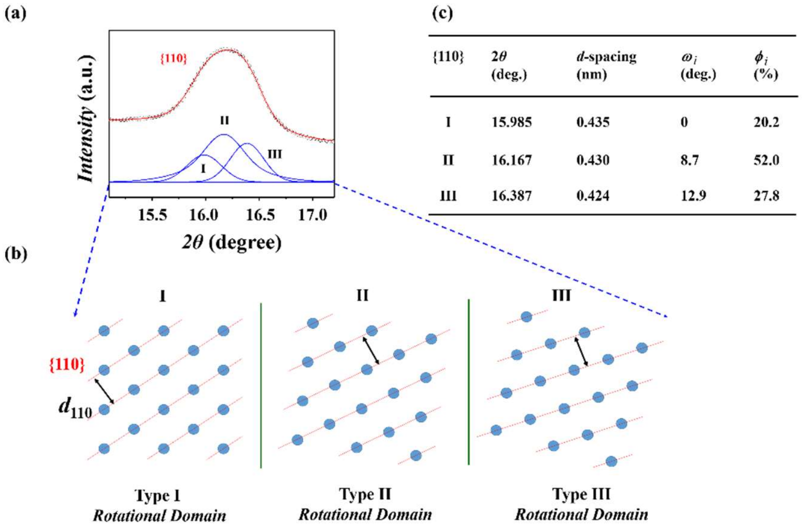

{110}	2θ (deg.)	d-spacing (nm)	ω_i (deg.)	ϕ_i (%)
I	15.985	0.435	0	20.2
II	16.167	0.430	8.7	52.0
III	16.387	0.424	12.9	27.8

Figure 4.15. (a) Enlarged {110} reflection profile of PVL-*rot*-PS-F film (as-cast film) obtained from the 1D scattering profile in Figure 4.10e. The symbols represent the measured data; the blue curves represent the scattering profiles obtained by the deconvolution of the {110} reflection profile; the red curve represents the sum of the deconvoluted scattering profiles in blue color. (b) Top views of orthorhombic lattices in three different rotational domains which were determined by the deconvolution analysis of the scattering profile in (a); d_{110} is the *d*-spacing of {110} reflection. (c) Deconvolution

analysis results of the scattering profile in (a); ω_i and ϕ_i are the rotational angle and relative volume fraction of orthorhombic lattice domain *i* respectively where the rotational axis is parallel to the *c*-axis of the lattice (which is also parallel to the out-of-plane of the film).

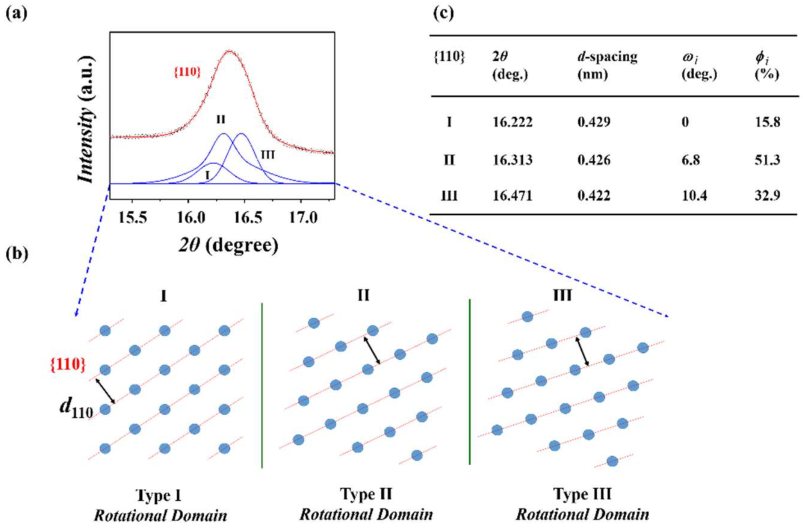

{110}	2θ (deg.)	*d*-spacing (nm)	ω_i (deg.)	ϕ_i (%)
I	16.222	0.429	0	15.8
II	16.313	0.426	6.8	51.3
III	16.471	0.422	10.4	32.9

Figure 4.16. (a) Enlarged {110} reflection profile of PVL-*rot*-PS-M film (as-cast film) obtained from the 1D scattering profile in Figure 4.10f. The symbols represent the measured data; the blue curves represent the scattering profiles obtained by the deconvolution of the {110} reflection profile; the red curve represents the sum of the deconvoluted scattering profiles in blue color. (b) Top views of orthorhombic lattices in three different rotational domains which were determined by the deconvolution analysis of the scattering profile in (a); d_{110} is the *d*-spacing of {110} reflection. (c) Deconvolution analysis results of the scattering profile in (a); ω_i and ϕ_i are the rotational angle and relative volume fraction of orthorhombic lattice domain *i* respectively where the rotational axis is parallel to the *c*-axis of the lattice (which is also parallel to the out-of-plane of the film).

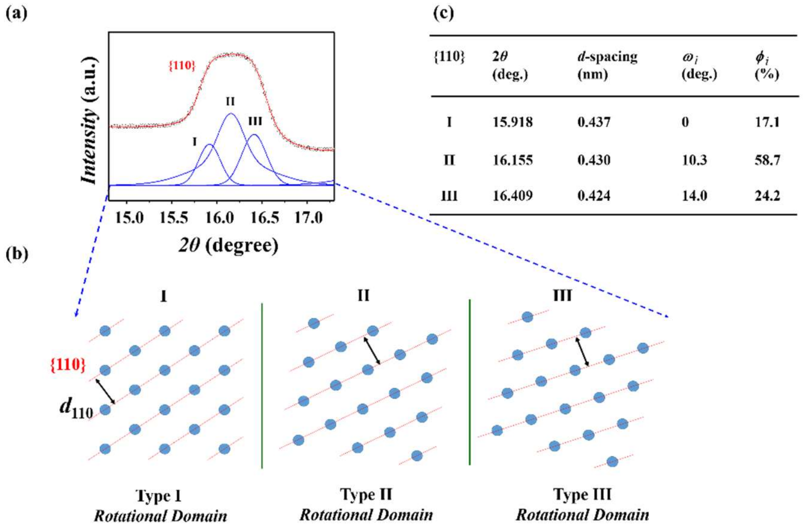

{110}	2θ (deg.)	*d*-spacing (nm)	ω_i (deg.)	ϕ_i (%)
I	15.918	0.437	0	17.1
II	16.155	0.430	10.3	58.7
III	16.409	0.424	14.0	24.2

Figure 4.17. (a) Enlarged {110} reflection profile of PVL-*b*-PS film (THF-annealed film) obtained from

the 1D scattering profile in Figure 4.11d. The symbols represent the measured data; the blue curves represent the scattering profiles obtained by the deconvolution of the {110} reflection profile; the red curve represents the sum of the deconvoluted scattering profiles in blue color. (b) Top views of orthorhombic lattices in three different rotational domains which were determined by the deconvolution analysis of the scattering profile in (a); d_{110} is the d-spacing of {110} reflection. (c) Deconvolution analysis results of the scattering profile in (a); ω_i and ϕ_i are the rotational angle and relative volume fraction of orthorhombic lattice domain i respectively where the rotational axis is parallel to the c-axis of the lattice (which is also parallel to the out-of-plane of the film).

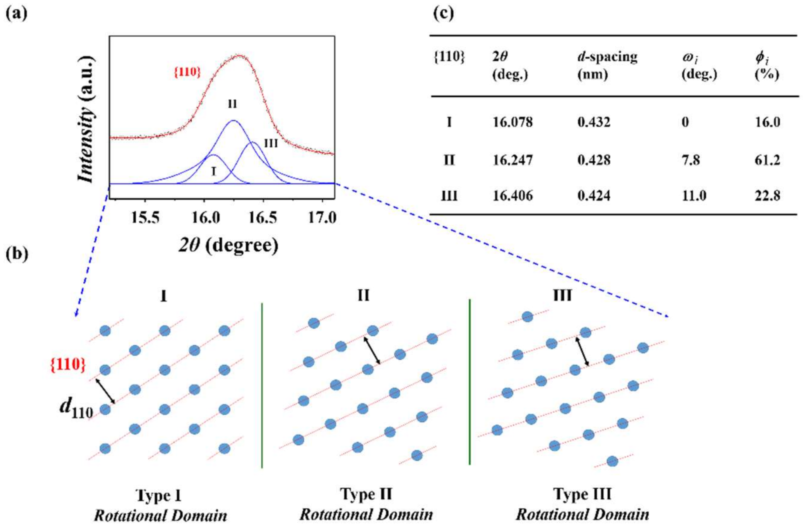

{110}	2θ (deg.)	*d*-spacing (nm)	ω_i (deg.)	ϕ_i (%)
I	16.078	0.432	0	16.0
II	16.247	0.428	7.8	61.2
III	16.406	0.424	11.0	22.8

Figure 4.18. (a) Enlarged {110} reflection profile of PVL-*rot*-PS-F film (THF-annealed film) obtained from the 1D scattering profile in Figure 4.11e. The symbols represent the measured data; the blue curves represent the scattering profiles obtained by the deconvolution of the {110} reflection profile; the red curve represents the sum of the deconvoluted scattering profiles in blue color. (b) Top views of orthorhombic lattices in three different rotational domains which were determined by the deconvolution analysis of the scattering profile in (a); d_{110} is the d-spacing of {110} reflection. (c) Deconvolution analysis results of the scattering profile in (a); ω_i and ϕ_i are the rotational angle and relative volume fraction of orthorhombic lattice domain i respectively where the rotational axis is parallel to the c-axis of the lattice (which is also parallel to the out-of-plane of the film).

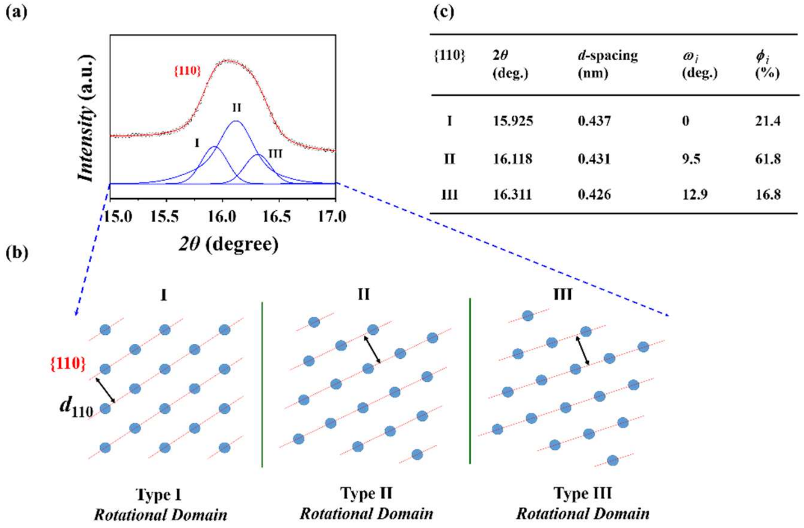

{110}	2θ (deg.)	d-spacing (nm)	ω_i (deg.)	ϕ_i (%)
I	15.925	0.437	0	21.4
II	16.118	0.431	9.5	61.8
III	16.311	0.426	12.9	16.8

Figure 4.19. (a) Enlarged {110} reflection profile of PVL-*rot*-PS-M film (THF-annealed film) obtained from the 1D scattering profile in Figure 4.11f. The symbols represent the measured data; the blue curves represent the scattering profiles obtained by the deconvolution of the {110} reflection profile; the red curve represents the sum of the deconvoluted scattering profiles in blue color. (b) Top views of orthorhombic lattices in three different rotational domains which were determined by the deconvolution analysis of the scattering profile in (a); d_{110} is the d-spacing of {110} reflection. (c) Deconvolution analysis results of the scattering profile in (a); ω_i and ϕ_i are the rotational angle and relative volume fraction of orthorhombic lattice domain i respectively where the rotational axis is parallel to the c-axis of the lattice (which is also parallel to the out-of-plane of the film).

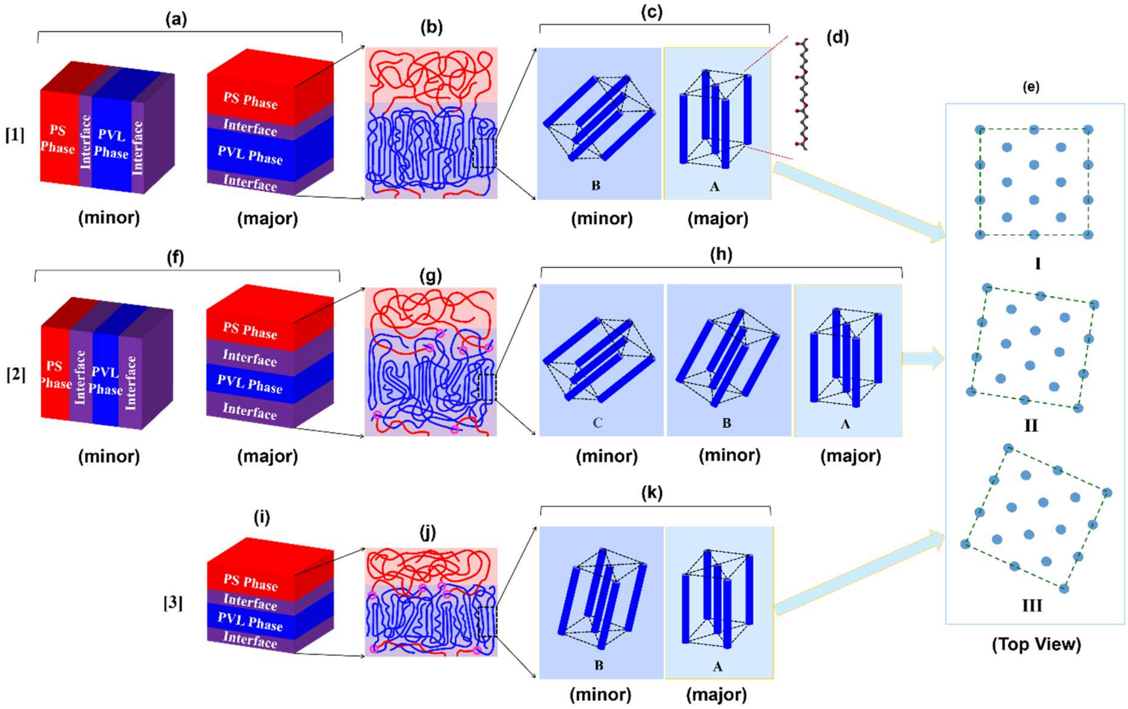

Figure 4.20. Schematic representations of the nanostructures, packing orders, and chain conformations of PVL-*b*-PS, PVL-*rot*-PS-F, and PVL-*rot*-PS-M in nanoscale films. [1] PVL-*b*-PS: (a) vertical and horizontal lamellar structures; (b) chain conformations and packings in the layers of horizontal lamellar structure in (a); (c) orientational domains (**A** and **B**) of orhothombic crystals formed in the PVL layer in (b); (d) fully-extended PVL repeat units corresponded to the lattice parameter *c* in the A-type crystal in (c); (e) rotational domains (**I**, **II**, and **III**) of orthorhombic crystals formed in the **A**-type orientational domains in (c). [2] PVL-*rot*-PS-F: (f) vertical and horizontal lamellar structures; (g) chain conformations and packings in the layers of horizontal lamellar structure in (f); (h) orientational domains (**A**, **B**, and **C**) of orhothombic crystals formed in the PVL layer in (g); (d) fully-extended PVL repeat units corresponded to the lattice parameter *c* in the **A**-type crystal in (h); (e) rotational domains (**I**, **II**, and **III**) of orthorhombic crystals formed in the A-type orientational domains in (h). [3] PVL-*rot*-PS-M: (i) horizontal lamellar structure; (j) chain conformations and packings in the layers of lamellar structure in (i); (k) orientational domains (**A** and **B**) of orhothombic crystals formed in the PVL layer in (j); (d) fully-extended PVL repeat units corresponded to the lattice parameter *c* in the **A**-type crystal in (k); (e) rotational domains (**I**, **II**, and **III**) of orthorhombic crystals formed in the **A**-type orientational domains in (k).

4.4 Conclusions

In this chapter, PVL-*rot*-PS-M, PVL-*rot*-PS-F and PVL-*b*-PS have been investigated in the aspects of thermal stability, phase transition behaviors, and nanoscale film morphology.

PVL-*rot*-PS-M is found to reveal the thermal stabilities of PVL axle and movable PS-linked rotaxane wheel independently, proving that the mechanical link can reserve fully the stabilities of individual block components. In PVL-*rot*-PS-F, the thermal stability of fixed PS-linked rotaxane wheel, however, is severely damaged due to the ionic linking character and counter anion; but the PVL axle retains its own stability reasonably well. The thermal stability is in the increasing order PVL-*rot*-PS-F << PVL-*rot*-PS-M < PVL-*b*-PS.

In cooling run from the melt, the PVL and PS components behave phase-separation which kinetically competes with the crystallization of PVL component. Practically, the phase-separation, however, takes place ahead of PVL crystallization because a mass transformation of PVL block chains is necessary to the nucleation and growing crystal sites. The phase-separation, as well as the PVL crystallization is significantly enhanced by the movable rotaxane wheel linker in PVL-*rot*-PS-M and, however, restricted and suppressed highly by the ionically-fixed rotaxane wheel linker in PVL-*rot*-PS-F and the covalent bond linker in PVL-*b*-PS. As a result, cold crystallization appears heavily in subsequent heating runs of PVL-*rot*-PS-F and PVL-*b*-PS.

In nanoscale films, PVL-*rot*-PS-M forms only horizontal lamellar structure as a result of phase-separation and fringed-micelle like crystals with orthorhombic lattice in the PVL layers; the PVL layers are composed of two different orientational crystal domains in which three different rotational lattice domains are present. Differently, PVL-*rot*-PS-F forms a mixture of horizontal and vertical lamellar structures in which the PVL layers consist of three kinds of orientational crystal domains as well as three different rotational lattice domains. Similar film morphology is observed for PVL-*b*-PS; but, there are two different orientational crystal domains in the PVL layers. The structural imperfect level is relatively higher in films of PVL-*rot*-PS-F and PVL-*b*-PS, compared to that of PVL-*rot*-PS-M. Thus, the film morphologies of PVL-*rot*-PS-F and PVL-*b*-PS could be enhanced discernibly by post THF-annealing; but, such THF-annealing effect could not be observed for the film morphology of PVL-*rot*-PS-M. Overall, the nanoscale film morphology characteristics are influenced by the natures of linkers between PVL and PS blocks; in particular, the movable rotaxane linker could make significantly positive impact on the film morphology and structural parameter details. In this chapter, the three layer model analysis was successful to parameterize the morphological details of PVL-PS pseudo miktoarm block copolymers in nanoscale thin films. In addition, the novel modeling analysis has also identified the rotaxane wheel's function as mechanical linkage between PVL axle and PS block as a critical topological feature impacting the overall phase-separation behavior of PVL-PS pseudo miktoarm block copolymers, successfully establishing new insights in the topology-morphology correlation of mechanically linked block copolymers.

4.5 References

1. Harada, A.; Li, J.; Kamachi, M. The Molecular Necklace: A Rotaxane Containing Many Threaded α-Cyclodextrins. *Nature*, **1992**, *356*, 325−327.
2. Leigh, D. A.; Morales, M. A. F.; Perez, E. M.; Wong, J. K. Y.; Saiz, C. G.; Slawin, A. M. Z.; Carmichael, A. J.; Haddleton, D. M.; Brouwer, A. M.; Buma, W. J.; Wurpel, G. W. H.; Leon, S.; Zerbetto, F. Patterning through Controlled Submolecular Motion: Rotaxane-Based Switches and Logic Gates that Function in Solution and Polymer Films. *Angew. Chem. Int. Ed.*, **2005**, *44*, 3062−3067.
3. Wenz, G.; Han, B. H.; Muller, A. Cyclodextrin Rotaxanes and Polyrotaxanes. *Chem. Rev.*, **2006**, *106*, 782−817.
4. Frampton, M. J.; Anderson, H. L. Insulated Molecular Wires. *Angew. Chem. Int. Ed.*, **2007**, *46*, 1028−1064.
5. Niu, Z.; Gibson, H. W. Polycatenanes. *Chem. Rev.*, **2009**, *109,* 6024–6046.
6. Fang, L.; Olson, M. A.; Benitez, D.; Tkatchouk, E.; Goddard, W. A.; Stoddart, J. F. Mechanically Bonded Macromolecules. *Chem. Soc. Rev.*, **2010**, *39*, 17−29.
7. Aoki, D.; Uchida, S.; Nakazono, K.; Koyama, Y.; Takata, T. Macromolecular [2]Rotaxanes: Effective Synthesis and Characterization. *ACS Macro Lett.*, **2013**, *2*, 461−465.
8. Chen, Z.; Aoki, D.; Uchida, S.; Marubayashi, H.; Nojima, S.; Takata, T. Effect of Component Mobility on the Properties of Macromolecular [2]Rotaxanes. *Angew. Chem. Int. Ed.*, **2016**, *55*, 2778-2781.
9. Ito, K. Slide-Ring Materials Using Topological Supramolecular Architecture. *Current Opinion Solid State Mater. Sci.*, **2010**, *14*, 28–34.
10. Bertrand, A.; Stenzel, M.; Fleury, E.; Bernard, J. Host–Guest Driven Supramolecular Assembly of Reversible Comb-Shaped Polymers in Aqueous Solution. *Polym. Chem.*, **2012**, *3*, 377−383.
11. Harada, A.; Hashidzume, A.; Yamaguchi, H.; Takashima, Y. Polymeric Rotaxanes. *Chem. Rev.*, **2009**, *109*, 5974−6023.
12. Zayed, J. M.; Biedermann, F.; Rauwald, U.; Scherman, O. A. Probing Cucurbit[8]uril-Mediated Supramolecular Block Copolymer Assembly in Water Using Diffusion NMR. *Polym. Chem.*, **2010**, *1*, 1434–1436.
13. Sambe, L.; B., K.; Stoffelbach, F.; Lyskawa, J.; Delattre, F.; Bria, M.; Sauvage, F. X.; Sliwa, M.; Humblot, V.; Charleux, B.; Cooke, G.; Woisel., P. Multi-Stimuli Responsive Supramolecular Diblock Copolymers. *Polym. Chem.*, **2014**, *5*, 1031−1036.
14. De Bo, G.; De Winter, J.; Gerbaux, P.; Fustin, C. A. Rotaxane-Based Mechanically Linked Block Copolymers. *Angew. Chem. Int. Ed.*, **2011**, *50*, 9093−9096.
15. Teuchert, C.; Michel, C.; Hausen, F.; Park, D.-Y.; Beckham, H. W.; Wenz, G. Cylindrical Polymer Brushes by Atom Transfer Radical Polymerization from Cyclodextrin−PEG Polyrotaxanes: Synthesis and Mechanical Stability. *Macromolecules*, **2013**, *46*, 2−7.
16. Lee, M.; Schoonover, D. V.; Gies, A. P.; Hercules, D. M.; Gibson, H. W. Synthesis of Complementary Host- and Guest-Functionalized Polymeric Building Blocks and Their Self-Assembling Behavior. *Macromolecules*, **2009**, *42*, 6483−6494.
17. Lee, M.; Moore, R. B.; Gibson, H. W. Supramolecular Pseudorotaxane Graft Copolymer from a Crown Ether Polyester and a Complementary Paraquat-Terminated Polystyrene Guest. *Macromolecules*, **2011**, *44*, 5987−5993.
18. Aoki, D.; Uchida, S.; Takata, T. Mechanically Linked Block/Graft Copolymers: Effective Synthesis via Functional Macromolecular [2]Rotaxanes, *ACS Macro Lett.* **2014**, *3*, 324−328.

19. Gibson, H. W.; Farcas, A.; Jones, J. W.; Ge, Z. X.; Huang, F. H.; Vergne, M.; Hercules, D. M. Supramacromolecular Self-Assembly: Chain Extension, Star and Block Polymers via Pseudorotaxane Formation from Well-Defined End-Functionalized Polymers. *J. Polym. Sci., Part A: Polym. Chem.*, **2009**, *47*, 3518−3543.
20. van Dongen, S. F. M.; Cantekin, S.; Elemans, J. A. A. W.; Rowan, A. E.; Nolte, R. J. M. Functional Interlocked Systems. *Chem. Soc. Rev.*, **2014**, *43*, 99−122.
21. Kureha, T.; Aoki, D.; Hiroshige, S.; Iijima, K.; Aoki, D.; Takata, T.; Suzuki, D. Decoupled Thermo- and pH-Responsive Hydrogel Microspheres Cross-Linked by Rotaxane Networks, *Angew. Chem. Int. Ed.*, **2017**, *56*, 15393–15396.
22. Iijima, K.; Aoki, D.; Otsuka, H.; Takata, T. Synthesis of Rotaxane Cross-Linked Polymers with Supramolecular Cross-Linkers Based on γ-CD and PTHF Macromonomers: The Effect of the Macromonomer Structure on the Polymer Properties. *Polymer*, **2017**, *128*, 392-396.
23. Aoki, D.; Takata, T. Mechanically Linked Supramolecular Polymer Architectures Derived from Macromolecular [2]Rotaxanes: Synthesis and Topology Transformation. *Polymer* **2017**, *128*, 276-296.
24. Takata, T.; Aoki, D. Topology-Transformable Polymers: Linear–Branched Polymer Structural Transformation via the Mechanical Linking of Polymer Chains. *Polymer J.*, **2018**, *50*, 127–147.
25. Gong, C. G.; Gibson, H. W. Self-Threading-Based Approach for Branched and/or Cross-Linked Poly(methacrylate rotaxane)s. *J. Am. Chem. Soc.*, **1997**, *119*, 5862-5866.
26. Imran, A. B.; Esaki, K.; Gotoh, H.; Seki, T.; Ito, K.; Sakai, Y.; Takeoka, Y. Extremely Stretchable Thermosensitive Hydrogels by Introducing Slide-Ring Polyrotaxane Cross-Linkers and Ionic Groups into the Polymer Network. *Nat. Commun.*, **2014**, *5*, 5124.
27. Kato, K.; Yasuda, T.; Ito, K. Peculiar Elasticity and Strain Hhardening Aattributable to Counteracting Eentropy of Chain and Ring in Slide-Ring Gels. *Polymer*, **2014**, *55*, 2614-2619.
28. Li, X.; Kang, H. L.; Shen, J. X.; Zhang, L. Q.; Nishi, T.; Ito, K.; Zhao, C. M.; Coates, P. Highly Toughened Polylactide with Novel Sliding Graft Copolymer by In Situ Reactive Compatibilization, Crosslinking and Chain Extension. *Polymer*, **2014**, *55*, 4313-4323.
29. Takashima, Y.; Sawa, Y.; Iwaso, K.; Nakahata, M.; Yamaguchi, H.; Harada, A. Supramolecular Materials Cross-Linked by Host-Guest Inclusion Complexes: The Effect of Side Chain Molecules on Mechanical Properties. *Macromolecules*, **2017**, *50*, 3254-3261.
30. Lee, B.; Park, Y.-H.; Hwang, Y.-T.; Oh, W.; Yoon, J.; Ree, M. Ultralow-*k* Nanoporous Organosilicate Dielectric Films Imprinted with Dendritic Spheres. *Nat. Mater.*, **2005**, *4*, 147–150.
31. Ree, M. Probing the Self-Assembled Nanostructures of Functional Polymers with Synchrotron Grazing Incidence X-Ray Scattering. *Macromol. Rapid Commun.*, **2014**, *35*, 930–959.
32. Kim, Y. Y.; Ree, B. J.; Kido, M.; Ko, Y.-G.; Ishige, R.; Hirai, T.; Wi, D.; Kim, J.; Kim, W. J.; Takahara, A.; Ree, M. High Performance n-Type Electrical Memory and Morphology-Induced Memory-Mode Tuning of A Well-Defined Brush Polymer Bearing Perylene Diimide Moieties. *Adv. Electronic Mater.*, **2015**, *1*, 1500197.
33. Durchschlag, H.; Zipper, P. Calculation of the Partial Volume of Organic Compounds and Polymers. *Progr. Colloid Polym. Sci.*, **1994**, *94*, 20–39.
34. Xiang, L.; Ryu, W.; Kim, H.; Ree, M. Precise Synthesis, Properties, and Structures of Cyclic Poly(*ε*-caprolactone)s. *Polymers*, **2018**, *10*, 577.
35. Pitt, C. G.; Chasalow, F. I.; Hibionada, Y. M. Aliphatic Polyesters, I. The Degradation of Poly(*ε*-caprolactone) In Vivo. *J. Appl. Polym. Sci.*, **1981**, *26*, 3779–3787.

36. Lee, S. W.; Yoon, J.; Kim, H. C.; Lee, B.; Chang, T.; Ree, M. Effect of Molecular Weight on the Surface Morphology, Molecular Reorientation, and Liquid Crystal Alignment Properties of Rubbed Polystyrene Films. *Macromolecules*, **2003**, *36,* 9905-9916.
37. Furuhashi, Y.; Sikorski, P.; Atkins, E.; Iwata, T.; Doi, Y. Structure and Morphology of the Aliphatic Polyester Poly(δ-valerolactone) in Solution-Grown, Chain-Folded Lamellar Crystals. *J. Polym. Sci.: Part B: Polym. Phys.*, **2001**, *39*, 2622–2634.

Chapter 5

Nanoscale Film Morphologies of Cyclic and Tadpole Block Copolyethers

5.1 Introduction

Cyclic poly(dimethylsiloxane) (*c*-PDMS) was reported in 1946 as the first synthetic cyclic polymer.[1-3] In 1949, a cyclic Gaussian polymer like flexible *c*-PDMS was first estimated to exhibit much smaller radius of gyration than that of the linear counterpart.[4] Later on, naturally occurring cyclic deoxyribonucleic acids (*c*-DNAs) were discovered.[5-8] In addition, natural cyclic proteins were found in bacteria, plants, fungi, and animals.[9,10] Cyclic polysaccharides were also occurred naturally.[11] With the discoveries of *c*-PDMS and naturally-occurring biopolymers revealing unique molecular architectures, polymer scientists have been inspired into the development of new synthetic methods of cyclic polymers in more efficient ways with high yield and high purity. As a result of development efforts, several synthetic schemes were demonstrated, producing a number of cyclic homopolymers.[12-29] They were followed by characterizations, exhibiting very unique physical features (for examples, higher thermal stability, higher glass transition temperature, higher melting temperature, lower viscosity, smaller radius of gyration, smaller hydrodynamic volume, and so on) quite different from the linear counterparts.[18-22,31-45]

The cyclic topology approach has been further extended to block copolymer systems. Great research effort has been made to develop the synthetic methods of cyclic block copolymers, and, as a result, various block copolymers possessing cyclic architectures have been reported.[17-19,31,32,46-51] Among those, a few block copolymer systems have been subjected to phase-separations and resulting morphological structures. Their micelle formations in solutions have been examined in a qualitative manner[52-56] as well as recently in a quantitative manner.[56-61] Collectively, it was confirmed that they form compact micelles, compared to the linear counterparts. Compared to the researches of micelles, their bulk morphologies have been investigated in more limited base.[55,62-65] Among the results reported so far, a main consensus is that they could produce phase-separated morphological features which are same with those of the linear counterparts in the same compositions.[55,62-64] In case of cyclic poly(styrene-*block*-isoprene)s (*c*-PS-*b*-PI polymers: ϕ_{PS} = 0.69–0.78, volume fraction of styrene unit), however, controversial bulk morphologies were reported; one research group found cylindrical morphologies for both the cyclic copolymer and the linear counterpart,[63] whereas another research group reported cylindrical morphology for the cyclic one and liquid-like micellar structure for the linear counterpart.[65] Different bulk morphologies were additionally found for one pair of cyclic poly(styrene-*block*-butadiene) (*c*-PS-*b*-BD: f_{PS} = 0.696, molar fraction of styrene unit) and linear counterpart (f_{PS} = 0.702) as well as for another pair of *c*-PS-*b*-BD (f_{PS} = 0.378) and linear counterpart (f_{PS} = 0.395).[62] For the pairs of cyclic block copolymers and linear counterparts revealing same types of bulk morphologies, the domain spacings in the cyclic copolymers were 5 to 16% smaller than those of the linear counterparts, depending on the copolymer systems.[55,62-64] Such domain spacing reductions are much lower than those (30–37 %) predicted theoretically.[66-68] Different from the bulk morphologies, thin film morphologies have been very rarely investigated. In fact, only one report appeared in the literature; for a cyclic poly(styrene-*block*-ethylene oxide) (*c*-PS-*b*-PEO) in thin film state (thickness unknown), the domain spacing of PEO cylinders was 33 % smaller than that of the linear counterpart.[69] This spacing reduction is in the range predicted theoretically.[66-68] Overall, the synthesis of block copolymers possessing cyclic architectures has been significantly advanced so far. To facilitate the better utilization of block copolymers bearing cyclic architectures, it is necessary to understand the relationships between their chemical topology, composition, morphology, and properties. However, their morphologies and properties have yet been explored in detail. In particular, the understanding of their nanoscale film morphologies remains in very early stages.

This chapter is the first report of nanoscale film morphology details of cyclic and tadpole-shaped block copolymers based on poly(*n*-decyl glycidyl ether) (PDGE) and poly(2-

(2-(2-methoxyethoxy)ethoxy)ethyl glycidyl ether) (PTEGGE): *c*-PDGE-*b*-PTEGGE, *tp*-*A*-PDGE-*b*-PTEGGE, and *tp*-*B*-PDGE-*b*-PTEGGE (Figure 5.1). The films have been investigated by synchrotron grazing incidence X-ray scattering (GIXS). This quantitative scattering analysis provides structural parameter details and furthermore key information on the correlations of morphological features and molecular topological effects. All block copolymers of this study reveal nanostructures, evidencing that the PDGE and PTEGGE blocks are immiscible regardless of their topologies and undergo micro-phase separations in films. Despite the same or almost equivalent volume fractions, they show different types of nanostructures depending on the molecular topologies, which are quite different from the expectation based on the volume fractions; distorted hexagonal cylinder structures, as well as lamellar structures are observed. The phase-separated domain spacing is found to significantly vary with the molecular topology. Compared to the linear counterpart, the domain spacing of *c*-PDGE-*b*-PTEGGE is 49.3−67.6 % smaller, which is almost twice smaller than those predicted theoretically and reported previously. Even for the nanostructures of *tp-A*-PDGE-*b*-PTEGGE and *tp*-*B*-PDGE-*b*-PTEGGE, the domain spacings are 25.0–32.5 % smaller than those of the linear counterpart. The cyclic and tadpole block copolymers further demonstrate better defined and oriented domain structures, compared to their linear counterpart. All structural details are discussed in correlations with the molecular topology effects.

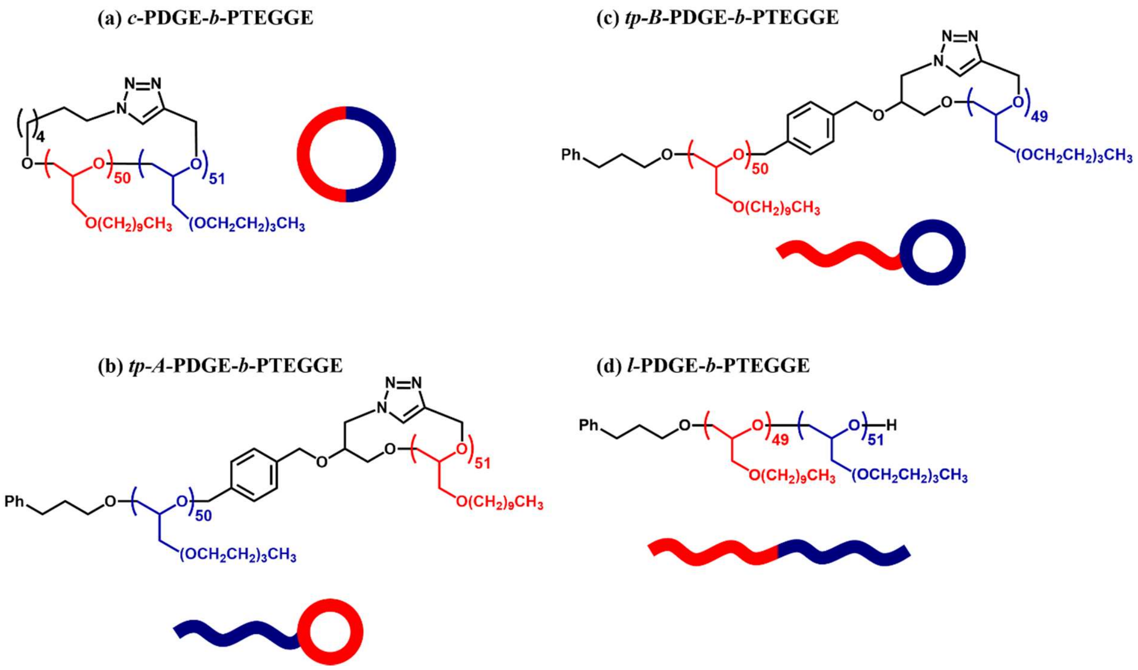
(a) *c*-PDGE-*b*-PTEGGE

(b) *tp-A*-PDGE-*b*-PTEGGE

(c) *tp-B*-PDGE-*b*-PTEGGE

(d) *l*-PDGE-*b*-PTEGGE

Figure 5.1 Chemical structures of cyclic and tadpole-shaped poly(*n*-decyl glycidyl ether-*block*-2-(2-(2-methoxyethoxy)ethoxy)ethyl glycidyl ether)s and their linear counterpart.

5.2 Experimental Section

c-PDGE-*b*-PTEGGE, *td-A*-PDGE-*b*-PTEGGE, and *td-B*-PDGE-*b*-PTEGGE were synthesized and characterized as described in the literature;[49,59] their linear counterpart and homopolymers were prepared additionally. Their molecular characteristics are summarized in Table 5.1.

Table 5.1. Molecular characteristics of various topological block copolymers and their homopolymers [a]

Polymer	$M_{n,NMR}$ [b] (kDa)	$Đ$ [c]	ρ_e [d] (nm^{-3})	ρ_m [e] (g/cm^3)	PDGE block		PTEGGE block	
					DP_{PDGE} [f]	ϕ_{PDGE} [g]	DP_{PTEGGE} [h]	ϕ_{PTEGGE} [i]
c-PDGE-*b*-PTEGGE	22.3	1.04			50	0.52	51	0.48
tp-A-PDGE-*b*-PTEGGE	22.2	1.04			50	0.52	51	0.48
tp-B-PDGE-*b*-PTEGGE	21.7	1.04			50	0.49	49	0.51 [i]
l-PDGE-*b*-PTEGGE	21.9	1.04			49	0.49	51	0.51
c-PDGE	11.0	1.02	310	0.92				
l-PDGE	11.1	1.03	341	1.01				
l-PTEGGE	11.2	1.04	353	1.05				

[a] Data from reference no. 49 and 59. [b] Number-average molecular weight in the unit of kDa (10^3 Da) of polymer determined by ^{1}H NMR spectroscopic analysis. [c] Dispersity value of polymer determined by size exclusion chromatography (SEC) analysis in tetrahydrofuran. [d] Electron density of polymer in films determined by X-ray reflectivity analysis. [e] Mass density of polymer in films obtained from the electron density determined by X-ray reflectivity analysis. [f] Number-average degree of polymerization of PDGE block determined by ^{1}H NMR spectroscopic analysis. [g] Volume fraction of PDGE block estimated from the $M_{n,NMR}$ and ρ_m data. [h] Number-average degree of polymerization of PTEGGE block determined by ^{1}H NMR spectroscopic analysis. [i] Volume fraction of PTEGGE block estimated from the $M_{n,NMR}$ and ρ_m data. [j] Volume fraction estimated from the assumption that the ρ_m of the cyclic PTEGGE block is reveals 8.9% lower than that of the linear analogue as observed in the linear and cyclic PDGE polymers; namely, the cyclic PTEGGE block is assumed to have $\rho_m = 0.96$ g/cm^3.

For the individual polymers, polymer solutions were prepared with a concentration of 0.5 wt% in tetrahydrofuran and filtered using disposable syringes equipped with polytetrafluoroethylene filter membranes of 0.2 μm pore size. Each polymer solution was deposited on silicon substrates by spin-coating and subsequent drying process in vacuum at room temperature for 24 h. The obtained films were measured to have a thickness of 100−120 nm by using a spectroscopic ellipsometer (Model M-2000, Woollam, Lincoln, NE, USA). All film samples were kept in a drying chamber at room temperature before measurements.

Synchrotron grazing incidence X-ray scattering (GIXS) measurements were conducted with an X-ray beam of 0.12095 nm wavelength λ at the 3C beamline[70-73] of the Pohang Accelerator Laboratory (PAL), Pohang, Korea. A two-dimensional (2D) charge-coupled detector (CCD) (model Rayonix 2D SX 165, Rayonix, Evanston, IL, USA) were employed. The incidence angle α_i of X-ray beam with respect to the film sample surface was set in the range 0.1270–0.1470°, which is between the critical angle of the polymer film and the silicon substrate ($\alpha_{c,f}$ and $\alpha_{c,s}$). Aluminum foils were used as a semi-transparent beam stop. The sample-to-detector distance (SDD) was set to be 2909.8 mm for grazing incidence small angle X-ray scattering (GISAXS) measurements and 212.5 mm for grazing incidence wide angle X-ray scattering (GIWAXS) measurements. Each scattering pattern was collected for 10–30 s. The scattering angles were corrected according to the positions of the X-ray beams reflected from the silicon substrate as well as by using precalibrated standards such as polystyrene-*block*-poly(ethylene-*random*-butylene)-*block*-polystyrene and silver behenate standards (Tokyo Chemical Inc., Tokyo, Japan).

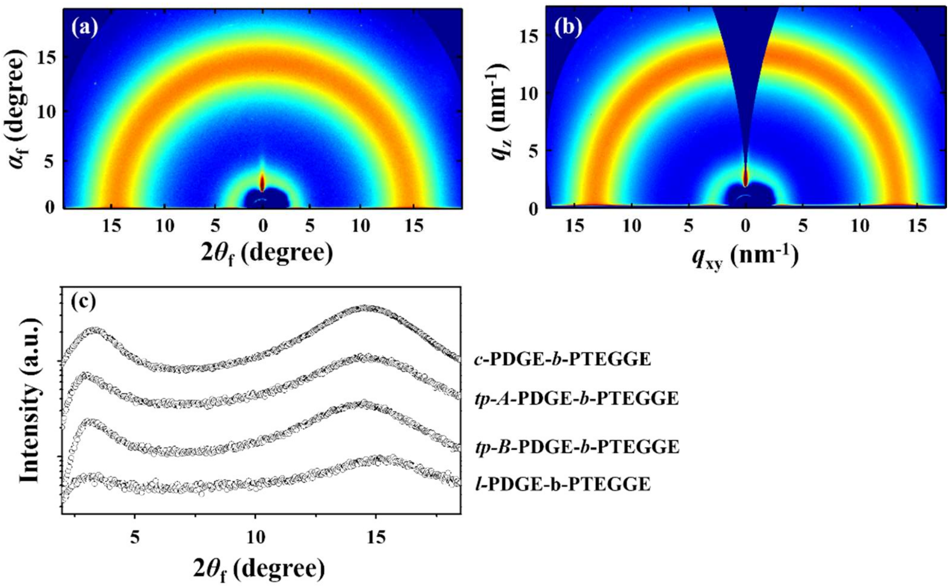

Figure 5.2. Representative GIWAXS data of the nanoscale films (100–120 nm thick) of block copolymers measured with SDD = 212.5 mm at room temperature using a synchrotron X-ray beam (λ = 0.12095 nm): (a) 2D scattering image in angle space ($2\theta_f$ and α_f) of *c*-PDGE-*b*-PTEGGE (α_i = 0.1491°); (b) 2D scattering image in scattering vector space (q_{xy} and q_z) obtained from the scattering image in (a); (c) in-plane scattering profiles extracted along the equatorial line at an α_f value over the range of 0.374° to 0.385° from the measured 2D scattering images, including the image in (a).

5.3 Results and Discussion

A representative 2D GIWAXS image is presented in Figure 5.2a-b, which has been measured for nanoscale films (100−120 nm thick) of *c*-PDGE-*b*-PTEGGE. The GIWAXS pattern reveals only two isotropic ring scatterings: one ring appears around 3.32° (2.09 nm *d*-spacing) and another around 14.59° (0.476 nm *d*-spacing). These are typical amorphous halos. Similar patterns were observed for the other block copolymer films (2D images not shown). In-plane scattering profiles have been extracted from the measured 2D scattering images and compared in Figure 5.2c. For each scattering profile, the scattering peak in the low angle region could be assigned for the mean interdistance between the polymer chains, whereas the that in the high angle region could correspond to the mean interdistance between the side chains under intramolecular and intermolecular interaction. Collectively, the GIWAXS results confirm that the block components of all copolymers are amorphous in the films at room temperature, revealing no crystalline characteristics.

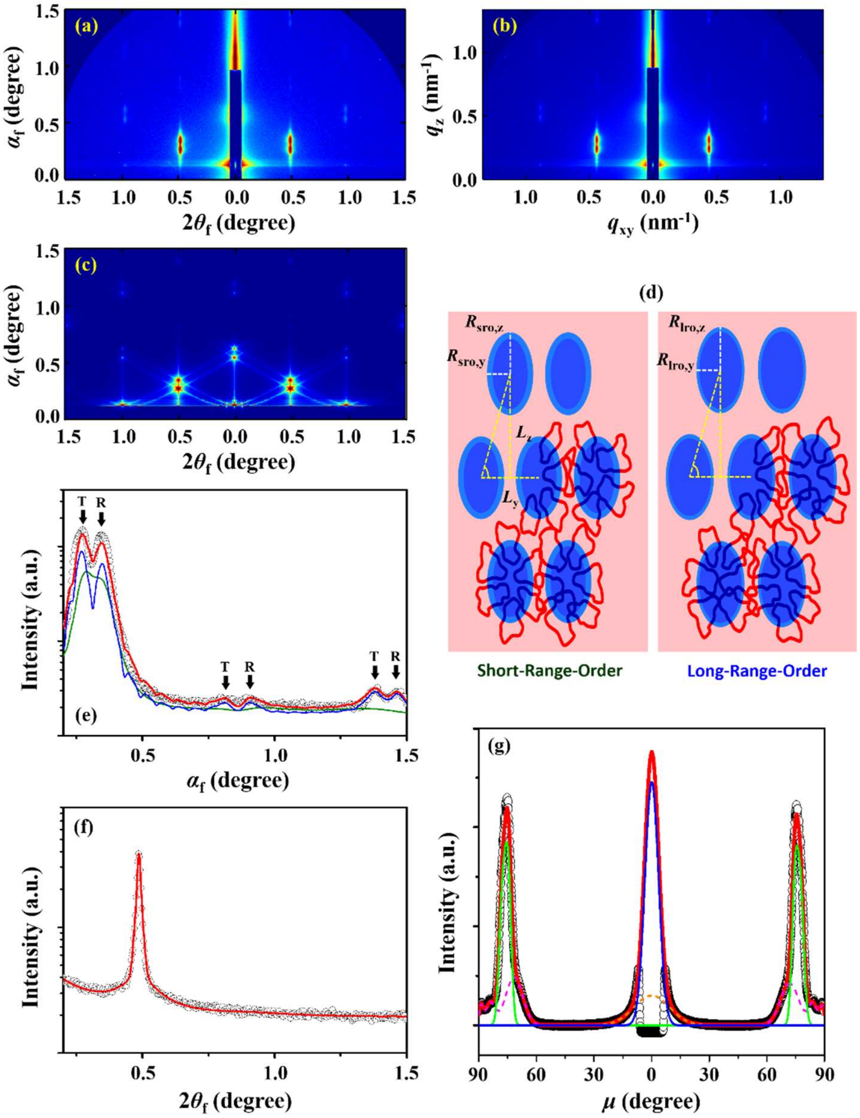

Figure 5.3. Representative GISAXS data of *c*-PDGE-*b*-PTEGGE films (100–120 nm thick) measured with $\alpha_i = 0.1276°$; SDD = 2909.8 mm at room temperature using a synchrotron X-ray beam ($\lambda = 0.12095$ nm): (a) 2D scattering image in angle space; (b) 2D scattering image in scattering vector space obtained from the scattering image in (a); (c) 2D scattering image reconstructed with the determined structural parameters; (d) hexagonally-packed cylindrical structure models in a front view; (e) out-of-plane scattering profile extracted along the meridian line at $2\theta_f = 0.485°$ from the scattering image in (a); (f) in-plane scattering profile along the equatorial line at $\alpha_f = 0.229°$ from the scattering image in (a). In (e) and (f), the black symbols are the measured data and the solid red lines were obtained by fitting the data using the GIXS formula of hexagonal cylindrical structure models in (d); the scattering peak generated by the reflected X-ray beam is marked with "**R**", whereas that generated by the transmitted X-ray beam is marked with "**T**". In (e), the red line is the sum of the green and blue lines where the green line is the scattering profile of short-range-ordered cylindrical domains and the blue line is the scattering profile of long-range-ordered cylindrical domains. (g) Azimuthal scattering profile extracted at $q = 0.564$ nm^{-1} from the scattering image in (b) where the black symbols are the measured data and the lines were obtained by the deconvolutions of the measured data: the blue and green solid lines are the scattering peaks of cylindrical domains in hexagonal packing order, the purple dot line is the Yoneda peak, the

brown dot line is a part of the reflected X-ray beam, and the red solid line is the sum of all deconvoluted peaks.

Figure 5.3a shows a representative GISAXS image of *c*-PDGE-*b*-PTEGGE films (100–120 nm thick) at room temperature; its q space image is given in Figure 5.3b. Two sets of scattering peaks are observed (Figure 5.3a): One set of peaks appear at ($2\theta_f = 0°$ and $\alpha_f = 0.547°$) and (0.485° and 0.274°), whereas another set of peaks appear at (0° and 0.603°) and (0.485° and 0.344°). Considering the GIXS optics, the first set of spots could be generated by the transmitted X-ray beam, whereas the second set of spots could be generated by the reflected X-ray beam. It is additionally noted that two groups of scattering spots appear along the meridian line at $2\theta_f = 0.485°$: One group of peaks are at $\alpha_f = 0.274°$, 0.827°, and 1.382°, which could be generated by the transmitted X-ray beam; another group of peaks at $\alpha_f = 0.344°$, 0.904°, and 1.460°, which could be generated by the reflected X-ray beam. The spot at (0° and 0.603°) is estimated to have a *d*-spacing value, which is close to that of the spot at (0.485° and 0.344°). For the spots at $\alpha_f = 0.344°$, 0.904°, and 1.460° along the meridian line at $2\theta_f = 0.485°$, their relative scattering vector lengths from the specular reflection position are found to be 1, $\sqrt{3}$, and 2, respectively. These are typical scattering characteristics of in-plane oriented (i.e., horizontal) cylindrical domains in a hexagonally-packed structure. Taking these structural clues into account, the scattering data were quantitatively analyzed by using the GIXS formula derived for hexagonally-packed cylinder model (Figure 5.3d); the GIXS formula detail is given in Section 1.4 of Chapter 1. The out-of-plane scattering profile extracted along the median line at $2\theta_f = 0.485°$, as well as the in-plane scattering profile extracted along the equatorial line at $\alpha_f = 0.229°$, could be reasonably well fitted with the GIXS formula of hexagonal cylinder structure model (Figures 5.3e-f). An additional analysis has been carried out on an azimuthal scattering profile extracted at $q = 0.564$ nm^{-1} from the q-space image and then analyzed (Figure 5.3g; Figure 5.3b) to get information on an orientation of the cylindrical domain packing in the film. The determined structural parameters are summarized in Table 5.2. From the determined structural parameters, a 2D GISAXS image has been reconstructed by using the GIXS formula. The reconstructed scattering image is in good agreement with the measured one (Figures 5.3a and 5.3c), confirming that the scattering data analysis has been done successfully.

The quantitative GISAXS analysis found that the in-plane oriented cylindrical domains are present in two different ordered states; the majority (60 vol%) of cylindrical domains reveal a short-range ordering, whereas the minority (40 vol%) of domains exhibit a long-range ordering. The cylinders in the short-range-ordered state have an ellipsoidal cross-section consisting of a relatively long radius $R_{\mathrm{sro,z}}$ of 4.70 nm [= 4.00 nm (core radius: r_{cz}) + 0.70 nm (shell thickness: t_{sz})] along the out-of-plane of the film (i.e., z-axis) and a short radius $R_{\mathrm{sro,y}}$ of 3.30 nm [= 2.50 nm (core radius: r_{cy}) + 0.80 nm (shell thickness: t_{sy})] along the in-plane of the film (i.e., y-axis). Thus, these cylindrical phases reveal directionally different domain spacings, L_{z} (11.80 nm along the z-axis, which corresponds to the mean interdistance between the arrays of the in-plane oriented cylinders) and L_{y} (8.25 nm along the y-axis, which corresponds to the mean center-to-center distance of the cylinders lain in the film plane). This hexagonal cylinder structure in the short-range-ordered state is found to have a positional distortion factor g of 0.06. In comparison, the cylindrical domains in the long-range-ordered state also have an ellipsoidal cross-section: $R_{\mathrm{lro,z}}$ (long radius, long-range-order) = 4.90 nm [= 4.40 nm (core radius: r_{cz}) + 0.50 nm (shell thickness: t_{sz})] and $R_{\mathrm{lro,y}}$ (short radius, long-range-order) = 3.30 nm [= 2.90 nm (core radius: r_{cy}) + 0.40 nm (shell thickness: t_{sy})]. The domain spacings are L_{z} = 12.17 nm and L_{y} = 8.45 nm. The g factor is 0.01 (which is much smaller than that of the short-range-ordered domains), confirming that the cylindrical domains are highly ordered, compared to those in the short-range-ordered state. The packed structure is found to have a second order orientation factor O_{s} of 0.994 ($\overline{\varphi} = 0°$, the mean value of the polar angle φ (i.e., orientation angle) between the orientation vector $\boldsymbol{n}$ (which is set along a direction normal to the {001} plane of horizontal hexagonal cylindrical structure) and the out-of-plane direction of the film; σ_{φ} = 1.63°, standard deviation for the polar angle φ). From the structural parameters, the volume fraction of cylindrical phase is estimated to be 50.0% for the short-range-ordered state and 49.4 % for the long-range-ordered state. In the cyclic copolymer, the volume fraction of the PDGE block is slightly higher than that of the PTEGGE block. Taking these into account, the cylindrical phase could be assigned to consist of the PTEGGE block chains, whereas the matrix phase is composed of the PDGE block chains.

Table 5.2. Morphological parameters of nanoscale films (100−120 nm thick) of topological polymers

Nanoscale film morphology	Topological polymer					
	c-PDGE-*b*-PTEGGE		*tp-A*-PDGE-*b*-PTEGGE	*tp-B*-PDGE-*b*-PTEGGE	*l*-PDGE-*b*-PTEGGE	
						
Hexagonal cylindrical structure	horizontal	horizontal	horizontal			
	short-range-order (sro)	*long-range-order* (lro)				
L_z[a] (nm)	11.80	12.17	18.00			
L_y[b] (nm)	8.25	8.45	11.10			
γ[c]	1.43	1.50	1.62			
r_{cz}[d] (nm)	4.00 (0.40)[r]	4.40 (0.50)	3.10 (0.70)			
r_{cy}[e] (nm)	2.50 (0.30)	2.90 (0.20)	1.90 (0.70)			
t_{sz}[f] (nm)	0.70 (0.30)	0.50 (0.05)	4.10 (1.00)			
t_{sy}[g] (nm)	0.80 (0.20)	0.40 (0.01)	2.50 (0.50)			
ε[h]	1.42	1.49	1.64			
g[i]	0.06	0.01	0.08			
ϕ[j] (vol%)	60	40				
$\overline{\varphi}$[k] (deg.)	0	0	0			
σ_φ[l] (deg.)	1.63	1.63	1.60			
O_s[m]	0.994	0.994	0.994			
Lamellar structure				horizontal	horizontal	vertical
D_L[n] (nm)				17.20	24.00	25.50
l_1[o] (nm)				2.60 (0.80)	9.40 (1.30)	9.00 (1.00)
l_2[p] (nm)				2.90 (0.40)	2.50 (0.80)	3.60 (1.70)
l_3[q] (nm)				8.80	9.60	9.30
g				0.04	0.33	0.35
$\overline{\varphi}$ (deg.)				0	0	90
σ_φ (deg.)				2.00	6.75	6.25
O_s				0.974	0.902	−0.210
ϕ (vol%)					50	50

[a]Mean interdistance between the arrays of the in-plane oriented cylindrical domains. [b]Mean center-to-center distance of the cylindrical domains lain in the film plane. [c]Ratio of L_z and L_y (= L_z/L_y). [d]Core radius of ellipsoidal cylindrical domain along the z-axis which is parallel to the out-of-plane of the film. [e]Core radius of ellipsoidal cylindrical domain along the y-axis which is parallel to the in-plane of the film. [f]Shell thickness of ellipsoidal cylindrical domain along the z-axis which is parallel to the out-of-plane of the film. [g]Shell thickness of ellipsoidal cylindrical domain along the y-axis which is parallel to the in-plane of the film. [h]Ellipsoidicity ratio (= polar radius/equatorial radius). [i]Paracrystal distortion factor of nanostructure (i.e., hexagonal cylinder structure or lamellar structure) along the z-axis which is parallel to the out-of-plane of the film. [j]Volume fraction in percent. [k]Mean value of the polar angle φ (i.e., orientation angle) between the orientation vector $\boldsymbol{n}$ (which is set along a direction normal to the {001} plane of horizontal hexagonal

cylindrical structure or the in-plane of lamellar structure) and the out-of-plane direction of the film. [l]Standard deviation for the polar angle φ. [m]Second order orientation factor of nanostructure (i.e., hexagonal cylindrical structure or lamellar structure). [n]Long period of lamellar structure. [o]Thickness of the l_1 layer. [p]Thickness of the l_2 layer. [q]Thickness of the l_3 layer. [r]Standard deviation.

Figures 5.4a and 5.4b present representative GISAXS images of *tp-A*-PDGE-*b*-PTEGGE films (100−120 nm thick) at room temperature. The scattering image resembles that of the cyclic counterpart film, but revealing much stronger and distinctive spots. The out-of-plane scattering profile extracted along the median line at $2\theta_f = 0.101°$, as well as the in-plane scattering profile extracted along the equatorial line at $\alpha_f = 0.192°$, could be reasonably well fitted with the GIXS formula of hexagonal cylinder structure model (Figures 5.4d-f). In addition, an azimuthal scattering profile has been extracted at $q = 0.417$ nm^{-1} from the *q*-space image and then analyzed (Figure 5.4g; Figure 5.4b), providing an orientation order of the cylindrical domain packing in the film. The determined structural parameters are summarized in Table 5.2. Figure 5.4c shows the 2D scattering image reconstructed from the determined structural parameters by using the GIXS formula, which is well matched with the measured one. The cylindrical domains are characteristic to reveal ellipsoidal cross-section rather than circular one: R_z (long radius, parallel to the out-of-plane of the film) = 7.20 nm [= 3.10 nm (core radius: r_{cz}) + 4.10 nm (shell thickness: t_{sz})], R_y (short radius, parallel to the in-plane of the film) = 4.40 nm [= 1.90 nm (core radius: r_{cy}) + 2.50 nm (shell thickness: t_{sy})], L_z (domain spacing, along the out-of-plane of the film) = 18.00 nm, L_y (domain spacing, along the in-plane of the film) = 11.00 nm, g (positional distortion factor) = 0.08, and O_s (second order orientation factor) = 0.994 ($\overline{\varphi} = 0°$ and $\sigma_\varphi = 1.60°$). From the structural parameters, the cylindrical phases have a volume fraction of 49.8 %. The volume fraction of the PTEGGE block in the tadpole copolymer is slightly lower than that of the PDGE block. Thus, the cylindrical domains could be assigned by the phase-separated linear PTEGGE block phases, whereas the matrix could be assigned by the cyclic PDGE block phase.

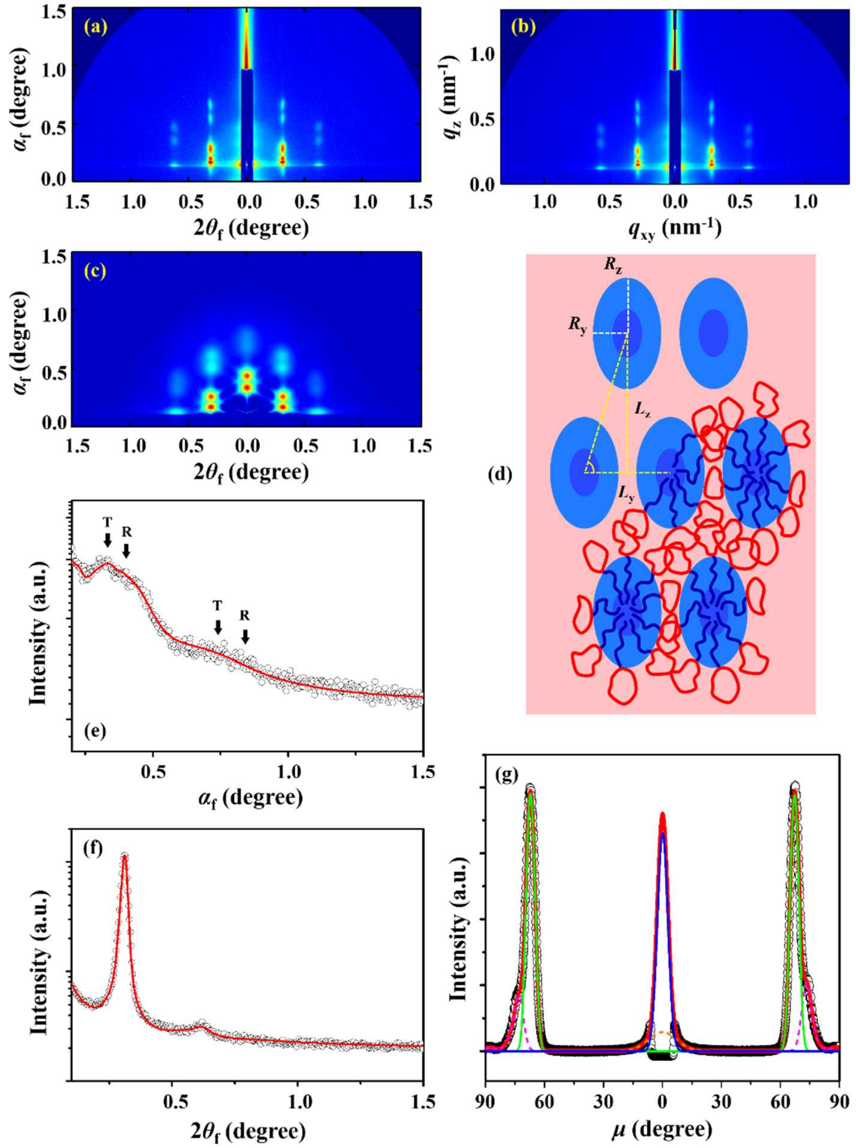

Figure 5.4. Representative GISAXS data of *tp*-*A*-PDGE-*b*-PTEGGE films (100–120 nm thick) measured with $\alpha_i = 0.1361°$; SDD = 2909.8 mm at room temperature using a synchrotron X-ray beam ($\lambda = 0.12095$ nm): (a) 2D scattering image in angle space; (b) 2D scattering image in scattering vector space obtained from the scattering image in (a); (c) 2D scattering image reconstructed with the determined structural parameters; (d) hexagonally-packed cylindrical structure model in a front view; (e) out-of-plane scattering profile extracted along the meridian line at $2\theta_f = 0.101°$ from the scattering image in (a); (f) in-plane scattering profile along the equatorial line at $\alpha_f = 0.192°$ from the scattering image in (a). In (e and f), the symbols are the measured data and the solid red lines were obtained by fitting the data using the GIXS formula of hexagonal cylindrical structure model; the scattering peak generated by the transmitted X-ray beam, is marked with "**T**", whereas that generated by the reflected X-ray beam is marked with "**R**". (g) Azimuthal scattering profile extracted at $q = 0.417$ nm^{-1} from the scattering image in (b); the black symbols are the measured data; the lines were obtained by the deconvolutions of the measured data: the blue and green solid lines are the scattering peaks of cylindrical domains in hexagonal packing order, the purple dot line is the Yoneda peak, the brown dot line is a part of the reflected X-ray beam, and the red solid line is the sum of all deconvoluted peaks.

The *tp-B*-PDGE-*b*-PTEGGE film has been found to present a 2D GISAXS pattern (Figures 5.5a-b), which is quite different from that of the *tp-A*-PDGE-*b*-PTEGGE film as well as of the *c*-PDGE-*b*-PTEGGE film. Two series of scattering spots are clearly distinguished along only the meridian line at $2\theta_f = 0°$: One series of spots appear at $\alpha_f = 0.351°$, $0.753°$ and $1.155°$, which were generated by the transmitted X-ray beam; another series of peaks appear at $\alpha_f = 0.460°$, $0.868°$ and $1.267°$, which were generated by the reflected X-ray beam. The spots $\alpha_f = 0.460°$, $0.868°$ and $1.267°$ are estimated to have the relative scattering vector lengths of 1, 2 and 3 respectively from the specular reflection position. The observation of these peaks is a clue that horizontal lamellar structure was formed in the film. The out-of-plane scattering profile extracted along the meridian line at $2\theta_f = 0.117°$, as well as the in-plane scattering profile extracted along the equatorial line at $\alpha_f = 0.202°$, could be satisfactorily fitted by using the GIXS formula derived for lamellar structure model (Figures 5.5d-f). An additional analysis has been conducted on the azimuthal scattering profile extracted at $q = 0.430\ \text{nm}^{-1}$ from the *q*-space image (Figure 5.5g; Figure 5.5b), in order to an orientation order of the lamellar structure formed in the film. The obtained structural parameters are summarized in Table 5.2. From the structural parameters, a scattering image has been reconstructed, showing good agreement with the measured pattern (Figures 5.5a and 5.5c). The horizontal lamellar structure is characteristic of having a long period D_L of 17.2 nm, a layer l_1 of 2.60 nm, a layer l_2 of 2.90 nm, and a layer l_3 of 8.80 nm, a positional distortion factor g of 0.04, and a second order orientation factor O_s of 0.974 ($\overline{\varphi} = 0°$, the mean value of the polar angle φ (i.e., orientation angle) between the orientation vector $\boldsymbol{n}$ (which is set along a direction normal to the in-plane of lamellar structure) and the out-of-plane direction of the film; $\sigma_\varphi = 2.00°$, standard deviation for the polar angle φ). In this tadpole copolymer, the PTEGGE block has slightly larger volume fraction, compared to that of the PDGE block. Hence, the l_3 layer could be assigned by the cyclic PTEGGE block phase, whereas the sum of the l_1 and l_2 layers could be assigned to the linear PDGE block phase.

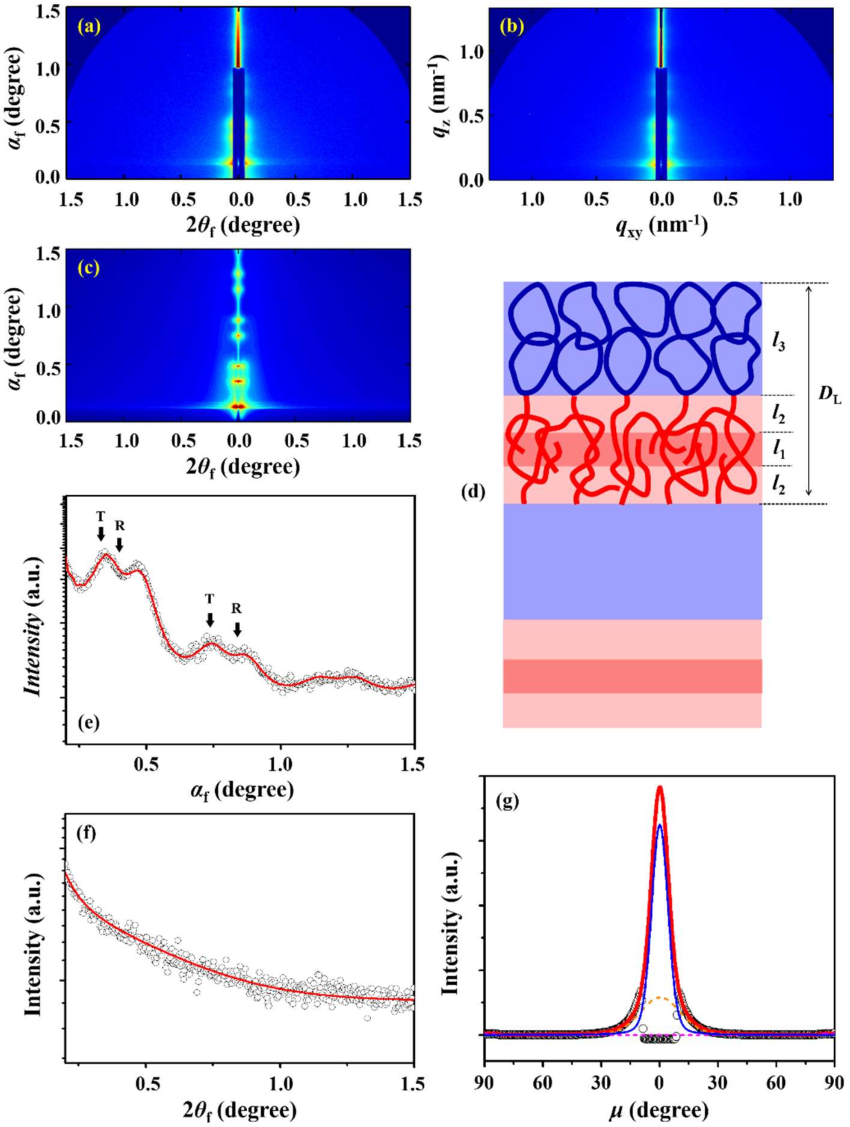

Figure 5.5. Representative GISAXS data of *tp-B*-PDGE-*b*-PTEGGE films (100–120 nm thick) measured with $\alpha_i = 0.1353°$; SDD = 2909.8 mm at room temperature using a synchrotron X-ray beam ($\lambda = 0.12095$ nm): (a) 2D scattering image in angle space; (b) 2D scattering image in scattering vector space obtained from the scattering image in (a); (c) 2D scattering image reconstructed with the determined structural parameters; (d) horizontal lamellar structure model in a front view; (e) out-of-plane scattering profile extracted along the meridian line at $2\theta_f = 0.117°$ from the scattering image in (a); (f) in-plane scattering profile along the equatorial line at $\alpha_f = 0.202°$ from the scattering image in (a). In (e and f), the symbols are the measured data and the solid red lines were obtained by fitting the data using the GIXS formula of lamellar structure model; the scattering peak generated by the transmitted X-ray beam, is marked with "**T**", whereas that generated by the reflected X-ray beam is marked with "**R**". (g) Azimuthal scattering profile extracted at $q = 0.430$ nm^{-1} from the scattering image in (b); the black symbols are the measured data; the lines were obtained by the deconvolutions of the measured data: the blue solid line is the first order scattering peak of lamellar structure, the purple dot line is the Yoneda peak, the brown dot line is a part of the reflected X-ray beam, and the red solid line is the sum of all deconvoluted peaks.

Figure 5.6a shows a representative scattering image of *l*-PDGE-*b*-PTEGGE films, which is somewhat different from that of the *tp-B*-PDGE-*b*-PTEGGE films A single broad scattering peak is discernible at $\alpha_f = 0.296°$ along the meridian line, whereas another broad peak is detected at $2\theta_f = 0.233°$ along the equatorial line (Figures 5.6e-f). The observation of these peaks may be clues that horizontal lamellar structure was formed together with vertical lamellar structure in the film. The GIXS formula based on lamellar structure model could successfully fit the out-of-plane scattering profile extracted along the meridian line at $2\theta_f = 0.101°$, as well as the in-plane scattering profile extracted along the equatorial line at $\alpha_f = 0.192°$ (Figures 5.6d-f). The scattering analysis has been additionally performed on the azimuthal scattering profile extracted at $q = 0.305$ nm^{-1} from the *q*-space image (Figure 5.6g; Figure 5.6b), providing important information that the film formed lamellar structure in two different kinds of orientational domains, namely horizontal lamellar structural domains (50 vol%) and vertical lamellar structural domains (50 vol%). This analysis provides further information on orientation details of the lamellar structures formed in the film. The determined structural parameters are summarized in Table 5.2. Moreover, a scattering image has been reconstructed, which is in good agreement with the measured one (Figures 5.6a and 5.6c). The horizontal lamellar structure is characteristic of having $D_L = 24.0$ nm, $l_1 = 9.4$ nm, $l_2 = 2.5$ nm, $l_3 = 9.6$ nm, $g = 0.33$, and $O_s = 0.902$ ($\overline{\varphi} = 0°$ and $\sigma_\varphi = 6.75°$). In comparison, the vertical lamellar structure is characteristic of having $D_L = 25.5$ nm, $l_1 = 9.0$ nm, $l_2 = 3.6$ nm, $l_3 = 9.3$ nm, $g = 0.35$, and $O_s = -0.210$ ($\overline{\varphi} = 90°$ and $\sigma_\varphi = 6.25°$). For both the horizontal and vertical lamellar structures, the l_1 value is slightly smaller than the l_3 value. Considering the linear chain characteristics of *l*-PDGE-*b*-PTEGGE, the individual blocks might equally contribute to the formation of their interfacial layer in the horizontal lamellar structure as well as in the vertical lamellar structure. The PDGE block has slightly lower volume fraction than that of the PTEGGE block, as listed in Table 5.1. Taking into account these facts, the l_1 layer could be assigned to the linear PDGE block phase, whereas the l_3 layer could be assigned to the phase-separated PTEGGE block phase; the l_2 layer could be assigned to the interfacial layer l_i between the PDGE and PTEGGE layers.

As described above, the quantitative GISAXS analyses have provided structural details on the nanoscale film morphologies of various topological diblock copolymers. Such the structural details are clearly evident for the effects of molecular topologies on the nanoscale film morphology of diblock copolymer as follows.

First, all topological block copolymers of this study have been determined to form phase-separated nanostructures in nanoscale films. These nanostructures are evidences that the polar and nonpolar blocks are immiscible and have undergone phase-separations.

Second, the domain spacing in the cylindrical structured *c*-PDGE-*b*-PTEGGE film is 32.4−34.4 % smaller in the out-of-plane of the film and 23.9−25.7 % smaller in the in-plane of the film, compared to that in the cylinder-structured *tp-A*-PDGE-*b*-PTEGGE film. These domain spacing reductions are so remarkable because, despite the pair of cyclic and tadpole-A block copolymers, they are comparable to those (30−37 %) predicted theoretically for pairs of cyclic and linear block copolymers[66-68] as well as that (33 %) reported previously for the pair of cyclic and linear poly(styrene-*block*-ethylene oxide)s in thin films.[69] Furthermore, the domain spacing reductions are much larger than those (5−16 %) observed for the pairs of cyclic and linear block copolymers in bulk states.[55,62-64]

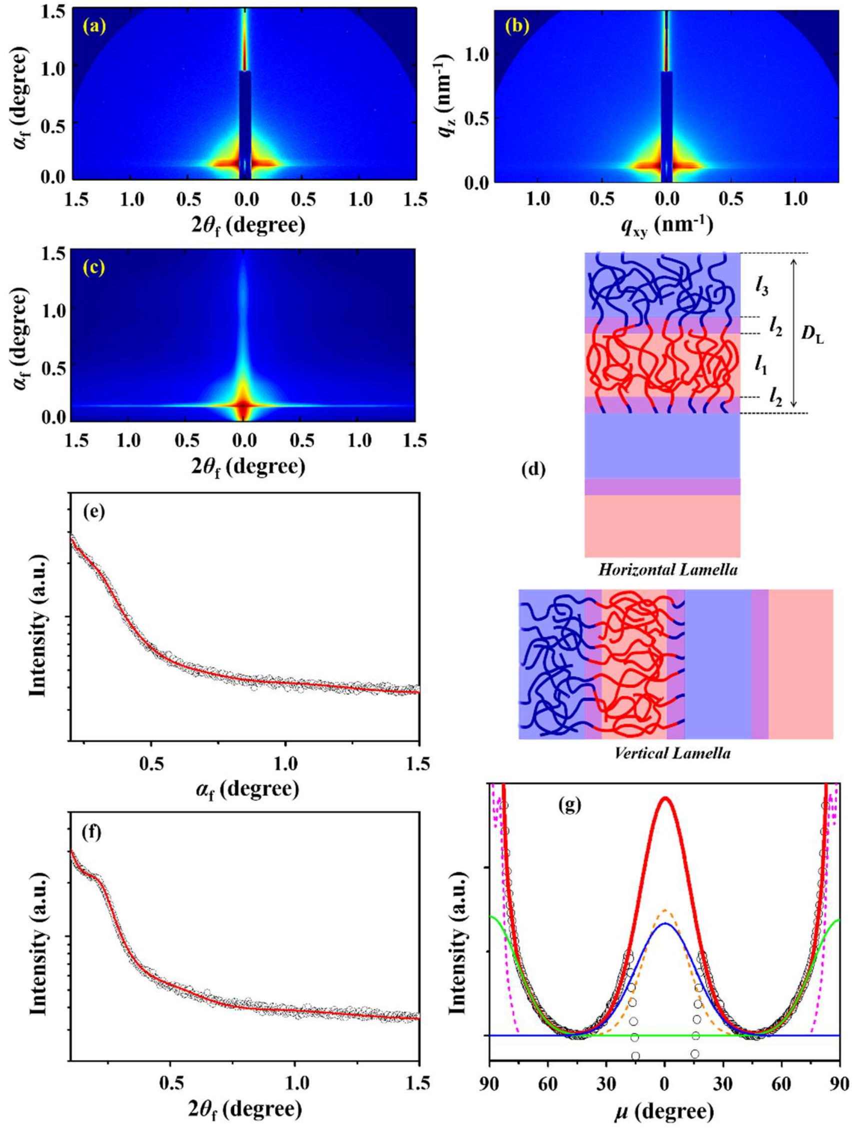

Figure 5.6. Representative GISAXS data of *l*-PDGE-*b*-PTEGGE films (100–120 nm thick) measured with $\alpha_i = 0.1454°$; SDD = 2909.8 mm at room temperature using a synchrotron X-ray beam ($\lambda = 0.12095$ nm): (a) 2D scattering image in angle space; (b) 2D scattering image in scattering vector space obtained from the scattering image in (a); (c) 2D scattering image reconstructed with the determined structural parameters; (d) lamellar structure model in a front view; (e) out-of-plane scattering profile extracted along the meridian line at $2\theta_f = 0.101°$ from the scattering image in (a); (f) in-plane scattering profile extracted along the equatorial line at $\alpha_f = 0.192°$ from the scattering image in (a). In (e and f), the symbols are the measured data and the solid red lines were obtained by fitting the data using the GIXS formula of lamellar structure models. (g) Azimuthal scattering profile extracted at $q = 0.305$ nm^{-1} from the scattering image in (b); the black symbols are the measured data; the lines were obtained by the deconvolutions of the measured data: the blue solid line is the first order scattering peak of horizontal lamellar structure, the green solid line is the first order scattering peak of vertical lamellar structure, the purple dot line is the Yoneda peak, the brown dot line is a part of the reflected X-ray beam, and the red solid line is the sum of all deconvoluted peaks.

Third, the domain spacing in the cylindrical structured *c*-PDGE-*b*-PTEGGE film is 49.3–53.7 % smaller in the out-of-plane of the film and 64.8–67.6 % smaller in the in-plane of the film, compared to those in the lamellar structured *l*-PDGE-*b*-PTEGGE film. The domain spacing reductions are much larger than those predicted theoretically for pairs of cyclic and linear block copolymers[66-68] and that reported previously for the pair of cyclic and linear poly(styrene-*block*-ethylene oxide)s in thin films.[69] Moreover, the domain spacing reductions are huge, compared to those observed for the pairs of cyclic and linear block copolymers in bulk states.[55,62-64] Collectively, the *c*-PDGE-*b*-PTEGGE system of this study, for the first time, demonstrates a huge reduction (49.3–67.6 %) in the domain spacing with respect to those of the linear counterpart.

Fourth, the domain spacing in the cylindrical structured *tp-A*-PDGE-*b*-PTEGGE film is 25.0–29.4 % smaller in the out-of-plane of the film and 53.8–56.5 % smaller in the in-plane of the film, compared to those in the lamellar structured *l*-PDGE-*b*-PTEGGE film. These domain reductions are comparable to or much larger than those predicted theoretically and reported previously for pairs of cyclic and linear block copolymers.[66-69] These results open up a new approach using tadpole block copolymer in order to significantly reduce domain spacing in the phase-separated nanostructure formation.

Fifth, the domain spacing in the lamellar structured *tp*-*B*-PDGE-*b*-PTEGGE film is 28.3–32.5 % smaller than those in the lamellar structured *l*-PDGE-*b*-PTEGGE film. This domain reduction is comparable to those predicted theoretically and reported previously for pairs of cyclic and linear block copolymers[66-69] but still much larger than those observed for the pairs of cyclic and linear block copolymers in bulk states.[55,62-64] This result again confirms that tadpole block copolymer is a new approach to significantly reduce domain spacing in the phase-separated nanostructure formation.

Sixth, the domain spacing of phase-separated nanostructure is in the increasing order: *c*-PDGE-*b*-PTEGGE (8.45−12.17 nm: 6.60−9.80 nm line and 1.65–2.40 nm space) < *tp-A*-PDGE-*b*-PTEGGE (11.10−18.00 nm: 8.80−14.40 nm line and 2.30–3.60 nm space) ≈ *tp-A*-PDGE-*b*-PTEGGE (17.20 nm: 8.80 nm line and 8.40 nm space) << *l*-PDGE-*b*-PTEGGE (24.00–25.50 nm: 12.10−12.90 nm line and 11.90−12.60 nm space). According to the International Technology Roadmap for Semiconductors (ITRS), the pitch in dynamic random access memory (DRAM) chips is scheduled to be 38 nm by this year (2019), 30 nm by 2021, 24 nm by 2024, 18 nm by 2027, and 16 nm by 2030; the pitch in microprocessor unit (MPU) chips is scheduled to be 24 nm by this year, 20 nm by 2021, and 12 nm by 2024−2030.[74] Such pitches correspond to the domain spacings in nanostructured polymers which can be used as nanolithographic materials. Taking this into account, the domain spacings of the nanostructured *c*-PDGE-*b*-PTEGGE, *tp-A*-PDGE-*b*-PTEGGE and *tp-A*-PDGE-*b*-PTEGGE can meet the pitches demanded for future advanced high performance DRAM and MPU chips. In particular, the domain spacings of *c*-PDGE-*b*-PTEGGE can meet further the pitches required for the development of the DRAM and MPU chips scheduled by 2030. Therefore, the film morphology results of this study suggest that the development and utilization of nanolithographic block copolymer materials in cyclic and tadpole topologies is a most suitable way to fabricate advanced DRAM and MPU chips in less than 20 nm pitches.

Seventh, in the nanoscale films, *c*-PDGE-*b*-PTEGGE has developed relatively well-defined and orientationally well-controlled domains via the phase-separation of the blocks, revealing smaller g factor value and higher O_s factor value (Table 5.2). In contrast, *l*-PDGE-*b*-PTEGGE has generated fuzzy (i.e., less-defined) domains in the same scale thin films; moreover, a mixture of horizontal and vertical nanostructures has been developed. Overall, the nanostructures of *l*-PDGE-*b*-PTEGGE show larger g factor value and lower O_s factor value (Table 5.2). These results are quite different from the relatively less defined domains in the *c*-

PS-*b*-PEO film and the more defined domains in the linear counterpart film.[69] These results collectively suggest that the *c*-PDGE-*b*-PTEGGE system of this study is a good potential candidate material for the production of well-defined and oriented nanostructure.

Eighth, in the nanoscale films, both *tp-A*-PDGE-*b*-PTEGGE and *tp-B*-PDGE-*b*-PTEGGE have produced well-defined and well-orientated domains, revealing smaller *g* factor values and higher O_s factor values, compared to their linear counterpart. These results indicate that the *tp-A*-PDGE-*b*-PTEGGE and *tp-B*-PDGE-*b*-PTEGGE systems are good potential for the production of well-defined and oriented nanostructures.

Ninth, the individual blocks of all topological diblock copolymers in this study have the almost same degree of polymerizations (i.e., the same chain lengths) as well as the almost same volume fractions. Both the blocks may be flexible in the view of chain characteristics. Thus, one can expect that they all form lamellar structures which consist of phase-separated polar and nonpolar block domains. As expected, *l*-PDGE-*b*-PTEGGE was found to form lamellar structure. *tp-B*-PDGE-*b*-PTEGGE (which consists of linear nonpolar and cyclic polar blocks) also formed lamellar structure. These results indicate that the cyclic PTEGGE block owns chain characteristics close to those of its linear counterpart and, indeed, makes no severe impact on the phase diagram of PDGE-*b*-PTEGGE. Surprisingly, both *c*-PDGE-*b*-PTEGGE and *tp-A*-PDGE-*b*-PTEGGE (which is composed of cyclic nonpolar and linear polar blocks) have, however, revealed hexagonal cylindrical structures, which are different from the expected lamellar structures. These hexagonal cylindrical structures are evidences that the chain characteristics of the PDGE block are changed and thus cause a shift in the phase diagram of PDGE-*b*-PTEGGE when it becomes either a half of the cyclic block copolymer or a cyclic form. Collectively the results give further information that the topological effects of the PDGE block are more significant in the nanoscale film morphology than those of the PTEGGE block.

Tenth, *c*-PDGE-*b*-PTEGGE, as well as *tp-A*-PDGE-*b*-PTEGGE formed horizontally-oriented ellipsoidal cylinder domains in the nanoscale films. Here, a question is raised: Why did they form ellipsoidal cylinders rather than spherical cylinders? These ellipsoidal cylinder formations may be attributed to at least two possible factors as follows. The first possible factor is a geometrical confinement effect due to the nanoscale films. In the formation of phase-separated domains in the nanoscale film, the cross-sectional growth of the PTEGGE cylinders may be relatively restricted in the in-plane of the film because of the presence of the semicyclic or cyclic PDGE matrix adhered physically onto the silicon substrate. In contrast, the PTEGGE cylinders' cross-sectional growth may be easier toward the air and vacuum interface. These asymmetric growths may lead to ellipsoidal PTEGGE cylinders. The second possible factor is the molecular topological effect. The ellipsoidicity ratio ε (= polar radius/equatorial radius) is 1.42−1.49 for the cylindrical domains composed of the semicyclic PTEGGE block chains in the matrix consisted of the semicyclic PDGE block chains, and 1.64 for the cylindrical domains composed of the linear PTEGGE block chains in the matrix consisted of the cyclic PDGE block chains. This ellipsoidicity difference may be attributed to the molecular topology difference in the PDGE blocks as well as in the PTEGGE blocks.

Finally, the L_z/L_y ratio (= γ) is 1.43−1.50 for the hexagonal cylinder structure in the *c*-PDGE-*b*-PTEGGE film and 1.62 for that in the *tp-A*-PDGE-*b*-PTEGGE film. These γ values are very far from that ($\sqrt{3}/2$) of a regular hexagonal cylinder structure. These results indicate that the hexagonal cylinder structure in the *c*-PDGE-*b*-PTEGGE film, as well as in the *tp-A*-PDGE-*b*-PTEGGE film is significantly distorted along the out-of-plane of the film. These structural distortions might result from the highly-ellipsoidal cylinder domains formed in the films. The structural distortion is more significant for the cylindrical domains in the *tp-A*-PDGE-*b*-PTEGGE film, compared to those in the *c*-PDGE-*b*-PTEGGE film. This difference may be counted as an evidence of the molecular topology effects.

5.4 Conclusions

In this chapter, the nanoscale film morphologies of a series of cyclic and tadpole block copolymers including their linear counterpart were investigated in details for the first time by using synchrotron GIXS analysis: *c*-PDGE-*b*-PTEGGE, *tp-A*-PDGE-*b*-PTEGGE, *tp-B*-PDGE-*b*-PTEGGE, and *l*-PDGE-*b*-PTEGGE. The quantitative GIXS analysis provides structural details on the nanoscale film morphologies and key features on the correlations between film morphology and molecular topology.

All topological block copolymers revealed nanostructures which were driven by the immiscibility due to a polarity difference between the blocks. The type of phase-separated nanostructure was highly dependent upon the molecular topology of the block copolymer: *c*-PDGE-*b*-PTEGGE and *tp-A*-PDGE-*b*-PTEGGE exhibited hexagonal cylindrical structures, whereas *tp-B*-PDGE-*b*-PTEGGE and *l*-PDGE-*b*-PTEGGE revealed lamellar structures. Furthermore, the domain spacing of phase-separated nanostructure was significantly dependent upon the block copolymer topology: *c*-PDGE-*b*-PTEGGE < *tp-A*-PDGE-*b*-PTEGGE ≈ *tp-A*-PDGE-*b*-PTEGGE << *l*-PDGE-*b*-PTEGGE. In particular, *c*-PDGE-*b*-PTEGGE generated 49.3–67.6 % smaller domains, compared to those of the linear counterpart. These domain spacing reductions are so remarkable because they are almost twice larger than those predicted theoretically and reported previously. In cases of *tp-A*-PDGE-*b*-PTEGGE and *tp-B*-PDGE-*b*-PTEGGE, the domains were 25.0–32.5 % smaller than those of the linear counterpart. These domain spacing reductions are comparable to those either predicted theoretically or observed previously. Moreover, the cyclic block copolymer and its tadpole counterparts developed well-defined and well-oriented domain structures, compared to the poorly developed domains of the linear counterpart.

In this chapter, quantitative analysis through three layer model and two phase elliptical hexagonal cylinder model was successful to parameterize the morphological details of cyclic and tadpole block copolymers in thin films. The two models successfully identified the cyclic and tadpole topologies as powerful strategies for producing well-defined, orientation-controlled, and miniaturized domain-based nanostructures, showing great potential for developing high performance nanolithographic materials with the pitches demanded for fabricating advanced semiconductor chips planned by ITRS. Overall, the novel model analysis have successfully established new insights in the topology-morphology correlation of cyclic and tadpole block copolymers.

5.5 References

1. Patnode, W.; Wilcock, D. F. Methylpolysiloxanes. *J. Am. Chem. Soc.***1946**, *68*, 358−363.
2. Hunter, M. J.; Hyde, J. F.; Warrick, E. L.; Fletcher, H. J. Organo-Silicon Polymers. The Cyclic Dimethyl Siloxanes. *J. Am. Chem. Soc.***1946**, *68*, 667−672.
3. Scott, D. W. Equilibria between Linear and Cyclic Polymers in Methylpolysiloxanes. *J. Am. Chem. Soc.* **1946**, *68*, 2294−2298.
4. Zimm, B. H; Stockmayer, W. H. The Dimensions of Chain Molecules Containing Branches and Rings. *J. Chem. Phys*. **1949**, *17*, 1301−1314.
5. Fiers, W.; Sinsheimer, R. L. The structure of the DNA of bacteriophage φX174: I. The action of exopolynucleotidases. *J. Mol. Biol.* **1962**, *5*, 408−419.
6. Fiers, W.; Sinsheimer, R. L. The Structure of the DNA of Bacteriophage φX174: II. Thermal Inactivation. *J. Mol. Biol.* **1962**, *5*, 420−423.
7. Dulbecco, R.; Vogt, M. Evidence for A Ring Structure of Polyoma Virus DNA. *Proc. Natl. Acad. Sci. USA* **1963**, *50*, 236−243.
8. Weil, R.; Vinograd, J. The Cyclic Helix and Cyclic Coil Forms of Polyoma Viral DNA. *Proc. Natl. Acad. Sci. USA* **1963**, *50*, 730−738.
9. Witherup, K.M.; Bogusky, M.J.; Anderson, P.S.; Ramjit, H.; Ransom, R.W.; Wood, T.; Sardana, M. Cyclopsychotride A, A Biologically Active, 31-Residue Cyclic Peptide Isolated from Psychotria Longipes. *J. Nat. Prod.* **1994**, *57*, 1619–1625.
10. Cascales, L.; Craik, D. J. Naturally Occurring Circular Proteins: Distribution, Biosynthesis and Evolution. *Org. Biomol. Chem.* **2010**, *8*, 5035–5047.
11. Dell, A.; Oates, J.; Lugowski, C.; Romanowska, E.; Kenne, L.; Lindberg, B. The Enterobacterial Common-Antigen, A Cyclic Polysaccharide. *Carbohydr. Res.* **1984**, *133*, 95–104.
12. Dodgson, K.; Semlyen, J. A. Studies of Cyclic and Linear Poly(dimethylsiloxanes): 1. Limiting Viscosity Number-Molecular Weight Relationships. *Polymer* **1977**, *18*, 1265−1268.
13. Hild, G.; Kohler, A.; Rempp, P. Synthesis of Ring-Shaped Macromolecules. *Eur. Polym. J.* **1980**, *16*, 525−527.
14. Roovers, J.; Toporowski, P. M. Synthesis of High Molecular Weight Ring Polystyrenes. *Macromolecules* **1983**, *16*, 843−849.
15. Kricheldorf, H. R.; Lee, S.-R.; Schittenhelm, N. Macrocycles, 1. Macrocyclic Polymerizations of (Thio)lactones–Stepwise Ring Expansion and Ring Contraction. *Macromol. Chem. Phys*. **1998**, *199*, 273–282.
16. Kricheldorf, H. R.; Eggerstedt, S. Macrocycles, 2. Living Macrocyclic Polymerization of ε-Caprolactone with 2,2-Dibutyl-2-stanna-1,3-dioxepane as Initiator. *Macromol. Chem. Phys.* **1998**, *199*, 283−290.
17. Hadjichristidis, N.; Pitsikalis, M.; Pispas, S.; Iatrou, H. Polymers with Complex Architecture by Living Anionic Polymerization. *Chem. Rev.* **2001**, *101*, 3747−3792.
18. Semlyen, J. A. Cyclic Polymers, 2nd ed., Kluwer Academic Publishers: Dordrecht, Netherlands, 2002.
19. Laurent B. A.; Grayson, S. M. Synthetic Approaches for the Preparation of Cyclic Polymers. *Chem. Soc. Rev.* **2009**, *38*, 2202–2213.
20. Kricheldorf, H. R. Cyclic Polymers: Synthetic Strategies and Physical Properties. *J. Polym. Sci. Part A: Polym. Chem.* **2010**, *48*, 251− 284.
21. Jia, Z.; Monteiro, M.J. Cyclic Polymers: Methods and Strategies. *J. Polym. Sci. Part A: Polym. Chem*. **2012**, *50*, 2085−2097.
22. Xiang, L.; Ryu, W.; Kim, H.; Ree, M. Precise Synthesis, Properties, and Structures of Cyclic Poly(ε-caprolactone)s. *Polymers* **2018**, *10*, 577.

23. Liu, B.; Wang, H.; Zhang, L.; Yang, G.; Liu, X.; Kim, I. A Facile Approach for the Synthesis of Cyclic Poly(*N*-isopropylacrylamide) Based on An Anthracene–Thiol Click Reaction. *Polym. Chem.* **2013**, *4*, 2428–2431.
24. Ogawa, T.; Nakazono K.; Aoki D.; Uchida S.; Takata T. Effective Approaches to Cyclic Polymer from Linear Polymer: Synthesis and Transformation of Macromolecular [1]Rotaxane. *ACS Macro Lett*. **2015**, *4*, 343−347.
25. Culkin, D. A.; Jeong, W.; Csihony, S.; Gomez, E. D.; Balsara, N.R.; Hedrick, J. L.; Waymouth, R. M. Zwitterionic Polymerization of Lactide to Cyclic Poly(lactide) by Using *N*-Heterocyclic Carbine Organocatalysts. *Angew. Chem. Int. Ed.* **2007**, *46*, 2627–2630.
26. Castro-Osma, J. A.; Alonso-Moreno, C.; García-Martinez, J. C.; Fernández-Baeza, J.; Sánchez-Barba, L. F.; Lara-Sánchez, A.; Otero, A. Ring-Opening (ROP) versus Ring-Extension (REP) Polymerization of *ε*-Caprolactone to Give Linear or Cyclic Polycaprolatones. *Macromolecules* **2013**, *46*, 6388−6394.
27. Wang, H.; Zhang, L.; Liu, B.; Han, B.; Duan, Z.; Qi, C.; Park, D.; Kim, I. Synthesis of High Molecular Weight Cyclic Poly(*ε*-caprolactone)s of Variable Ring Size Based on A Light-Induced Ring-Closure Approach. *Macromol. Rapid Commun*. **2015**, *36*, 1646−1650.
28. Isono, T.; Sasamori, T.; Honda, K.; Mato, Y.; Yamamoto, T.; Tajima, K.; Satoh, T. Multicyclic Polymer Synthesis through Controlled/Living Cyclopolymerization of α,ω-Dinorbornenyl-Functionalized Macromonomers. *Macromolecules* **2018**, *51*, 3855–3864.
29. Mato, Y.; Honda, K.; Tajima, K.; Yamamoto, T.; Isono, T.; Satoh, T. A Versatile Synthetic Strategy for Macromolecular Cages: Intramolecular Consecutive Cyclization of Star-Shaped Polymers. *Chem. Sci.* **2019**, *10*, 440–446.
30. Yamamoto, T.; Hosokawa, M.; Nakamura, M.; Sato, S.-i.; Isono, T.; Tajima, K.; Satoh, T.; Sato, M.; Tezuka, Y.; Saeki, A.; Kikkawa, Y. Synthesis, Isolation, and Properties of All Head-to-Tail Cyclic Poly(3-hexylthiophene): Fully Delocalized Exciton over the Defect-Free Ring Polymer. *Macromolecules* **2018**, *51*, 9284–9293.
31. Durmaz, H.; Dag, A.; Hizal, G.; Tunca, U. Cyclic Homo and Block Copolymers Through Sequential Double Click Reactions. *J. Polym. Sci. Part A: Polym. Chem.* **2010**, *48*, 5083–5091.
32. Tezuka, Y., Ed., Topological Polymer Chemistry: Progress of Cyclic Polymers in Syntheses, Properties and Functions, World Scientific: Hackensack, NJ, USA, 2013.
33. Jacobson, H.; Stockmayer, W. H. Intramolecular Reaction in Polycondensations. II. Ring-Chain Equilibrium in Polydecamethylene Adipate. *J. Chem. Phys.* **1950**, *18*, 1607–1612.
34. Geiser, D.; Höcker, H. Synthesis and Investigation of Macrocyclic Polystyrene. *Macromolecules* **1980**, *13*, 653–656.
35. Prentis, J. J. Spatial Correlations in A Self-Repelling Ring Polymer. *J. Chem. Phys.* **1982**, *76*, 1574−1583.
36. Roovers, J. The Melt Properties of Ring Polystyrenes. *Macromolecules* **1985**, *18*, 1359−1361.
37. Lee, H. C.; Lee, H.; Lee, W.; Chang, T.; Roovers, J. Fractionation of Cyclic Polystyrene from Linear Precursor by HPLC at The Chromatographic Critical Condition. *Macromolecules* **2000**, *33*, 8119−8121.
38. Hur, K.; Winkler, R. G.; Yoon, D. Y. Comparison of Ring and Linear Polyethylene from Molecular Dynamics Simulations. *Macromolecules* **2006**, *39*, 3975−3977.
39. Hur, K.; Jeong, C.; Winkler, R. G.; Lacevic, N.; Gee, R. H.; Yoon, D. Y. Chain Dynamics of Ring and Linear Polyethylene Melts from Molecular Dynamics Simulations. *Macromolecules* **2011**, *44*, 2311−2315.

40. Qiu, X.-P.; Tanaka, F.; Winnik, F. M. Temperature-Induced Phase Transition of Well-Defined Cyclic Poly(*N*-isopropylacrylamide)s in Aqueous Solution. *Macromolecules* **2007**, *40*, 7069–7071.
41. Ren, J. M.; Satoh, K.; Goh, T. K.; Blencowe, A.; Nagai, K.; Ishitake, K.; Christofferson, A. J.; Yiapanis, G.; Yarovsky, I.; Kamigaito, M.; Qiao, G. G. Stereospecific Cyclic Poly(methyl methacrylate) and Its Topology-Guided Hierarchically Controlled Supramolecular Assemblies. *Angew. Chem. Int. Ed.* **2014**, *53*, 459–464.
42. Shin, E. J.; Jeong, W.; Brown, H. A.; Koo, B. J.; Hedrick, J. L.; Waymouth, R. M. Crystallization of Cyclic Polymers: Synthesis and Crystallization Behavior of High Molecular Weight Cyclic Poly(ε-caprolactone)s. *Macromolecules* **2011**, *44*, 2773–2779.
43. Cooke, J.; Viras, K.; Yu, G.-E.; Sun, T.; Yonemitsu, T.; Ryan, A. J.; Price, C.; Booth, C. Large Cyclic Poly(oxyethylene)s: Chain Folding in The Crystalline State Studied by Raman Spectroscopy, X-ray Scattering, and Differential Scanning Calorimetry. *Macromolecules* **1998**, *31*, 3030–3039.
44. Zhu, X.; Zhou, N.; Zhang, Z.; Sun, B.; Yang, Y.; Zhu, J.; Zhu, X. Cyclic Polymers with Pendent Carbazole Units: Enhanced Fluorescence and Redox Behavior. *Angew. Chem. Int. Ed.* **2011**, *50*, 6615–6618.
45. Su, H.; Chen, H.; Díaz, A.; Casas, M. T.; Ouiggalí, J.; Hoskins, J. N.; Grayson, S. N.; Pérez, R. A.; Müller, A. J. New Insight on The Crystallization and Melting of Cyclic PCL Chains on The Basis of A Modified Thomson-Gibbs Equation. *Polymer* **2013**, *54*, 846−859.
46. Ishizu, K.; Ichimura, A. Synthesis of Cyclic Diblock Copolymers by Interfacial Condensation. *Polymer* **1998**, *39*, 6555−6558.
47. Schmidt, B. V. K. J.; Fechler, N.; Falkenhagen, J.; Lutz, J.-F. Controlled Folding of Synthetic Polymer Chains Through The Formation of Positionable Covalent Bridges. *Nat. Chem.* **2011**, *3*, 234−238.
48. Wan, X.; Liu, T.; Liu, S. Synthesis of Amphiphilic Tadpole-Shaped Linear-Cyclic Diblock Copolymers via Ring-Opening Polymerization Directly Initiating from Cyclic Precursors and Their Application as Drug Nanocarriers. *Biomacromolecules* **2011**, *12*, 1146–1154.
49. Isono, T.; Satoh, Y.; Miyachi, K.; Chen, Y.; Sato, S.-i.; Tajima, K.; Satoh, T.; Kakuchi, T. Synthesis of Linear, Cyclic, Figure-Eight-Shaped, and Tadpole Shaped Amphiphilic Block Copolyethers via t-Bu-P4-Catalyzed RingOpening Polymerization of Hydrophilic and Hydrophobic Glycidyl Ethers. *Macromolecues* **2014**, *47*, 2853−2863.
50. Satoh, Y.; Matsuno, H.; Yamamoto, T.; Tajima, K.; Isono, T.; Satoh, T. Synthesis of Well-Defined Three- and Four-Armed Cage-Shaped Polymers via “Topological Conversion” from Trefoil- and Quatrefoil- Shaped Polymers. *Macromolecules* **2017**, *50*, 97−106.
51. Shingu, T.; Yamamoto, T.; Tajima, K.; Isono, T.; Satoh, T. Synthesis of μ-ABC Tricyclic Miktoarm Star Polymer via Intramolecular Click Cyclization. *Polymers* **2018**, *10*, 877.
52. Honda, S.; Yamamoto, T.; Tezuka, Y. Topology-Directed Control on Thermal Stability: Micelles Formed from Linear and Cyclized Amphiphilic Block Copolymers. *J. Am. Chem. Soc.* **2010**, *132*, 10251−10253.
53. Minatti, E.; Borsali, R.; Schappacher, M.; Deffieux, A.; Soldi, V.; Narayanan, T.; Putaux, J.-L. Effect of Cyclization of Polystyrene/Polyisoprene Block Copolymers on Their Micellar Morphology. *Macromol. Rapid Commun.* **2002**, *23*, 978–982.
54. Lonsdale, D. E.; Monteiro, M. J. Synthesis and Self-Assembly of Amphiphilic Macrocyclic Block Copolymer Topologies. *J. Polym. Sci. Part A: Polym. Chem.* **2011**, *49*, 4603–4612.

55. Honda, S.; Koga, M.; Tokita, M.; Yamamoto, T.; Tezuka, Y. Phase Separation and Self-Assembly of Cyclic Amphiphilic Block Copolymers with A Main-Chain Liquid Crystalline Segment. *Polym. Chem.* **2015**, *6*, 4167–4176.
56. Williams, R. J.; Dove, A. P.; O'Reilly, R. K. Self-Assembly of Cyclic Polymers. *Polym. Chem.* **2015**, *6*, 2998–3008.
57. Zhao, Y.; Liu, Y.-T.; Lu, Z.-Y.; Sun, C.-C. Effect of Molecular Architecture on The Morphology Diversity of The Multicompartment Micelles: A Dissipative Particle Dynamics Simulation Study. *Polymer* **2008**, *49*, 4899–4909.
58. Heo, K.; Kim, Y. Y.; Kitazawa, Y.; Kim, M.; Jin, K. S.; Yamamoto, T.; Ree, M. Structural Characteristics of Amphiphilic Cyclic and Linear Block Copolymer Micelles in Aqueous Solutions. *ACS Macro Lett.* **2014**, *3*, 233−239.
59. Ree, B. J.; Satoh, Y.; Jin, K. S.; Isono, T.; Kim, W. J.; Kakuchi, T.; Satoh, T.; Ree, M. Well-Defined Stable Nanomicelles Self-Assembled by Brush Cyclic and Tadpole Copolymer Amphiphiles: A Versatile Smart Carrier Platform. *NPG Asia Materials* **2017**, *9*, e453.
60. Ree, B. J.; Satoh, T.; Yamamoto, T. Micelle Structure Details and Stabilities of Cyclic Block Copolymer Amphiphile and Its Linear Analogues. *Polymers* **2019**, *11*, 163.
61. Ree, B. J.; Lee, J.; Satoh, Y.; Kwon, K.; Isono, T.; Satoh, T.; Ree, M. A Comparative Study of Dynamic Light and X-ray Scatterings on Micelles of Topological Polymer Amphiphiles. *Polymers* **2018**, *10*, 1347.
62. Zhu, Y. Q.; Gido, S. P.; Iatrou, H.; Hadjichristidis, N.; Mays, J. W. Microphase Separation of Cyclic Block Copolymers of Styrene and Butadiene and of Their Corresponding Linear Triblock Copolymers. *Macromolecules* **2003**, *36*, 148−152.
63. Takano, A.; Kadoi, O.; Hirahara, K.; Kawahara, S.; Isono, Y.; Suzuki, J.; Matsushita, Y. Preparation and Morphology of Ring-Shaped Polystyrene-block-polyisoprenes, *Macromolecules* **2003**, *36*, 3045−3050.
64. Lescanec, R. L.; Hajduk, D. A.; Kim, G. Y.; Gan, Y.; Yin, R.; Gruner, S. M.; Hogen-Esch, T. E.; Thomas, E. L. Comparison of the Lamellar Morphology of Microphase-Separated Cyclic Block Copolymers and Their Linear Precursors. *Macromolecules* **1995**, *28*, 3485−3489.
65. Lecommandoux, S.; Borsali, R.; Schappacher, M.; Deffieux, A.; Narayanan, T.; Rochas, C. Microphase Separation of Linear and Cyclic Block Copolymers Poly(styrene-b-isoprene): SAXS Experiments. *Macromolecules* **2004**, *37*, 1843−1848.
66. Marko, J. F. Microphase Separation of Block Copolymer Rings. *Macromolecules* **1993**, *26*, 1442−1444.
67. Jo, W. H.; Jang, S. S. Monte Carlo Simulation of The Order–Disorder Transition of A Symmetric Cyclic Diblock Copolymer System. *J. Chem. Phys.* **1999**, *111*, 1712−1720.
68. Zhang, G.; Fan, Z.; Yang, Y.; Qiu, F. Phase Behaviors of Cyclic Diblock Copolymers. *J. Chem. Phys.* **2011**, *135*, 174902.
69. Poelma, J. E.; Ono, K.; Miyajima, D.; Aida, T.; Satoh, K.; Hawker, C. J. Cyclic Block Copolymers for Controlling Feature Sizes in Block Copolymer Lithography. *ACS Nano* **2012**, *6*, 10845−10854.
70. Lee, B.; Park, Y.-H.; Hwang, Y.-T.; Oh, W.; Yoon, J.; Ree, M. Ultralow-*k* Nanoporous Organosilicate Dielectric Films Imprinted with Dendritic Spheres. *Nat. Mater.* **2005**, *4*, 147–150.
71. Ree, M. Probing the Self-Assembled Nanostructures of Functional Polymers with Synchrotron Grazing Incidence X-Ray Scattering. *Macromol. Rapid Commun.* **2014**, *35*, 930–959.
72. Kim, Y. Y.; Ree, B. J.; Kido, M.; Ko, Y.-G.; Ishige, R.; Hirai, T.; Wi, D.; Kim, J.; Kim, W. J.; Takahara, A.; Ree, M. High Performance n-Type Electrical Memory and

Morphology-Induced Memory-Mode Tuning of A Well-Defined Brush Polymer Bearing Perylene Diimide Moieties. *Adv. Electronic Mater.* **2015**, *1*, 1500197.

73. Ree, B. J.; Aoki, D.; Kim, J.; Satoh, T.; Takata, T.; Ree, M. Macromolecular [2]Rotaxanes Linked with Polystyrene: Properties and Nanoscale Film Morphologies. *Macromolecules* **2019**, *52*, 5325−5336.
74. Semiconductor Industry Association, *The International Technology Roadmap for Semiconductors 2.0, 2015 Edition*, 2015; www.itrs2.net/

Chapter 6

Nanoscale Film Morphologies of Bicyclic Block Copolyethers

6.1 Introduction

Cyclic polymers have gained great attention from academia and industry because of unique features in properties due to the chain-endless nature.[1-10] However, they have been challenged in the aspect of synthesis because of difficulties in the cyclization reaction and subsequent purification. To overcome such difficulties, much research effort has been made so far; as a result, several synthetic methods have been developed, introduced some cyclic block polymers.[3-25] Interestingly, a few figure-eight-shaped (i.e., *bicyclic*) homoblock polymer systems have been synthesized from styrene and ethylene oxide monomers: (cyclic polystyrene)-*block*-(cyclic polystyrene),[26-29] [cyclic poly(ethylene oxide)-*block*-[cyclic poly(ethylene oxide)].[30] Bicyclic heteroblock copolymer systems have also been reported: (cyclic polystyrene)-*block*-[cyclic poly(ε-caprolactone)],[31,32] [cyclic poly(ethylene oxide)]-*block*-[cyclic poly(tetrahydrofuran)],[32] and [cyclic poly(ethylene oxide)]-*block*-(cyclic polystyrenen).[33] In addition, a series of bicyclic heteroblock copolymers in various topologies has been prepared successfully.[34] Overall, significant progress has been made on the synthesis and chemical composition analysis of cyclic polymers including bicyclic polymers. Nevertheless, they have been yet understood in detail due to severe limits in the material availabilities as well as in the characterization effort of properties and morphologies.[35-58] In particular, the nanoscale film morphologies of bicyclic block copolymers could yet be examined.

In this chapter, the nanoscale film morphologies of a series of *bicyclic* heteroblock copolymers composed of poly(*n*-decyl glycidyl ether) (PDGE) and poly(2-(2-(2-methoxyethoxy)ethoxy)ethyl glycidyl ether) (PTEGGE): *Bicycle-A, B, C,* and *D* is reported for the first time (Figure 6.1; Table 6.1). They have been investigated by synchrotron grazing incidence X-ray scattering (GIXS). This quantitative GIXS analysis provides structural parameter details. Due to the immiscibility of PDGE and PTEGGE blocks, all bicyclic copolymers form phase-separated nanostructures. *Bicycle-A* forms cylindrical structure; but the others form lamellar structures. All nanostructures show remarkably reduced domain spacings, which could not be achievable from the linear block copolymer counterpart. Such exceptionally smaller domain spacings have yet been predicted even theoretically. All nanostructural details are discussed in correlations with the molecular topology effects.

(a) ***Bicycle-A*** **(c)** ***Bicycle-B***

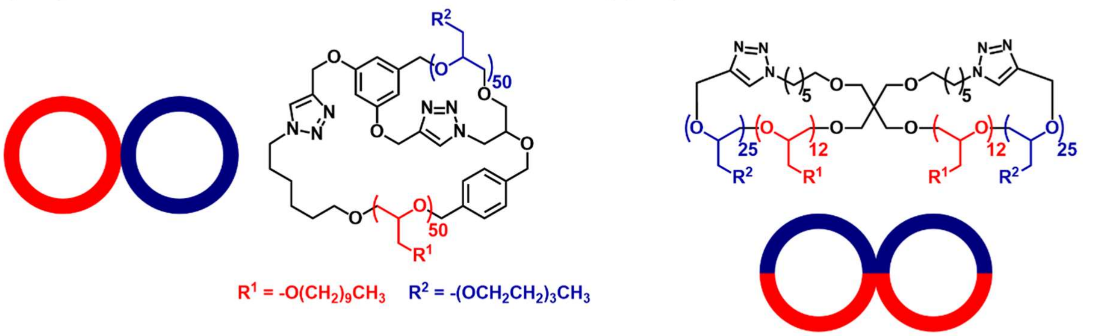

(b) ***Bicycle-C*** **(d)** ***Bicycle-D***

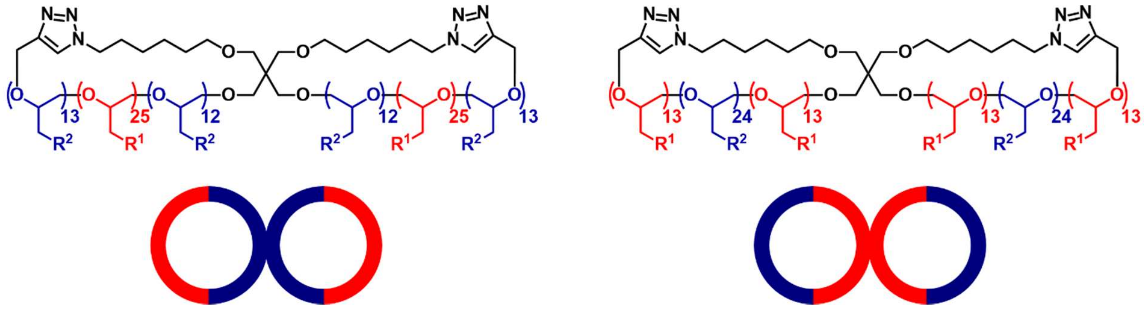

Figure 6.1. Chemical structures of bicyclic poly(*n*-decyl glycidyl ether-*block*-2-(2-(2-methoxyethoxy)ethoxy)ethyl glycidyl ether)s in various topologies.

Table 6.1. Molecular characteristics of various bicyclic heteroblock copolymers and their homopolymers [a]

Polymer	$M_{n,NMR}$ [b] (kDa)	$Đ$ [c]	ρ_e [d] (nm^{-3})	ρ_m [e] (g/cm^3)	PDGE block		PTEGGE block	
					DP_{PDGE} [f]	ϕ_{PDGE} [g]	DP_{PTEGGE} [h]	ϕ_{PTEGGE} [i]
Bicycle-A	22.2	1.04			50	0.504	50	0.496
Bicycle-B	21.8	1.06			52	0.514	48	0.486
Bicycle-C	22.2	1.03			50	0.504	50	0.496
Bicycle-D	22.3	1.03			49	0.524	51	0.476
l-PDGE	11.1	1.03	341	1.01				
l-PTEGGE	11.2	1.04	353	1.05				

[a]Data from reference no. 34 and 48. [b]Number-average molecular weight in the unit of kDa (10^3 Da) of polymer determined by ^{1}H NMR spectroscopic analysis. [c]Dispersity value of polymer determined by size exclusion chromatography (SEC) analysis in tetrahydrofuran. [d]Electron density of polymer in films determined by X-ray reflectivity analysis. [e]Mass density of polymer in films obtained from the electron density determined by X-ray reflectivity analysis. [f]Number-average degree of polymerization of PDGE block determined by ^{1}H NMR spectroscopic analysis. [g]Volume fraction of PDGE block estimated from the $M_{n,NMR}$ and ρ_m data. [h]Number-average degree of polymerization of PTEGGE block determined by ^{1}H NMR spectroscopic analysis. [i]Volume fraction of PTEGGE block estimated from the $M_{n,NMR}$ and ρ_m data.

6.2 Experimental Section

Four different *bicyclic* PDGE-*b*-PTEGGE polymers were synthesized and characterized as reported previously in the literature;[34] in addition, their linear counterpart and homopolymers were prepared in chapter 5.[34,48] The molecular characteristics of these polymers are summarized in Table 6.1. For each bicyclic block copolymer, a solution with 0.5 wt% concentration was prepared in tetrahydrofuran and filtrated via a disposable syringe equipped with polytetrafluoroethylene filter membrane (0.2 μm pores). The prepared polymer solutions were spin-coated onto silicon substrates and followed by drying in vacuum at room temperature for 24 h. Thicknesses of the obtained films were measured by using a spectroscopic ellipsometer (Model M-2000, Woollam, Lincoln, NE, USA); the film thicknesses ranged in 100−120 nm. The individual film samples were stored in a vacuum chamber at room temperature before measurements.

Wide and small angle grazing incidence X-ray scattering (GIWAXS and GISAXS) measurements were conducted with an X-ray beam of 0.12095 nm wavelength λ at the PLS-II 3C beamline[59-61] (3rd-generation synchrotron radiation facility with 3.0 GeV power, Pohang Accelerator Laboratory, Pohang, Korea) using a two-dimensional (2D) charge-coupled detector (CCD) (model Rayonix 2D SX 165, Rayonix, Evanston, IL, USA). The sample-to-detector distance (SDD) was set by 213.5 mm for GIWAXS measurements and 2909.8 mm for GISAXS measurements; the incidence angle α_i of X-ray beam with respect to the film sample surface was set in the range 0.1270–0.1450°, which was between the critical angles of the polymer film and the silicon substrate ($\alpha_{c,f}$ and $\alpha_{c,s}$). A set of aluminum foils was used as a semi-transparent beam stop. Each scattering pattern was collected for 10−30 s. The scattering angles were corrected according to the positions of the X-ray beams reflected from the silicon substrate as well as by using precalibrated standards such as polystyrene-*block*-poly(ethylene-*random*-butylene)-*block*-polystyrene and silver behenate standards (Tokyo Chemical Inc., Tokyo, Japan).

6.3 Results and Discussion

All nanoscale films (100−120 nm thick) of bicyclic block copolymers reveal featureless GIWAXS images, as shown in Figure 6.2. Only two halo scattering rings are discernible. For the individual copolymers, one halo ring appears around 3.0° (ca. 2.3 nm *d*-spacing), which corresponds to the mean interdistance between the polymer chains; another ring is observed around 15.0° (ca. 4.6 nm *d*-spacing), which is attributed to the mean interdistance between the polymer chain and the side group and between the side groups. Overall, in all films at room temperature the PDGE and PTEGGE blocks are amorphous, showing no crystalline natures.

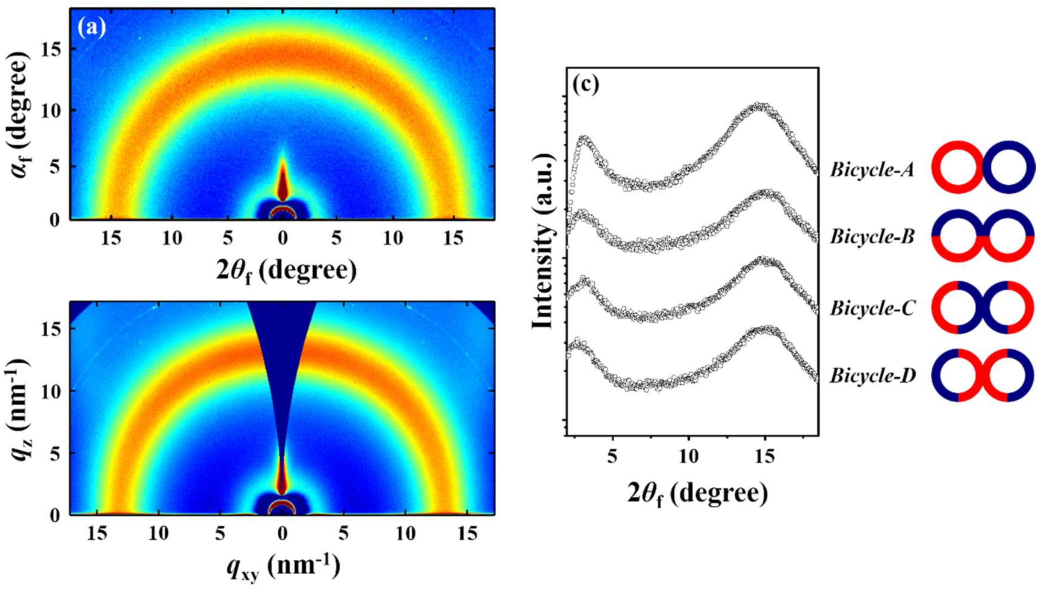

Figure 6.2. Representative GIWAXS data of the nanoscale films (100–120 nm thick) of bicyclic heteroblock copolymers measured with SDD = 213.5 mm at room temperature using a synchrotron X-ray beam (λ = 0.12095 nm): (a) 2D scattering image in angle space ($2\theta_f$ and α_f) of *Bicycle-A* (α_i = 0.1378°); (b) 2D scattering image in scattering vector space (q_{xy} and q_z) obtained from the scattering image in (a); (c) in-plane scattering profiles extracted along the equatorial line at α_f = 0.244° or 0.245° from the measured 2D scattering images, including the image in (a).

Different from the featureless GIWAXS images, featured GISAXS images are clearly discernible for all copolymer films, as shown in Figures 6.3a-b, 6.4a-b, 6.5a-b, and 6.6a-b. The scattering data inform that the PDGE and PTEGGE blocks in all topological bicyclic block copolymers are immiscible and thus undergo phase-separations through the nanoscale film fabrication process, forming nanostructures. The GISAXS images have been quantitatively investigated as follows.

The *Bicycle-A* film reveals two sets of scattering spots due to the grazing incidence optic setup (Figures 6.3a-b). The first set includes the scattering spots at ($2\theta_f$ = 0.000° and α_f = 0.489°), ($2\theta_f$ = 0.000° and α_f = 1.000°), ($2\theta_f$ = 0.401° and α_f = 0.228°), ($2\theta_f$ = 0.401° and α_f = 0.703°), and so on, which were generated by the transmitted X-ray beam. The second set includes the scattering spots at ($2\theta_f$ = 0.000° and α_f = 0.575°), ($2\theta_f$ = 0.000° and α_f = 1.112°), ($2\theta_f$ = 0.401° and α_f = 0.320°), ($2\theta_f$ = 0.401° and α_f = 0.801°), and so on, which were generated by the reflected X-ray beam. The spots at ($2\theta_f = 0.000°$ and $\alpha_f = 0.489°$) and ($2\theta_f = 0.000°$ and $\alpha_f = 1.000°$) in the transmitted pattern, as well as those at ($2\theta_f = 0.000°$ and $\alpha_f = 0.575°$) and ($2\theta_f = 0.000°$ and $\alpha_f = 1.112°$) in the reflected pattern, are estimated to have a relative scattering vector length of 1 and 2 from the specular reflection position, respectively. The spots at ($2\theta_f = 0.401°$ and $\alpha_f = 0.228°$) and ($2\theta_f = 0.401°$ and $\alpha_f = 0.703°$) in the transmitted pattern, as well as those at ($2\theta_f = 0.401°$ and $\alpha_f = 0.320°$) and ($2\theta_f = 0.401°$ and $\alpha_f = 0.801°$) in the reflected pattern, have a relative scattering vector length of 1 and $\sqrt{3}$ from the specular reflection position, respectively. Overall, these spots are typically characteristic of scatterings from a hexagonal packing order of cylindrical domains lain in the film plane. With these information, one-dimensional (1D) scattering profiles have been extracted from the 2D scattering image and then analyzed in detail. An out-of-plane and in-plane scattering profile (which were extracted along the median line at $2\theta_f = 0.179°$ and along the equatorial line at $\alpha_f = 0.220°$) are successfully analyzed using the grazing incidence X-ray scattering (GIXS) formula of hexagonal (HEX) cylinder structure model (Figures 6.3e-f; Figure 6.3d); a detail of the GIXS formula based on HEX cylinder structure model is given in Section 1.4 of Chapter 1. An azimuthal scattering profile has been additionally extracted at $q = 0.450$ nm^{-1} from the q-space image and followed by quantitative analysis (Figure 6.3g), providing the degree of structural orientation. All obtained dimensional parameters are summarized in Table 6.2.

The cylindrical domains are characteristic of structural feature in the following. The domain spacing is 11.70 nm (= L_z) along the out-of-plane of the film and 8.00 nm (= L_y) along the in-plane of the film. The ratio γ of L_z and L_y is 1.46, which is much larger than that (= $\sqrt{3}/2$) of regular HEX structure. This large γ value informs that the HEX cylindrical structure is highly distorted along the out-of-plane of the film. The individual cylinders reveal a cross-section consisted of a long radius R_z of 5.80 nm along the out-of-plane of the film and a short radius R_y of 2.60 nm along the in-plane of the film; here, R_z is the sum of a core part r_{cz} and a shell part t_{sz}, whereas R_y consists of a core part r_{cy} and a shell part t_{sy}. From these radii, the ellipsoidicity ratio ε is estimated to be 2.23. These cross-sectional characteristics suggest that the significant distortion of the HEX cylindrical structure is caused by the highly ellipsoidal nature of the cylindrical domains. From the structural parameters, the overall domains are estimated to have a volume fraction of 43.4 %. The volume fraction of the PDGE block in the copolymer is slightly higher than that of the PTEGGE block. Therefore, the cylindrical domains and the matrix could be made of the PTEGGE block chains and the PDGE block chains respectively. The HEX cylindrical structure is determined to show a positional distortion factor g of 0.09. This g value is reasonably small, suggesting that the HEX cylindrical structure formed in the film is stable dimensionally. The HEX structure further reveals a second order orientation factor O_s of 0.980 ($\overline{\varphi} = 0°$, the mean value of the polar angle φ (i.e., orientation angle) between the orientation vector $\boldsymbol{n}$ set along a direction normal to the {001} plane of HEX structure and the out-of-plane direction of the film; $\sigma_\varphi = 6.65°$, standard deviation for the polar angle φ). From these structural parameters, a 2D GISAXS image has been reconstructed by using the GIXS formula and compared with the measured raw scattering image (Figures 6.3a and 6.3c). They are in good agreement, again confirming that the quantitative analysis of the *Bicycle-A* film's GISAXS data was done successfully.

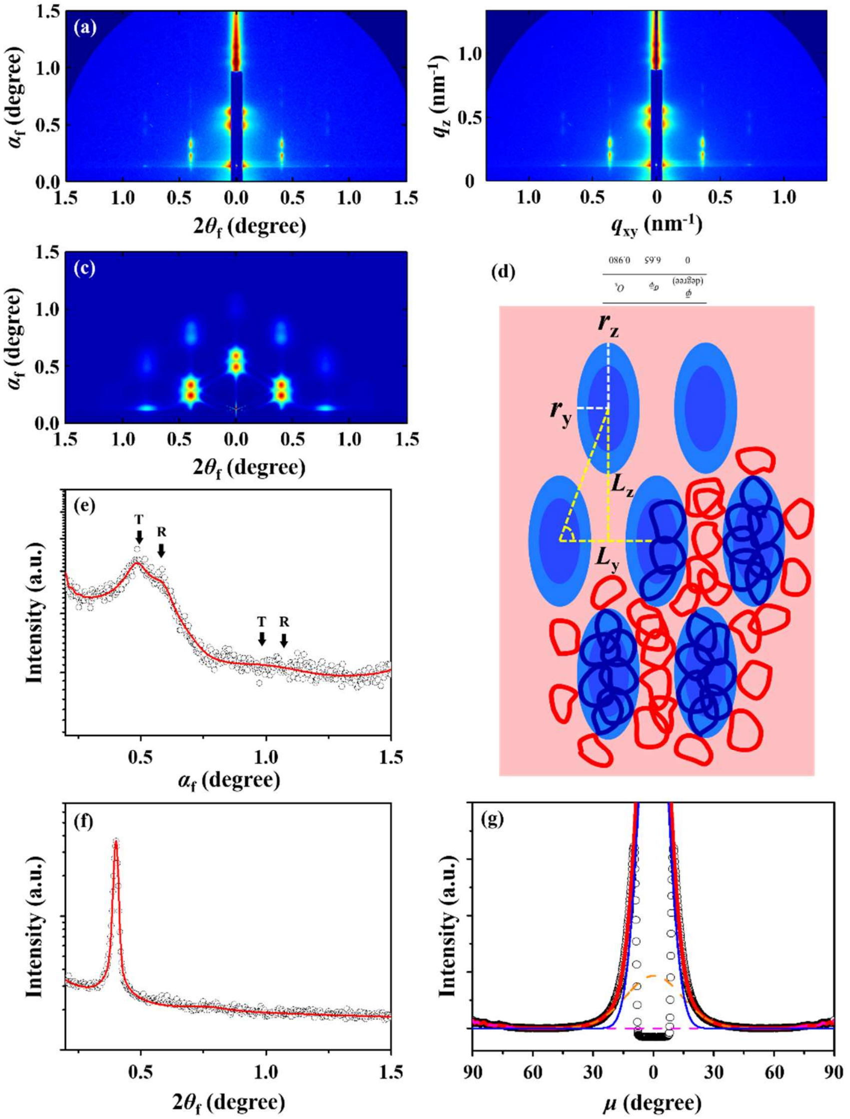

Figure 6.3. Representative GISAXS data of *Bicycle-A* films (100–120 nm thick) measured with α_i = 0.1361°; SDD = 2909.8 mm at room temperature using a synchrotron X-ray beam (λ = 0.12095 nm): (a) 2D scattering image in angle space; (b) 2D scattering image in scattering vector space obtained from the scattering image in (a); (c) 2D scattering image reconstructed with the determined structural parameters; (d) schematic horizontal HEX cylindrical structure (front view); (e) out-of-plane scattering profile extracted along the meridian line at $2\theta_f$ = 0.179° from the scattering image in (a); (f) in-plane scattering profile along the equatorial line at α_f = 0.220° from the scattering image in (a). In (e) and (f), the black symbols are the measured data and the solid red lines were obtained by fitting the data using the GIXS formula of hexagonal cylindrical structure model; the scattering peak generated by the reflected X-ray beam is marked with "**R**", whereas that generated by the transmitted X-ray beam is marked with "**T**". (g) Azimuthal scattering profile extracted at q = 0.450 nm^{-1} from the scattering image in (b); the black symbols are the measured data; the lines were obtained by the deconvolutions of the measured data: the blue and green solid lines are the scattering peaks of cylindrical domains in hexagonal packing order, the purple dot line is the Yoneda peak, the brown dot line is a part of the reflected X-ray beam, and the red solid line is the sum of all deconvoluted peaks.

The *Bicycle-B* film reveals a distinctive 2D GISAXS image, as shown in Figures 6.4a-b; the scattering image is quite different from that of the *Bicycle-A* film. In the image, only two scattering rings apparently appear but heavily overlapped; one was generated by the transmitted X-ray beam and another by the reflected X-ray beam (Figure 6.4e). They are suspected to be the first-order scattering peak of nanostructure in the film. The peaks are relatively stronger in intensity higher along the meridian line as well as the equatorial line, compared to the other directions. Furthermore, they are much stronger in intensity along the equatorial line than along the meridian line. Except these, no higher order scattering peaks are discernible. The observation of this scattering image suggests the presence of a lamellar structure poorly developed in the film. With this clue, the scattering pattern has been further analyzed in detail. An out-of-plane scattering profile, which was extracted along the meridian line at $2\theta_f = 0.065°$, could be well analyzed by using the GIXS formula derived for lamellar structure model (Figures 6.4d-e; Section 1.4 of Chapter 1). An in-plane scattering profile, which was extracted along the equatorial line at $\alpha_f = 0.201°$, could also be analyzed satisfactorily by using the same GIXS formula (Figure 6.4f). Moreover, an azimuthal scattering profile, which was extracted at $q = 0.525$ nm^{-1} from the q-space image, could be analyzed in detail, finding the orientations of nanostructure and their relative populations in the film (Figures 6.4b; Figure 6.5g). The obtained structural details are summarized in Table 6.2.

Table 6.2. Morphological parameters of nanoscale films (100−120 nm thick) of various bicyclic heteroblock copolymers

Nanoscale film morphology	Bicyclic heteroblock copolymers					
	Bicycle-A	*Bicycle-B*		*Bicycle-C*	*Bicycle-D*	
	○○	○○		○○	○○	
HEX cylindrical structure	horizontal					
L_z[a] (nm)	11.70					
L_y[b] (nm)	8.00					
γ[c]	1.46					
R_z[d] (nm)	3.80					
R_y[e] (nm)	3.80					
r_cz[f] (nm)	3.80 (0.70)[t]					
r_cy[g] (nm)	1.70 (0.30)					
t_sz[h] (nm)	2.00 (0.30)					
t_sy[i] (nm)	0.90 (0.20)					
ε[j]	2.23					
g[k]	0.09					
$\bar{\varphi}$[l] (deg.)	0					
σ_φ[m] (deg.)	6.65					
O_s[n]	0.980					
ϕ[o] (vol%)	100					
Lamellar structure		horizontal	vertical	horizontal	horizontal	vertical
D_L[p] (nm)		11.05	11.30	6.93	7.32	7.50
l_1[q] (nm)		3.90 (0.50)	3.70 (0.30)	2.35 (0.60)	2.40 (0.60)	2.20 (0.90)
l_2[r] (nm)		1.50 (0.50)	1.90 (0.70)	1.10 (0.20)	1.20 (0.40)	1.50 (0.50)
l_3[s] (nm)		4.15	3.80	2.38	2.52	2.30
g		0.28	0.28	0.12	0.15	0.28
$\bar{\varphi}$ (deg.)		0	83.40	0	0	70.00
σ_φ (deg.)		9.35	29.65	2.50	2.05	13.40
O_s		0.961	-0.738	0.972	0.991	-0.007
ϕ (vol%)		6	94	100	95	5

[a] Mean interdistance between the arrays of the in-plane oriented cylindrical domains. [b] Mean center-to-center distance of the cylindrical domains lain in the film plane. [c] Ratio of L_z and L_y (= $L_\mathrm{z}/L_\mathrm{y}$). [d] Long radius of ellipsoidal cylindrical domain along the *z*-axis which is parallel to the out-of-plane of the film. [e] Short radius of ellipsoidal cylindrical domain along the *y*-axis which is parallel to the in-plane of the film. [f] Core radius of ellipsoidal cylindrical domain along the *z*-axis which is parallel to the out-of-plane of the film. [g] Core radius of ellipsoidal cylindrical domain along the *y*-axis which is parallel to the in-plane of the film. [h] Shell thickness of ellipsoidal cylindrical domain along the *z*-axis which is parallel to the out-of-plane of the film. [i] Shell thickness of ellipsoidal cylindrical domain along the *y*-axis which is parallel to the in-plane of the film. [j] Ellipsoidicity ratio (= polar radius/equatorial radius). [k] Paracrystal distortion factor of nanostructure (i.e., hexagonal cylinder structure or lamellar structure) along the *z*-axis which is parallel to the out-of-plane of the film. [l] Mean value of the polar angle φ (i.e., orientation angle) between the orientation vector ***n*** (which is set along a direction normal to the {001} plane of horizontal hexagonal cylindrical structure or the in-plane of lamellar structure) and the out-of-plane direction of the film. [m] Standard deviation for the polar angle φ. [n] Second order orientation factor of nanostructure (i.e., hexagonal cylindrical structure or lamellar

structure). [o]Volume fraction in percent. [p]Long period of lamellar structure. [q]Thickness of the l_1 layer. [r]Thickness of the l_2 layer, i.e., interfacial layer. [s]Thickness of the l_3 layer. [t]Standard deviation.

The scattering data analysis has confirmed that the nanostructure formed in the *Bicycle-B* film is characterized by exhibiting a mixture of horizontal and vertical lamellar structures. The horizontal and vertical lamellar structures are estimated to be 6 and 94% in volume fraction, respectively. The g factor is relatively high (0.28) for both of the orientational structures, indicating that the horizontal and vertical lamellar structures were poorly developed in the film. The horizontal lamellar structure is characterized by exhibiting a long period D_L of 11.05 nm, a layer l_1 of 3.90 nm, an interfacial layer l_2 of 1.50 nm, a layer l_3 of 4.15 nm, and an orientation factor O_s of 0.961 ($\overline{\varphi} = 0°$, the mean value of the polar angle φ between the orientation vector $\boldsymbol{n}$ set along a direction normal to the in-plane of horizontal lamellar structure) and the out-of-plane direction of the film, and $\sigma_\varphi = 9.35°$, standard deviation for the polar angle φ). For the vertical lamellar structure, $D_L = 11.30$ nm, $l_1 = 3.70$ nm, $l_2 = 1.90$ nm, $l_3 = 3.80$ nm, and $O_s = -0.738$ ($\overline{\varphi} = 83.40°$ and $\sigma_\varphi = 29.65°$). The O_s and σ_φ results inform that the horizontal lamellar structure has relatively higher degree of orientation order than that of the vertical lamellar structure. The volume fraction of the PTEGGE block in the copolymer is slightly lower than that of PDGE block. Thus, the l_1 and l_3 1ayers could be assigned by the PTEGGE block phase and the PDGE block phase, respectively; the l_2 1ayer is the interfacial layer l_i between the PDGE and PTEGGE block phases (Figure 6.4d). In addition, from the determined structural parameters, a scattering image has been reconstructed, showing good agreement with the measured pattern (Figures 6.4a and 6.5c).

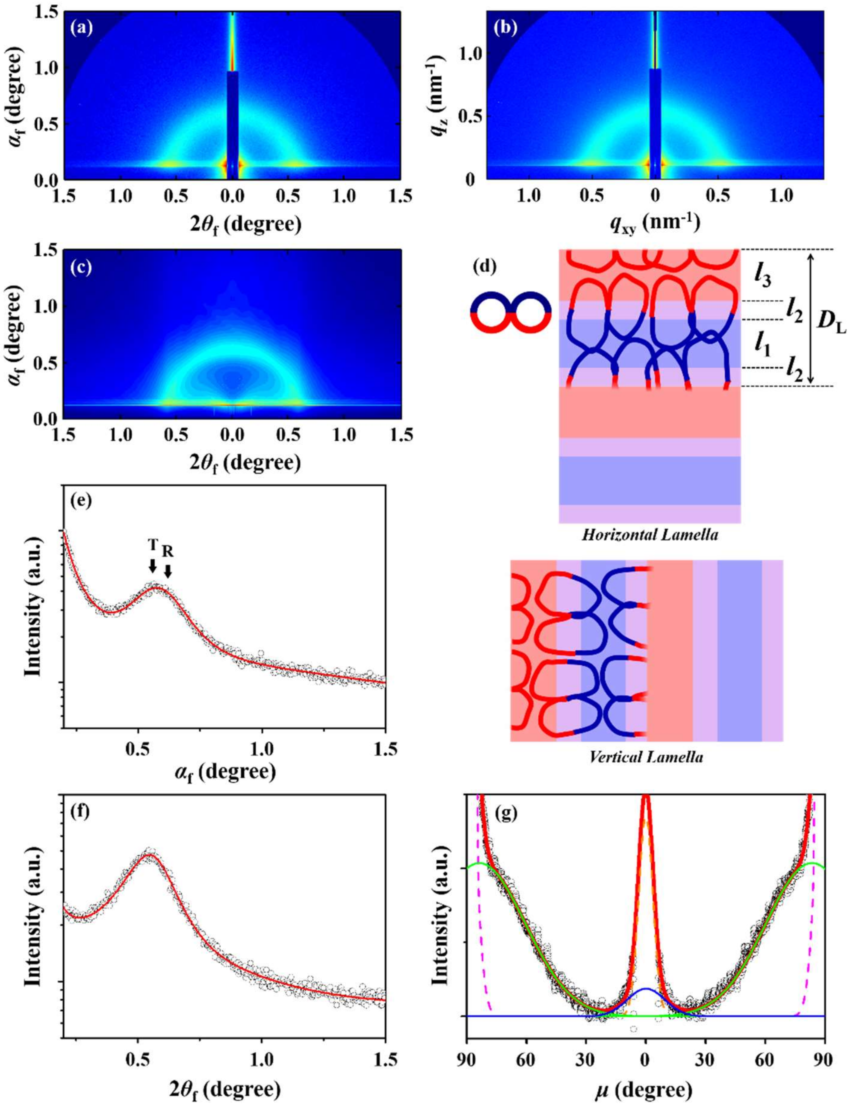

Figure 6.4. Representative GISAXS data of *Bicycle-B* films (100–120 nm thick) measured with α_i = 0.1283°; SDD = 2909.8 mm at room temperature using a synchrotron X-ray beam (λ = 0.12095 nm): (a) 2D scattering image in angle space; (b) 2D scattering image in scattering vector space obtained from the scattering image in (a); (c) 2D scattering image reconstructed with the determined structural parameters; (d) schematic horizontal and vertical lamellar structures in a front view; (e) out-of-plane scattering profile extracted along the meridian line at $2\theta_f$ = 0.065° from the scattering image in (a); (f) in-plane scattering profile along the equatorial line at α_f = 0.201° from the scattering image in (a). In (e and f), the symbols are the measured data and the solid red lines were obtained by fitting the data using the GIXS formula of lamellar structure model; the scattering peak generated by the transmitted X-ray beam, is marked with "**T**", whereas that generated by the reflected X-ray beam is marked with "**R**". (g) Azimuthal scattering profile extracted at q = 0.525 nm^{-1} from the scattering image in (b) where the black symbols are the measured data and the lines were obtained by the deconvolutions of the measured data: the blue solid line is the first order scattering peak of horizontal lamellar structure, the green solid line is the first order scattering peak of vertical lamellar structure, the purple dot line is the Yoneda peak, the brown dot line is a part of the reflected X-ray beam, and the red solid line is the sum of all deconvoluted peaks.

Figures 6.5a displays a representative scattering image of the *Bicycle-C* films. The scattering image is more clearly distinctive and highly anisotropic rather than ring-like. Scattering spots appear only along the meridian line; one spot at $\alpha_f = 0.919°$ was generated by the transmitted X-ray beam and another at $\alpha_f = 1.085°$ by the reflected X-ray beam (Figure 6.5e). These spots are the first-order peaks originated from a lamellar structure oriented horizontally in the film plane. As shown in Figure 6.5e-f, out-of-plane and in-plane scattering profiles (which were extracted along the meridian line at $2\theta_f = 0.132°$ and along the equatorial line at $2\theta_f = 0.190°$) could be satisfactorily fitted by using the GIXS formula derived for lamellar structure model (Figure 6.5d). An azimuthal scattering profile has been extracted at $q = 0.833$ nm^{-1} from the q-space image (Figure 6.5b), and then analyzed, giving information on the orientation of lamellar structure (Figure 6.5g). The obtained structural parameters are summarized in Table 6.2.

The analysis has found that *Bicycle-C* formed only horizontal lamellar structure in the film: $D_L = 6.93$ nm, $l_1 = 2.35$ nm, $l_2 = 1.10$ nm ($= l_i$), $l_3 = 2.38$ nm, $g = 0.12$, and $O_s = 0.972$ ($\overline{\varphi} = 0°$ and $\sigma_\varphi = 2.50°$). Considering the volume fractions of the blocks in the copolymer, the l_1 layer could be assigned by the PTEGGE block phase, whereas the l_3 layer could be assigned by the PDGE block phase. The scattering image reconstructed with the determined structural parameters is agreed well with the measured one (Figures 6.5a and 6.5c). Overall, *Bicycle-C* formed more well-defined lamellar structure, compared to those of *Bicycle-B*.

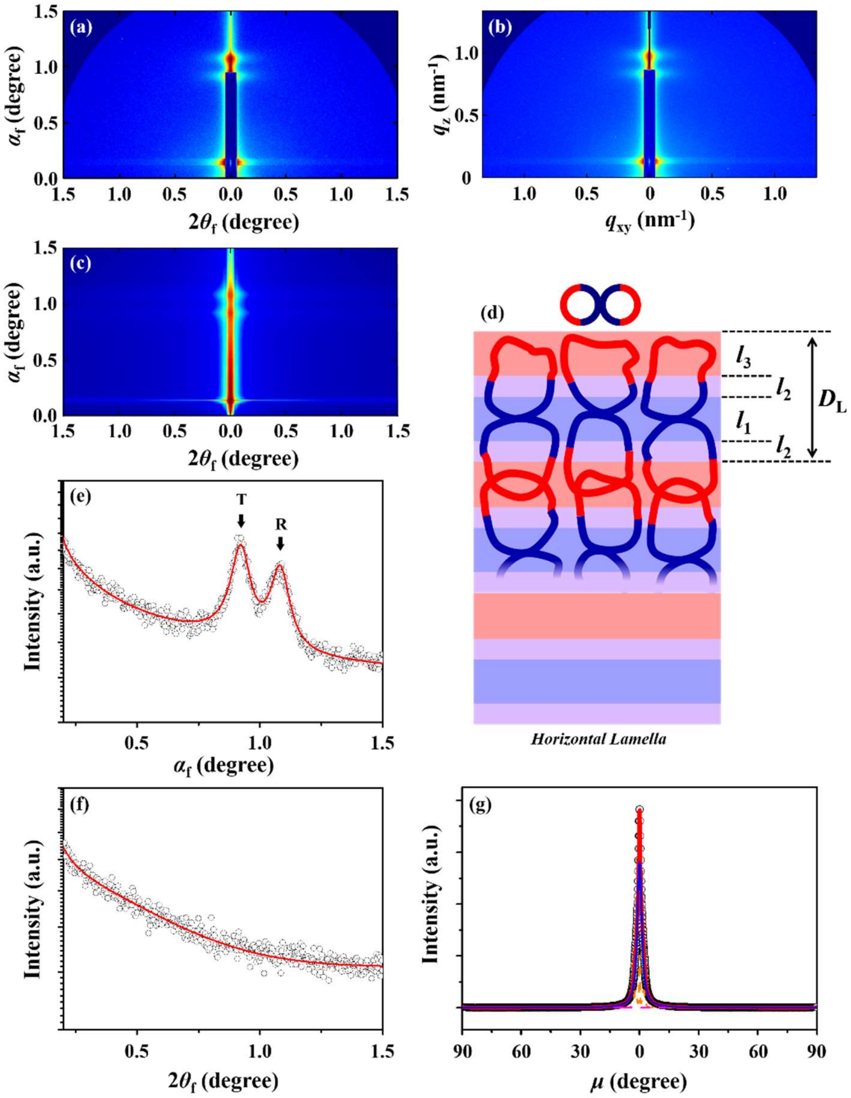

Figure 6.5. Representative GISAXS data of *Bicycle-C* films (100–120 nm thick) measured with α_i = 0.1447°; SDD = 2909.8 mm at room temperature using a synchrotron X-ray beam (λ = 0.12095 nm): (a) 2D scattering image in angle space; (b) 2D scattering image in scattering vector space obtained from the scattering image in (a); (c) 2D scattering image reconstructed with the determined structural parameters; (d) schematic horizontal lamellar structure (front view); (e) out-of-plane scattering profile extracted along the meridian line at $2\theta_f$ = 0.132° from the scattering image in (a); (f) in-plane scattering profile along the equatorial line at α_f = 0.190° from the scattering image in (a). In (e and f), the symbols are the measured data and the solid red lines were obtained by fitting the data using the GIXS formula of lamellar structure model; the scattering peak generated by the transmitted X-ray beam, is marked with "**T**", whereas that generated by the reflected X-ray beam is marked with "**R**". (g) Azimuthal scattering profile extracted at q = 0.833 nm^{-1} from the scattering image in (b) where the black symbols are the measured data and the lines were obtained by the deconvolutions of the measured data: the blue solid line is the first order scattering peak of lamellar structure, the purple dot line is the Yoneda peak, the brown dot line is a part of the reflected X-ray beam, and the red solid line is the sum of all deconvoluted peaks.

Figures 6.6a-b show a representative scattering image of the *Bicycle-D* films. This image apparently resembles in part that of the *Bicycle-B* film. Relatively stronger two scattering spots appear at α_f = 0.842° and 1.046° along the meridian line; a much weaker spot is discernible at $2\theta_f$ = 0.903° along the equatorial line. The appearance of these spots suggests that a horizontal lamellar structure of relatively higher population is present together with a vertical lamellar structure of lower population in the film. With these information, the scattering data have been analyzed in a quantitative manner as conducted for those of the *Bicycle-B* and *C* films. The extracted 1D scattering profiles could be well fitted with the GIXS formula based on lamellar structure model, as shown in Figures 6.6d-f. An azimuthal scattering profile has been additionally extracted and analyzed (Figure 6.6g). Furthermore, a scattering image has been reconstructed from the determined structural parameters (Figure 6.6c); the constructed image is well matched with the measured one, reconfirming that the scattering data analysis was done successfully. All obtained structural parameters are summarized in Table 6.2.

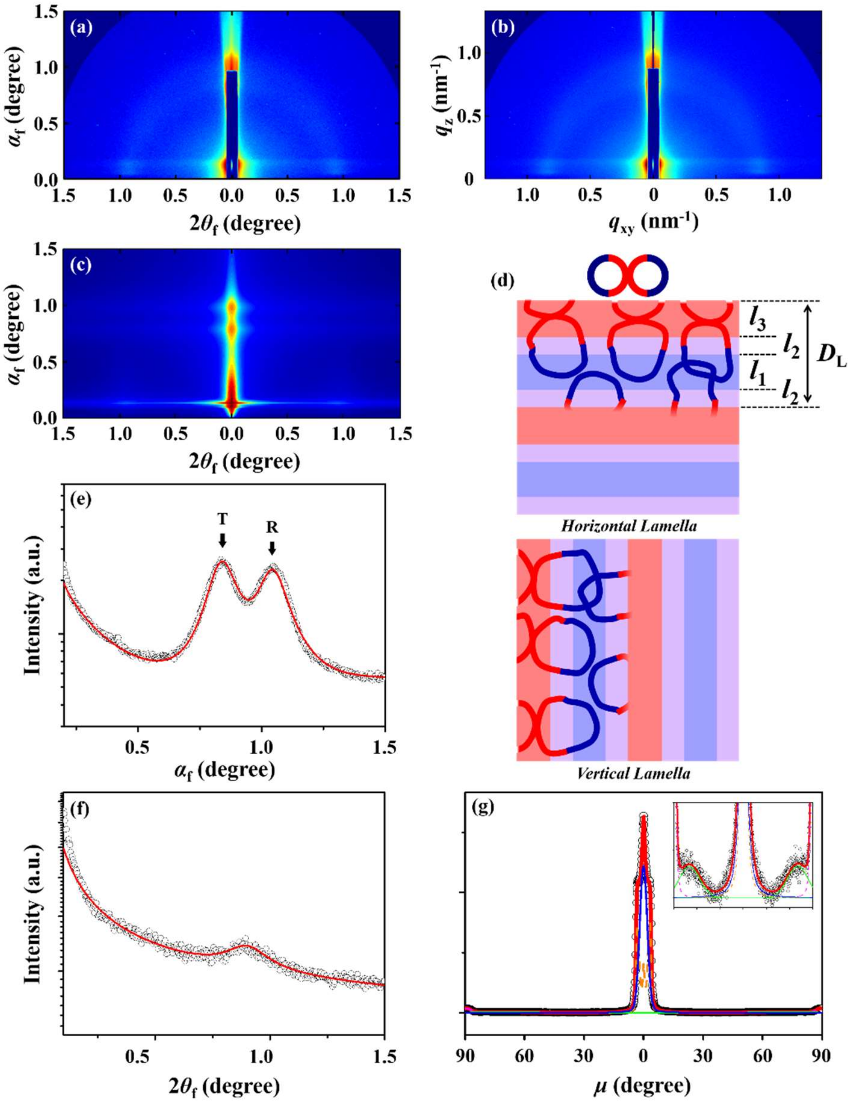

Figure 6.6. Representative GISAXS data of *Bicycle-D* films (100–120 nm thick) measured with α_i = 0.1276°; SDD = 2909.8 mm at room temperature using a synchrotron X-ray beam (λ = 0.12095 nm): (a) 2D scattering image in angle space; (b) 2D scattering image in scattering vector space obtained from the scattering image in (a); (c) 2D scattering image reconstructed with the determined structural parameters; (d) schematic horizontal and vertical lamellar structures in a front view; (e) out-of-plane scattering profile extracted along the meridian line at $2\theta_f$ = 0.065° from the scattering image in (a); (f) in-plane scattering profile extracted along the equatorial line at α_f = 0.197° from the scattering image in (a). In (e and f), the symbols are the measured data and the solid red lines were obtained by fitting the data using the GIXS formula of lamellar structure models. (g) Azimuthal scattering profile extracted at q = 0.825 nm^{-1} from the scattering image in (b) where the black symbols are the measured data and the lines were obtained by the deconvolutions of the measured data: the blue solid line is the first order scattering peak of horizontal lamellar structure, the green solid line is the first order scattering peak of vertical lamellar structure, the purple dot line is the Yoneda peak, the brown dot line is a part of the reflected X-ray beam, and the red solid line is the sum of all deconvoluted peaks.

The scattering analysis found that for the *Bicycle-D* film, a horizontal lamellar structure is present as a major structural component (95 vol%), together with a vertical lamellar structure (5 vol%). For the horizontal lamellar structure, D_L = 7.32 nm, l_1 = 2.40 nm, l_2 = 1.20 nm, l_3 = 2.52 nm, g = 0.15, and O_s = 0.991 ($\overline{\varphi}$ = 0° and σ_φ= 2.05°). For the vertical lamellar structure, D_L = 7.50 nm, l_1 = 2.20 nm, l_2 = 1.50 nm, l_3 = 2.30 nm, g = 0.28, and O_s = –0.007 ($\overline{\varphi}$ = 70.00° and σ_φ= 13.40°). Considering the volume fractions of the blocks in the copolymer, the l_1 and l_3 layers could be assigned by the PTEGGE block chain phase and the PDGGE block chain phase, respectively; the l_2 layer corresponds to the interfacial phase l_i. Overall, the horizontal lamellar structure, as the major component, exhibits higher positional stability and preferential orientation, compared to the vertical lamellar structure in the minor portion.

As discussed above, all bicyclic block copolymers have revealed various nanostructures due to the phase-separations between the block components through the nanoscale film fabrication process. The determined film morphology details are further understood in terms of molecular topological effects in the following.

First, *Bicycle-A* is composed of two different homoblock-based rings in equivalent volume fractions. Adopting a widely known volume fraction rule, one can expect phase-separated lamellar structure for the *Bicycle-A* film. Surprisingly, *Bicycle-A* (which is composed of homoblock-based rings), however, forms HEX cylindrical structure, which is different from the expectation. The HEX cylindrical structure is further quite different from the lamellar structure formed in the film of the linear diblock counterpart that obeys the generally known volume fraction rule.[62] Therefore, the HEX cylindrical structure of *Bicycle-A* is a clear clue of the molecular topology effects on the nanostructure formation of bicyclic block copolymer.

Second, one question is raised for *Bicycle-A*: Why does the bicyclic block copolymer form cylindrical structure rather than lamellar structure? In fact, the volume fraction rule generally known in the phase-separated structure formation of diblock copolymer stands on the equivalent block chain characteristics including flexibility (or rigidity) and assembling behavior. In the case of PDGE and PTEGGE block chains, their chain flexibilities may be different each other because of the different bristles even though their backbones are same; it is generally known that *n*-alkane is relatively less flexible than linear-aliphatic ether. Moreover, their assembling behaviors may be different because of the different chemical natures; for example, the *n*-decyl bristles in the PDGE block interact each other via van der Waals force, whereas the 2-(2-(2-methoxyethoxy)ethoxy)ethyl bristles in the PTEGGE block interact together via van der Waals force and hydrogen-bonding formation. In the linear diblock counterpart, such different chain characteristics may not be large enough to override the volume fraction rule, consequently forming typical lamellar structure. However, the difference in the chain characteristics may be enhanced by the ring topology formation of the PDGE block as well as of the PTEGE block. Such amplified difference in the chain characteristics may cause to shift the phase-diagram to the PTEGGE component and indeed induce the cyclized blocks to override the volume fraction rule, revealing cylindrical structure rather than lamellar structure.

Third, the HEX cylindrical structure of *Bicycle-A* is highly distorted, revealing $\gamma = 1.46$ ($= L_z/L_y$) which is much larger than that ($\sqrt{3/2}$) of regular HEX cylindrical structure. Such the large distortion is attributed to the cylindrical PTEGGE block domains having highly ellipsoidal cross-section ($\varepsilon = 2.23$, ellipsoidicity ratio). This ellipsoidal cylinder formation may be caused by a geometrical confinement effect due to the nanoscale film; namely, during phase-separation, the cross-sectional growth of cylindrical PTEGGE block phases may be less restricted toward the air and vacuum interface, compared to the in-plane of the film adhered onto the substrate.

Fourth, another question is raised for the other bicyclic block copolymers (*Bicycle-B, C,* and *D*): Why do they all form lamellar structures, as observed in the linear diblock counterpart? For *Bicycle-B, C,* and *D*, the individual ring components are always composed of the PDGE and PTEGGE block components even in the various types. Thus, such the ring compositions may lead to no discernible or very small amplifications in differentiating chain characteristics. Namely, for the individual bicyclic copolymers, the net differences in the chain characteristics due to the ring geometry formations may not be significant to cause substantial shifts in the phase-diagram and form different nanostructural morphologies against the volume fraction rule.

Fifth, the reduction level of domain spacing is 51.2−67.6 % for the nanostructured *Bicycle-A* film, 52.9−56.7 % for the nanostructured *Bicycle-B* film, 71.1−72.8 % for the nanostructured *Bicycle-C* film, and 68.8−71.3 % for the nanostructured *Bicycle-D* film, compared to the domain spacing (24.00−25.50 nm) of the nanostructures formed in the linear diblock counterpart film as described in chapter 5.[62] These domain spacing reductions are significantly larger than those (5−16 %) observed for the pairs of cyclic and linear block copolymers in bulk states[53-56] and that achieved previously for the pair of cyclic and linear poly(styrene-*block*-ethylene oxide)s in thin films.[58] It is additionally noted that the domain spacing reductions are roughly two times larger than those (30−37 %) predicted theoretically for pairs of cyclic and linear block copolymers.[63-65]

Sixth, the domain spacing reduction is 0.8−3.0 % for the nanostructured *Bicycle-A* film, 4.2–6.4 % for the nanostructured *Bicycle-B* film, 16.0–41.3 % for the nanostructured *Bicycle-C* film, and 9.1–37.7 % for the nanostructured *Bicycle-D* film, even compared to the domain spacing (8.25–11.80 nm) of the nanostructures formed in the single cyclic diblock counterpart film as described in chapter 5.[62] In particular, the highly reduced domain spacings of the nanostructured *Bicycle-C* and *D* films are so remarkable.

Seventh, *Bicycle-A* reveals only HEX cylindrical structure. Therefore, *Bicycle-A* is a suitable material for the production of cylindrical nanostructures.

Eighth, *Bicycle-B* forms mainly vertical lamellar structure (94 vol%). Hence, *Bicycle-B* is a good candidate material for the production of vertical lamellar nanostructures.

Ninth, *Bicycle-C* exhibits only horizontal lamellar structure. *Bicycle-D* also reveals mainly horizontal lamellar structure (95 vol%). Indeed, *Bicycle-C*, as well as *Bicycle-D* is a good candidate for the fabrication of horizontal lamellar nanostructures.

Finally, all bicyclic block copolymers of this study have demonstrated remarkably reduced domain spacings, which could not be achieved from the linear block counterpart: linear diblock (24.00−25.50 nm, domain spacing) >> *Bicycle-A* (11.70 nm) > *Bicycle-B* (11.05−11.30 nm) >> *Bicycle-D* (7.32−7.50 nm) > *Bicycle-C* (6.93 nm). Collectively, this study opens up that bicyclic block copolymers are a new powerful approach to develop nanolithographic materials which can deliver the pitches required for the production of future advanced semiconductor chips (dynamic random access memory (DRAM) chip: the pitch is scheduled to be 30 nm by 2021, 24 nm by 2024, 18 nm by 2027, and 16 nm by 2030; microprocessor unit (MPU) chip: the pitch in is scheduled by 20 nm by 2021, and 12 nm by 2024−2030) in the International Technology Roadmap for Semiconductors.[66]

6.4 Conclusions

In this chapter, detailed investigation on the nanoscale film morphologies of a series of bicyclic block copolymers in various molecular topologies by using synchrotron GIXS measurements and data analysis have been attempted for the first time. This quantitative scattering analysis has confirmed that all bicyclic block copolymers of this study formed nanostructures attributed to the phase-separations of the block components. The types and parameter details of the nanostructures are found to be highly dependent upon the molecular topologies.

Bicycle-A (which is composed of two different homoblock-based rings in equivalent volume fractions) favorably forms HEX cylindrical nanostructure. In contrast, the other bicyclic copolymers consisted of diblock-based rings generate lamellar nanostructures, as observed for the linear counterpart and as further expected by the volume fraction rule.

In summary, this chapter has demonstrated the quantitative analysis through three layer model and two phase elliptical hexagonal cylinder model was successful in parameterizing the morphological details of bicyclic block copolymers in thin films. The two models successfully identified each individual variations of bicyclic topologies as critical factors for miniaturizing domain spacings, which could never be achievable from the linear counterpart. Among the bicyclic copolymers, *Bicycle-C* produces the smallest domain spacing. Overall, the novel model analysis have successfully established new insights in the topology-morphology correlation of bicyclic block copolymers.

6.5 References

1. Patnode, W.; Wilcock, D. F. Methylpolysiloxanes. *J. Am. Chem. Soc.***1946**, *68*, 358−363.
2. Hunter, M. J.; Hyde, J. F.; Warrick, E. L.; Fletcher, H. J. Organo-Silicon Polymers. The Cyclic Dimethyl Siloxanes. *J. Am. Chem. Soc.***1946**, *68*, 667−672.
3. Semlyen, J. A. Cyclic Polymers, 2nd ed., Kluwer Academic Publishers: Dordrecht, Netherlands, 2002.
4. Hadjichristidis, N.; Iatrou, H.; Pitsikalis, M.; Mays, J. Macromolecular architectures by living and controlled/living polymerizations. *Prog. Polym. Sci.* **2006**, 31, 1068−1132.
5. Laurent B. A.; Grayson, S. M. Synthetic Approaches for the Preparation of Cyclic Polymers. *Chem. Soc. Rev.* **2009**, *38*, 2202–2213.
6. Kricheldorf, H. R. Cyclic Polymers: Synthetic Strategies and Physical Properties. *J. Polym. Sci. Part A: Polym. Chem.* **2010**, *48*, 251− 284.
7. Yamamoto, T.; Tezuka, Y. Topological polymer chemistry: a cyclic approach toward novel polymer properties and functions. Polym. Chem. 2011, 2, 1930−1941.
8. Jia, Z.; Monteiro, M.J. Cyclic Polymers: Methods and Strategies. *J. Polym. Sci. Part A: Polym. Chem*. **2012**, *50*, 2085−2097.
9. Tezuka, Y., Ed., Topological Polymer Chemistry: Progress of Cyclic Polymers in Syntheses, Properties and Functions, World Scientific: Hackensack, NJ, USA, 2013.
10. Jia, Z.; Monteiro, M.J. Synthesis of Cyclic Polymers via Ring Closure. *Adv. Polym. Sci.* **2013**, *262*, 295−328.
11. Geiser, D.; Höcker, H. Synthesis and Investigation of Macrocyclic Polystyrene. *Macromolecules* **1980**, *13*, 653–656.
12. Hild, G.; Kohler, A.; Rempp, P. Synthesis of Ring-Shaped Macromolecules. *Eur. Polym. J.* **1980**, *16*, 525−527.
13. Roovers, J.; Toporowski, P. M. Synthesis of High Molecular Weight Ring Polystyrenes. *Macromolecules* **1983**, *16*, 843−849.
14. Culkin, D. A.; Jeong, W.; Csihony, S.; Gomez, E. D.; Balsara, N.R.; Hedrick, J. L.; Waymouth, R. M. Zwitterionic Polymerization of Lactide to Cyclic Poly(lactide) by Using *N*-Heterocyclic Carbine Organocatalysts. *Angew. Chem. Int. Ed.* **2007**, *46*, 2627–2630.
15. Durmaz, H.; Dag, A.; Hizal, G.; Tunca, U. Cyclic Homo and Block Copolymers Through Sequential Double Click Reactions. *J. Polym. Sci. Part A: Polym. Chem.* **2010**, *48*, 5083–5091.
16. Liu, B.; Wang, H.; Zhang, L.; Yang, G.; Liu, X.; Kim, I. A Facile Approach for the Synthesis of Cyclic Poly(*N*-isopropylacrylamide) Based on An Anthracene–Thiol Click Reaction. *Polym. Chem.* **2013**, *4*, 2428–2431.
17. Castro-Osma, J. A.; Alonso-Moreno, C.; García-Martinez, J. C.; Fernández-Baeza, J.; Sánchez-Barba, L. F.; Lara-Sánchez, A.; Otero, A. Ring-Opening (ROP) versus Ring-Extension (REP) Polymerization of *ε*-Caprolactone to Give Linear or Cyclic Polycaprolatones. *Macromolecules* **2013**, *46*, 6388−6394.
18. Ogawa, T.; Nakazono K.; Aoki D.; Uchida S.; Takata T. Effective Approaches to Cyclic Polymer from Linear Polymer: Synthesis and Transformation of Macromolecular [1]Rotaxane. *ACS Macro Lett*. **2015**, *4*, 343−347.
19. Wang, H.; Zhang, L.; Liu, B.; Han, B.; Duan, Z.; Qi, C.; Park, D.; Kim, I. Synthesis of High Molecular Weight Cyclic Poly(*ε*-caprolactone)s of Variable Ring Size Based on A Light-Induced Ring-Closure Approach. *Macromol. Rapid Commun*. **2015**, *36*, 1646−1650.
20. Satoh, Y.; Matsuno, H.; Yamamoto, T.; Tajima, K.; Isono, T.; Satoh, T. Synthesis of Well-Defined Three- and Four-Armed Cage-Shaped Polymers via "Topological

Conversion" from Trefoil- and Quatrefoil- Shaped Polymers. *Macromolecules* **2017**, *50*, 97−106.

21. Xiang, L.; Ryu, W.; Kim, H.; Ree, M. Precise Synthesis, Properties, and Structures of Cyclic Poly(ε-caprolactone)s. *Polymers* **2018**, *10*, 577.
22. Shingu, T.; Yamamoto, T.; Tajima, K.; Isono, T.; Satoh, T. Synthesis of μ-ABC Tricyclic Miktoarm Star Polymer via Intramolecular Click Cyclization. *Polymers* **2018**, *10*, 877.
23. Isono, T.; Sasamori, T.; Honda, K.; Mato, Y.; Yamamoto, T.; Tajima, K.; Satoh, T. Multicyclic Polymer Synthesis through Controlled/Living Cyclopolymerization of α,ω-Dinorbornenyl-Functionalized Macromonomers. *Macromolecules* **2018**, *51*, 3855–3864.
24. Yamamoto, T.; Hosokawa, M.; Nakamura, M.; Sato, S.-i.; Isono, T.; Tajima, K.; Satoh, T.; Sato, M.; Tezuka, Y.; Saeki, A.; Kikkawa, Y. Synthesis, Isolation, and Properties of All Head-to-Tail Cyclic Poly(3-hexylthiophene): Fully Delocalized Exciton over the Defect-Free Ring Polymer. *Macromolecules* **2018**, *51*, 9284–9293.
25. Mato, Y.; Honda, K.; Tajima, K.; Yamamoto, T.; Isono, T.; Satoh, T. A Versatile Synthetic Strategy for Macromolecular Cages: Intramolecular Consecutive Cyclization of Star-Shaped Polymers. *Chem. Sci.* **2019**, *10*, 440–446.
26. Schmidt, B. V. K. J.; Fechler, N.; Falkenhagen, J.; Lutz, J.-F. Controlled Folding of Synthetic Polymer Chains Through The Formation of Positionable Covalent Bridges. *Nat. Chem.* **2011**, *3*, 234−238.
27. Shi, G.-Y.; Pan, C.-Y. Synthesis of Well-Defined Figure-of-Eight Shaped Polymers by a Combination of ATRP and Click Chemistry. *Macromol. Rapid Commun.* **2008**, *29*, 1672−1678.
28. Lee, T.; Oh, J.; Jeong, J.; Jung, H.; Huh, J.; Chang, T.; Paik, H.-j. Figure-Eight-Shaped and Cage-Shaped Cyclic Polystyrenes. *Macromolecules* **2016**, *49*, 3672−3680.
29. Zhao, J.; Zhou, Y.; Li, Y.; Pan, X.; Zhang, W.; Zhou, N.; Zhang, K.; Zhang, Z.; Zhu, X. Modular construction of macrocycle-based topological polymers via high-efficient thiol chemistry. *Polym. Chem.* **2015**, *6*, 2879−2891.
30. Zhao, Z.; Zhu, Q.; Wang, Z.; Lu, J.; Jin, Z.; Liu, H. A Dicyclic Scaffold for Programmed Monocyclic and Polycyclic Polymer Architectures. *Macromolecules* **2017**, *50*, 8907−8915.
31. Shi, G.-Y.; Sun, J.-T.; Pan, C.-Y. Well-Defined Miktocycle Eight-Shaped Copolymers Composed of Polystyrene and Poly(ε-caprolactone): Synthesis and Characterization. *Macromol. Chem. Phys.* **2011**, *212*, 1305−1315.
32. Hatakeyama, F.; Yamamoto, T.; Tezuka, Y. Systematic Synthesis of Block Copolymers Consisting of Topological Amphiphilic Segment Pairs from *kyklo*- and *kentro*-Telechelic PEO and Poly(THF). *ACS Macro Lett.* **2013**, *2*, 427−431.
33. Fan, X.; Huang, B.; Wang, G.; Huang, J. Synthesis of Amphiphilic Heteroeight-Shaped Polymer Cyclic-[Poly(ethylene oxide)-b-polystyrene]$_2$ via "Click" Chemistry. *Macromolecules* **2012**, *45*, 3779−3786.
34. Isono, T.; Satoh, Y.; Miyachi, K.; Chen, Y.; Sato, S.-i.; Tajima, K.; Satoh, T.; Kakuchi, T. Synthesis of Linear, Cyclic, Figure-Eight-Shaped, and Tadpole Shaped Amphiphilic Block Copolyethers via t-Bu-P4-Catalyzed RingOpening Polymerization of Hydrophilic and Hydrophobic Glycidyl Ethers. *Macromolecues* **2014**, *47*, 2853−2863.
35. Zimm, B. H; Stockmayer, W. H. The Dimensions of Chain Molecules Containing Branches and Rings. *J. Chem. Phys*. **1949**, *17*, 1301−1314.
36. Prentis, J. J. Spatial Correlations in A Self-Repelling Ring Polymer. *J. Chem. Phys.* **1982**, *76*, 1574−1583.
37. Roovers, J. The Melt Properties of Ring Polystyrenes. *Macromolecules* **1985**, *18*, 1359−1361.

38. Lee, H. C.; Lee, H.; Lee, W.; Chang, T.; Roovers, J. Fractionation of Cyclic Polystyrene from Linear Precursor by HPLC at The Chromatographic Critical Condition. *Macromolecules* **2000**, *33*, 8119−8121.
39. Su, H.; Chen, H.; Díaz, A.; Casas, M. T.; Ouiggalí, J.; Hoskins, J. N.; Grayson, S. N.; Pérez, R. A.; Müller, A. J. New Insight on The Crystallization and Melting of Cyclic PCL Chains on The Basis of A Modified Thomson-Gibbs Equation. *Polymer* **2013**, *54*, 846−859.
40. Ren, J. M.; Satoh, K.; Goh, T. K.; Blencowe, A.; Nagai, K.; Ishitake, K.; Christofferson, A. J.; Yiapanis, G.; Yarovsky, I.; Kamigaito, M.; Qiao, G. G. Stereospecific Cyclic Poly(methyl methacrylate) and Its Topology-Guided Hierarchically Controlled Supramolecular Assemblies. *Angew. Chem. Int. Ed.* **2014**, *53*, 459–464.
41. Cooke, J.; Viras, K.; Yu, G.-E.; Sun, T.; Yonemitsu, T.; Ryan, A. J.; Price, C.; Booth, C. Large Cyclic Poly(oxyethylene)s: Chain Folding in The Crystalline State Studied by Raman Spectroscopy, X-ray Scattering, and Differential Scanning Calorimetry. *Macromolecules* **1998**, *31*, 3030–3039.
42. Honda, S.; Yamamoto, T.; Tezuka, Y. Topology-Directed Control on Thermal Stability: Micelles Formed from Linear and Cyclized Amphiphilic Block Copolymers. *J. Am. Chem. Soc.* **2010**, *132*, 10251−10253.
43. Minatti, E.; Borsali, R.; Schappacher, M.; Deffieux, A.; Soldi, V.; Narayanan, T.; Putaux, J.-L. Effect of Cyclization of Polystyrene/Polyisoprene Block Copolymers on Their Micellar Morphology. *Macromol. Rapid Commun.* **2002**, *23*, 978–982.
44. Lonsdale, D. E.; Monteiro, M. J. Synthesis and Self-Assembly of Amphiphilic Macrocyclic Block Copolymer Topologies. *J. Polym. Sci. Part A: Polym. Chem.* **2011**, *49*, 4603–4612.
45. Williams, R. J.; Dove, A. P.; O'Reilly, R. K. Self-Assembly of Cyclic Polymers. *Polym. Chem.* **2015**, *6*, 2998–3008.
46. Zhao, Y.; Liu, Y.-T.; Lu, Z.-Y.; Sun, C.-C. Effect of Molecular Architecture on The Morphology Diversity of The Multicompartment Micelles: A Dissipative Particle Dynamics Simulation Study. *Polymer* **2008**, *49*, 4899–4909.
47. Heo, K.; Kim, Y. Y.; Kitazawa, Y.; Kim, M.; Jin, K. S.; Yamamoto, T.; Ree, M. Structural Characteristics of Amphiphilic Cyclic and Linear Block Copolymer Micelles in Aqueous Solutions. *ACS Macro Lett.* **2014**, *3*, 233−239.
48. Ree, B. J.; Satoh, Y.; Jin, K. S.; Isono, T.; Kim, W. J.; Kakuchi, T.; Satoh, T.; Ree, M. Well-Defined Stable Nanomicelles Self-Assembled by Brush Cyclic and Tadpole Copolymer Amphiphiles: A Versatile Smart Carrier Platform. *NPG Asia Materials* **2017**, *9*, e453.
49. Ree, B. J.; Satoh, T.; Yamamoto, T. Micelle Structure Details and Stabilities of Cyclic Block Copolymer Amphiphile and Its Linear Analogues. *Polymers* **2019**, *11*, 163.
50. Ree, B. J.; Lee, J.; Satoh, Y.; Kwon, K.; Isono, T.; Satoh, T.; Ree, M. A Comparative Study of Dynamic Light and X-ray Scatterings on Micelles of Topological Polymer Amphiphiles. *Polymers* **2018**, *10*, 1347.
51. Qiu, X.-P.; Tanaka, F.; Winnik, F. M. Temperature-Induced Phase Transition of Well-Defined Cyclic Poly(*N*-isopropylacrylamide)s in Aqueous Solution. *Macromolecules* **2007**, *40*, 7069–7071.
52. Wan, X.; Liu, T.; Liu, S. Synthesis of Amphiphilic Tadpole-Shaped Linear-Cyclic Diblock Copolymers via Ring-Opening Polymerization Directly Initiating from Cyclic Precursors and Their Application as Drug Nanocarriers. *Biomacromolecules* **2011**, *12*, 1146–1154.

53. Honda, S.; Koga, M.; Tokita, M.; Yamamoto, T.; Tezuka, Y. Phase Separation and Self-Assembly of Cyclic Amphiphilic Block Copolymers with A Main-Chain Liquid Crystalline Segment. *Polym. Chem.* **2015**, *6*, 4167–4176.
54. Zhu, Y. Q.; Gido, S. P.; Iatrou, H.; Hadjichristidis, N.; Mays, J. W. Microphase Separation of Cyclic Block Copolymers of Styrene and Butadiene and of Their Corresponding Linear Triblock Copolymers. *Macromolecules* **2003**, *36*, 148−152.
55. Takano, A.; Kadoi, O.; Hirahara, K.; Kawahara, S.; Isono, Y.; Suzuki, J.; Matsushita, Y. Preparation and Morphology of Ring-Shaped Polystyrene-block-polyisoprenes, *Macromolecules* **2003**, *36*, 3045−3050.
56. Lescanec, R. L.; Hajduk, D. A.; Kim, G. Y.; Gan, Y.; Yin, R.; Gruner, S. M.; Hogen-Esch, T. E.; Thomas, E. L. Comparison of the Lamellar Morphology of Microphase-Separated Cyclic Block Copolymers and Their Linear Precursors. *Macromolecules* **1995**, *28*, 3485−3489.
57. Lecommandoux, S.; Borsali, R.; Schappacher, M.; Deffieux, A.; Narayanan, T.; Rochas, C. Microphase Separation of Linear and Cyclic Block Copolymers Poly(styrene-b-isoprene): SAXS Experiments. *Macromolecules* **2004**, *37*, 1843−1848.
58. Poelma, J. E.; Ono, K.; Miyajima, D.; Aida, T.; Satoh, K.; Hawker, C. J. Cyclic Block Copolymers for Controlling Feature Sizes in Block Copolymer Lithography. *ACS Nano* **2012**, *6*, 10845−10854.
59. Kim, Y. Y.; Ree, B. J.; Kido, M.; Ko, Y.-G.; Ishige, R.; Hirai, T.; Wi, D.; Kim, J.; Kim, W. J.; Takahara, A.; Ree, M. High Performance n-Type Electrical Memory and Morphology-Induced Memory-Mode Tuning of A Well-Defined Brush Polymer Bearing Perylene Diimide Moieties. *Adv. Electronic Mater.* **2015**, *1*, 1500197.
60. Ree, B. J.; Aoki, D.; Kim, J.; Satoh, T.; Takata, T.; Ree, M. Macromolecular [2]Rotaxanes Linked with Polystyrene: Properties and Nanoscale Film Morphologies. *Macromolecules* **2019**, *52*, 5325−5336.
61. Ree, B. J.; Aoki, D.; Kim, J.; Satoh, T.; Takata, T.; Ree, M. Phase Transition Behaviors and Nanoscale Film Morphologies of Poly(δ-valerolactone) Axles Bearing Movable and Fixed Rotaxane Wheels. *Macromol. Rapid Commun.* **2019**, *40*, 1900334.
62. Ree, B. J. Materials from Chapter 5 of this Ph.D. Dissertation. Unpublished work, 2019.
63. Marko, J. F. Microphase Separation of Block Copolymer Rings. *Macromolecules* **1993**, *26*, 1442−1444.
64. Jo, W. H.; Jang, S. S. Monte Carlo Simulation of The Order–Disorder Transition of A Symmetric Cyclic Diblock Copolymer System. *J. Chem. Phys.* **1999**, *111*, 1712−1720.
65. Zhang, G.; Fan, Z.; Yang, Y.; Qiu, F. Phase Behaviors of Cyclic Diblock Copolymers. *J. Chem. Phys.* **2011**, *135*, 174902.
66. Semiconductor Industry Association, *The International Technology Roadmap for Semiconductors 2.0, 2015 Edition*, 2015; www.itrs2.net/.

Chapter 7

Nanoscale Film Morphologies of Tricyclic Block Copolyethers

7.1 Introduction

Since cyclic polymers were introduced in 1940s,[1,2] they have gained great attraction because of unusual properties associated with the chain-endless nature.[3-10] With aids of anionic, cationic, and radical polymerizations, ring-expansion reactions, and end-group coupling reactions, the syntheses of cyclic polymers have been advanced significantly for the last two decades, produced several cyclic polymers so far.[3-18]

In particular, trefoil-shaped (i.e., tricyclic) polymers, as an attractive polymer topology group, have been proposed.[3-10] Therefore, research effort has been made to develop tricyclic polymer topologies. As a result, a few tricyclic polymers have been synthesized successfully: tricyclic polystyrenes,[19] tricyclic polytetrahydrofurans,[20] (cyclic polystyrene)-*block*-[cyclic poly(tert-butyl acrylate)]-*block*-[cyclic poly(methyl acrylate)],[21] [cyclic poly(decyl glycidyl ether)-*block*-[cyclic poly(dec-9-enyl glycidyl ether)-*block*-[cyclic poly(2-(2-(2-methoxyethoxy) ethoxy) ethyl glycidyl ether)]s,[22] and various topological tricyclic [poly(*n*-decyl glycidyl ether)]-*block*-[poly(2-(2-(2-methoxyethoxy)ethoxy)ethyl glycidyl ether)]s.[23] Nevertheless, these interesting cyclic polymers could yet be understood in the aspect of structure and properties.

This chapter reports the first quantitative investigation results on the morphological structures of various topological *tricyclic* block copolymers composed of poly(*n*-decyl glycidyl ether) (PDGE) and poly(2-(2-(2-methoxyethoxy)ethoxy)ethyl glycidyl ether) (PTEGGE) in equivalent volume fractions. Synchrotron grazing incidence X-ray scattering analysis finds that they form phase-separated morphologies in nanoscale films. Interestingly, they all reveal significantly reduced domain spacings, which could not be achievable from the linear block copolymer counterpart. The domain spacing reduction level is dependent upon the tricyclic copolymer topologies. Furthermore, the structural parameters are varied with the molecular topologies.

(a) *Tricycle-A*

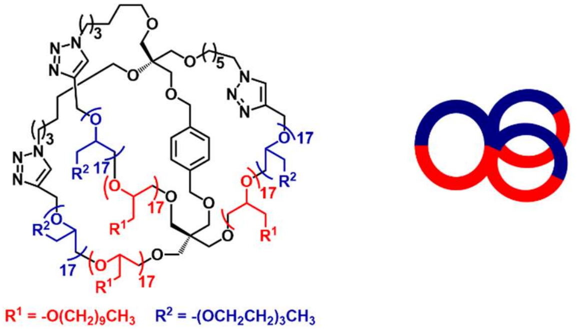

(b) *Tricycle-B*

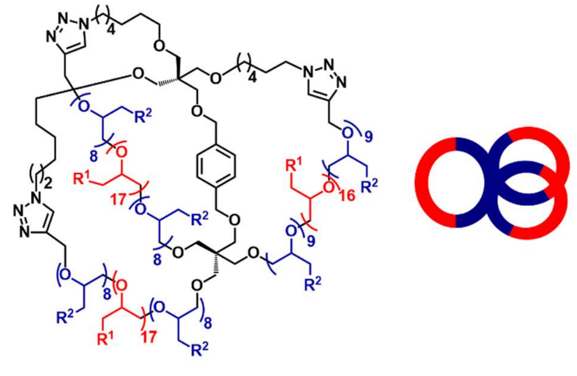

(b) *Tricycle-C*

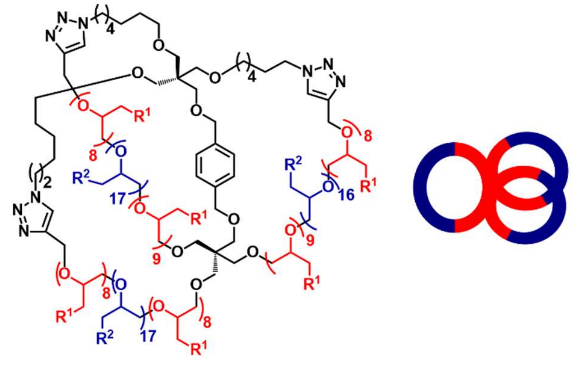

Figure 7.1. Chemical structures of tricyclic heteroblock copolymers in various topologies.

Table 7.1. Molecular characteristics of various topological tricyclic heteroblock copolymers and their homopolymers [a]

Polymer	$M_{n,NMR}$ [b] (kDa)	$Đ$ [c]	ρ_e [d] (nm^{-3})	ρ_m [e] (g/cm^3)	PDGE block		PTEGGE block	
					DP_{PDGE} [f]	ϕ_{PDGE} [g]	DP_{PTEGGE} [h]	ϕ_{PTEGGE} [i]
Tricycle-A	22.9	1.03			51	0.504	51	0.496
Tricycle-B	22.7	1.03			50	0.504	50	0.496
Tricycle-C	22.2	1.03			50	0.504	50	0.496
l-PDGE	11.1	1.03	341	1.01				
l-PTEGGE	11.2	1.04	353	1.05				

[a]Data from reference no. 23 and 24. [b]Number-average molecular weight in the unit of kDa (10^3 Da) of polymer determined by ^{1}H NMR spectroscopic analysis. [c]Dispersity value of polymer determined by size exclusion chromatography (SEC) analysis in tetrahydrofuran. [d]Electron density of polymer in films determined by X-ray reflectivity analysis. [e]Mass density of polymer in films obtained from the electron density determined by X-ray reflectivity analysis. [f]Number-average degree of polymerization of PDGE block determined by ^{1}H NMR spectroscopic analysis. [g]Volume fraction of PDGE block estimated from the $M_{n,NMR}$ and ρ_m data. [h]Number-average degree of polymerization of PTEGGE block determined by ^{1}H NMR spectroscopic analysis. [i]Volume fraction of PTEGGE block estimated from the $M_{n,NMR}$ and ρ_m data.

7.2 Experimental Section

A series of tricyclic block copolymers of PDGE and PTEGGE was synthesized and characterized as reported previously in the literature.[23] The molecular characteristics of these polymers are summarized in Table 7.1. For the individual copolymers, solutions with 0.5 wt% concentration were prepared in tetrahydrofuran and filtrated via a disposable syringe equipped with polytetrafluoroethylene filter membrane (0.2 μm pores). Each solution was spin-cast onto silicon substrates, then dried in vacuum at room temperature for 24 h. The obtained copolymer films were measured to have a thickness of 100–120 nm by using a spectroscopic ellipsometer (Model M-2000, Woollam, Lincoln, NE, USA). The films were kept at room temperature in vacuum before use.

Wide angle grazing incidence X-ray scattering (GIWAXS) measurements were carried out at a sample-to-detector distance (SDD) of 214.7 mm and an incidence angle α_i of 0.1380–0.1850° using an X-ray beam of 0.12411 nm wavelength λ (which was produced at the PLS-II

3C beamline of Pohang Accelerator Laboratory, Pohang, Korea)[25-27] and a two-dimensional (2D) charge-coupled detector (CCD) (model Rayonix 2D SX 165, Rayonix, Evanston, IL, USA). Small angle grazing incidence X-ray scattering (GISAXS) measurements were performed with SDD = 2951.3 mm at the 3C beamline. All scattering measurements were conducted at room temperature and a set of aluminum foils was used as a semi-transparent beam stop. The scattering data collection time ranged in 10–30 s. To correct the scattering angles, a precalibrated polystyrene-*block*-poly(ethylene-*random*-butylene)-*block*-polystyrene and silver behenate standards (Tokyo Chemical Inc., Tokyo, Japan) were employed; in addition, the positions of the X-ray beams reflected from the silicon substrate were used.

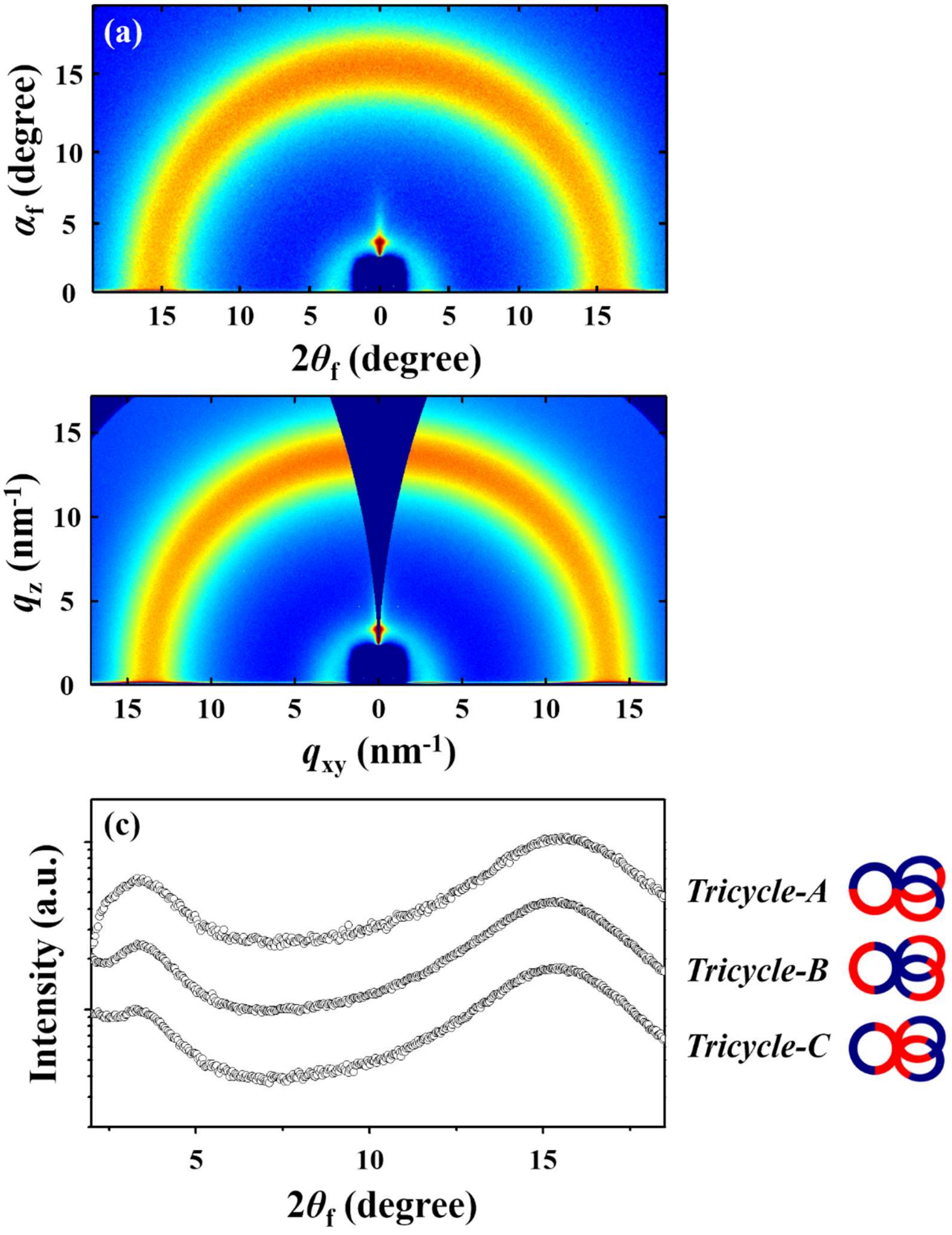

Figure 7.2. Representative GIWAXS data of the nanoscale films (100–120 nm thick) of tricyclic heteroblock copolymers measured with SDD = 214.7 mm at room temperature using a synchrotron X-ray beam (λ = 0.12411 nm): (a) 2D scattering image in angle space ($2\theta_f$ and α_f) of *Tricycle-A* (α_i = 0.1845°); (b) 2D scattering image in scattering vector space (q_{xy} and q_z) obtained from the scattering image in (a); (c) in-plane scattering profiles extracted along the equatorial line at α_f = 0.290° from the measured 2D scattering images, including the image in (a).

7.3 Results and Discussion

All nanoscale tricyclic block copolymer films in 100–120 nm thick show typically featureless GIWAXS images, which were measured at room temperature, as shown in Figure 7.2. These results indicate that all films are amorphous. In the scattering images, they all reveal only two halo scattering rings. For the individual copolymers, one halo ring appears weakly around 3.4° (ca. 2.1 nm *d*-spacing), which may originate from the mean interchain distance; another halo ring is discernible more strongly around 15.4° (ca. 0.46 nm *d*-spacing), which may result from the mean interdistance between the polymer chain and the side group as well as that between the side groups. The GIWAXS results inform that the blocks are amorphous in all tricyclic copolymer films at room temperature. The films have been further subjected to GISAXS analysis in order to get more information on any nanostructures possibly developed in the films.

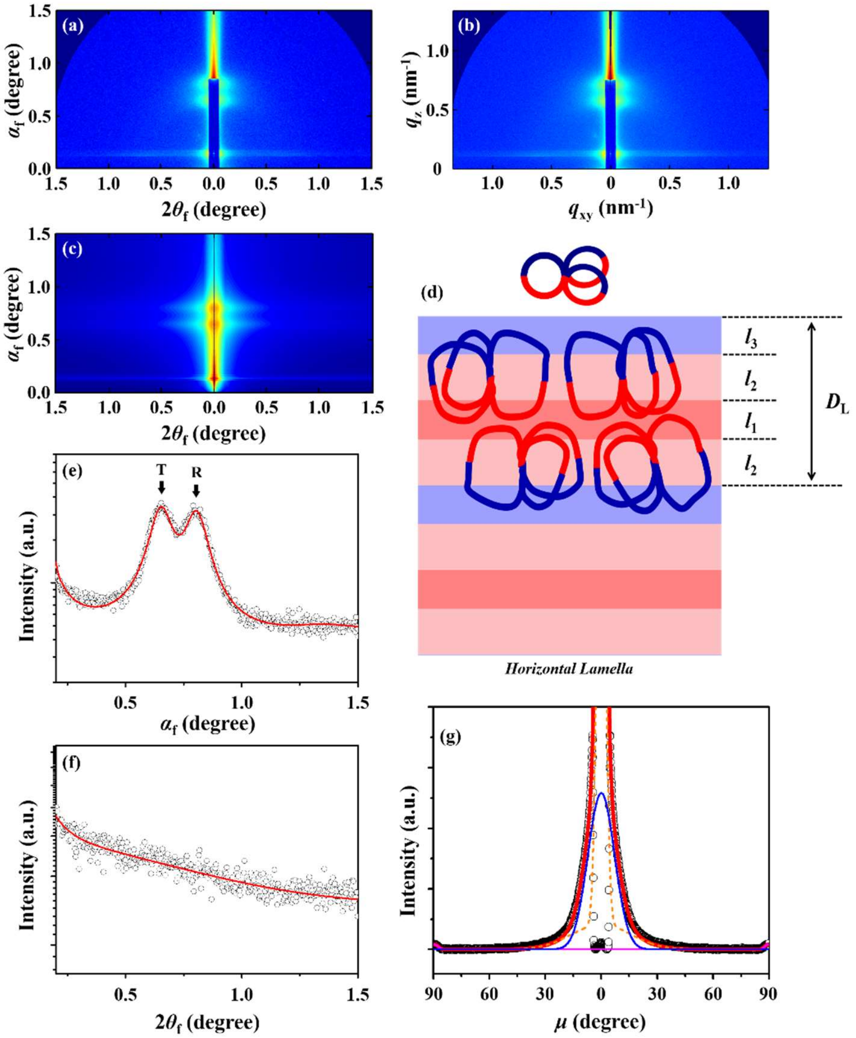

Figure 7.3. Representative GISAXS data of *Tricycle-A* films (100–120 nm thick) measured with α_i = 0.1461°; SDD = 2951.3 mm at room temperature using a synchrotron X-ray beam (λ = 0.12411 nm): (a) 2D scattering image in angle space; (b) 2D scattering image in scattering vector space obtained from the scattering image in (a); (c) 2D scattering image reconstructed with the determined structural parameters; (d) lamellar structure in a front view; (e) out-of-plane scattering profile extracted along the meridian line at $2\theta_f$ = 0.177° from the scattering image in (a); (f) in-plane scattering profile along the equatorial line at α_f = 0.192° from the scattering image in (a). In (e) and (f), the black symbols are the measured data and the solid red lines were obtained by fitting the data using the GIXS formula of lamellar structure model; the scattering peak generated by the reflected X-ray beam is marked with "**R**", whereas that generated by the transmitted X-ray beam is marked with "**T**". (g) Azimuthal scattering profile extracted at q = 0.712 nm^{-1} from the scattering image in (b) where the black symbols are the measured data and the lines were obtained by the deconvolutions of the measured data: the blue solid line is the scattering peak of lamellar structure, the purple dot line is the Yoneda peak, the brown dot line is a part of the reflected X-ray beam, and the red solid line is the sum of all deconvoluted peaks.

Figure 7.3a presents a representative of the 2D GISAXS images measured from the *Tricycle-A* films. The scattering image exhibits only two spots along the meridian line. Considering the GISAXS optics, the scattering spot at $\alpha_f = 0.66°$ might be generated by the transmitted X-ray beam, whereas that at $\alpha_f = 0.80°$ might be caused by the reflected X-ray beam. Overall, this fully anisotropic image is a typical characteristic of scattering pattern from a horizontally-oriented lamellar structure in the film. For examples, the one-dimensional (1D) scattering profiles, which were extracted along the meridian line at $2\theta_f = 0.177°$ and along the equatorial line at $\alpha_f = 0.192°$ from the 2D image, are successfully analyzed by using the grazing incidence X-ray scattering (GIXS) formula derived with lamellar structure model (Section 1.4 of Chapter 1), as displayed in Figures 7.3e and 7.3f. These analyses confirm the presence of lamellar nanostructure in the film, providing structural parameter details. The analysis has been extended for an azimuthal scattering profile extracted at $q = 0.712$ nm^{-1} from the q-space image in Figure 7.3b. The azimuthal profile has been analyzed in a quantitative manner (Figure 7.3g), providing important information that the lamellar structure in the film is horizontally oriented. The obtained structural details are summarized in Table 7.2.

Figure 7.3c presents a 2D scattering image reconstructed from the obtained structural parameters using the GIXS formula. This reconstructed image is well matched with the measured 2D scattering pattern, again confirming that the scattering data have been analyzed satisfactorily.

The scattering analysis has found that the nanostructure in the film is stacked by horizontally-oriented lamellae in which each lamella has a long period D_L of 9.80 nm. The lamella is composed of a layer l_1 of 2.30 nm, an interfacial layer l_2 of 2.70 nm, and a layer l_3 of 2.10 nm. Taking into account the volume fraction of the PDGE block which is slightly larger than that of the PTEGGE block, the l_1 sublayer can be assigned to the PDGE block chain phase; thus, the l_3 sublayer can be assigned to the PTEGGE block chain phase. This lamellar structure could result from the phase-separation of the block chains during the film formation process. Here, it is noteworthy that the domain spacing (D_L = 9.80 nm) is uncommonly very small. The domain spacing is only 38.4–40.8 % of that (24.0–25.5 nm) of the linear block copolymer counterpart.[28] This domain spacing reduction is remarkably huge, compared to those predicted theoretically and observed previously for monocyclic block copolymers and linear counterparts.[29-36]

For the lamellar structure, the second order orientation factor O_s is 0.977, which is reasonably high. But, the positional distortion factor g is somewhat large (0.15). These results collectively inform that the lamellar nanostructure is confirmed to be oriented preferentially in the film plane and stable dimensionally in a reasonable level.

From all structural parameters determined above, a schematic nanostructure could be drawn for the nanoscale film morphology of *Tricycle-A*, as shown in Figure 7.3d. Overall, *Tricycle-A* has nicely demonstrated the formation of dimensionally stable horizontal lamellar structure with unusually small phase-domains.

Table 7.2. Morphological parameters of nanoscale films (100−120 nm thick) of various topological tricyclic heteroblock copolymers

Nanoscale film morphology	Tricyclic heteroblock copolymers				
	Tricycle-A 	*Tricycle-B* 		*Tricycle-C* 	
Lamellar structure	horizontal	horizontal	Vertical	horizontal	Vertical
D_{L}[a] (nm)	9.80	6.05	6.00	6.10	6.10
l_1[b] (nm)	2.30 (1.10)[j]	1.50 (0.40)	1.50 (0.40)	1.80 (0.30)	1.60 (0.40)
l_2[c] (nm)	2.70 (0.80)	1.50 (0.60)	1.50 (0.70)	1.20 (0.30)	1.40 (0.30)
l_3[d] (nm)	2.10	1.55	1.50	1.90	1.70
g[e]	0.15	0.14	0.21	0.30	0.24
$\overline{\varphi}$[f] (deg.)	0	0	89.2	0	90
σ_{φ}[g] (deg.)	7.20	1.10	0.50	18.62	27.73
O_{s}[h]	0.977	0.992	-0.497	0.790	-0.210
ϕ[i] (vol%)	100	99.9	0.1	41.1	58.9

[a]Long period of lamellar structure. [b]Thickness of the l_1 layer. [c]Thickness of the l_2 layer, i.e., interfacial layer. [d]Thickness of the l_3 layer. [e]Paracrystal distortion factor of nanostructure (i.e., lamellar structure) along the *z*-axis which is parallel to the out-of-plane of the film. [f]Mean value of the polar angle φ (i.e., orientation angle) between the orientation vector ***n*** (which is set along a direction normal to the in-plane of lamellar structure) and the out-of-plane direction of the film. [g]Standard deviation for the polar angle φ. [h]Second order orientation factor of nanostructure (i.e., lamellar structure). [i]Volume fraction in percent. [j]Standard deviation.

The nanoscale films of *Tricycle-B* exhibit a clearly distinctive GISAXS pattern (Figure 7.4a). The scattering image apparently resembles that of the *Tricycle-A* film, suggesting that a horizontal lamellar structure is present in the *Tricycle-B* film. With this information, the scattering image has been attempted to be analyzed in a manner similar to that employed for the *Tricycle-A* film. The 1D scattering profiles extracted from the 2D scattering image are satisfactorily analyzed by the GIXS formula based on lamellar structure model (Figures 7.4e-f). An azimuthal scattering profile is extracted from the 2D image in the *q*-space (Figure 7.4b) and then analyzed successfully (Figure 7.4g). The obtained structural details are listed in Table 7.2.

The GISAXS analysis has found that a mixture of phase-separated nanostructures is present in the film. The film is characteristic of having morphology details as follows. The morphology consists of mainly horizontal lamellar structured phases (99.9 vol%) together with vertical lamellar structured phases in a very small fraction (0.1 vol%). For the horizontal lamellar structure, D_{L} = 6.05 nm, l_1 = 1.50 nm, l_2 = 1.50 nm (= l_{i}), l_3 = 1.55 nm, O_{s} = 0.992, and g = 0.14. Similar structural parameters are determined for the vertical lamellar structure. Taking into account the volume fractions of the blocks, the l_1 and l_3 sublayers can be assigned by the PTEGGE and PDGE block chain phases respectively.

A 2D scattering image has been reconstructed with the determined structural parameters using the GIXS formula (Figure 7.4c). The reconstructed image is in good agreement with the measured one. With these structural analysis results, a schematic nanostructure could be drawn for the morphology of the *Tricycle-B* film (Figure 7.4d). Overall, the *Tricycle-B* film reveals a morphology similar to that observed in the *Tricycle-A* film. However, it is remarkable that the dimensional parameters (particularly, domain spacing) are relatively smaller than those of the morphology in the *Tricycle-A* film. In particular, the domain spacing is 61.2–61.7 % of that in the *Tricycle-A* film. These results collectively suggest that the molecular topology of *Tricycle-B* is more effective to reduce domain spacing, compared to *Tricycle-A*.

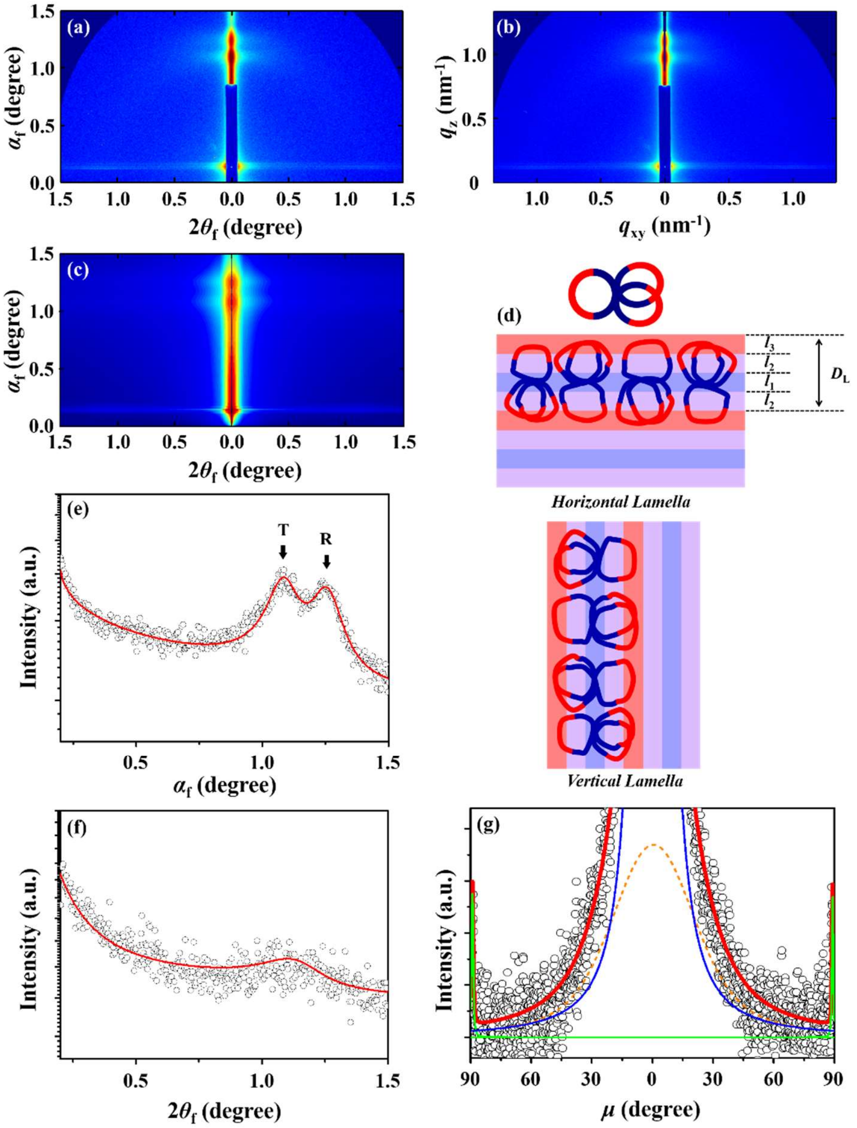

Figure 7.4. Representative GISAXS data of *Tricycle-B* films (100–120 nm thick) measured with α_i = 0.1476°; SDD = 2951.3 mm at room temperature using a synchrotron X-ray beam (λ = 0.12411 nm): (a) 2D scattering image in angle space; (b) 2D scattering image in scattering vector space obtained from the scattering image in (a); (c) 2D scattering image reconstructed with the determined structural parameters; (d) horizontal lamellar structure model in a front view; (e) out-of-plane scattering profile extracted along the meridian line at $2\theta_f$ = 0.117° from the scattering image in (a); (f) in-plane scattering profile along the equatorial line at α_f = 0.191° from the scattering image in (a). In (e and f), the symbols are the measured data and the solid red lines were obtained by fitting the data using the GIXS formula of lamellar structure model; the scattering peak generated by the transmitted X-ray beam, is marked with "**T**", whereas that generated by the reflected X-ray beam is marked with "**R**". (g) Azimuthal scattering profile extracted at q = 1.100 nm^{-1} from the scattering image in (b); the black symbols are the measured data; the lines were obtained by the deconvolutions of the measured data: the blue solid line is the first order scattering peak of horizontal lamellar structure, the green solid line is the first order scattering peak of vertical lamellar structure, the purple dot line is the Yoneda peak, the brown dot line is a part of the reflected X-ray beam, and the red solid line is the sum of all deconvoluted peaks.

Figures 7.5a displays a representative scattering image of the *Tricycle-C* films. The scattering image apparently is somewhat different from those of the *Tricycle-A* and *B* films. One scattering spot appears around 1.10° (= $2\theta_f$) along the equatorial line. Another spot is weakly discernible around 1.02° (= α_f) along the meridian line. These spots are apparently overlapped with a scattering ring. The spot along the equatorial line may be an indication that vertical lamellar structure is present in the film. Another spot along the meridian line may suggest the presence of lamellar structure in the film. Taking into consideration these, the scattering pattern has been further analyzed. The 1D scattering profiles have been extracted along the meridian line at $2\theta_f = 0.071°$ and along the equatorial line at $\alpha_f = 0.200°$ from the 2D image and well fitted by using the GIXS formula derived with lamellar model (Figures 7.5e-f). Moreover, an azimuthal scattering profile has extracted at q = 0.977 nm^{-1} from the q-space image (Figure 7.5b) and then analyzed in a quantitative manner (Figure 7.5g). The determined structural details are listed in Table 7.2.

The scattering analysis finds that in the film horizontal and vertical lamellar structures are present together in a volume fraction of 41.1 and 58.9 %, respectively. The vertical lamellar structure is characterized to reveal a dimension set of D_L = 6.10 nm, l_1 = 1.80 nm, l_i = 1.20 nm, and l_3 = 1.90 nm. A similar dimension set is observed for the horizontal lamellar structure. The domain spacings are smaller than that of the *Tricycle-A* film but very close to those of the *Tricycle-B* films. Indeed, *Tricycle-C* is a more efficient topology to reduce domain spacing, compared to *Tricycle-A*.

The vertical lamellar structure exhibits relatively lower g value (0.24) than that (0.30) of the horizontal lamellar structure, indicating that the vertical lamellar structure is slightly more stable than the horizontal one. However, the vertical lamellar structure shows larger σ_φ value (which is the standard deviation of the polar angle φ between the orientation vector $\boldsymbol{n}$ set along a direction normal to the in-plane of lamellar structure and the out-of-plane direction of the film), compared to that of the horizontal one. Namely, the vertical lamellar structure behaves less orientational order than that of the horizontal one.

These *g* values are almost twice larger than those of the lamellae in the *tricycle-A* and *B* films. The σ_φ values are also much larger than those of the lamellae in the *Tricycle-A* and *B* films. Namely, the *g* factor, as well as the σ_φ value is in the increasing order, respectively: *Tricycle-B* < *Tricycle-A* << *Ticycle-C*. Furthermore, the scattering pattern of the *Tricycle-C* film is less distinctive and much weaker in intensity, compared to those of the *Tricycle-A* and *B* films. The *Tricycle-B* film exhibits more clearly distinctive and intense scattering image than the *Tricycle-A*. When compared to *Bicycle-C* (∞) copolymer from chapter 6, *Tricycle-B* copolymer demonstrates approximately 13% reduction in domain spacing of the lamellar structure with similar value for the *g* factor and nearly unaffected control over the orientation of the lamellar structure. This indicates that *Tricycle-B* maintains the structural ordering despite the domain spacing reduction, which is a remarkable result.

Overall, the *Tricycle-B* topology has demonstrated well-defined, better preferentially oriented, and more stable lamellar structure with smaller domain spacing in nanoscale films, compared to the *Tricycle-A* and *Tricycle-C* topologies.

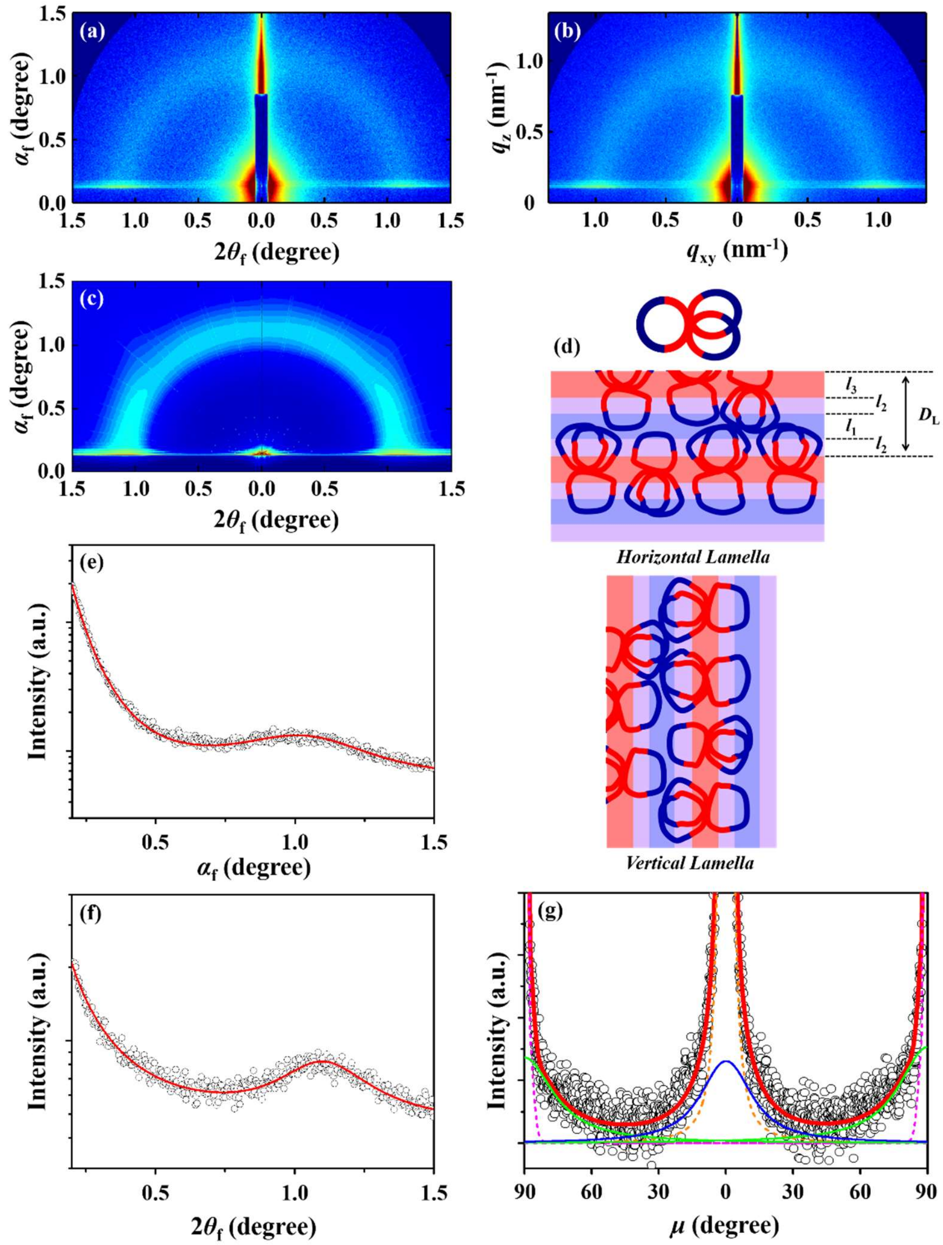

Figure 7.5. Representative GISAXS data of *Tricycle-C* films (100–120 nm thick) measured with α_i = 0.1384°; SDD = 2951.3 mm at room temperature using a synchrotron X-ray beam (λ = 0.12411 nm): (a) 2D scattering image in angle space; (b) 2D scattering image in scattering vector space obtained from the scattering image in (a); (c) 2D scattering image reconstructed with the determined structural parameters; (d) horizontal lamellar structure model in a front view; (e) out-of-plane scattering profile extracted along the meridian line at $2\theta_f$ = 0.071° from the scattering image in (a); (f) in-plane scattering profile along the equatorial line at α_f = 0.200° from the scattering image in (a); (g) azimuthal scattering profile extracted at q = 0.977 nm^{-1} from the scattering image in (b) where the black symbols are the measured data and the lines were obtained by the deconvolutions of the measured data: the blue solid line is the first order scattering peak of horizontal lamellar structure, the green solid line is the first order scattering peak of vertical lamellar structure, the purple dot line is the Yoneda peak, the brown dot line is a part of the reflected X-ray beam, and the red solid line is the sum of all deconvoluted peaks.

7.4 Conclusions

Three different tricyclic topologies of PDGE and PTEGGE blocks in equivalent volume fractions have been investigated in detail by synchrotron GIXS analysis. The quantitative GIXS analysis provides the morphology details of the topological heteroblock copolymers in nanoscale films.

All three copolymers form amorphous films at room temperature. However, they all exhibit lamellar nanostructures resulted from the phase-separations between the blocks through the film fabrication processes. The stability, orientation, and dimensional parameters of the nanostructure are varied with the molecular topologies. Both the dimensional stability and orientation orders are in the increasing order: *Tricycle-C* << *Tricycle-A* < *Tricycle-B*. The domain spacing is in the decreasing order: *Tricycle-A* >> *Tricycle-C* > *Tricycle-B*. Overall, the *Tricycle-B* topology demonstrates most well-defined lamellar structure with the highest stability and orientation as well as the smallest domain spacing.

In summary, this chapter has demonstrated the quantitative analysis through three layer model was successful in parameterizing the morphological details of tricyclic block copolymers in thin films. All nanostructures analyzed by the modeling analysis have been identified with exceptionally smaller domain spacings than that of the linear counterpart. The domain spacing reductions are within the range of 59.1−76.5 %; these huge reductions could not be achieved with monocyclic block copolymer systems. Moreover, the domain spacings (less than 10 nm) demonstrated in this study can meet the pitches required for advanced semiconductors with high performance being scheduled for production in 2030 by the International Technology Roadmap for Semiconductors.[37] Therefore, the study opens up that tricyclic heteroblock copolymer systems (in particular, *Tricycle-A* and *Tricycle-B* type topologies) are a most efficient candidates for developing high performance nanolithographic materials being demanded for manufacturing future high performance semiconductors. Overall, the novel model analysis have successfully established new insights in the topology-morphology correlation of tricyclic block copolymers.

7.5 References

1. Patnode, W.; Wilcock, D. F. Methylpolysiloxanes. *J. Am. Chem. Soc.***1946**, *68*, 358−363.
2. Zimm, B. H; Stockmayer, W. H. The Dimensions of Chain Molecules Containing Branches and Rings. *J. Chem. Phys*. **1949**, *17*, 1301−1314.
3. Semlyen, J. A. Cyclic Polymers, 2nd ed., Kluwer Academic Publishers: Dordrecht, Netherlands, 2002.
4. Laurent, B. A.; Grayson, S. M. Synthetic Approaches for the Preparation of Cyclic Polymers. *Chem. Soc. Rev.* **2009**, *38*, 2202–2213.
5. Kricheldorf, H. R. Cyclic Polymers: Synthetic Strategies and Physical Properties. *J. Polym. Sci. Part A: Polym. Chem.* **2010**, *48*, 251− 284.
6. Yamamoto, T.; Tezuka, Y. Topological polymer chemistry: a cyclic approach toward novel polymer properties and functions. Polym. Chem. 2011, 2, 1930−1941.
7. Lonsdale, D. E.; Monteiro, M. J. Synthesis and Self-Assembly of Amphiphilic Macrocyclic Block Copolymer Topologies. *J. Polym. Sci. Part A: Polym. Chem.* **2011**, *49*, 4603–4612.
8. Jia, Z.; Monteiro, M.J. Cyclic Polymers: Methods and Strategies. *J. Polym. Sci. Part A: Polym. Chem*. **2012**, *50*, 2085−2097.
9. Jia, Z.; Monteiro, M.J. Synthesis of Cyclic Polymers via Ring Closure. *Adv. Polym. Sci.* **2013**, *262*, 295−328.
10. Tezuka, Y., Ed., Topological Polymer Chemistry: Progress of Cyclic Polymers in Syntheses, Properties and Functions, World Scientific: Hackensack, NJ, USA, 2013.
11. Isono, T.; Satoh, Y.; Miyachi, K.; Chen, Y.; Sato, S.-i.; Tajima, K.; Satoh, T.; Kakuchi, T. Synthesis of Linear, Cyclic, Figure-Eight-Shaped, and Tadpole Shaped Amphiphilic Block Copolyethers via t-Bu-P4-Catalyzed RingOpening Polymerization of Hydrophilic and Hydrophobic Glycidyl Ethers. *Macromolecues* **2014**, *47*, 2853−2863.
12. Wang, H.; Zhang, L.; Liu, B.; Han, B.; Duan, Z.; Qi, C.; Park, D.; Kim, I. Synthesis of High Molecular Weight Cyclic Poly(*ε*-caprolactone)s of Variable Ring Size Based on A Light-Induced Ring-Closure Approach. *Macromol. Rapid Commun*. **2015**, *36*, 1646−1650.
13. Zhao, Z.; Zhu, Q.; Wang, Z.; Lu, J.; Jin, Z.; Liu, H. A Dicyclic Scaffold for Programmed Monocyclic and Polycyclic Polymer Architectures. *Macromolecules* **2017**, *50*, 8907−8915.
14. Xiang, L.; Ryu, W.; Kim, H.; Ree, M. Precise Synthesis, Properties, and Structures of Cyclic Poly(*ε*-caprolactone)s. *Polymers* **2018**, *10*, 577.
15. Isono, T.; Sasamori, T.; Honda, K.; Mato, Y.; Yamamoto, T.; Tajima, K.; Satoh, T. Multicyclic Polymer Synthesis through Controlled/Living Cyclopolymerization of α,ω-Dinorbornenyl-Functionalized Macromonomers. *Macromolecules* **2018**, *51*, 3855–3864.
16. Yamamoto, T.; Hosokawa, M.; Nakamura, M.; Sato, S.-i.; Isono, T.; Tajima, K.; Satoh, T.; Sato, M.; Tezuka, Y.; Saeki, A.; Kikkawa, Y. Synthesis, Isolation, and Properties of All Head-to-Tail Cyclic Poly(3-hexylthiophene): Fully Delocalized Exciton over the Defect-Free Ring Polymer. *Macromolecules* **2018**, *51*, 9284–9293.
17. Mato, Y.; Honda, K.; Tajima, K.; Yamamoto, T.; Isono, T.; Satoh, T. A Versatile Synthetic Strategy for Macromolecular Cages: Intramolecular Consecutive Cyclization of Star-Shaped Polymers. *Chem. Sci.* **2019**, *10*, 440–446.
18. Zhao, J.; Zhou, Y.; Li, Y.; Pan, X.; Zhang, W.; Zhou, N.; Zhang, K.; Zhang, Z.; Zhu, X. Modular construction of macrocycle-based topological polymers via high-efficient thiol chemistry. Polym. Chem. 2015, 6, 2879−2891.
19. Lonsdale, D. E.; Monteiro, M. J. Various Polystyrene Topologies Built from Tailored Cyclic Polystyrene *via* CuAAC reactions. *Chem. Commun.* **2010**, *46*, 7945–7947.

20. Tomikawa, Y.; Fukata, H.; Ko, Y. S.; Yamamoto, T.; Tezuka, Y. Construction of Double-Eight and Double-Trefoil Polymer Topologies with Core-Clickable *kyklo*-Telechelic Precursors. *Macromolecules* **2014**, *47*, 8214-8223.
21. Jia, Z.F.; Lonsdale, D.E.; Kulis, J.; Monteiro, M. J. Construction of a 3-Miktoarm Star from Cyclic Polymers. *ACS Macro Lett.* **2012**, 1, 780–783.
22. Shingu, T.; Yamamoto, T.; Tajima, K.; Isono, T.; Satoh, T. Synthesis of μ-ABC Tricyclic Miktoarm Star Polymer via Intramolecular Click Cyclization. *Polymers* **2018**, *10*, 877.
23. Satoh, Y.; Matsuno, H.; Yamamoto, T.; Tajima, K.; Isono, T.; Satoh, T. Synthesis of Well-Defined Three- and Four-Armed Cage-Shaped Polymers via "Topological Conversion" from Trefoil- and Quatrefoil- Shaped Polymers. *Macromolecules* **2017**, *50*, 97−106.
24. Ree, B. J.; Satoh, Y.; Jin, K. S.; Isono, T.; Kim, W. J.; Kakuchi, T.; Satoh, T.; Ree, M. Well-Defined Stable Nanomicelles Self-Assembled by Brush Cyclic and Tadpole Copolymer Amphiphiles: A Versatile Smart Carrier Platform. *NPG Asia Materials* **2017**, *9*, e453.
25. Kim, Y. Y.; Ree, B. J.; Kido, M.; Ko, Y.-G.; Ishige, R.; Hirai, T.; Wi, D.; Kim, J.; Kim, W. J.; Takahara, A.; Ree, M. High Performance n-Type Electrical Memory and Morphology-Induced Memory-Mode Tuning of A Well-Defined Brush Polymer Bearing Perylene Diimide Moieties. *Adv. Electronic Mater.* **2015**, *1*, 1500197.
26. Ree, B. J.; Aoki, D.; Kim, J.; Satoh, T.; Takata, T.; Ree, M. Macromolecular [2]Rotaxanes Linked with Polystyrene: Properties and Nanoscale Film Morphologies. *Macromolecules* **2019**, *52*, 5325−5336.
27. Ree, B. J.; Aoki, D.; Kim, J.; Satoh, T.; Takata, T.; Ree, M. Phase Transition Behaviors and Nanoscale Film Morphologies of Poly(δ-valerolactone) Axles Bearing Movable and Fixed Rotaxane Wheels. *Macromol. Rapid Commun*. **2019**, *40*, 1900334
28. Ree, B. J. Materials from Chapter 5 of this Ph.D. Dissertation. Unpublished work, 2019.
29. Marko, J. F. Microphase Separation of Block Copolymer Rings. *Macromolecules* **1993**, *26*, 1442−1444.
30. Jo, W. H.; Jang, S. S. Monte Carlo Simulation of The Order–Disorder Transition of A Symmetric Cyclic Diblock Copolymer System. *J. Chem. Phys.* **1999**, *111*, 1712−1720.
31. Zhang, G.; Fan, Z.; Yang, Y.; Qiu, F. Phase Behaviors of Cyclic Diblock Copolymers. *J. Chem. Phys.* **2011**, *135*, 174902.
32. Honda, S.; Koga, M.; Tokita, M.; Yamamoto, T.; Tezuka, Y. Phase Separation and Self-Assembly of Cyclic Amphiphilic Block Copolymers with A Main-Chain Liquid Crystalline Segment. *Polym. Chem*. **2015**, *6*, 4167–4176.
33. Zhu, Y. Q.; Gido, S. P.; Iatrou, H.; Hadjichristidis, N.; Mays, J. W. Microphase Separation of Cyclic Block Copolymers of Styrene and Butadiene and of Their Corresponding Linear Triblock Copolymers. *Macromolecules* **2003**, *36*, 148−152.
34. Takano, A.; Kadoi, O.; Hirahara, K.; Kawahara, S.; Isono, Y.; Suzuki, J.; Matsushita, Y. Preparation and Morphology of Ring-Shaped Polystyrene-block-polyisoprenes, *Macromolecules* **2003**, *36*, 3045−3050.
35. Lescanec, R. L.; Hajduk, D. A.; Kim, G. Y.; Gan, Y.; Yin, R.; Gruner, S. M.; Hogen-Esch, T. E.; Thomas, E. L. Comparison of the Lamellar Morphology of Microphase-Separated Cyclic Block Copolymers and Their Linear Precursors. *Macromolecules* **1995**, *28*, 3485−3489.
36. Poelma, J. E.; Ono, K.; Miyajima, D.; Aida, T.; Satoh, K.; Hawker, C. J. Cyclic Block Copolymers for Controlling Feature Sizes in Block Copolymer Lithography. *ACS Nano* **2012**, *6*, 10845−10854.
37. Semiconductor Industry Association, *The International Technology Roadmap for Semiconductors 2.0, 2015 Edition*, 2015; www.itrs2.net/.

Chapter 8

Nanoscale Film Morphologies of Cage Block Copolyethers

8.1 Introduction

Synthetic cyclic polymers were first introduced in 1940s as a new interesting polymer family[1-3] and then found to behave topological effects in properties due to the molecular geometry and the absence of chain ends.[4] Immediately, the synthesis of new cyclic polymers and their derivatives has been challenged in the polymer community. As a result of much research effort, several synthetic methods have been developed, producing various topological cyclic polymers.[5-18] The development effort has been focused mainly for monocyclic polymers and their derivatives because of synthetic feasibilities.[5-14]

In contrast, multicyclic polymer topologies have been reported in a limit base because of severe difficulties in the synthesis.[10-12,15-19] Despite the synthetic difficulties, a few fused multicyclic polymers (i.e., cage-shaped polymers) have been prepared successfully: homoblock-based cages: cage-shaped polytrahydrofurans,[18-22] polystyrenes,[23-25] and poly(ε-caprolactone)s;[26] heterblock-based cages: cages consisted of poly(*n*-decyl glycidyl ether) and poly(2-(2-(2-methoxyethoxy)ethoxy)ethyl glycidyl ether) blocks.[27] Nevertheless, morphologies and properties of these polymeric cages have yet be understood.

This chapter is the first report on the morphology details on various cage-shaped block copolymers composed of poly(*n*-decyl glycidyl ether) (PDGE) and poly(2-(2-(2-methoxyethoxy)ethoxy)ethyl glycidyl ether) (PTEGGE) in equivalent volume fractions. Synchrotron grazing incidence X-ray scattering (GIXS) analysis finds that they form phase-separated morphologies in thin films. Interestingly, they reveal different types of nanostructure depending on the cage topologies. Excitingly, they all produce significantly reduced domain spacings, which could not be achievable from the linear block copolymer counterpart. The degree of domain spacing reduction is dependent upon the cage topologies. The structural parameters are varied further with the molecular topologies.

(a) *Cage-A*

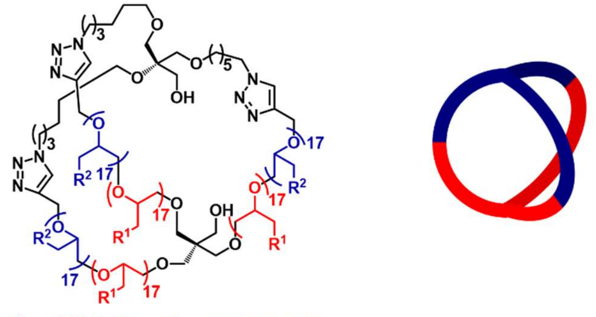

R^1 = -O(CH$_2$)$_9$CH$_3$ R^2 = -(OCH$_2$CH$_2$)$_3$CH$_3$

(b) *Cage-B*

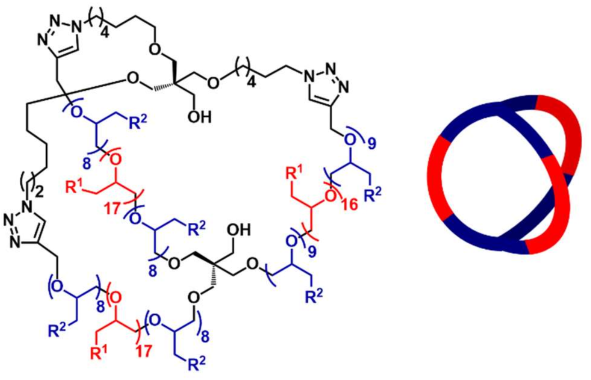

(c) *Cage-C*

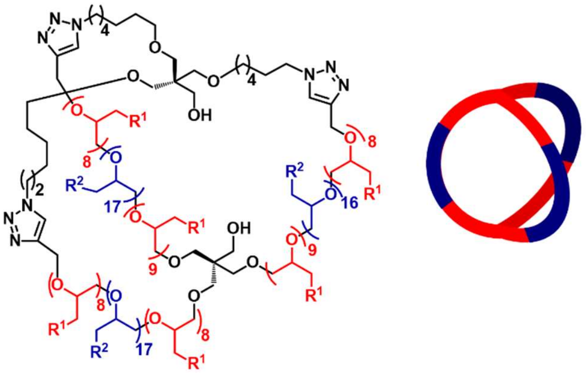

Figure 8.1 Chemical structures of cage-shaped heteroblock copolymers in various topologies.

Table 8.1 Molecular characteristics of various cage-shaped heteroblock copolymers and their homopolymers [a]

Polymer	$M_{n,NMR}$[b] (kDa)	$Đ$[c]	ρ_e[d] (nm^{-3})	ρ_m[e] (g/cm^3)	PDGE block		PTEGGE block	
					DP_{PDGE}[f]	ϕ_{PDGE}[g]	DP_{PTEGGE}[h]	ϕ_{PTEGGE}[i]
Cage-A	22.6	1.02			49	0.494	51	0.506
Cage-B	22.6	1.02			50	0.504	50	0.496
Cage-C	22.6	1.03			50	0.504	50	0.496
l-PDGE	11.1	1.03	341	1.01				
l-PTEGGE	11.2	1.04	353	1.05				

[a] Characterization data from references no. 27 and 28. [b] Number-average molecular weight in the unit of kDa (10^3 Da) of polymer determined by ^{1}H NMR spectroscopic analysis. [c] Dispersity value of polymer determined by size exclusion chromatography (SEC) analysis in tetrahydrofuran. [d] Electron density of polymer in films determined by X-ray reflectivity analysis. [e] Mass density of polymer in films obtained from the electron density determined by X-ray reflectivity analysis. [f] Number-average degree of polymerization of PDGE block determined by ^{1}H NMR spectroscopic analysis. [g] Volume fraction of PDGE block estimated from the $M_{n,NMR}$ and ρ_m data. [h] Number-average degree of polymerization of PTEGGE block determined by ^{1}H NMR spectroscopic analysis. [i] Volume fraction of PTEGGE block estimated from the $M_{n,NMR}$ and ρ_m data.

8.2 Experimental Section

A series of cage-shaped heteroblock copolymers of PDGE and PTEGGE was synthesized and characterized as reported previously in the literature.[27,28] The molecular characteristics of the copolymers are listed in Table 8.1. For the individual copolymers, solutions with 0.5 wt% concentration were prepared in tetrahydrofuran and filtrated via disposable syringes equipped with polytetrafluoroethylene filter membranes (0.2 μm pore size). Each solution was spin-cast onto silicon substrates, then dried in vacuum at room temperature for 24 h. The obtained copolymer films were measured to have a thickness of 100–120 nm by using a spectroscopic ellipsometer (Model M-2000, Woollam, Lincoln, NE, USA). The films were kept at room temperature in vacuum before use.

GIXS measurements were conducted at the 3D Beamline of the PLS-II facility (3.0 GeV power), Pohang Accelerator Laboratory, Pohang, Korea.[29-31] The sample-to-detector distance (SDD) was set 214.7 mm for wide angle grazing incidence X-ray scattering

(GIWAXS) measurements and 2951.3 mm for small angle grazing incidence X-ray scattering (GISAXS) measurements. An X-ray beam of 0.12411 nm wavelength λ was used and the incidence angle α_i was set in the range of 0.1254–0.1850° with respect to the film plane. A two-dimensional (2D) charge-coupled detector (CCD) (model Rayonix 2D SX 165, Rayonix, Evanston, IL, USA) was employed; a set of aluminum foils was used as a semi-transparent beam stop. The scattering data collection time ranged in 10–30 s. All scattering measurements were conducted at room temperature. The scattering angles were corrected by using a precalibrated polystyrene-*block*-poly(ethylene-*random*-butylene)-*block*-polystyrene and silver behenate standards (Tokyo Chemical Inc., Tokyo, Japan) were employed; the positions of the X-ray beams reflected from the silicon substrate were used additionally.

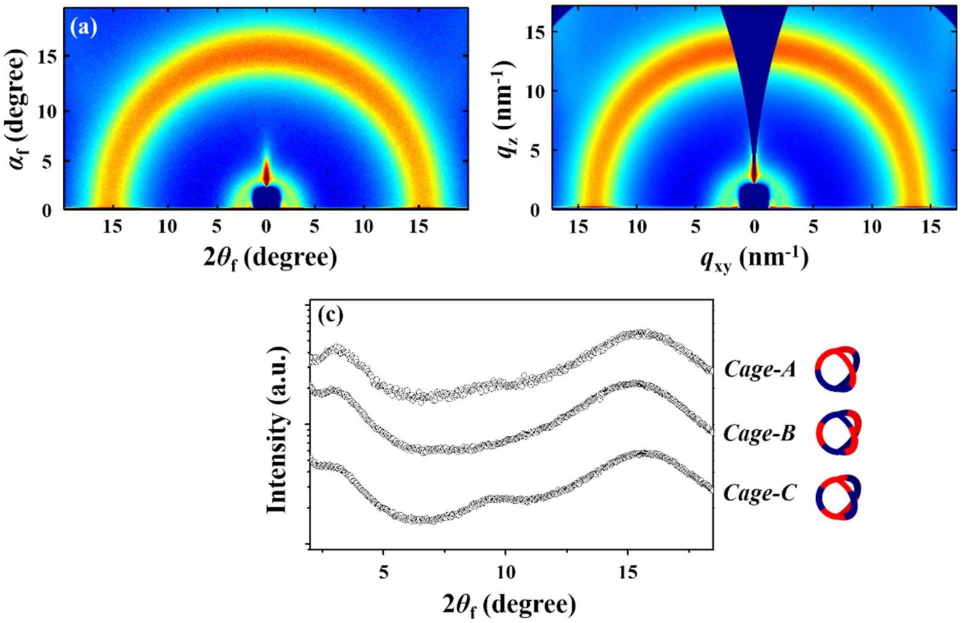

Figure 8.2 Representative GIWAXS data of the nanoscale films (100–120 nm thick) of cage-shaped heteroblock copolymers measured with SDD = 214.7 mm at room temperature using a synchrotron X-ray beam (λ = 0.12411 nm): (a) 2D scattering image in angle space ($2\theta_f$ and α_f) of *Cage-B* (α_i = 0.1740°); (b) 2D scattering image in scattering vector space (q_{xy} and q_z) obtained from the scattering image in (a); (c) in-plane scattering profiles extracted along the equatorial line at chosen α_f values (0.300° for *Cage-A*, 0.279° for *Cage-B*, and 0.290° for *Cage-C*) from the measured 2D scattering images, including the image in (a).

8.3 Results and Discussion

All three cage-shaped heteroblock copolymers in nanoscale films (100–120 nm thick) present featureless characteristics in the GIWAXS patterns (Figure 8.2). They show one halo ring around 3.1° (ca. 2.3 nm *d*-spacing) and another halo ring around 15.6° (ca. 0.46 nm *d*-spacing). Considering the *d*-spacing values, the first halo ring in the low angle region may originate from the mean interdistance of the polymer chains and the second one in the high angle region may be caused by the mean interdistance between the polymer chain and the side group as well as that between the side groups. Collectively, these GIWAXS results inform that the block components in all cage copolymers reveal amorphous natures at room temperature, forming no crystallites.

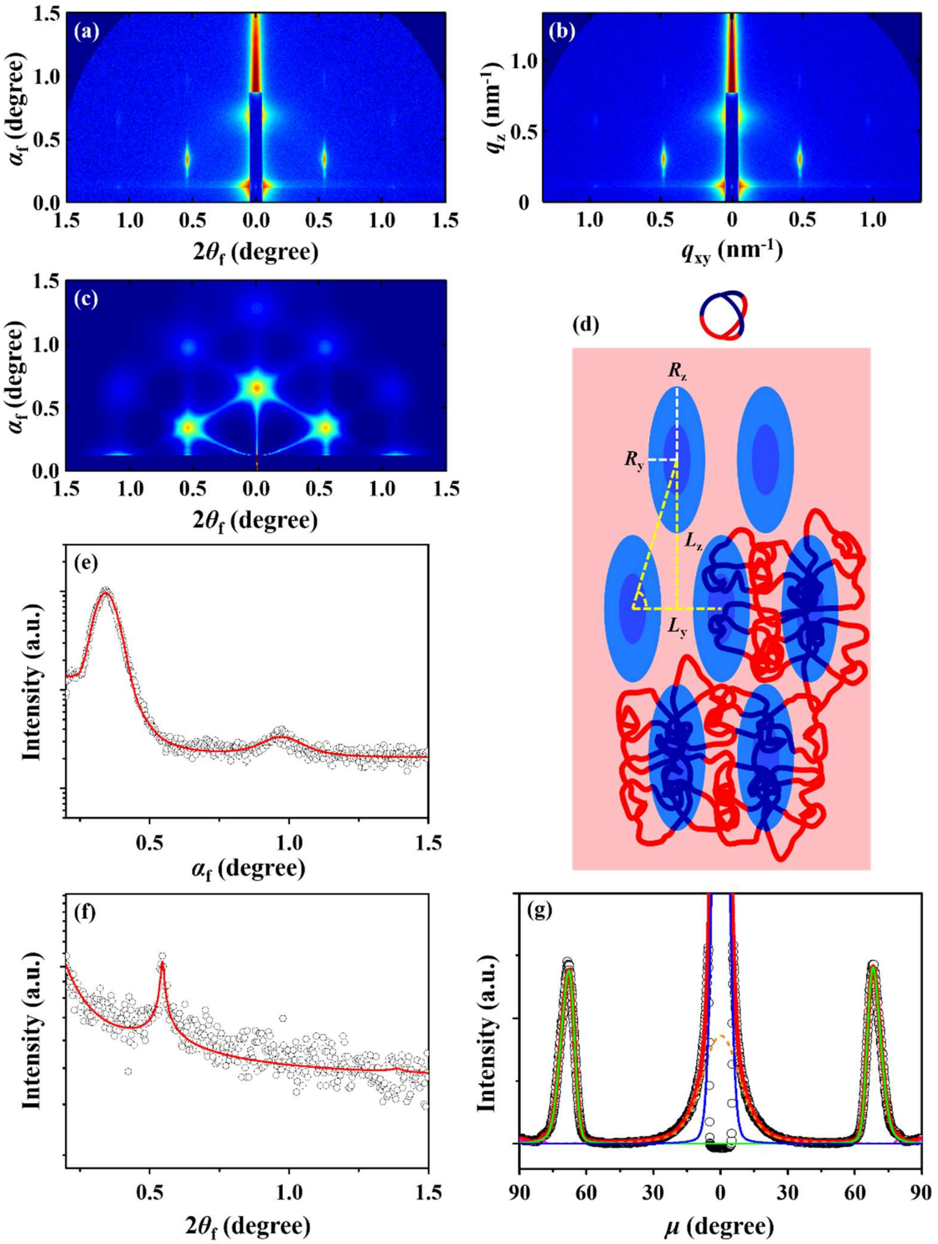

Figure 8.3 Representative GISAXS data of *Cage-A* films (100–120 nm thick) measured with α_i = 0.1254°; SDD = 2951.3 mm at room temperature using a synchrotron X-ray beam (λ = 0.12411 nm): (a) 2D scattering image in angle space; (b) 2D scattering image in scattering vector space obtained from the scattering image in (a); (c) 2D scattering image reconstructed with the determined structural parameters; (d) lamellar structure in a front view; (e) out-of-plane scattering profile extracted along the meridian line at $2\theta_f$ = 0.544° from the scattering image in (a); (f) in-plane scattering profile along the equatorial line at α_f = 0.182° from the scattering image in (a); (g) azimuthal scattering profile extracted at q = 0.607 nm^{-1} from the scattering image in (b) where the black symbols are the measured data; the lines were obtained by the deconvolutions of the measured data: the blue and green solid lines are the scattering peaks of cylindrical domains in a hexagonal packing order, the purple dot line is the Yoneda peak, the brown dot line is a part of the reflected X-ray beam, and the red solid line is the sum of all deconvoluted peaks.

Figure 8.3a presents a representative of the 2D GISAXS images measured from the *Cage-A* films. Two scattering spot appears at $\alpha_f = 0.690°$ and $1.303°$ along the meridian line at $2\theta_f = 0°$; the spot at the lower angle is very strong in intensity and, however, that at the larger angle is very weak. These spots are approximated to have the relative scattering vector lengths of 1 and 2 respectively from the specular reflection position of the used X-ray beam. Additional two spots are observed at $\alpha_f = 0.344°$ and $0.969°$ along the meridian line at $2\theta_f = 0.544°$. Their relative scattering vector lengths are estimated to be 1 and $\sqrt{3}$ respectively from the specular reflection position. The *d*-spacing of the spots at ($2\theta_f = 0°$ and $\alpha_f = 0.690°$) is close to that of that at ($2\theta_f = 0.544°$ and $\alpha_f = 0.344°$). Furthermore, the *d*-spacing of the spots at ($2\theta_f = 0°$ and $\alpha_f = 1.303°$) is similar to that of the peak at ($2\theta_f = 0.544°$ and $\alpha_f = 0.969°$). These correlations collectively suggest that the observed scattering spots originate from horizontally-oriented cylinders in a hexagonal (HEX) packing order. With these information, one-dimensional (1D) scattering profiles have been extracted along the meridian and equatorial lines, as displayed in Figures 8.3e-f. The extracted 1D scattering profiles are satisfactorily fitted by using the GIXS formula derived with HEX cylindrical structure model (Section 1.4 of Chapter 1), giving nanostructural parameters (Table 8.2). An azimuthal scattering profile has additionally be extracted at $q = 0.607$ nm^{-1} from the *q*-space image (Figure 8.3b) and then analyzed successfully (Figure 8.3g), providing orientational information on the nanostructure (Table 8.2).

This GISAXS analysis confirms the presence of cylindrical domains in the *Cage-A* film. These cylindrical domains are an indication that the PDGE and PTEGGE blocks were phase-separated through the film fabrication process. The spacing of the cylindrical domains is determined to be 10.85 nm (= L_z) in the out-of-plane of the film but 6.50 nm (= L_y) in the film plane. The L_z/L_y ratio (= γ) is 1.67, which is much larger than that ($\sqrt{3}/2$) of a regular HEX cylinder structure. The cylindrical domains have a radius R_z of 5.40 nm [= 2.60 (r_{cz}, core radius) + 2.80 nm (t_{sz}, shell thickness)] along the out of the plane of the film and a radius R_y of 2.10

nm [= 1.00 (r_{cy}, core radius) + 1.10 nm (t_{sy}, shell thickness)] along the film plane, consequently revealing an ellipsoidal cross-section; the ellipsoidicity ε is 2.57, which is uncommonly high. Hence, the directional anisotropy in the domain spacing, as well as the significantly large distortion in the HEX structure is attributed to the cylindrical domains with the highly ellipsoidicity value. The second order orientation factor O_{s} is 0.994 with $\overline{\varphi}$ = 0° (the mean value of the polar angle φ between the orientation vector ***n*** set along a direction normal to the {001} plane of HEX structure and the out-of-plane direction of the film) and σ_{φ} = 3.10° (standard deviation for the polar angle φ). The positional distortion factor g is only 0.06. These results collectively inform that the HEX structure is highly distorted in the packing and, nevertheless, stable dimensionally and further preferentially well oriented in the film plane.

From the dimensional parameters, the volume fractions of the cylinders and matrix are estimated to be 50.5 and 49.5 % respectively. For *Cage-A*, the volume fraction of the PTEGGE block is slightly larger than that of the PDGE block. Therefore, the cylindrical domain is assigned by the phase-separated PTEGGE block phase; the matrix is assigned to the PDGE phase.

From the obtained structural parameters, a scattering image has been reconstructed by using the GIXS formula. The reconstructed scattering image is well matched with the measured pattern (Figure 8.3c), again confirming that the scattering data analysis has been done successfully. Furthermore, with the analysis results, the nanostructure formed in the *Cage-A* film could be schematically drawn, as shown in Figure 8.3d.

Here, a question is raised: Why were the PTEGGE cylinders formed with unusually high ellipsoidicity? Such the ellipsoidal cylinders may result from directionally different growths in the phase-separation process due to the nanoscale film confined geometrically by the substrate and the air (or vacuum). The phase-separation and growth may be relatively more favorable toward the air or vacuum interface, namely the out-of-plane of the film, than toward the in-plane of the film adhered onto the substrate.

Another question is raised: Why did *Cage-A* form HEX cylindrical structure even though the almost equivalent volume fractions of the block components? This HEX structure is very interesting because it is far from the lamellar structure of the linear block copolymer counterpart.[32] Additionally, the *Tricycle-A* copolymer from chapter 7 also presents lamellar morphology. This unusual HEX structure formation may be attributed to the unique *Cage-A* topology effect which possibly promotes to differentiate the chain characteristics of the blocks.

Finally, it is noteworthy that remarkably small domain spacings were achieved by the *Cage-A* topology. The domain spacings are only 25.5−45.2 % of that (24.00–25.50 nm) of the nanostructure formed in the linear counterpart. The domain spacing reductions (54.8−74.5 %) are very significant, which could not be achievable by the pairs of monocyclic block copolymers and linear counterparts.[33-40]

Table 8.2 Morphological parameters of nanoscale films (100–120 nm thick) of various cage-shaped heteroblock copolymers

Thin film morphology	Cage-shaped heteroblock copolymers				
	Cage-A	*Cage-B*		*Cage-C*	
HEX cylindrical structure	horizontal				
L_{z}[a] (nm)	10.85				
L_{y}[b] (nm)	6.50				
γ[c]	1.67				
R_{z}[d] (nm)	5.40				
R_{y}[e] (nm)	2.10				
r_{cz}[f] (nm)	2.60 (0.30)[t]				
r_{cy}[g] (nm)	1.00 (0.20)				
t_{sz}[h] (nm)	2.80 (0.60)				
t_{sy}[i] (nm)	1.10 (0.30)				
ε[j]	2.57				
g[k]	0.06				
$\overline{\varphi}$[l] (deg.)	0				
σ_{φ}[m] (deg.)	3.10				
O_{s}[n]	0.991				
ϕ[o] (vol%)	100				
Lamellar structure		horizontal	vertical	horizontal	vertical
D_{L}[p] (nm)		6.95	6.90	6.50	6.70
l_1[q] (nm)		2.10 (0.30)	2.10 (0.30)	1.60 (0.50)	1.70 (0.30)
l_2[r] (nm)		1.30 (0.20)	1.30 (0.20)	1.60 (0.60)	1.60 (0.50)
l_3[s] (nm)		2.25	2.20	1.70	1.80
g		0.33	0.31	0.35	0.28
$\overline{\varphi}$ (deg.)		0	70.00	0	90
σ_{φ} (deg.)		18.35	16.20	6.13	27.55
O_{s}		0.829	-0.212	0.969	-0.221
ϕ (vol%)		34.5	65.5	33.9	66.1

[a] Mean interdistance between the arrays of the in-plane oriented cylindrical domains. [b] Mean center-to-center distance of the cylindrical domains lain in the film plane. [c] Ratio of L_{z} and L_{y} (= $L_{\mathrm{z}}/L_{\mathrm{y}}$). [d] Long radius of ellipsoidal cylindrical domain along the z-axis which is parallel to the out-of-plane of the film. [e] Short radius of ellipsoidal cylindrical domain along the y-axis which is parallel to the in-plane of the film. [f] Core radius of ellipsoidal cylindrical domain along the z-axis which is parallel to the out-of-plane of the film. [g] Core radius of ellipsoidal cylindrical domain along the y-axis which is parallel to the in-plane of the film. [h] Shell thickness of ellipsoidal cylindrical domain along the z-axis which is parallel to the out-of-plane of the film. [i] Shell thickness of ellipsoidal cylindrical domain along the y-axis which is parallel to the in-plane of the film. [j] Ellipsoidicity ratio (= polar radius/equatorial radius). [k] Paracrystal distortion factor of nanostructure (i.e., hexagonal cylinder structure or lamellar structure) along the z-axis which is parallel to the out-of-plane of the film. [l] Mean value of the polar angle φ (i.e., orientation angle) between the orientation vector $\boldsymbol{n}$ (which is set along a direction normal to the {001} plane of horizontal hexagonal cylindrical structure or the in-plane of lamellar structure) and the out-of-plane direction of the film. [m] Standard deviation for the polar angle φ. [n] Second order orientation factor of nanostructure (i.e., hexagonal cylindrical structure or lamellar structure).

[o]Volume fraction in percent. [p]Long period of lamellar structure. [q]Thickness of the l_1 layer. [r]Thickness of the l_2 layer, i.e., interfacial layer *i*. [s]Thickness of the l_3 layer. [t]Standard deviation.

The *Cage-B* films show a GISAXS image which is very different from that of the *Cage-A* film. The image apparently exhibits a scattering ring overlapped with one spot at $\alpha_f = 0.926°$ along the meridian line and another spot at $2\theta_f = 0.989°$ along the equatorial line (Figures 8.4a). The spot along the meridian line may be the first order scattering peak originated from a horizontally-oriented lamellar structure; that along the equatorial line may come from a vertically-oriented lamellar structure. Therefore, the scattering pattern has been attempted further by using the GIXS formula derived with lamellar structure model (Section 1.4 of Chapter 1). The 1D scattering profiles, which have been extracted at $2\theta_f = 0.087°$ along the meridian line and at $\alpha_f = 0.210°$ along the equatorial line from the 2D scattering pattern, are fitted successfully (Figures 8.4e-f), providing structural parameters of the lamellae present in the film. An azimuthal scattering profile has been extracted at $q = 0.843$ nm^{-1}, including the two scattering spots described above, from the 2D image in *q*-space (Figure 8.4b), and analyzed in a quantitative manner, providing orientational details of the lamellae in the film (Figure 8.4g); furthermore, this analysis confirms the presence of horizontal and vertical lamellae in a mixture. The determined structural parameters and orientational information are listed in Table 8.2. With these structural parameters, a 2D scattering image is reconstructed using the GIXS formula, as shown in Figure 8.4c; the reconstructed image is in good agreement with the measured scattering pattern.

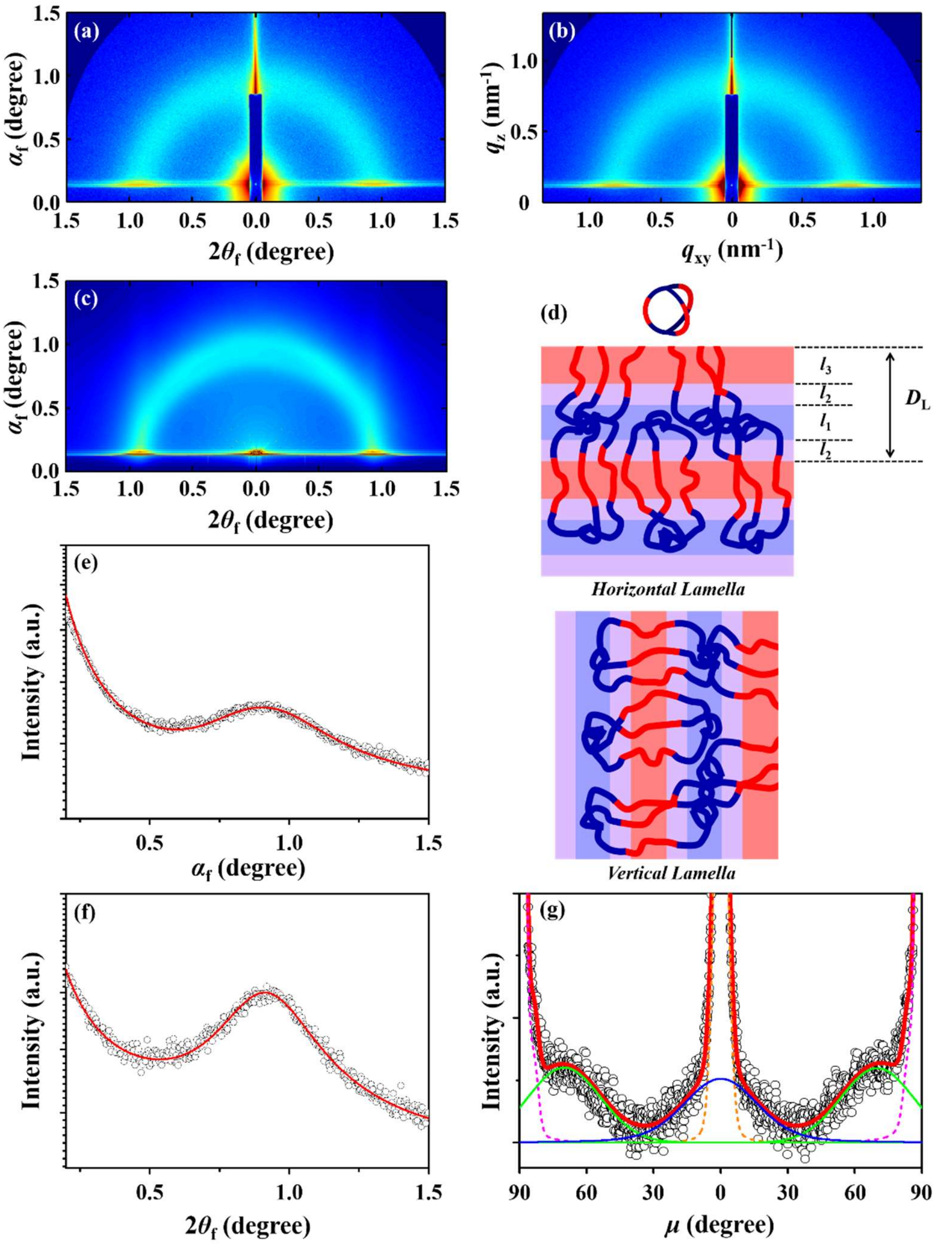

Figure 8.4 Representative GISAXS data of *Cage-B* films (100–120 nm thick) measured with α_i = 0.1438°; SDD = 2951.3 mm at room temperature using a synchrotron X-ray beam (λ = 0.12411 nm): (a) 2D scattering image in angle space; (b) 2D scattering image in scattering vector space obtained from the scattering image in (a); (c) 2D scattering image reconstructed with the determined structural parameters; (d) horizontal lamellar structure model in a front view; (e) out-of-plane scattering profile extracted along the meridian line at $2\theta_f$ = 0.087° from the scattering image in (a); (f) in-plane scattering profile along the equatorial line at α_f = 0.210° from the scattering image in (a); (g) azimuthal scattering profile extracted at q = 0.843 nm^{-1} from the scattering image in (b) where the black symbols are the measured data and the lines were obtained by the deconvolutions of the measured data: the blue solid line is the first order scattering peak of horizontal lamellar structure, the green solid line is the first order scattering peak of vertical lamellar structure, the purple dot line is the Yoneda peak, the brown dot line is a part of the reflected X-ray beam, and the red solid line is the sum of all deconvoluted peaks.

In the film, horizontal and vertical lamellae are found to be present with the volume fractions of 34.5 and 65.5 % respectively. For the horizontal lamellae, the domain spacing D_L (i.e., long period) is 6.95 nm, which consists of the l_1 layer of 2.10 nm, the l_2 layer of 1.30 nm, and the l_3 layer of 2.25 nm. A similar set of dimension parameters is observed for the vertical lamellae. The volume fraction of the PDGE block in *Cage-B* is slightly larger than that of the PTEGGE block. Thus, the l_1 and l_3 layers can be assigned by the PTEGGE and PDGE block phases respectively; the l_2 layer is the interfacial layer l_i between the PTEGGE and PDGE block phases. Both g factor and σ_φ value are slightly smaller for the vertical lamellae, compared to the horizontal lamellae. These results suggest that the vertical lamellar structure is slightly more stable dimensionally and oriented more preferentially, compared to the horizontal lamellar structure. From these structural details, the determined lamellar morphologies are schematically drawn (Figure 8.4d).

Overall, it is interesting that *Cage-B* forms phase-separated lamellar structures, as observed for the linear counterpart.[32] The lamellar morphology is quite different from the cylindrical morphology of *Cage-A*. Therefore, the *Cage-B* topology seems to cause less influences on the chain characteristics of the blocks, compared to the *Cage-A* topology. More interestingly, the morphology of *Cage-B* reveals relatively smaller domain spacing, compared to that of *Cage-A*.

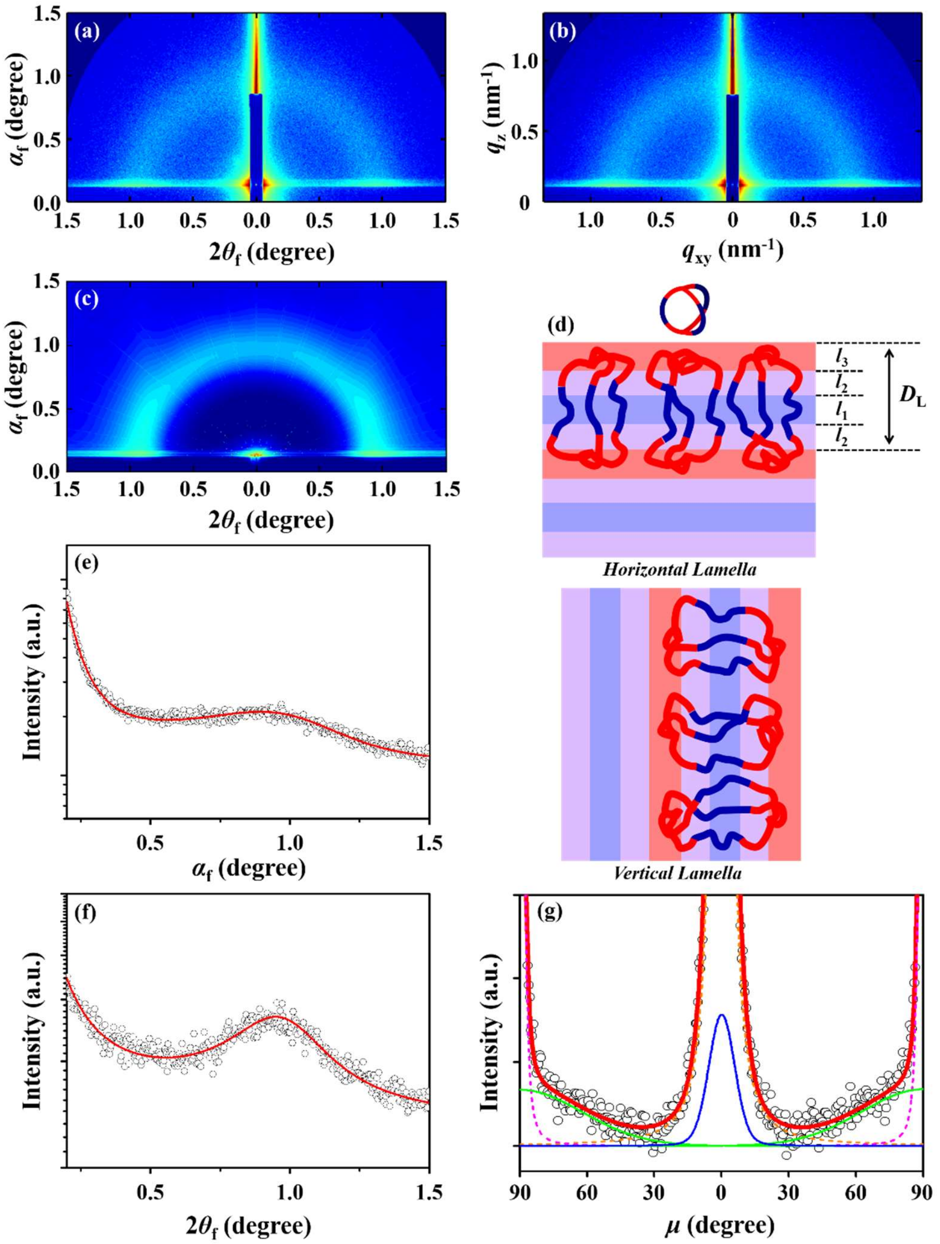

Figure 8.5 Representative GISAXS data of *Cage-C* films (100–120 nm thick) measured with α_i = 0.1392°; SDD = 2951.3 mm at room temperature using a synchrotron X-ray beam (λ = 0.12411 nm): (a) 2D scattering image in angle space; (b) 2D scattering image in scattering vector space obtained from the scattering image in (a); (c) 2D scattering image reconstructed with the determined structural parameters; (d) horizontal lamellar structure model in a front view; (e) out-of-plane scattering profile extracted along the meridian line at $2\theta_f$ = 0.071° from the scattering image in (a); (f) in-plane scattering profile along the equatorial line at α_f = 0.199° from the scattering image in (a); (g) azimuthal scattering profile extracted at q = 0.827 nm^{-1} from the scattering image in (b) where the black symbols are the measured data and the lines were obtained by the deconvolutions of the measured data: the blue solid line is the first order scattering peak of horizontal lamellar structure, the green solid line is the first order scattering peak of vertical lamellar structure, the purple dot line is the Yoneda peak, the brown dot line is a part of the reflected X-ray beam, and the red solid line is the sum of all deconvoluted peaks.

Figure 8.5a shows a representative scattering image of the *Cage-C* films. The scattering pattern is apparently similar with that of the *Cage-B* film. The scattering image has been analyzed satisfactorily as carried out for those of the *Cage-B* film (Figures 8.5b-c, 8.5e-f, and 8.5g; Table 8.2).

The analysis finds that in the film, horizontal and vertical lamellae co-exist in volume fractions of 33.9 and 6.1 % respectively. The horizontal lamellar structure is characteristic of revealing a set of structural parameters: D_L = 6.50 nm, l_1 = 1.60 nm, l_2 = 1.60 nm (= l_i), l_3 = 1.70 nm, g = 0.35, and σ_φ = 6.13. Similar structural parameters are determined for the vertical lamellar structure. However, the vertical lamellae exhibit slightly smaller g value but much larger σ_φ value, compared to those of the horizontal lamellae. Taking into consideration the volume fractions of the blocks, the l_1 and l_3 layers can be assigned by the PTEGGE and PDGE block phases respectively. The determined lamellar morphologies are schematically drawn in Figure 8.5d.

Overall, *Cage-C* behaves to form lamellar morphology, which is similar to that of the *Cage-B* film. However, the domain spacings are slightly smaller than those of the *Cage-B* film. These results suggest that the *Cage-C* topology also causes less impacts on the chain characteristics of the blocks, leading to the formation of lamellar structures. Additionally,

8.4 Conclusions

This study is the first report of the nanoscale film morphology details of cage-shaped heteroblock copolymers in three different topologies: *Cage-A*, *B*, and *C*.

The synchrotron GIWAXS analysis confirmed that for all cage copolymers, the PDGE and PTEGGE blocks are amorphous at room temperature, exhibiting no crystallite assemblies. However, the GISAXS analysis found that all cage copolymers form nanostructures resulted from the phase-separations of their blocks through the film formation process. They exhibit different types of nanostructures depending on the cage topologies. *Cage-A* forms cylindrical morphology, whereas *Cage-B* and *C* reveal lamellar morphologies. The domain spacing of nanostructure, as well as the dimensional stability and orientation varies with the cage topologies. The domain spacing is in the decreasing order: *Cage-A* >> *Cage-B* > *Cage-C*. Both the dimensional stability and orientation orders are in the increasing order: *Cage-B* ~ *Cage-C* << *Cage-A*.

In summary, this chapter has demonstrated the quantitative analysis through three layer model and two phase elliptical hexagonal cylinder model was successful in parameterizing the morphological details of cage type topologies of block copolyethers in thin films. The two models successfully identified each individual variations of cage topologies as critical factors for determining the type of morphology as well as miniaturizing domain spacings, which could never be achievable from the linear counterpart. Specifically, the domain spacings range from 6.50 to 10.85 nm depending on the cage topologies. These domain spacings are only 25.5–45.2 % of that of the linear counterpart film. In particular, the *Cage-B* and *Cage-C* topologies are relatively more efficient for reducing domain spacing. Overall, this study has demonstrated that cage-shaped heteroblock copolymer systems are a powerful and effective route to develop high performance nanolithographic materials for producing future high performance semiconductors based on pitches of 10 nm or less. Overall, the novel model analysis have successfully established new insights in the topology-morphology correlation of bicyclic block copolymers.

8.5 References

1. Patnode, W.; Patnode, W.; Wilcock, D. F. Methylpolysiloxanes. *J. Am. Chem. Soc.***1946**, *68*, 358−363.
2. Hunter, M. J.; Hyde, J. F.; Warrick, E. L.; Fletcher, H. J. Organo-Silicon Polymers. The Cyclic Dimethyl Siloxanes. *J. Am. Chem. Soc.***1946**, *68*, 667−672.
3. Scott, D. W. Equilibria between Linear and Cyclic Polymers in Methylpolysiloxanes. *J. Am. Chem. Soc.* **1946**, *68*, 2294−2298.
4. Zimm, B. H; Stockmayer, W. H. The Dimensions of Chain Molecules Containing Branches and Rings. *J. Chem. Phys*. **1949**, *17*, 1301−1314.
5. Semlyen, J. A.; Cyclic Polymers, 2nd ed., Kluwer Academic Publishers: Dordrecht, Netherlands, 2002.
6. Endo, K. Synthesis and Properties of Cyclic Polymers. *Adv. Polym. Sci.* **2008**, *217*, 121−183.
7. Laurent, B. A.; Grayson, S. M. Synthetic Approaches for the Preparation of Cyclic Polymers. *Chem. Soc. Rev.* **2009**, *38*, 2202–2213.
8. Kricheldorf, H. R. Cyclic Polymers: Synthetic Strategies and Physical Properties. *J. Polym. Sci. Part A: Polym. Chem.* **2010**, *48*, 251− 284.
9. Lonsdale, D. E.; Monteiro, M. J. Synthesis and Self-Assembly of Amphiphilic Macrocyclic Block Copolymer Topologies. *J. Polym. Sci. Part A: Polym. Chem.* **2011**, *49*, 4603–4612.
10. Jia, Z.; Monteiro, M.J. Cyclic Polymers: Methods and Strategies. *J. Polym. Sci. Part A: Polym. Chem*. **2012**, *50*, 2085−2097.
11. Jia, Z.; Monteiro, M.J. Synthesis of Cyclic Polymers via Ring Closure. *Adv. Polym. Sci.* **2013**, *262*, 295−328.
12. Tezuka, Y., Ed., Topological Polymer Chemistry: Progress of Cyclic Polymers in Syntheses, Properties and Functions, World Scientific: Singapore, 2013.
13. Wang, H.; Zhang, L.; Liu, B.; Han, B.; Duan, Z.; Qi, C.; Park, D.; Kim, I. Synthesis of High Molecular Weight Cyclic Poly(ε-caprolactone)s of Variable Ring Size Based on A Light-Induced Ring-Closure Approach. *Macromol. Rapid Commun*. **2015**, *36*, 1646−1650.
14. Xiang, L.; Ryu, W.; Kim, H.; Ree, M. Precise Synthesis, Properties, and Structures of Cyclic Poly(ε-caprolactone)s. *Polymers* **2018**, *10*, 577.
15. Isono, T.; Satoh, Y.; Miyachi, K.; Chen, Y.; Sato, S.-i.; Tajima, K.; Satoh, T.; Kakuchi, T. Synthesis of Linear, Cyclic, Figure-Eight-Shaped, and Tadpole Shaped Amphiphilic Block Copolyethers via t-Bu-P4-Catalyzed RingOpening Polymerization of Hydrophilic and Hydrophobic Glycidyl Ethers. *Macromolecues* **2014**, *47*, 2853−2863.
16. Zhao, Z.; Zhu, Q.; Wang, Z.; Lu, J.; Jin, Z.; Liu, H. A Dicyclic Scaffold for Programmed Monocyclic and Polycyclic Polymer Architectures. *Macromolecules* **2017**, *50*, 8907−8915.
17. Isono, T.; Sasamori, T.; Honda, K.; Mato, Y.; Yamamoto, T.; Tajima, K.; Satoh, T. Multicyclic Polymer Synthesis through Controlled/Living Cyclopolymerization of α,ω-Dinorbornenyl-Functionalized Macromonomers. *Macromolecules* **2018**, *51*, 3855–3864.
18. Tezuka, Y. Topological polymer chemistry for designing multicyclic macromolecular architectures. *Polymer J.* **2012**, *44*, 1159–1169.
19. Tezuka, Y.; Tsuchitani, A.; Yoshioka, Y.; Oike, H. Synthesis of θ-Shaped Poly(THF) by Electrostatic Self-Assembly and Covalent Fixation with Three-Armed Star Telechelics Having Cyclic Ammonium Salt Groups. *Macromolecules* **2003**, *36*, 65–70.

20. Igari, M.; Heguri, H.; Yamamoto, T.; Tezuka, Y. Folding Construction of Doubly *Fused* Tricyclic, β- and γ-Graph Polymer Topologies with *kyklo*-Telechelic Precursors Obtained through an Orthogonal Click/ESA-CF Protocol. *Macromolecules* **2013**, *46*, 7303−7315.
21. Tezuka, Y.; Fujiyama, K. Construction of Polymeric *δ*-Graph: A Doubly Fused Tricyclic Topology. *J. Am. Chem. Soc.* **2005**, *127*, 6266–6270.
22. Kyoda, K.; Yamamoto, T.; Tezuka, Y. Programmed Polymer Folding with Periodically Positioned Tetrafunctional Telechelic Precursors by Cyclic Ammonium Salt Units as Nodal Points. *J. Am. Chem. Soc.* **2019**, *141*, 7526−7536.
23. Jeong, J.; Kim, K.; Lee, R.; Lee, S.; Kim, H.; Jung, H.; Kadir, M. A.; Jang, Y.; Jeon, H. B. Matyjaszewski, K.; Chang, T.; Paik, H. J. Preparation and Analysis of Bicyclic Polystyrene. *Macromolecules* **2014**, *47*, 3791–3796.
24. Zhao, J.; Zhou, Y.; Li, Y.; Pan, X.; Zhang, W.; Zhou, N.; Zhang, K.; Zhang, Z.; Zhu, X. Modular construction of macrocycle-based topological polymers via high-efficient thiol chemistry. *Polym. Chem.* **2015**, *6*, 2879−2891.
25. Mohanty, A. K.; Ye, J.; Ahn, J.; Yun, T.; Lee, T.; Kim, K.-s.; Jeon, H. B.; Chang, T.; Paik, H.-j. Topologically Reversible Transformation of Tricyclic Polymer into Polyring Using Disulfide/Thiol Redox Chemistry. *Macromolecules* **2018**, *51*, 5313-5322.
26. Mato, Y.; Honda, K.; Tajima, K.; Yamamoto, T.; Isono, T.; Satoh, T. A Versatile Synthetic Strategy for Macromolecular Cages: Intramolecular Consecutive Cyclization of Star-Shaped Polymers. *Chem. Sci.* **2019**, *10*, 440–446.
27. Satoh, Y.; Matsuno, H.; Yamamoto, T.; Tajima, K.; Isono, T.; Satoh, T. Synthesis of Well-Defined Three- and Four-Armed Cage-Shaped Polymers via "Topological Conversion" from Trefoil- and Quatrefoil- Shaped Polymers. *Macromolecules* **2017**, *50*, 97−106.
28. Ree, B. J.; Satoh, Y.; Jin, K. S.; Isono, T.; Kim, W. J.; Kakuchi, T.; Satoh, T.; Ree, M. Well-Defined Stable Nanomicelles Self-Assembled by Brush Cyclic and Tadpole Copolymer Amphiphiles: A Versatile Smart Carrier Platform. *NPG Asia Materials* **2017**, *9*, e453.
29. Kim, Y. Y.; Ree, B. J.; Kido, M.; Ko, Y.-G.; Ishige, R.; Hirai, T.; Wi, D.; Kim, J.; Kim, W. J.; Takahara, A.; Ree, M. High Performance n-Type Electrical Memory and Morphology-Induced Memory-Mode Tuning of A Well-Defined Brush Polymer Bearing Perylene Diimide Moieties. *Adv. Electronic Mater.* **2015**, *1*, 1500197.
30. Ree, B. J.; Aoki, D.; Kim, J.; Satoh, T.; Takata, T.; Ree, M. Macromolecular [2]Rotaxanes Linked with Polystyrene: Properties and Nanoscale Film Morphologies. *Macromolecules* **2019**, *52*, 5325−5336.
31. Ree, B. J.; Aoki, D.; Kim, J.; Satoh, T.; Takata, T.; Ree, M. Phase Transition Behaviors and Nanoscale Film Morphologies of Poly(*δ*-valerolactone) Axles Bearing Movable and Fixed Rotaxane Wheels. *Macromol. Rapid Commun*. **2019**, *40*, 1900334
32. Ree, B. J. Materials from Chapter 5 of this Ph.D. Dissertation. Unpublished work, 2019.
33. Honda, S.; Yamamoto, T.; Tezuka, Y. Topology-Directed Control on Thermal Stability: Micelles Formed from Linear and Cyclized Amphiphilic Block Copolymers. *J. Am. Chem. Soc.* **2010**, *132*, 10251−10253.
34. Zhu, Y. Q.; Gido, S. P.; Iatrou, H.; Hadjichristidis, N.; Mays, J. W. Microphase Separation of Cyclic Block Copolymers of Styrene and Butadiene and of Their Corresponding Linear Triblock Copolymers. *Macromolecules* **2003**, *36*, 148−152.
35. Takano, A.; Kadoi, O.; Hirahara, K.; Kawahara, S.; Isono, Y.; Suzuki, J.; Matsushita, Y. Preparation and Morphology of Ring-Shaped Polystyrene-block-polyisoprenes, *Macromolecules* **2003**, *36*, 3045−3050.
36. Lescanec, R. L.; Hajduk, D. A.; Kim, G. Y.; Gan, Y.; Yin, R.; Gruner, S. M.; Hogen-Esch, T. E.; Thomas, E. L. Comparison of the Lamellar Morphology of Microphase-

Separated Cyclic Block Copolymers and Their Linear Precursors. *Macromolecules* **1995**, *28*, 3485−3489.

37. Marko, J. F. Microphase Separation of Block Copolymer Rings. *Macromolecules* **1993**, *26*, 1442−1444.
38. Jo, W. H.; Jang, S. S. Monte Carlo Simulation of The Order–Disorder Transition of A Symmetric Cyclic Diblock Copolymer System. *J. Chem. Phys.* **1999**, *111*, 1712−1720.
39. Zhang, G.; Fan, Z.; Yang, Y.; Qiu, F. Phase Behaviors of Cyclic Diblock Copolymers. *J. Chem. Phys.* **2011**, *135*, 174902.
40. Poelma, J. E.; Ono, K.; Miyajima, D.; Aida, T.; Satoh, K.; Hawker, C. J. Cyclic Block Copolymers for Controlling Feature Sizes in Block Copolymer Lithography. *ACS Nano* **2012**, *6*, 10845−10854.

Chapter 9

Conclusions

In this dissertation, the impact of various polymer topologies upon the nanoscale thin film morphological features of various homopolymers and block copolymers has been evaluated using quantitative modeling analysis of synchrotron X-ray scattering measurements through two novel models developed for this dissertation: the three layer model and the two phase elliptical hexagonal cylinder model. The subjects of polymer topology-morphology correlation investigation was held over two major categories: semi-crystalline hompolymers and a range of block copolymer systems. Homopolymers included two systems based on semi-crystalline polymers, poly(*ε*-caprolactone) (PCL) and poly(*δ*-valerolactone) (PVL). PCL homopolymer system demonstrated the impact of linear, cyclic, star, and cage topologies on the crystallization behavior and resulting lamellar formation. PVL homopolymer system demonstrated the topological effect of movable and ionically-fixed rotaxane wheels on the crystallization behavior and resulting lamellar formation. Block copolymers included a system of PVL and amorphous polystyrene (PS), and an extensive system based on poly(*n*-decyl glycidyl ether) (PDGE) and poly(2-(2-(2-methoxyethoxy)ethoxy)ethyl glycidyl ether) (PTEGGE). PVL and PS system demonstrated the impact of pseudo-miktoarm topology on the PVL crystallization behavior and the phase separation between PVL and PS blocks. PDGE and PTEGGE system, in which neither of the blocks exhibit semi-crystalline behavior, demonstrated the impact of linear, tadpole, monocyclic, bicyclic, tricyclic, and cage topologies on the phase separation beween PDGE and PTEGGE blocks. A summary of the important achievements and scientific insights from the studies is as follows:

Chapter 2 "Nanoscale Film Morphologies and Chain Conformations of Topological Poly(ε-caprolactone)s"

A cage-shaped PCL polymer and its various counterparts have been examined in terms of thermal stability and phase transitions by using TGA and DSC analyses. The nanoscale film morphologies of this series of topological PCL polymers have been investigated quantitatively by using synchrotron GISAXS and GIWAXS analyses.

The PCL polymers show topology and end group dependent thermal stabilities: *l*-PCL$_{3k}$-*B* ~ *l*-PCL$_{3k}$-*A* < *cg*-PCL$_{9k}$ ~ *cy*-PCL$_{6k}$ < *st*-PCL$_{9k}$. In particular, the highest stability of *st*-PCL$_{9k}$ could be attributed to the capped chain ends rather than the topology effect.

The phase transitions (nonisothermal crystallization and subsequent crystal melting transitions: T_c, T_{m1}, T_{m2}, heat of fusion of crystallization, heat of fusion of crystal melting, and crystallinity) are also dependent upon the molecular topologies as well as the bulkinesses of joints and end groups.

All PCL homopolymers always form lamellar structures based on orthorhombic crystal lattice in nanoscale films, regardless of the molecular topologies as well as the bulkinesses of joints and end groups. Both *cg*-PCL$_{9k}$ and *st*-PCL$_{9k}$ tend to form a mixture of horizontal (major) and vertical (minor) lamellar structures, whereas all other counterparts form only horizontal lamellar structures. The structural parameters, including overall crystallinity and orientational orthorhombic crystal domains, vary with the molecular topologies, and the bulkinesses of joints and end groups. Overall, the structural parameter details could not be rationalized easily in regard to the effects of molecular topology, joint and end group because the functions of molecular topologies are either against or cooperative to those of joints and end groups. In this chapter, the novel three layer model was successful in precisely and accurately parameterizing the morphological details as well as differentiating the extent of topological impact upon the self-assembly behavior of topological PCL homopolymers in thin films, providing useful insights in the topology-morphology correlation of semi-crystalline polymers.

Chapter 3 "Nanoscale Film Morphologies and Chain Conformations of Poly(δ-valerolactone) Bearing Mobile and Immobile Rotaxane Wheels"

PVL and its [2]rotaxanes (PVL-*rot*-F and PVL-*rot*-M) have been investigated in a comparative manner from views of thermal stability, phase transitions and nanoscale film morphology using thermalgravimetry analysis (TGA), differential scanning calorimetry (DSC), grazing incidence X-ray scattering (GIXS) techiques. These analyses have found the topological effects of fixed and movable rotaxane moieties on the fundamental properties and morphological structure of PVL as follows.

Compared to the pristine PVL, PVL axle containing ionically-fixed rotaxane moiety with its counter anion exhibited severely reduced thermal stability while slightly decreased thermal stability was observed for PVL axle with movable rotaxane wheel. All crystallization and crystal melting transition parameters of PVL axle are also reduced by the ionically-fixed rotaxane with the counter anion, but more significantly lowered by the movable rotaxane. Nevertheless, PVL-*rot*-M is confirmed to form a certain fraction of crystals that undergo melting transition at same temperature as the crystals formed by PVL-*rot*-F.

All polymers were found to form horizontal lamellar structures in nanoscale thin films, regardless of the presences of fixed and movable rotaxane moieties. Moreover, the crystalline layers in the lamellar structure are composed of three different rotational lattice domains, regardless of the fixed and movable rotaxane moieties. These microstructure formations are originated from an inherently excellent self-assembling ability of PVL as well as the relatively low volume fraction of roxtane moiety compared to that of the PVL axle.

However, structural details of such horizontal lamellar structure are discernibly influenced by the fixed and movable rotaxane moieties. The crystalline layer is thinned by the fixed and movable rotaxanes. The long period, as well as the sum of interfacial and amorphous layers is thickened by the fixed and movable rotaxanes. Both fixed and movable rotaxane moieties further cause to form tilted orientational crystal lattice domains as very minor portions in addition to the vertically-oriented lattice domain formation of PVL. The ionically-fixed rotaxane moiety tends to be highly populated in the interfacial layer rather than in the amorphous layer, resulting in thickening of the interfacial layer. In contrast, the movable rotaxane moiety is populated in both interfacial and amorphous layers, causing thickenings in the interfacial and amorphous layers. In this chapter, the novel three layer model was successful in parameterizing the morphological details with precision and also identifying the rotaxane wheel's influence as a topological feature on the self-assembly behavior of PVL axles in thin films, successfully establishing new insights in the topology-morphology correlation of semi-crystalline polymers.

Chapter 4 "Nanoscale Film Morphologies and Chain Conformations of Pseudo Miktoarm Block Copolymers based on Poly(δ-valerolactone) Macromolecular Rotaxane Linked to Polystyrene"

Thermal stability, phase transition behaviors, and nanoscale film morphology of PVL-*rot*-PS-M, PVL-*rot*-PS-F and PVL-*b*-PS have been investigated through TGA, DSC, GIXS techniques.

PVL-*rot*-PS-M is found to reveal the thermal stabilities of PVL axle and movable PS-linked rotaxane wheel independently, proving that the rotaxane wheel as the mechanical link can fully reserve the stabilities of individual block components. In PVL-*rot*-PS-F, however, the thermal stability of fixed PS-linked rotaxane wheel is severely hampered by the ionic linking character and counter anion; but the PVL axle retains its own stability reasonably well. The thermal stability could be concluded to depend on the chemical components rather than topological factors, and is in the increasing order PVL-*rot*-PS-F << PVL-*rot*-PS-M < PVL-*b*-PS.

In the cooling process from the melt state, the PVL and PS components undergo phase-separation which kinetically competes with the crystallization of PVL component. Practically, the phase-separation occurs ahead of PVL crystallization because a mass transformation of PVL block chains is necessary to the nucleation and growing crystal sites. The phase-separation, as well as the PVL crystallization is significantly enhanced by the pseudo-miktoarm topology in PVL-*rot*-PS-M where PVL axle retains chain mobility. As for PVL-*rot*-PS-F and PVL-*b*-PS, however, the fixed miktoarm and conventional linear topology restrict and suppress PVL chain mobility. As a result, cold crystallization appears heavily in subsequent heating processes for PVL-*rot*-PS-F and PVL-*b*-PS.

In nanoscale films, PVL-*rot*-PS-M forms only horizontal lamellar structure as a result of phase-separation and fringed-micelle like crystals with orthorhombic lattice in the PVL layers; the PVL layers are composed of two different orientational crystal domains in which three different rotational lattice domains are present. Differently, PVL-*rot*-PS-F forms a mixture of horizontal and vertical lamellar structures in which the PVL layers consist of three kinds of orientational crystal domains as well as three different rotational lattice domains. Similar film morphology is observed for PVL-*b*-PS; but, there are two different orientational crystal domains in the PVL layers. The structural imperfect level is relatively higher in films of PVL-*rot*-PS-F and PVL-*b*-PS, compared to that of PVL-*rot*-PS-M. Thus, the film morphologies of PVL-*rot*-PS-F and PVL-*b*-PS could be enhanced discernibly by post THF-annealing; but, such THF-annealing effect could not be observed for the film morphology of PVL-*rot*-PS-M. Overall, the nanoscale film morphology characteristics are influenced by the natures of linkers between PVL and PS blocks; in particular, the movable rotaxane linker could make significantly positive impact on the film morphology and structural parameter details. In this chapter, the three layer model analysis was successful to parameterize the morphological details of PVL-PS pseudo miktoarm block copolymers in nanoscale thin films. In addition, the novel modeling analysis has also identified the rotaxane wheel's function as mechanical linkage between PVL axle and PS block as a critical topological feature impacting the overall phase-separation behavior of PVL-PS pseudo miktoarm block copolymers, successfully establishing new insights in the topology-morphology correlation of mechanically linked block copolymers.

Chapter 5 "Nanoscale Film Morphologies of Cyclic and Tadpole Block Copolyethers"

The nanoscale film morphologies of a series of cyclic and tadpole block copolymers including their linear counterpart were investigated in details for the first time by using synchrotron GIXS analysis: *c*-PDGE-*b*-PTEGGE, *tp-A*-PDGE-*b*-PTEGGE, *tp-B*-PDGE-*b*-PTEGGE, and *l*-PDGE-*b*-PTEGGE. The quantitative GIXS analysis provides structural details on the nanoscale film morphologies and key features on the correlations between film morphology and molecular topology.

All topological block copolymers revealed nanostructures which were driven by the immiscibility due to a polarity difference between PDGE and PTEGGE blocks. The type of phase-separated nanostructure was highly dependent upon the molecular topology of the block copolymer: *c*-PDGE-*b*-PTEGGE and *tp-A*-PDGE-*b*-PTEGGE exhibited hexagonal cylindrical structures, whereas *tp-B*-PDGE-*b*-PTEGGE and *l*-PDGE-*b*-PTEGGE revealed lamellar structures. Furthermore, the domain spacing of phase-separated nanostructure showed significant dependence on the block copolymer topology: *c*-PDGE-*b*-PTEGGE < *tp-A*-PDGE-*b*-PTEGGE ≈ *tp-A*-PDGE-*b*-PTEGGE << *l*-PDGE-*b*-PTEGGE. In particular, *c*-PDGE-*b*-PTEGGE generated 49.3–67.6 % smaller domains, compared to those of the linear counterpart. These domain spacing reductions are so remarkable because they are almost twice larger than those predicted theoretically and reported previously. In cases of *tp-A*-PDGE-*b*-PTEGGE and *tp-B*-PDGE-*b*-PTEGGE, the domains were 25.0–32.5 % smaller than those of the linear counterpart. These domain spacing reductions are comparable to those either predicted theoretically or observed previously. Moreover, the cyclic block copolymer and its tadpole counterparts developed well-defined and well-oriented domain structures, compared to the poorly developed domains of the linear counterpart.

In this chapter, quantitative analysis through three layer model and two phase elliptical hexagonal cylinder model was successful to parameterize the morphological details of cyclic and tadpole block copolymers in thin films. The two models successfully identified the cyclic and tadpole topologies as powerful strategies for producing well-defined, orientation-controlled, and miniaturized domain-based nanostructures, showing great potential for developing high performance nanolithographic materials with the pitches demanded for fabricating advanced semiconductor chips planned by ITRS. Overall, the novel model analysis have successfully established new insights in the topology-morphology correlation of cyclic and tadpole block copolymers.

Chapter 6 "Nanoscale Film Morphologies of Bicyclic Block Copolyethers"

The nanoscale film morphologies of a series of bicyclic block copolymers in various molecular topologies was investigated by using synchrotron GIXS measurements and data analysis. The quantitative scattering analysis has confirmed that all bicyclic block copolymers formed nanostructures attributed to the phase-separations of the block components, PDGE and PTEGGE. The types and parameter details of the nanostructures are found to be highly dependent upon the molecular topologies.

In summary, this chapter has demonstrated the quantitative analysis through three layer model and two phase elliptical hexagonal cylinder model was successful in parameterizing the morphological details of bicyclic block copolymers in thin films. The two models successfully identified each individual variations of bicyclic topologies as critical factors for miniaturizing domain spacings, which could never be achievable from the linear counterpart. Among the bicyclic copolymers, *Bicycle-C* produces the smallest domain spacing. Overall, the novel model analysis have successfully established new insights in the topology-morphology correlation of bicyclic block copolymers.

Chapter 7 “Nanoscale Film Morphologies of Tricyclic Block Copolyethers”

Three different tricyclic topologies of PDGE and PTEGGE blocks in equivalent volume fractions have been investigated in detail by synchrotron GIXS analysis. The quantitative GIXS analysis confirmed the lamellar nanostructures resulting from the phase-separations between the blocks through the film fabrication processes. The stability, orientation, and dimensional parameters of the nanostructure are varied with the molecular topologies. Both the dimensional stability and orientation orders are in the increasing order: *Tricycle-C* << *Tricycle-A* < *Tricycle-B*. The domain spacing is in the decreasing order: *Tricycle-A* >> *Tricycle-C* > *Tricycle-B*. Overall, the *Tricycle-B* topology demonstrates most well-defined lamellar structure with the highest stability and orientation as well as the smallest domain spacing.

In summary, this chapter has demonstrated the quantitative analysis through three layer model was successful in parameterizing the morphological details of tricyclic block copolymers in thin films. All nanostructures analyzed by the modeling analysis have been identified with exceptionally smaller domain spacings than that of the linear counterpart. The domain spacing reductions are within the range of 59.1−76.5 %; these huge reductions could not be achieved with monocyclic block copolymer systems. Moreover, the domain spacings (less than 10 nm) demonstrated in this study can meet the pitches required for advanced semiconductors with high performance being scheduled for production in 2030 by the International Technology Roadmap for Semiconductors.[37] Therefore, the study opens up that tricyclic heteroblock copolymer systems (in particular, *Tricycle-A* and *Tricycle-B* type topologies) are a most efficient candidates for developing high performance nanolithographic materials being demanded for manufacturing future high performance semiconductors. Overall, the novel model analysis have successfully established new insights in the topology-morphology correlation of tricyclic block copolymers.

Chapter 8 "Nanoscale Film Morphologies of Cage Block Copolyethers"

The nanoscale film morphology of cage-shaped heteroblock copolymers in three different topologies, *Cage-A*, *B*, and *C*, were conducted through detailed GIXS analysis. The synchrotron GIWAXS analysis confirmed that for all cage copolymers, the PDGE and PTEGGE blocks are amorphous at room temperature, exhibiting no crystallite assemblies. However, the GISAXS analysis found that all cage copolymers form nanostructures resulted from the phase-separations of their blocks through the film formation process. They exhibit different types of nanostructures depending on the cage topologies. *Cage-A* forms horizontal hexagonal cylinder structure, whereas *Cage-B* and *C* reveal horizontal lamellar structures. The domain spacing of nanostructures, as well as the dimensional stability and orientation varies with the cage topologies. The domain spacing is in the decreasing order: *Cage-A* >> *Cage-B* > *Cage-C*. Both the dimensional stability and orientation orders are in the increasing order: *Cage-B* ~ *Cage-C* << *Cage-A*.

In summary, this chapter has demonstrated the quantitative analysis through three layer model and two phase elliptical hexagonal cylinder model was successful in parameterizing the morphological details of cage type topologies of block copolyethers in thin films. The two models successfully identified each individual variations of cage topologies as critical factors for determining the type of morphology as well as miniaturizing domain spacings, which could never be achievable from the linear counterpart. Specifically, the domain spacings range from 6.50 to 10.85 nm depending on the cage topologies. These domain spacings are only 25.5–45.2 % of that of the linear counterpart film. In particular, the *Cage-B* and *Cage-C* topologies are relatively more efficient for reducing domain spacing. Overall, this study has demonstrated that cage-shaped heteroblock copolymer systems are a powerful and effective route to develop high performance nanolithographic materials for producing future high performance semiconductors based on pitches of 10 nm or less. Overall, the novel model analysis have successfully established new insights in the topology-morphology correlation of bicyclic block copolymers.

In conclusion, a thorough investigation regarding the correlation between polymer topology and thin film morphology has been successfully carried out for selected cases of homopolymers and block copolymers via quantitative analysis of synchrotron X-ray scattering measurements through theoretical models newly developed in this dissertation: the three layer model and the two phase elliptical hexagonal cylinder model. The two novel models have successfully analyzed and obtained significant scientific insights regarding how polymer topology impacts the resulting nanoscale film morphology. Based on the model analysis results, the linear, cyclic, star, cage, and rotaxane topology greatly influence the phase behavior, chain conformation, and chain packing behavior of semi-crystalline homopolymers. Modeling analysis have successfully revealed that polymer topology is an effective tool for refining and controlling the overall polymer morphology in nanoscale film. Pseudo-miktoarm, linear, tadpole, monocyclic, bicyclic, tricyclic, and cage topologies, in conjunction with the block arrangement within the topology, bring great impact to the thin film morphology of block copolymers. Cyclical and cage topologies are especially effective in reducing the domain spacings of phase-separated structures with varied levels of ordering. Such topologies bring previously unattainable levels of miniaturization of morphological structures when compared to conventional linear topology. The analysis results obtained from the novel models present detailed insights that aid the fundamental comprehension of how polymer topology impacts the chain conformation and self-assembly behavior in thin film. The three layer model and the two phase elliptical hexagonal cylinder models have, therefore, demonstrated highly competent levels of capability in quantitatively analyzing and parameterizing the nanoscale film morphologies of a wide range of topological polymers with accuracy and precision. It could be stated that the two novel models present great capacity to be utilized for more diverse topics within topology-morphology investigations and critically contribute to the future development of topological polymers for various potential applications.